Engineered nanofluidic platforms for single molecule detection, analysis and manipulation

Paolo Cadinu

Department of Bioengineering
Imperial College London

A thesis submitted in partial fulfilment of the requirement for the degree of Doctor of Philosophy

April 2019

Abstract

Since the pioneering studies on single ion-channel recordings in 1976, single molecule methods have evolved into powerful tools capable of probing biological systems with unprecedented detail.

In this work, we build on the versatility of a type of nanofluidic devices, called nanopipettes, to explore novel modes of single molecule detection and manipulation with the aim of improving spatial and temporal control of biomolecules.

In particular, a novel nanopore configuration is presented, where biomolecules were individually confined into a zeptoliter volume bridging two adjacent nanopores at the tip of a nanopipette. As a result of this confinement, the transport of biomolecules such as DNA and proteins was slow down by nearly three orders of magnitude, leading to an improved sensitivity and superior signal-to-noise performances compared to conventional nanopore sensing. Active ways of controlling the transport of biomolecule by combining the advantages of nanopore single-molecule sensing and Field-Effect Transistors are also presented. These hybrid platforms were fabricated in a simple two step process which integrates a gold electrode at the apex of a nanopipette. We show that these devices were effective in modulating the charge density of the nanopore and in actively switching "on" and "off" the transport of DNA through the nanopore.

Finally, a nanoscale dielectrophoretic nanotweezer device has been developed for high resolution manipulation and interrogation of individual entities. Two closely spaced carbon nanoelectrodes were embedded at the apex of a nanopipette. Voltage and frequency applied to the electrodes generated a highly localized force capable of trapping and manipulating a broad range of biomolecules. These dielectrophoretic nanotweezers were suitable for probing complex biological environments and a new technique for minimally invasive single-cell nanobiopsy was established. Such study provides encouraging results on how nanopipette-based platforms can be integrated as a future tool for routinely interrogating molecules at the nanoscale.

Declaration

I hereby state that the work contained in this thesis is my own, or appropriately referenced in the text or in the acknowledgements if pertaining to other individuals.

Paolo Cadinu
April 2019

Acknowledgements

Without any doubt this is the most important part of this work. My first thoughts go to my supervisors: Prof. Joshua B. Edel and Dr. Sylvain Ladame. For introducing me to biosensing and to the single-molecule world, for the precious time you dedicated me in the lab, for constantly stimulating my scientific curiosity, for leaving me plenty of freedom to work on new ideas, for leaving your office doors open all the time, for shaping me as a scientist, Thank you!

I would like to express my sincere gratitude to Prof. Emmanuel Drakakis who always supported and encouraged my choices. Thank you!

My profound esteem goes to Dr. Binoy Paulose Nadappuram, a friend, a colleague and for sure a game changer during this time as a PhD student. Much of this work was performed in close collaboration with him. For all the time I spent with you in the lab, for teaching me many things, for countless conversations on science and beyond. Thank you!

I am incredibly grateful to have encountered Dr. Aleksandar P. Ivanov and Jasmine Sze along this PhD. Since the first day Alex shared his tremendous experience constantly providing precious advices at work and outside. With Jasmine I shared the office, lab-work (e.g. her precious help on anything concerning ssDNA), ideas and tons of good moments. Thank you!

Among the many people I had the chance to work with at Imperial I would like to thank Viktoria Urland for her help with microfluidics stuffs, Dr. Jorge Garcia Gonzalez for providing cells whenever was needed, Liang Xue for countless gold depositions on the nanopore-FET project, Dana Al Sulaiman for feedback on this thesis and for introducing me to the world of hydrogels, Dr. Colin Crick, Dr. Leonora Velleman and Dr. Agnieszka Rutkowska for their help in chemistry matters, Giulia Campolo for the protein detection with nanobridge, Dr. Yanjun Zhang for the SICM measurements, Avijit Barik and Prof. Sang-Hyun Oh for simulations. Thank you!

I would also like to thank to Prof. Ramon Vilar, Prof. Yuri Korchev and Prof. Tim Albrecht for sharing their knowledge and opening the doors of their labs when I need it. Thank you!

To this thesis remarkable inputs and feedback came from (not yet famous) neuroscientists, engineers and even an economist. Dr. Benjamin Hardcastle (monumental at SW7 2AZ and outdoor), Dr. Luca Annecchino, Dr. Pietro Maoddi and Davide Perretti. Thank you!

Behind the scenes, other members of the labs, friends at Imperial and outside were source of motivation and inspiration: Brian, Rozie, Ronja, Maria Laura, Matthew, Marion, Joe, Ilias, Marie, George, Alex, Chiara, Agostino, Javi, Fernan, Anita, Chiara, Jane, Isobel, Shenglin, Chris, Francesca, Billy, Raquel, Eva, Ren, Siri, Ben. Thank you!

A babbo, mamma e mio fratello Antonello.

Table of contents

List of figures

Nomenclature

Roman Symbols

$\alpha - HL$	α -hemolysin
AFM	Atomic Force Microscopy
C_q	Quantification Cycle
CM	Clausius-Mossotti factor
CV	Cyclic Voltammetry
DEP	Dielectrophoresis
DNA	Deoxyribonucleic Acid
$dsDNA$	double stranded DNA
ECD	Equivalent Charge Deficit
EDL	Electric Double Layer
$EDTA$	Ethylenediaminetetraacetic Acid
$emCCD$	electron multiplying Charge Coupled Device
ETF	Electrothermal Flow
F_{DEP}	Dielectrophoretic Force
FEM	Finite Element Method
FET	Field-Effect Transistor
kbp	kilobase pair

MSD	Mean Square Displacement
N.A.	Numerical Aperture
PCR	Polymerase Chain Reaction
pDEP/*nDEP*	positive/negative DEP
PDF	Probability Density Function
pI	isoelectric point
R_g	Radius of gyration
RNA	Ribonucleic Acid
SECCM	Scanning Electrochemical Cell Microscopy
SECM	Scanning Electrochemical Microscopy
SEM	Scanning Electron Microscopy
SERS	Surface-Enhanced Raman Spectroscopy
SICM	Scanning Ion Conductance Microscopy
SNR	Signal-to-Noise Ratio
ssDNA	single stranded DNA
TEM	Transmission Electron Micrscopy
Tris	Tris(hydroxymethyl)aminomethane
V_{pp}	peak-to-peak Voltage
WD	Working Distance
WE	Working electrode
FWHM	Full Width Half Maximum

Chapter 1

Introduction

1.1 Single molecule detection

The future holds the promise for personalized medicine where DNA sequencing and high-throughput diagnostics is performed routinely, at affordable cost and rapid turnaround times [1]. The field of single molecule biophysics is turning these promises into reality enabling researchers to probe, monitor and detect molecules one at a time. The ability to perform such sensitive measurement is a vitally important aspect in medical applications where it is necessary to investigate rare species or study the heterogeneity of a population otherwise hidden in the noise of an ensemble type of measurement. Whereas a plethora of single molecule techniques have been proposed, working with single entities in complex systems remains a challenge.

This thesis describes the development of new nanofluidic tools aimed at improving detection and manipulation of individual biomolecules. On one hand, within the context of solid state nanopore sensing, it proposes new strategies aimed at improving sensitivity: by controlling analyte transport through a nanoscale channel, temporal and spatial resolution are enhanced. On the other hand this thesis focuses on developing a novel hybrid single molecule technique where nanofluidics, in the form of nanoprobes, fluorescent microscopy and dielectrophoresis converge together allowing to study and manipulate individual biomolecules in solution and in a more complex scenario such as single cell for targeted sub-cellular biopsies.

1.2 Single molecule detection and manipulation: an overview

Over the last 20 years, breathtaking technological advances have allowed the development of a remarkable variety of methods study molecules at the single-molecule level (**Figure 1.1**).

Nowadays, the field is steadily expanding; however, all current techniques can be clustered in macro-categories depending on the nature of their interaction with the molecule. The first group includes optical spectroscopy, under which fluorescence spectroscopy is among the most commonly explored technique. Other established techniques which belong to this category include confocal microscopy, total internal reflection, single molecule stochiometry, and Förster Resonance Energy Transfer (FRET) [2, 3].

In 1994, the surpassing of the long-standing issue of the diffraction limit was predicted [4]. Since then, fluorescent microscopy has experienced a new beginning where several super-resolution microscopy variants have been proposed [5], all based on the same idea of confining the probing volume. Consequently, the applications of single fluorophore detection expanded to the biological sciences field. Notable applications include resolving the structure of various viral [6] and bacterial [7] proteins or investigating the organization, dynamics and maintenance of subcellular entities in live cells [8] such as bacterial nucleoid during the cell cycle [7].

Another extremely valuable optical spectroscopic technique is Raman spectroscopy [9]. Raman spectroscopy is a method for studying the inelastic scattering of light and unlike the aforementioned fluorescence, it provides the unique chemical fingerprint of an individual molecule by probing its vibrational states [10, 11]. Although Raman spectroscopy is outside the main interest of this thesis, it is important to mention that surface-enhanced Raman spectroscopy (SERS) and tip-enhanced Raman spectroscopy (TERS) have emerged as analytical tools to probe environments at a molecular level [9]. A second macro area is single molecule force spectroscopy. The most common force spectroscopy techniques [12, 13] are optical tweezers, magnetic tweezers and atomic force microscopy which permit measurements of force (0.01-10^4 pN) and displacement (0.1-10 nm) generated by single molecules ranging from cells to small molecules and proteins. For example, this accurate control of force has been used to study the mechanical unfolding of RNA structures [14] and more generally to study the complex unfolding of single proteins and nucleic acid structures [15]. Most significantly perhaps, optical tweezers, have allowed scientists to experimentally observe the central dogma of biology: individual base pair steps of transcribing RNA polymerase advancing along DNA [16].

In correlation with the impressive progress accomplished in the field of computer power in the last decade, there was a fast development of new computational models and simulations for biological queries[17]. Since biomolecular systems display a hierarchical nature in time and space, it is reasonable to model them starting from their constituent building blocks. Indeed, atomistic modelling and coarse grained modelling have been developed and applied for many years[18]. As observed experimentally, it is possible to make theoretical predictions

about how a protein interacts with other biomacromolecules undergoing unfolding-folding transitions, or study aggregation processes. Starting from monomers, it is possible to understand the process that generates ordered or disordered fibrils and all the intermediate aggregates that occur as a result of distinct aggregation pathways [19, 17].

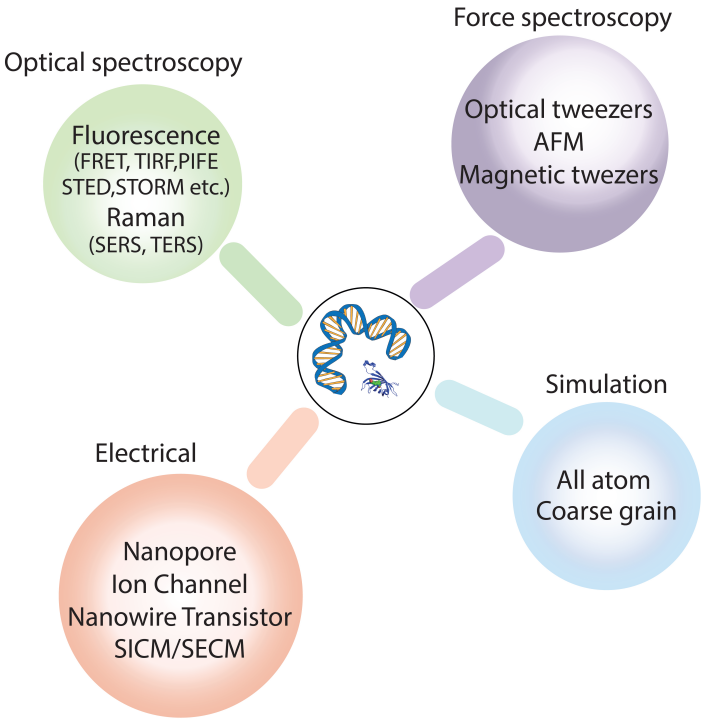

Fig. 1.1 Single Molecule techniques. A panorama of the most popular techniques employed in the field of single molecule detection and manipulation. Depending on the type of interaction exherted on the molecule, the techniques can be grouped into one of four categories: optical spectroscopy, force spectroscopy, electrical approaches, or simulation/computational approaches. Adapted with permission from [20]. Copyright (2014) Nature Publishing Group.

Despite the fantastic contribution to single molecule science that the abovementioned approaches have provided so far, there are still technical challenges to be addressed:

- Labels. Fluorescent spectroscopy and force spectroscopy both require labels. Labels can have the potential side-effect of interfering with the biological process under investigation. Labelling not only limits the number of species or analytes that can be studied, but it also removes the potential to probe intermediate species being generated during the observation/investigation/analysis. Even if Raman spectroscopy does not technically require any label, generally the output signal that most molecules generate is low whether using SERS or TERS, so labels, known as Raman reporters, are in fact often used to overcome this limitation.

- Probe degradation. In the specific case of fluorescent spectroscopy, the stability of the fluorophore is crucial. The number of oxygen species, which are responsible for pho-

tobleaching, are normally minimized using oxygen scavengers. However, especially when measuring in vivo, oxygen radicals are still present. On top of photodamage, sample heating has to be considered for both fluorescent spectroscopy (e.g. Super resolution microscopy), Raman spectroscopy (SERS) and force spectroscopy (e.g.optical tweezers). Additionally, AFM tips experience degradation due to low specificity when exposed to complex media.

- Computing power. Practical applications are still limited due to algorithmic efficiency available computing power. For example, even using a supercomputer dedicated to atomistic molecular dynamics simulations, it is possible to simulate small and fast processes such as folding of small proteins. The maximum number of atoms involved in the simulation is still "limited" to one hundred thousand which is still far from simulating a complex scenario.

There is a single molecule category, established around electrical detection and manipulation of single molecules, that provides elegant solutions to these problems. Within this area, the leading technology is nanopore. Broadly speaking nanopore sensing is inspired by Coulter counter and consists of either a single or an array of nanometric apertures located in an electrically insulated membrane. They are used for the label-free detection of DNA, RNA, proteins, polymers as well as small molecules. Nanopore sensors have already demonstrated outstanding molecular abilities by sequencing individual DNA molecules in a cheap and time-efficient manner. This platform is now commercialized by a company called Oxford Nanopore. That said, applications are by no means restricted to DNA sequencing and in order to understand why nanopore represents a leap ahead in single molecule technology, it is essential to point out the advantages of nanopore platforms. First, nanopore is label free hence it does not interfere with the process under examination, and it is not subjected to probe degradation or analyte damage because of destructive reading. This implies that monitoring for long time is not an issue and there is no set limits to the number of interacting species that can be explored in a given sample. Selectivity can be easily implemented by tuning analyte affinity to the nanopore via chemical modification [21]. Secondly, nanopore is one of the few techniques that allows single-molecule measurements to be performed with sufficient speed and high statistical accuracy [22]. This is not a trivial problem and is linked to the different concentration regimes in which sensing, single molecule experiments and biological interactions normally occur. More specifically, assuming a measurement volume of 1 fL, and an average diffusion coefficient for biomolecules of 10^{-7}cm s^{-1}, the concentration at which single molecule techniques operate ranges from 1 pM-1 nM [22]. These numbers ensure that, at any given time point, there is not more than one molecule in the probing volume. On the other hand low sample concentration also means longer acquisition times. In an ideal

scenario, a single molecule system should be able to operate in complex environments where the analyte concentration spans several order of magnitudes. For instance, to investigate a biological process (e.g. enzymatic reactions), it is expected to operate at relatively high concentrations (nM to mM) while for diagnostic and biosensing applications, it should operate at relatively low concentrations (e.g. the concentration of biologically relevant proteins present in serum was estimated to range between pM to fM [23]). In reality, the concentration regime at which most of the current single molecule techniques function does not span from fM to mM but it is strongly limited and therefore it represents a clear limitation. While the upper threshold has been expanded in various ways by molecule confinement (e.g. zero mode waveguides [24]) or reducing the probing volume (e.g. STED), nanopore technology was able to improve the more intricate issue of low detection limit and consequent long measurement time required to have quantitative analysis; in the case of nanopore, the time between one event and the next follows the opposite trend with concentration. For instance by employing a nanopore sensor in conjunction with the alternating current technique of dielectrophoretic trapping, detection of 5fM DNA was achieved within two minutes with more than 600 events recorded [25].

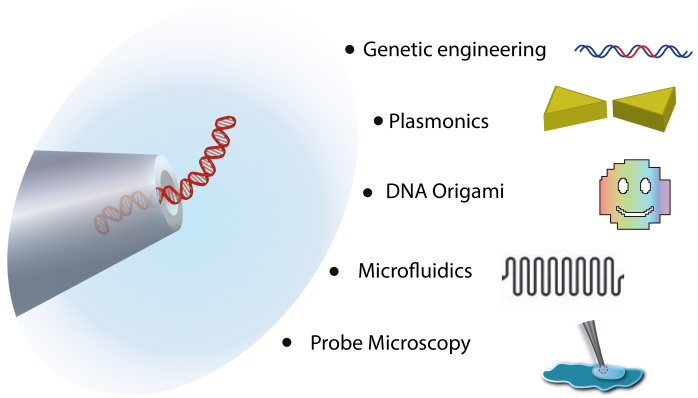

Fig. 1.2 Combining nanopore and other single molecule techniques. Nanopore sensing is an extremely flexible platform which provides the possibility of integration with other single molecule and non single molecule methods to maximize detection and manipulation at the nanoscale. Examples are Genetic engineering, plasmonics, DNA origami, Microfluidics, SICM, SECM and similar probe-based microscopy techniques.

In general, every sensing strategy has both advantages and disadvantages. Nanopore is not excluded from the list. Therefore it is clear that there is not only one solution or method to perform detection and manipulation at the nanoscale level meaning that depending on variables such as required temporal resolution, spatial resolution, sample complexity, just to name a few, some methods perform better than others. Again, this is not as simple as it sounds because it conceals an extremely powerful concept: how versatile is a platform

so that it can integrate and run simultaneously with other techniques for a more accurate analysis or manipulation? Nanopores, and particularly a sub-class called nanopipettes, are extremely flexible and aside from all the possible detection configuration that it can assume when used on its own (e.g. pulse resistive mode [26], tunneling, Field-Effect Transistor [27], electrochemical [28], fluorescence [29]), the major merit comes from all the possible other techniques (single molecule and not) it can be used in conjunction with (**Figure 1.2**). Integration with plasmonics enabling spectroscopy, microfluidics, DNA origami, genetic engineering, probe microscopy techniques, nanofabrication and nanopatterning allows for not only incrementation of the information content, but also (as will be discussed in this thesis) the reconfiguration of the same tool into a single molecule manipulator in quasi-physiological conditions or in-vitro environments.

These premises lay the grounds for why nanopore or nanopipette is the device of choice for this project. The following section briefly introduces the reader to the basic principles of nanopore sensing describing some cutting-edge applications and open challenges which are beneficial to fully understand the motivation behind this work.

1.3 Nanopore technology

Nanopore devices constitute an established powerful class of single-molecule sensors whose detection principle is similar to that of the Coulter counter typically used for the detection of micrometer-sized particles. The Coulter method measures spike-like decreases in electrical impedance produced by a particle suspended in an electrolyte solution. The sensing region is represented by a small opening equipped with electrodes. When particles are driven through the aperture, they result in partial blocking of the ionic current which is related to the volume of the particle itself [30]. Similarly a nanopore sensor consists of either a single or an array of nanometric apertures located in an electrically insulated membrane which separates two reservoir filled with electrolyte solution. However, nanopore apertures are a thousand times smaller than those used for Coulter counters, thus nanopore enables detection of nano-sized objects. Broadly speaking, when a voltage is applied between the two chambers, charged species (e.g. DNA) are electrodynamically threaded through the pore and, by recording the ionic current flow, it is possible to identify individual analytes due to the pore conductance modulations they generate upon passage. This detection mechanism, called pulse resistive sensing, is one of the most popular detection mechanisms; however, it is not the only one (alternative detection mechanisms includes, among others, tunneling-based readout, field effect sensing, optical detection [31–33]).

Depending on the nature of the nanopore and the membrane that supports it, nanopores are classified into two main categories: biological nanopore or solid state nanopore.

1.3.1 Biological pores

Biological pores are complex protein assemblies (or alternatively self-assembled peptides) that perform one of the most crucial, yet elementary, processes of life: transporting ions and electrically charged molecules such as oligonucleotides or proteins from one region of the cell to another in an heterogeneous electrolytic medium [34]. Depending on their chemical composition and structure they act as molecular gateways allowing molecules with certain molecular weight, electric charge or specific chemical footprint to go through while rejecting all others [35]. In nature, there are several types of biological pores which are responsible for a range of different physiological functions:

- *Ion channel proteins.* Transport of ions (e.g. Na^+, K^+, Ca^{2+}) across membranes, regulation of membrane potential, preserving cell homeostasis of ion concentrations and signal transduction.
- *Nuclear Pore Complex.* Transport of proteins, oligonucleotides and small molecules across the nuclear membrane.
- *Porins.* Transport water soluble analytes across membranes of bacteria and other small organelles.
- *Aquaporins.* Transport of water molecules across lipid membranes.
- *Membrane attack complex (or Terminal complement complex).* It is related to an immune system response; it is responsible for forming a transmembrane channel on the surface of the pathogen cell disrupting its membrane and ultimately leading the cell to death.
- *Translocator protein pores of the endoplasmic reticulum.* Responsible for moving proteins across the surface of the endoplasmic reticulum.
- *Antimicrobial and toxin peptides pores.* Transport of proteins into the target cell as well as cell lysis of microbial cells.
- *Viral pores.* Transport of nucleocapsid inside the targeted cell.
- *Amyloid pores.* Potentially involved in neurodegenerative disorders such as Alzheimer and Parkinson diseases due to the aberrant protein regulation.

In the field of nanobiotechnology,the term nanopore was associated with single molecule sensing in 1994 when Bezrukov gave the first demonstration that a biological pore can serve as a single molecule sensor [36]. Using an alamethicin pore mounted on a lipid bilayer, he reported conductance amplitude modulation upon the passage of poly(ethylene glycol) across the membrane [36]

The concept of biological nanopore sensors was further refined in 1996 when Kasianowicz and co-workers brilliantly demonstrated that single-stranded RNA and DNA could be detected by monitoring the ionic current across a α-hemolysin (α-HL) protein channel seated on a lipid bilayer [37]. The bacterial protein pore α-HL was and still is extremely popular within the nanopore community. One of the reasons was the immediate uncovering of its crystal structure with almost atomic resolution with X-ray crystallography: seven identical protomers from Staphylococcus aureus self-assemble into a mushroom-shaped structure consisting of 14-stranded transmembrane β barrel and a cap region with external dimensions of 10 nm x 10 nm. The lumen of the pore has a diameter ranging from 4.6 nm to 1.4 nm in the narrowest point [38, 39] proving that the channel is sufficiently large to accommodate single-stranded polynucleotides. Another reason that follows from the first is the possibility of genetically and chemically engineering the pore to target a specific analyte [40]. In addition to robustness, because of the lack of any moving part inside the pore, the small dimension of the pore aperture and its highly reproducible sub-nm self-assembly precision, make α-HL extremely attractive for single molecule sensing applications. However, over the time, as shown in **Figure 1.3**, α-HL has been accompanied by novel biological pores, with different structures, dimensions and charges. Although initially designed for DNA sequencing, biological nanopores have been customized for specific applications that include detection of metal ions [41], nucleotide mutations [42], proteins [43, 44] and circulating microRNA [45, 46].

One of the main aspects of the pore architecture is the pore size that is defined as the narrowest point along the vertical axis of the aperture. It is important to point out the relation between pore size and sensitivity. In an ideal scenario the sensitivity is maximum when the molecule is slightly smaller than the pore itself so that it occupies the most space while still being able to translocate. In a more simple way: the sensitivity is at its optimum point if the pore can "hug" the molecule while it is passing through. Following this concept α-HL pore (1.4 nm pore diameter), but also OmpG (1.3 nm), MspA (1.2 nm) and AeL (1.0 nm) are suitable for small analytes such as single stranded nucleic acids. However, for other larger molecules such as dsDNA or proteins, ClyA and phi29 motor pores, with a pore diameter of 3.3 nm and 3.6 nm respectively, work better.

Biological Nanopore	α-HL	OmpG	MspA	AeL	Phi29 Motor	ClyA
Structure	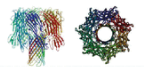	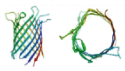	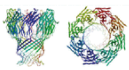	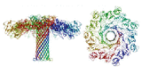	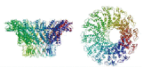	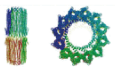
Critical Dimension	1.4 nm	1.3 nm	1.2 nm	1.0 nm	3.6 nm	3.3 nm
Type of Analytes	Small molecules, RNA, ssDNA, dsDNA, proteins	Small molecules, proteins	ssDNA, dsDNA	ssDNA, proteins	Small molecules, ssDNA, dsDNA, proteins	dsDNA, proteins

Fig. 1.3 Biological nanopores. Most commonly used biological nanopore with structure and type of analyte detected. Adapted with permission from [47]. Copyright (2017) American Chemical Society.

Sensitivity is also a function of the length of the sensing region along the z-axis of the pore. For example the sensing region of α-HL is about 5 nm (equivalent to the constriction domain of the β barrels) while for MspA it is almost ten times smaller at 0.6 nm. This has a huge impact in applications like DNA sequencing where ultra high spatial resolution is required. At any given time, no more than 3-4 nucleotides occupy the sensing region of MspA compared to 20 nucleotides for α-HL.

All the most common biological pores listed above shared several key advantages: given the quasi-atomic precision during the pore self-assembly mechanism, reproducibility is definitely a core feature. Every pore presents the same chemical composition, geometrical structure and charges. Surface modification is the second core feature. Fine tuning the charges present inside the pore by altering the chemical structure or adding new functional groups in specific locations via genetic engineering is of the highest precision in biological pores [48].

While offering major improvements in single molecule detection, biological pores have the following limitations:

- Lipid bilayer limited stability (dependent on voltage applied, pH and over the time) [35]
- Restricted tuning range of pore size (sets constraints on the molecular weight of the analyte that can be investigated)
- Limited control over the nanopore insertion within the lipid bilayer membrane [35]
- Nanopore position changes over time because of 2D diffusion [35]

1.3.2 Solid State Nanopores

In solid state nanopores, the lipid bilayer is replaced with a polymeric or inorganic membrane. Historically, the materials of choice were Si and SiN. This is because of the 30+ years (or decades) of experience accumulated in the fabrication of MOSFET for integrated circuits. In the early 2000, Intel was able to commercialize Pentium 4 CPU, which consisted of 125 million transistors manufactured using 90 nm CMOS technology allowing INTEL to make the gate of every transistor about 45 nm in width and and about 1 nm in thickness [49, 50]. This remarkable nano fabrication quality and the ability to cost-effectively mass produce nano devices were extremely attractive for the nanopore community. In addition CMOS scaling rush was far to be over hence more technological advancement would likely have happened in the near future.

In 2001, Li and co-workers reported a method called "ion beam sculpting" that allowed them to fabricate nanopore down to 1.8nm in diameter [51]. A low energy ion beam (FIB) was used to open an aperture on a Si_3N_4 membrane while a feedback-controlled ion sputtering system was used to count the ions transmitted through the opening pore and measure the sample temperature, both crucial parameters to monitor during the pore opening. The device was then used to detect 500 bp DNA molecules in solution. FIB based fabrication was proposed with a range of different ions including He, Ne, Kr, Ga, Xe, Kr [52–54] but the equipment cost limited its extensive usage and adoption. An important advancement happened when transmission electron microscope (TEM) was proposed to achieve the same goal [55]. Starting from a Silicon-on-insulator (SOI) wafer, an initial pore was opened by wet etching and then refined with TEM. Surprisingly, depending on the initial pore diameter, if below 50 nm or above 80 nm, TEM was able to shrink or expand the aperture respectively. In addition, the visual quasi-atomically precise feedback of the TEM made the fabrication of sub-10nm extremely reliable. Recently, conceiving pores smaller than 1nm was achieved by either using electron beam-induced sputtering in a scanning transmission electron microscope (STEM) [56] or by electrochemically removing atoms in a mobybdenim disulfide (MoS_2 membrane). To date, a broad range of supporting membrane materials (both organic and inorganic [21]) have been exploited with a growing interest in 2D materials such as graphene [57–60], boron nitride (BN) [61], hafnium oxide (HfO_2 [62]) and mobybdenim disulfide (MoS_2 [63–65]). 2D materials offer the possibility of creating atomically thin nanopores comparable to the spacing between DNA bases (a graphene layer has a nominal thickness of 0.34 nm) [66], resulting in extremely high spatial resolution. For instance, Feng and co-workers were able to identify single nucleotides in solution by using a MoS_2 nanopore with an ionic liquid/water viscosity gradient system [64]. Solid State nanopores have been employed in a myriad of applications aside from DNA sequencing which, to date,

have mostly been realized with biological nanopores but not yet with solid state nanopores. Applications include detection of dsDNA [67], ssDNA [68], RNA [69, 70], proteins [71], protein/protein [72] or protein/DNA complexes [73, 74], screening RNA targeted drugs [75], or applications that involve monitoring chemical and biochemical reactions, genomic mapping or investigating biophysical phenomena.

For example, nanopores were used to study the self-entanglement of DNA as a function of a broad range of lengths (2.7 kbp up to 166 kbp) [76]. This is of particular interest because there is a lack of experimental techniques to investigate this phenomena. Starting from single DNA event recordings, they produced statistical analysis of the knotting probability but more interestingly about the location of the knots along the strand. Apart from the long and expensive fabrication process, solid state nanopores have the issue of high translocation speed that limits their ability to not only discriminate between one nucleotide base and the other (as in the case of sequencing) but also to differentiate between oligonucleotides of different lengths. This issue, to which biological pores are not immune, is particularly problematic in the case of detecting proteins. On top of non-specific adsorption onto the surface and thus pore blockage, the main challenges of protein detection are their high translocation velocity and poor signal-to-noise ratio (SNR) [77]. An elegant solution to partially circumvent this issue is by chemically modifying the pore with metal, organic, or inorganic materials which provides more specificity while selectively limiting non-specific interactions [78, 21, 72, 79, 80]. Furthermore, fine-tuning of parameters such as viscosity, pH (close to the isoelectric point (pI) of the analyte), and temperature has proven to impact the analyte velocity and thus detection sensitivity [31]. In general the solid-state nanopore field is still undergoing further technical advances to better control the transport of molecules across the pore, limit molecule fluctuation, increase the SNR performances (reduce noise) and further reduce the fabrication cost.

1.3.3 Nanopipettes

Nanopipettes are becoming an increasingly popular choice among the solid state nanopore community due to the following attractive features [81, 82]: nanopipettes are extremely easy to fabricate and do not require expensive instruments. The starting material is quartz or borosilicate capillaries which are exposed to laser-assisted heating then mechanically pulled by commercially available instruments. The geometry of a nanopipette is conically shaped and the pore size can be tuned by varying the pulling parameters. In less than 10s it is possible to fabricate a nanopore aperture in the order of tens to hundreds of nanometers (**Figure 1.4**) with an estimated cost of less than 50p. Running costs of clean room facilities, equipment maintenance, trained personnel and starting material (e.g. MoS_2, Si wafers etc.)

for conventional solid-state nanopore are orders of magnitude higher if compared with nanopipettes. To date, the most adopted CO_2-based bench-top laser puller is manufactured and commercialized by Sutter Instrument company (USA), priced around £10k.

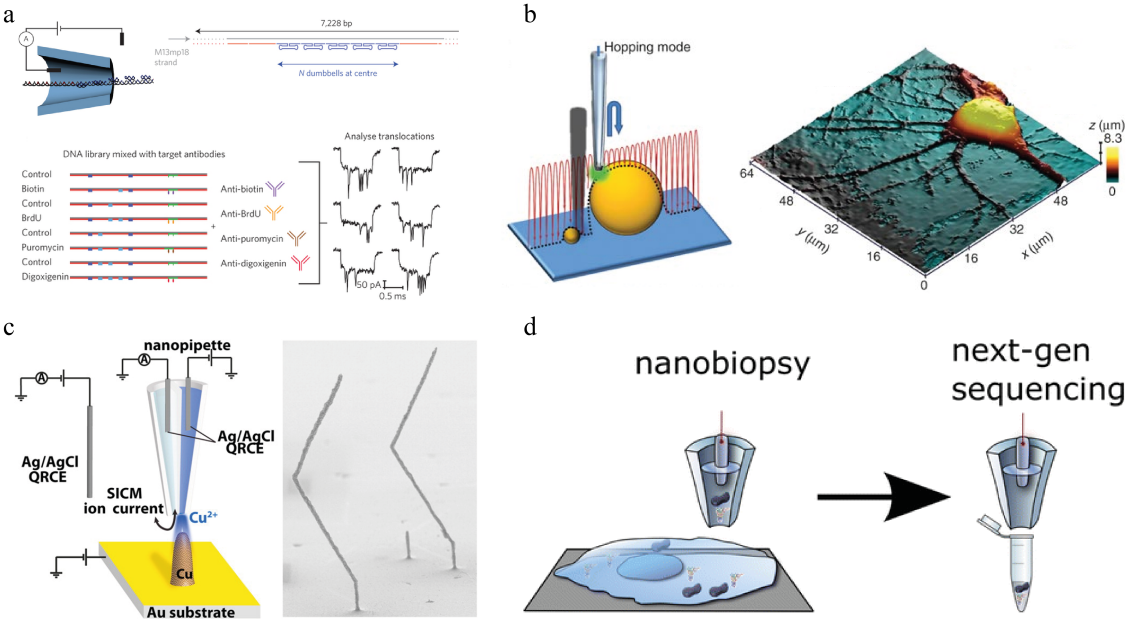

Fig. 1.4 Applications of nanopipettes. Nanopipettes are an extremely versatile tool offering the possibility of serving different purposes. (a) *Biosensing.* Multiplex detection of antibodies using DNA structure as digital barcode to identify a unique analyte. A single stranded DNA is used as the backbone architecture in which one antigen for the antibody detection and unique barcode associated to the specific antibody is obtained by incorporating protruding DNA structures. Adapted with permission from [83]. Copyright (2016) Nature Publishing Group. (b) *SICM imaging*. On the left an illustration of the feedback hopping mechanism used in scanning ion conductance microscopy the pipette approaches the sample from a starting position that is above any of the surface features avoiding any contact due to lateral displacement. On the right a three- dimensional topographical rendered image of a hippocampal pyramidal neuron optimized using an adaptive scanning algorithm. Adapted with permission from [84]. Copyright (2009) Nature Publishing Group. (c) *Nanofabrication.* On the left a schematic representation of the setup employed for deposition of 3D high aspect ratio Cu features on a gold electrode surface by using a dual barrel pipette. On the right SEM images of 3D electrochemically printed Cu architecture. Adapted with permission from [85]. Copyright (2016) American Chemical Society. (d) *Single-cell biopsy.* Schematic setup used for nanobiopsy: SICM apparatus is used to approach, penetrate and withdraw from a targeted cell. Cellular content was aspirated aspirated via electrowetting and then further analyzed using sequencing machine. Adapted with permission from [86]. Copyright (2014) American Chemical Society.

Historically, micropipettes were firstly used as intracellular micro-electrodes (1902) [87] and later used in the patch-clamp method to detect voltages and currents from ions channels (1976). Nowadays nanopipettes are useful tools that found applications in exploring the nano-world. Nanopipettes, as with the other types of solid state nanopores, can be used as single molecule biosensors to detect a plethora of analytes such as dsDNA [88, 82], ssDNA [29, 89], proteins [90–92] and DNA-protein complexes [93, 94]. Additional functionality is imparted on nanopipettes by functionalization of the glass surface with chemical groups [95] or by incorporating a DNA origami architecture inside the pore. For instance, 3D funnel shaped DNA origami was mounted on nanopipettes [96] using a DNA leash as a guide for the origami insertion. This hybrid structure constituted by DNA and nanopore have been reported for detection of DNA and proteins [97, 96, 98] proving to be an elegant and

efficient alternative to biological nanopore to precisely control the pore structure and surface. Nanopipettes have also been merged with segmented flow microfluidics allowing real time analysis of droplet microreactors at molecular level

Unlike other nanopore architectures, the high aspect ratio of nanopipettes enable facile coupling with xyz precision control stages, allowing the tip of the nanopipette to be used as an imaging tool in scanning probe microscopy. For instance scanning ion conductance microscopy (SICM) [99] and scanning electrochemical microscopy (SECM) [100] offered an alternative approach to monitor the surface topography and the electrochemical activity of the substrate (See [101, 102] for a detailed review of some applications)

Finally nanopipettes can be used to handle ultrasmall volumes of liquid (nano to zeptoliter). In this modality it can serve as a nanofabrication tool [85] in applications such as controlled deposition of nanodots and freestanding nanowires using the electrochemical fountain pen [103–106]. It can also be employed as an instrument for drug delivery [107, 108](up to single molecule sensitivity[26]) and single cell surgery by non-invasively probing intracellular compartments [109, 86]. For instance, minimally invasive nanobiopsy technology was developed to extract as little as 50 fL out of single cell using a glass nanopipette. The extracted fluid, containing RNA, mitochondrial DNA and other nucleic acids were analyzed by next generation sequencing techniques to look for abnormalities such as mutations in mitochondrial DNA. The development of nanobiopsy techniques at single cell level, which part of this thesis will be devoted to, could open new avenues in cancer research: researchers might be able to monitor cells at different time points hence elucidating key cellular processes such as differentiation or the role of heterogeneity in primary tumors which are strictly related to disease progression and the effectiveness of novel drugs [110].

1.4 Transport in Solid State Nanopore

As mentioned earlier, nanopore sensing originates from the Coulter counter apparatus used to size and count particles dispersed in an electrolyte solution. A typical experimental setup consists of an insulating membrane with a nanometric orifice that connects two reservoirs filled with electrolyte solutions. Two non-polarizable electrodes, normally Ag/AgCl are used to apply a potential between the compartments. Commonly, but not always, the electrolyte of choice is potassium chloride because of the almost identical ion mobility of K^+ and Cl^- in solution. Upon application of a constant bias, a steady ionic current is established across the pore (**Figure 1.5 a**). Given the high value of nanopore resistance, typically in the MΩ-GΩ regime, the potential drop across the pore ($\Delta\Phi_{pore}$) is almost equivalent to the voltage applied (V_{bias}). As shown in equation 1.1, the potential drops occurring across the solution

($\Delta\Phi_{sol}$)and at the electrode/solution interfaces ($\Delta\Phi_{electr}$) are considered negligible due to the ideal non-polarizable nature of the electrodes having large electrochemically active areas and due to the high electrolyte conductivity σ_s of the electrolyte which is normally at concentration above 10 mM.

$$V_{bias} = \Delta\Phi_{electr} + \Delta\Phi_{sol} + \Delta\Phi_{pore} \approx \Delta\Phi_{pore} \tag{1.1}$$

Pore geometry,surface charge and electrolyte concentration are key parameters to take into account when calculating the nanopore conductance. For instance, if we assume a long and narrow pore of cylindrical shape (L_{pore}»d_{pore}) the overall resistance, in the limit of high salt concentration and neglecting surface charge effect is calculated as following:

$$R_{pore} = \frac{4L_{pore}}{\sigma\pi d_{pore}} \tag{1.2}$$

where σ is the solution conductivity, L_{pore} the length of the channel and d_{pore} the pore diameter. It is clear that for small L_{pore}, as in the case of 2D-materials where edge effects originating from the electric field distribution at the entrance of the pore become dominant, this model does not hold and the contribution of the so-called access resistance has to be taken into account. The access resistance is defined as the contribution of the electric field lines converging to the mouth of the pore. More specifically, this resistance has been firstly modelled by Hille as an electrode having semi-spherical shape located on top of the pore entrance. Considering a pore of cylindrical shape, it can be calculated:

$$R_{access}^{Hille} = \frac{1}{\sigma_s \pi d_{pore}} \tag{1.3}$$

A more detailed model was developed by Hall who pictured the access resistance as a disc-shaped electrode rather than a hemisphere:

$$R_{access}^{Hall} = \frac{1}{\sigma_s d_{pore}} \tag{1.4}$$

The total resistance can be assumed to be the sum of the access resistance with the pore channel resistance (the resistances are thought to be in series):

$$R_{pore} = R_{channel} + 2R_{access} = \frac{1}{\sigma_s}\left(\frac{4L_{pore}}{\pi d_{pore}^2} + \frac{1}{d_{pore}}\right) \tag{1.5}$$

From the equation above it is clear the contribution of R_{access} becomes dominant for small values of d_{pore} and L_{pore}. For instance, with nanopores that are built on single-layer membrane (e.g. MoS_2, graphene) the expression above becomes:$R_{pore} = \frac{1}{\sigma_s d_{pore}}$.

To simplify our discussion on pore conductance, from now onwards, we will consider pores with high aspect ratio (L_{pore}»d_{pore}) where the channel resistance is dominant over the so-called access resistance. High aspect ratio means high surface to volume ratio, therefore surface effects such as electric double layer (EDL) might potentially have a large impact over the ion flow. As reported experimentally, the conductance is the sum of two contributes: at high salt concentration (>100 mM) the conductance is governed mainly by the bulk concentration of ions in solution and geometrical parameters (first term in the equation) while at low salt concentration the mobile counterions K^+ shielding the negative charges present on the pore surface tend to dominate the ionic current (second term of the equation) (**Figure 1.5 b**)[111].

$$G = \frac{\pi}{4}\frac{d_{pore}^2}{L_{pore}}((\mu_k + \mu_{Cl})n_{KCl}e + \mu_K \frac{4\sigma}{d_{pore}}) \tag{1.6}$$

where d_{pore} is the diameter, L_{pore} is the length of a cylindrical nanopore, n_{KCl} is the number density of potassium or chloride ions, e is the elementary charge, σ is the surface charge density in the nanopore, and μ_K and μ_{Cl} are the electrophoretic mobilities of potassium and chloride ions, which are 7.616×10^{-8} m^2/V s and 7.909×10^{-8} m^2/V s respectively.

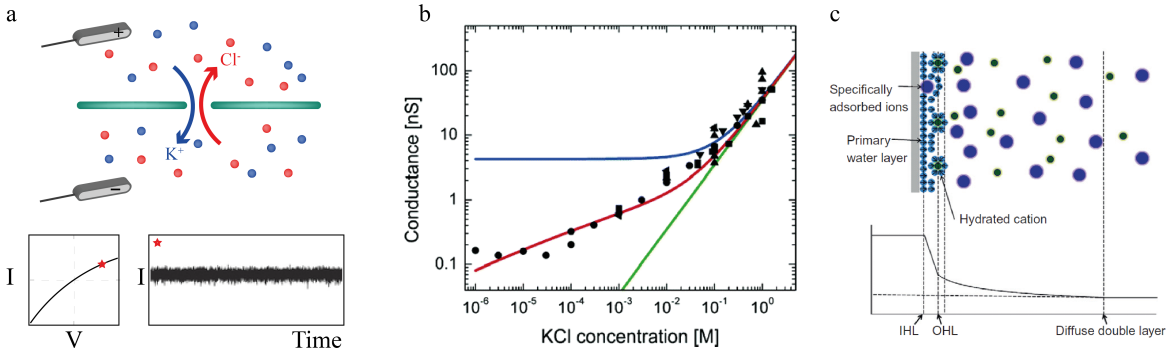

Fig. 1.5 Principles of nanopore measurements. (a) Schematic of a typical nanopore sensing experiment. A nanopore separates two chambers filled with electrolyte (KCl in this example). Two non-polarizable electrodes(for example Ag/AgCl), located on either side of the aperture, are used to apply a transmembrane potential which results in a constant ionic current. Current voltage characteristics (bottom part of the graph) are used to characterize the nanopore (e.g. establishing the pore size or evaluating the presence of any charge induced effect). Normally a constant bias is applied producing a steady ionic current flow which represents the baseline signal.(b) The graph illustrates the salt concentration dependence of nanopore conductance highlighting the role of surface charge at low ionic strength. The black dots are the results of experimental measurements while the green, blue, and red lines show the results for theoretical models as if it was in bulk solution, a model for constant surface charge, and a model for a variable surface charge, respectively. (c) Ion distribution in the electric double layer at a solid/liquid interface described according to the Gouy-Chapman-Stern model. It consists of an inner layer where ions are bound to the surface (Stern layer) and an outer diffuse layer where ions are mobile and they are distributed according to the Boltzmann distribution. The electrical potential decreases exponentially and the characteristic length is equal to the Debye length λ_D. Bottom panel of (a) adapted with permission from [112]. Copyright (2012) Elsevier. (b) Adapted with permission from [111]. Copyright (2006) American Chemical Society. (c) Adapted with permission from [113]. Copyright (2013) William Andrew.

Due to the fixed charges present at the solid interface, an oppositely charged region of counterions is formed at the liquid interface to maintain an overall electroneutrality. For instance quartz nanopipettes are characterized by the presence of silanol groups (Si^-, SiOH) on the surface [114, 115]. This shielding region is called EDL, and, the Stern-Gouy-Chapman theory can be used to model this electrostatic interaction such as accumulation and depletion of K^+ and Cl^- on the surface. This model is shown in **Figure 1.5 c** and it is composed by three layers. The first layer, referred to as the inner Helmholtz plane, consists of non-hydrated ions specifically absorbed to the surface. In the second layer, outer Helmholtz plane, consists of counterions which are partially or fully hydrated. The third and outermost layer consists of a diffuse layer of mobile ions as opposed to the first layer where ions are considered to be bound to the surface. In the diffuse layer, ions are distributed according to the Boltzmann distribution where the potential decays exponentially with a characteristic distance called the Debye length that is expressed using the Debye-Henkel approximation [116]:

$$\lambda_D = \left(\frac{\varepsilon_0 \varepsilon_r k_B T}{e^2 \sum n_i^{\infty} z_i^2}\right)^{\frac{1}{2}} \tag{1.7}$$

Where ε_0 and ε_r are permittivity constants, k_B is the Boltzmann constant, T the absolute temperature, e is the charge of one electron, $n_i^{\infty} = 10^3\, N_A\, c_i$ is the bulk volume density $[m^{-3}]$, z_i is the valency of ion i, N_A Avogadro number and c_i molar concentration.

At low ionic strength because of the large EDL, there is an excess of counterions inside the nanopore and exclusion of co-ions from the nanopore aperture due to electrostatic interactions with the surface charge. This exclusion enrichment effect (EEE) [117] alters the anion permeability in the channel. The permeselectivity induced by the EEE together with asymmetric pore geometries and non-uniform surface charge in a nanopore leads to diode-like voltage-current curves at symmetric electrolyte conditions which is called ionic current rectification and it was first observed in quartz nanopipettes [118, 119].
As for biological pores, charged biomolecules such as DNA, can be electrophoretically driven across the pore if they are located in close proximity to the aperture. The process is initially governed by the diffusion constant of the analyte together with the applied voltage. The rate at which the analyte approaches the pore entrance is given by the Einstein-Smoluchowski equation [120]: $J = 2\pi c D r_p$ where c is the bulk analyte concentration, D the diffusion constant, and r_p the radius of the pore. When the molecule is located within the capture volume of the pore it experiences a strong electric field. The pore represents an entropic barrier for molecules larger than the pore diameter(e.g. DNA with radius of gyration » $pore_{radius}$). This free energy barrier is normally overcome by increasing the applied electric field pulling the molecule through to the other side (**Figure 1.6 a,b**).

When a DNA molecule is transported across, the resulting change in conductance is described by the following equation with the approximation of cylinder-like pore geometry [111]:

$$\Delta G = \frac{1}{L_{pore}}(-\frac{\pi}{4}d_{DNA}^2(\mu_k + \mu_{Cl})n_{KCl}e + \mu_K^* q_{l,DNA}^*) \tag{1.8}$$

where d_{DNA} is DNA molecule diameter, μ^*_K is the effective electrophoretic mobility of potassium ions moving along the DNA, $q^*_{l,DNA}$ is the effective charge on DNA per unit length(assumed to be constant). The equation summarizes the combination of two effects.

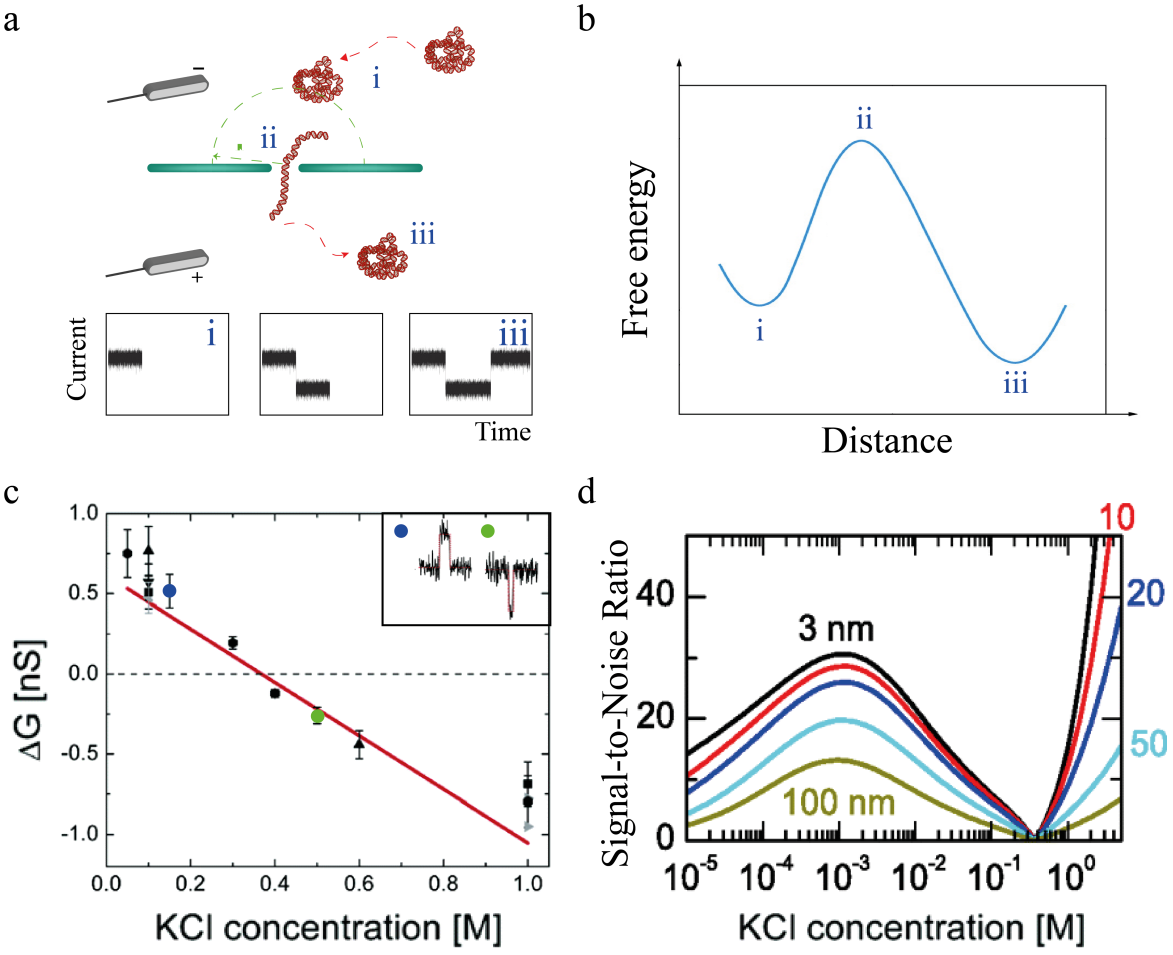

Fig. 1.6 Basics of DNA translocation across a nanopore. (a) DNA transport across a pore. Initially DNA is freely diffusing in the solution. When its random walk brings it in close proximity to the pore (within the capture volume having radius r), the DNA is subjected to a high electric field and it is electrophoretically translocated through the pore to the opposite chamber. (b) Free energy behaviour of DNA transported through across the pore. When the DNA chain happens to be confined in the pore (the radius of the pore is smaller than the radius of gyration of the DNA), its entropy, which is related to the number of possible conformations it can assume, decreases and the free energy increases as a consequence.(c) Conductance modulation as a function of salt concentration. Depending on the salt concentration, above or below 360 $\pm$ 40 mM, DNA translocation can give rise to negative or positive conductance modulation. The two conditions are commonly referred to as depletion or enhancement(inset: example of one event in depletion and one event in enhancement at 500 mM and 150 mM salt concentration).(d) SNR of dsDNA translocation as a function of salt concentration. Optimum conditions for SNR are: small pore diameter and low salt concentration. (a),(b) adapted from[121]. (c) Adapted with permission from [111]. Copyright (2006) American Chemical Society. (d) adapted with permission from [122]. Copyright (2008) National Academy of Sciences.

On one hand, the ion flow diminishes as a result of the space occupied by DNA inside the channel. On the other hand, the ion flow increases due to the shielding counterions brought in by the DNA. The first effect is predominant at high salt concentrations while the second effect is predominant at low salt concentrations. The two regimes are known as depletion or enhancement because of their negative or positive conductance modulation. At around 400 mM these two phenomena are equal in magnitude hence any charged analyte passes the pore undetected because no modulation is recorded in the ionic current. Therefore 400 mM salt concentration is also a minima for the SNR which as shown in the **Figure 1.6 d** has a local maxima at low salt concentration(around 1 mM) and it is strongly dependent on the pore size as confirmed by the equation given above.

Each translocation event is characterized by a current amplitude(which might include a main peak and sub-peaks according to the analyte conformation or complex utilized) and translocation time (or dwell time) which, among others, can reveal information about the size, conformation and binding affinity. In addition, the equivalent charge density (ECD), which constitutes the excluded charge from the nanopore channel during a translocation event, is useful to discriminate different analytes or different conformations of the same analyte.

1.5 Thesis scope and objectives

1.5.1 Challenges

To date one of the major limitation for single molecule detection via nanopore sensing is the sub-optimal control, in time and space, of the analyte when in the sensing region. Improving temporal and spatial resolution control is a fundamental aspect and a clear example is represented by DNA or protein sequencing using nanopore technologies: these tasks require the ability to move a DNA strand (or a protein in its denatured form) by sub-namometric intervals and being able to read the information at each step. However achieving high temporal and spatial resolution is far from trivial. With current solid state nanopore architectures, molecules translocate across the pore at high velocities which, together with their stochastic fluctuations, limit the amount of information that one can retrieve. It is not a surprise that, since its inception, researchers in the nanopore community proposed several solutions to better control the analyte motion including i) tuning the nanopore shape and geometry, ii) introducing new materials (e.g. 2D materials) iii) tuning the physicochemical parameters (e.g. viscosity, temperature, pH, ionic strength gradients) of the solution that separates the two compartments iv) chemically modifying the pore surface. The efficacy of these solutions appear to be restricted to sub-categories of analytes (e.g. proteins and

nucleic acids in a certain M.W. range, pH range etc.). In fact, one has to take into account another layer of complexity which arises from the varied characteristics, geometry, size, charge, just to mention a few, that those analytes present. For example pore geometry implies that molecules larger than the pore aperture are unable to cross the pore and therefore being detected; chemical modification is even more selective towards a particular species with a certain charge (e.g. electrostatic interaction) or chemical affinity (e.g. protein-aptamer interaction, when the aptamer is chemically attached to the nanopore surface). It is clear that a comprehensive solution that is effective, irrespectively of the analyte (or analytes) characteristics, and without affecting negatively the device sensitivity is still missing.

The problem of manipulating biomolecules extends far beyond the sensing region. Bringing molecules to the detector and more in general, being able to govern molecule dynamics outside the detection region is entangled with the detection process itself. Part of the problem stems on detecting rare events (in terms of particle detected) without compromising the measurement time. When working with low abundant species (e.g. $\leq$ nM) and small probing volume ($\leq$ fL), as in the case of single molecule setups, the time required for these molecules to reach the detection area might be long (e.g. limited by diffusion) leading to a long measurement time. Although techniques based on optical, magnetic, mechanical and electric forces (e.g. optical tweezers, magnetic tweezers, scanning probe microscopes) have been proposed to manipulate analytes (for some even with atomic resolution) their throughput is generally very low and in some cases their usability is limited either because labelling is necessary or due to the incompatibility with a complex sample (e.g. cell, cell extract, serum).

1.5.2 Thesis overview

The subject of this thesis focuses on developing new strategies aimed at improving the detection and manipulation of biomolecules by taking advantage of flexible and easy to fabricate devices such as nanopipettes. In fact, nanopipettes can be configured as a single molecule detector within the frame of nanopore sensing, or alternatively, they can be configured as a nanoscopic handle probes to manipulate biomolecules.

In **Chapter 2** we present a novel nanopore sensing strategy based around a zeptolitre electrolytic bridge located at the tip of a dual barrel nanopipette. The rationale behind this approach consists on physically controlling the transport of a molecule by confining it in this nanoscale electrolyte bridge which also acts as detection volume. As a result of this trapping molecules velocity is reduced and readout signals benefit of significantly higher SNR. The platform is characterized using both mixture of nucleic acids and protein and its performances are compared with conventional solid state nanopores.

Chapter 3 focuses on molecules manipulation by using dielectrophoresis as driving force. The device, called nanotweezers, consists of two nanolectrodes positioned at the tip of quartz nanopipette. It is possible to manipulate (and track by using fluorescence microscopy) a broad range of analytes: initially nanotweezers are characterized with polystyrene beads and then they proved effective with dsDNA, ssDNA and proteins of different sizes and labelled with a single or multiple fluorophores. Furthermore, potentialities of this newly developed platform are assessed with a proof of principle experiment where they are utilized to perform minimally invasive single cell nanobiopsy: specific nuclear or cytoplasmic cellular compartments were targeted for molecule extraction and further analysis. In **Chapter 4** a novel ionic field effect nanopore architecture based around dual barrel nanopipettes was developed. As a result of the electric field arising from the gate the device works as a molecular nanoswitch allowing the control over DNA molecules delivery from the nanopipette. Conclusions of this work are presented in **Chapter 5** where achievements are summarized along with future research directions.

References

[1] M. Francis S. Collins, M.D., Ph.D., and Harold Varmus, "A New Initiative on Precision Medicine," *N. Engl. J. Med.*, vol. 58, no. 1, pp. 13–28, 2015.

[2] C. Bustamante, "In singulo Biochemistry: When Less Is More," *Annu. Rev. Biochem.*, vol. 77, no. 1, pp. 45–50, 2008.

[3] T. Ha and P. Tinnefeld, "Photophysics of Fluorescent Probes for Single-Molecule Biophysics and Super-Resolution Imaging," *Annu. Rev. Phys. Chem.*, vol. 63, no. 1, pp. 595–617, 2012.

[4] S. W. Hell and J. Wichmann, "Breaking the diffraction resolution limit by stimulated emission: stimulated-emission-depletion fluorescence microscopy," *Opt. Lett.*, vol. 19, no. 11, p. 780, 1994.

[5] S. W. Hell, "Far-Field Optical Nanoscopy," *Science*, vol. 316, no. 5828, pp. 1153–1158, 2007.

[6] M. Lelek, F. Di Nunzio, R. Henriques, P. Charneau, N. Arhel, and C. Zimmer, "Superresolution imaging of HIV in infected cells with FlAsH-PALM," *Proc. Natl. Acad. Sci.*, vol. 109, no. 22, pp. 8564–8569, 2012.

[7] A. Gahlmann and W. E. Moerner, "Exploring bacterial cell biology with single-molecule tracking and super-resolution imaging," *Nat. Rev. Microbiol.*, vol. 12, no. 1, pp. 9–22, 2013.

[8] B. Huang, M. Bates, and X. Zhuang, "Super-Resolution Fluorescence Microscopy," *Annu. Rev. Biochem.*, vol. 78, no. 1, pp. 993–1016, 2009.

[9] A. B. Zrimsek, N. Chiang, M. Mattei, S. Zaleski, M. O. McAnally, C. T. Chapman, A.-I. Henry, G. C. Schatz, and R. P. Van Duyne, "Single-Molecule Chemistry with Surface- and Tip-Enhanced Raman Spectroscopy," *Chem. Rev.*, vol. 117, no. 11, pp. 7583–7613, 2017.

[10] K. Kneipp, Y. Wang, H. Kneipp, L. T. Perelman, I. Itzkan, R. R. Dasari, and M. S. Feld, "Single Molecule Detection Using Surface-Enhanced Raman Scattering (SERS)," *Phys. Rev. Lett.*, vol. 78, no. 9, pp. 1667–1670, 1997.

[11] S. Nie, "Probing Single Molecules and Single Nanoparticles by Surface-Enhanced Raman Scattering," *Science*, vol. 275, no. 5303, pp. 1102–1106, 1997.

[12] Y. Seol and K. C. Neuman, "SnapShot: Force Spectroscopy and Single-Molecule Manipulation," *Cell*, vol. 153, no. 5, pp. 1168–1168.e1, 2013.

[13] K. C. Neuman and A. Nagy, "Single-molecule force spectroscopy: optical tweezers, magnetic tweezers and atomic force microscopy," *Nat. Methods*, vol. 5, no. 6, pp. 491–505, 2008.

[14] J. Liphardt, "Reversible Unfolding of Single RNA Molecules by Mechanical Force," *Science*, vol. 292, no. 5517, pp. 733–737, 2001.

[15] X. Zhuang and M. Rief, "Single-molecule folding," *Curr. Opin. Struct. Biol.*, vol. 13, no. 1, pp. 88–97, 2003.

[16] E. A. Abbondanzieri, W. J. Greenleaf, J. W. Shaevitz, R. Landick, and S. M. Block, "Direct observation of base-pair stepping by RNA polymerase," *Nature*, vol. 438, no. 7067, pp. 460–465, 2005.

[17] S. Kmiecik, D. Gront, M. Kolinski, L. Wieteska, A. E. Dawid, and A. Kolinski, "Coarse-Grained Protein Models and Their Applications," *Chem. Rev.*, vol. 116, no. 14, pp. 7898–7936, 2016.

[18] S. Takada, "Coarse-grained molecular simulations of large biomolecules," *Curr. Opin. Struct. Biol.*, vol. 22, no. 2, pp. 130–137, 2012.

[19] A. Morriss-Andrews and J. E. Shea, "Simulations of protein aggregation: Insights from atomistic and coarse-grained models," *J. Phys. Chem. Lett.*, vol. 5, no. 11, pp. 1899–1908, 2014.

[20] T. Ha, "Single-molecule methods leap ahead," *Nat. Methods*, vol. 11, no. 10, pp. 1015–1018, 2014.

[21] X. Hou, W. Guo, and L. Jiang, "Biomimetic smart nanopores and nanochannels," *Chem. Soc. Rev.*, vol. 40, no. 5, p. 2385, 2011.

[22] J. J. Gooding and K. Gaus, "Single-Molecule Sensors: Challenges and Opportunities for Quantitative Analysis," *Angew. Chemie Int. Ed.*, vol. 55, no. 38, pp. 11354–11366, 2016.

[23] D. M. Rissin, C. W. Kan, T. G. Campbell, S. C. Howes, D. R. Fournier, L. Song, T. Piech, P. P. Patel, L. Chang, A. J. Rivnak, E. P. Ferrell, J. D. Randall, G. K. Provuncher, D. R. Walt, and D. C. Duffy, "Single-molecule enzyme-linked immunosorbent assay detects serum proteins at subfemtomolar concentrations," *Nat. Biotechnol.*, vol. 28, no. 6, pp. 595–599, 2010.

[24] M. J. Levene, J. Korlach, S. W. Turner, M. Foquet, H. G.Craighead, and W. W. Webb, "Zero-Mode Waveguides for Singlr-Molecule Analysis at High Concentrations," *Science*, vol. 299, no. 5607, pp. 682–686, 2003.

[25] K. J. Freedman, L. M. Otto, A. P. Ivanov, A. Barik, S.-H. Oh, and J. B. Edel, "Nanopore sensing at ultra-low concentrations using single-molecule dielectrophoretic trapping," *Nat. Commun.*, vol. 7, p. 10217, 2016.

[26] A. P. Ivanov, P. Actis, P. Jönsson, D. Klenerman, Y. Korchev, and J. B. Edel, "On-demand delivery of single DNA molecules using nanopipets," *ACS Nano*, vol. 9, no. 4, pp. 3587–3594, 2015.

[27] Y. Zhang, J. Clausmeyer, B. Babakinejad, A. López Córdoba, T. Ali, A. Shevchuk, Y. Takahashi, P. Novak, C. Edwards, M. Lab, S. Gopal, C. Chiappini, U. Anand, L. Magnani, R. C. Coombes, J. Gorelik, T. Matsue, W. Schuhmann, D. Klenerman, E. V. Sviderskaya, and Y. Korchev, "Spearhead Nanometric Field-Effect Transistor Sensors for Single-Cell Analysis," *ACS Nano*, 2016.

[28] K. McKelvey, B. P. Nadappuram, P. Actis, Y. Takahashi, Y. E. Korchev, T. Matsue, C. Robinson, and P. R. Unwin, "Fabrication, Characterization, and Functionalization of Dual Carbon Electrodes as Probes for Scanning Electrochemical Microscopy (SECM)," *Anal. Chem.*, vol. 85, no. 15, pp. 7519–7526, 2013.

[29] L. Ying, S. S. White, A. Bruckbauer, L. Meadows, Y. E. Korchev, and D. Klenerman, "Frequency and Voltage Dependence of the Dielectrophoretic Trapping of Short Lengths of DNA and dCTP in a Nanopipette," *Biophys. J.*, vol. 86, no. 2, pp. 1018–1027, 2004.

[30] S. M. Bezrukov, "Ion channels as molecular coulter counters to probe metabolite transport," *J. Membr. Biol.*, vol. 174, no. 1, pp. 1–13, 2000.

[31] S. Carson and M. Wanunu, "Challenges in DNA motion control and sequence readout using nanopore devices," *Nanotechnology*, vol. 26, no. 7, pp. 1–14, 2015.

[32] Y. Liu and L. Yobas, "Slowing DNA Translocation in a Nanofluidic Field-Effect Transistor," *ACS Nano*, vol. 10, no. 4, pp. 3985–3994, 2016.

[33] B. McNally, A. Singer, Z. Yu, Y. Sun, Z. Weng, and A. Meller, "Optical recognition of converted DNA nucleotides for single-molecule DNA sequencing using nanopore arrays," *Nano Lett.*, vol. 10, no. 6, pp. 2237–2244, 2010.

[34] J. Darnell, H. Lodish, and D. Baltimore, *Molecular Cell Biology*. New York: Scientific American Books, 1990.

[35] S. Howorka and Z. Siwy, "Nanopore analytics: sensing of single molecules.," *Chem. Soc. Rev.*, vol. 38, no. 8, pp. 2360–2384, 2009.

[36] S. M. Bezrukov, I. Vodyanoy, and V. A. Parsegian, "Counting polymers moving through a single ion channel.," *Nature*, vol. 370, no. 6487, pp. 279–281, 1994.

[37] J. J. Kasianowicz, E. Brandin, D. Branton, and D. W. Deamer, "Characterization of individual polynucleotide molecules using a membrane channel," *Proc. Natl. Acad. Sci. U. S. A.*, vol. 93, no. 24, pp. 13770–3, 1996.

[38] L. Song, M. R. Hobaugh, C. Shustak, S. Cheley, H. Bayley, and J. E. Gouaux, "Structure of Staphylococcal alpha -Hemolysin, a Heptameric Transmembrane Pore," *Science*, vol. 274, no. 5294, pp. 1859–1865, 1996.

[39] Z. S. Siwy and Stefan Howoeka, "Engineered voltage-responsive nanopores," *Chem. Soc. Rev.*, vol. 39, no. 3, pp. 1115–1132, 2010.

[40] O. Braha, H. Bayley, L.-Q. Gu, S. Conlan, and S. Cheley, "Stochastic sensing of organic analytes by a pore-forming protein containing a molecular adapter," *Nature*, vol. 398, no. 6729, pp. 686–690, 1999.

[41] O. Braha, L. Q. Gu, L. Zhou, X. Lu, S. Cheley, and H. Bayley, "Simultaneous stochastic sensing of divalent metal ions.," *Nat. Biotechnol.*, vol. 18, no. 9, pp. 1005–1007, 2000.

[42] C. Cao, Y.-L. Ying, Z.-L. Hu, D.-F. Liao, H. Tian, and Y.-T. Long, "Discrimination of oligonucleotides of different lengths with a wild-type aerolysin nanopore," *Nat. Nanotechnol.*, no. April, pp. 1–7, 2016.

[43] M. Kukwikila and S. Howorka, "Nanopore-Based Electrical and Label-Free Sensing of Enzyme Activity in Blood Serum," *Anal. Chem.*, vol. 87, no. 18, pp. 9149–9154, 2015.

[44] L. Wang, Y. Han, S. Zhou, and X. Guan, "Real-time label-free measurement of HIV-1 protease activity by nanopore analysis," *Biosens. Bioelectron.*, vol. 62, pp. 158–162, 2014.

[45] Y. Wang, D. Zheng, Q. Tan, M. X. Wang, and L.-Q. Gu, "Nanopore-based detection of circulating microRNAs in lung cancer patients," *Nat. Nanotechnol.*, vol. 6, no. 10, pp. 668–674, 2011.

[46] K. Tian, Z. He, Y. Wang, S. J. Chen, and L. Q. Gu, "Designing a polycationic probe for simultaneous enrichment and detection of microRNAs in a nanopore," *ACS Nano*, vol. 7, no. 5, pp. 3962–3969, 2013.

[47] W. Shi, A. K. Friedman, and L. A. Baker, "Nanopore Sensing," *Anal. Chem.*, vol. 89, no. 1, pp. 157–188, 2017.

[48] F. Haque, J. Li, H. C. Wu, X. J. Liang, and P. Guo, "Solid-state and biological nanopore for real-time sensing of single chemical and sequencing of DNA," *Nano Today*, vol. 8, no. 1, pp. 56–74, 2013.

[49] S. Thompson, M. Armstrong, C. Auth, M. Alavi, M. Buehler, R. Chau, S. Cea, T. Ghani, G. Glass, T. Hoffman, C.-H. Jan, C. Kenyon, J. Klaus, K. Kuhn, Z. Ma, B. Mcintyre, K. Mistry, A. Murthy, B. Obradovic, R. Nagisetty, P. Nguyen, S. Sivakumar, R. Shaheed, L. Shifren, B. Tufts, S. Tyagi, M. Bohr, and Y. El-Mansy, "A 90-nm Logic Technology Featuring Strained-Silicon," *IEEE Trans. Electron Devices*, vol. 51, no. 11, pp. 1790–1797, 2004.

[50] S. Thompson, N. Anand, M. Armstrong, C. Auth, B. Arcot, M. Alavi, P. Bai, J. Bielefeld, R. Bigwood, J. Brandenburg, M. Buehler, S. Cea, V. Chikarmane, C. Choi, R. Frankovic, T. Ghani, G. Glass, W. Han, T. Hoffmann, M. Hussein, P. Jacob, A. Jain, C. Jan, S. Joshi, C. Kenyon, J. Klaus, S. Klopcic, J. Luce, Z. Ma, B. Mcintyre, K. Mistry, A. Murthy, P. Nguyen, H. Pearson, T. Sandford, R. Schweinfurth, R. Shaheed,

S. Sivakumar, M. Taylor, B. Tufts, C. Wallace, P. Wang, C. Weber, and M. Bohr, "A 90 nm logic technology featuring 50 nm strained silicon channel transistors, 7 layers of Cu interconnects, low k ILD, and 1 μm/sup 2/ SRAM cell," in *Dig. Int. Electron Devices Meet.*, pp. 61–64, IEEE, 2002.

[51] J. Li, D. Stein, C. McMullan, D. Branton, M. J. Aziz, and J. a. Golovchenko, "Ion-beam sculpting at nanometre length scales," *Nature*, vol. 412, no. 6843, pp. 166–169, 2001.

[52] Q. Cai, B. Ledden, E. Krueger, J. A. Golovchenko, and J. Li, "Nanopore sculpting with noble gas ions," *J. Appl. Phys.*, vol. 100, no. 2, 2006.

[53] J. Yang, D. C. Ferranti, L. a. Stern, C. a. Sanford, J. Huang, Z. Ren, L.-C. Qin, and A. R. Hall, "Rapid and precise scanning helium ion microscope milling of solid-state nanopores for biomolecule detection.," *Nanotechnology*, vol. 22, no. 28, p. 285310, 2011.

[54] J. Gierak, A. Madouri, A. L. Biance, E. Bourhis, G. Patriarche, C. Ulysse, D. Lucot, X. Lafosse, L. Auvray, L. Bruchhaus, and R. Jede, "Sub-5 nm FIB direct patterning of nanodevices," *Microelectron. Eng.*, vol. 84, no. 5-8, pp. 779–783, 2007.

[55] A. J. Storm, J. H. Chen, X. S. Ling, H. W. Zandbergen, and C. Dekker, "Fabrication of solid-state nanopores with single-nanometre precision.," *Nat. Mater.*, vol. 2, pp. 537–540, 2003.

[56] E. Kennedy, Z. Dong, C. Tennant, and G. Timp, "Reading the primary structure of a protein with 0.07 nm3 resolution using a subnanometre-diameter pore," *Nat. Nanotechnol.*, no. July, pp. 1–14, 2016.

[57] S. Garaj, W. Hubbard, a. Reina, J. Kong, D. Branton, and J. a. Golovchenko, "Graphene as a subnanometre trans-electrode membrane.," *Nature*, vol. 467, no. 7312, pp. 190–193, 2010.

[58] G. F. Schneider, S. W. Kowalczyk, V. E. Calado, G. Pandraud, H. W. Zandbergen, L. M. K. Vandersypen, and C. Dekker, "DNA Translocation through Graphene Nanopores," *Nano Lett.*, vol. 10, no. 8, pp. 3163–3167, 2010.

[59] C. A. Merchant, K. Healy, M. Wanunu, V. Ray, N. Peterman, J. Bartel, M. D. Fischbein, K. Venta, Z. Luo, A. T. C. Johnson, and M. Drndić, "DNA Translocation through Graphene Nanopores," *Nano Lett.*, vol. 10, no. 8, pp. 2915–2921, 2010.

[60] M. D. Fischbein and M. Drndić, "Electron beam nanosculpting of suspended graphene sheets," *Appl. Phys. Lett.*, vol. 93, no. 11, 2008.

[61] S. Liu, B. Lu, Q. Zhao, J. Li, T. Gao, Y. Chen, Y. Zhang, Z. Liu, Z. Fan, F. Yang, L. You, and D. Yu, "Boron nitride nanopores: Highly sensitive DNA single-molecule detectors," *Adv. Mater.*, vol. 25, no. 33, pp. 4549–4554, 2013.

[62] J. Larkin, R. Henley, D. C. Bell, T. Cohen-Karni, J. K. Rosenstein, and M. Wanunu, "Slow DNA Transport through Nanopores in Hafnium Oxide Membranes," *ACS Nano*, vol. 7, no. 11, pp. 10121–10128, 2013.

[63] J. Feng, K. Liu, M. Graf, M. Lihter, R. D. Bulushev, D. Dumcenco, D. T. L. Alexander, D. Krasnozhon, T. Vuletic, A. Kis, and A. Radenovic, "Electrochemical Reaction in Single Layer MoS 2 : Nanopores Opened Atom by Atom," *Nano Lett.*, vol. 15, no. 5, pp. 3431–3438, 2015.

[64] J. Feng, K. Liu, R. D. Bulushev, S. Khlybov, D. Dumcenco, A. Kis, and A. Radenovic, "Identification of single nucleotides in MoS2 nanopores," *Nat. Nanotechnol.*, vol. 10, no. 12, pp. 1070–1076, 2015.

[65] K. Liu, J. Feng, A. Kis, and A. Radenovic, "Atomically thin molybdenum disulfide nanopores with high sensitivity for dna translocation," *ACS Nano*, vol. 8, no. 3, pp. 2504–2511, 2014.

[66] S. J. Heerema and C. Dekker, "Graphene nanodevices for DNA sequencing," *Nat. Nanotechnol.*, vol. 11, no. 2, pp. 127–136, 2016.

[67] W. H. Pitchford, H.-J. Kim, A. P. Ivanov, H.-M. Kim, J.-S. Yu, R. J. Leatherbarrow, T. Albrecht, K.-B. Kim, and J. B. Edel, "Synchronized Optical and Electronic Detection of Biomolecules Using a Low Noise Nanopore Platform," *ACS Nano*, vol. 9, no. 2, pp. 1740–1748, 2015.

[68] D. Fologea, M. Gershow, B. Ledden, D. S. McNabb, J. A. Golovchenko, and J. Li, "Detecting single stranded DNA with a solid state nanopore," *Nano Lett.*, vol. 5, no. 10, pp. 1905–1909, 2005.

[69] O. K. Zahid, F. Wang, J. A. Ruzicka, E. W. Taylor, and A. R. Hall, "Sequence-Specific Recognition of MicroRNAs and Other Short Nucleic Acids with Solid-State Nanopores," *Nano Lett.*, vol. 16, no. 3, pp. 2033–2039, 2016.

[70] M. Wanunu, T. Dadosh, V. Ray, J. Jin, L. McReynolds, and M. Drndić, "Rapid electronic detection of probe-specific microRNAs using thin nanopore sensors," *Nat. Nanotechnol.*, vol. 5, no. 11, pp. 807–14, 2010.

[71] D. Fologea, B. Ledden, D. S. McNabb, and J. Li, "Electrical characterization of protein molecules by a solid-state nanopore," *Appl. Phys. Lett.*, vol. 91, no. 5, p. 053901, 2007.

[72] R. Wei, V. Gatterdam, R. Wieneke, R. Tampé, and U. Rant, "Stochastic sensing of proteins with receptor-modified solid-state nanopores," *Nat. Nanotechnol.*, vol. 7, no. 4, pp. 257–263, 2012.

[73] C. Plesa, J. W. Ruitenberg, M. J. Witteveen, and C. Dekker, "Detection of Individual Proteins Bound along DNA Using Solid-State Nanopores," *Nano Lett.*, vol. 15, no. 5, pp. 3153–3158, 2015.

[74] A. Squires, E. Atas, and A. Meller, "Nanopore sensing of individual transcription factors bound to DNA," *Sci. Rep.*, vol. 5, p. 11643, 2015.

[75] M. Wanunu, S. Bhattacharya, Y. Xie, Y. Tor, A. Aksimentiev, and M. Drndic, "Nanopore Analysis of Individual RNA/Antibiotic Complexes," *ACS Nano*, vol. 5, no. 12, pp. 9345–9353, 2011.

[76] C. Plesa, D. Verschueren, S. Pud, J. van der Torre, J. W. Ruitenberg, M. J. Witteveen, M. P. Jonsson, A. Y. Grosberg, Y. Rabin, and C. Dekker, "Direct observation of DNA knots using a solid-state nanopore," *Nat. Nanotechnol.*, vol. 11, no. 8, pp. 1–6, 2016.

[77] C. Plesa, S. W. Kowalczyk, R. Zinsmeester, A. Y. Grosberg, Y. Rabin, and C. Dekker, "Fast Translocation of Proteins through Solid State Nanopores," *Nano Lett.*, vol. 13, pp. 658–663, feb 2013.

[78] H. Zhang, Y. Tian, and L. Jiang, "Fundamental studies and practical applications of bio-inspired smart solid-state nanopores and nanochannels," *Nano Today*, no. 29, pp. 1–21, 2016.

[79] B. N. Miles, A. P. Ivanov, K. a. Wilson, F. Doğan, D. Japrung, and J. B. Edel, "Single molecule sensing with solid-state nanopores: novel materials, methods, and applications," *Chem. Soc. Rev.*, vol. 42, no. 1, pp. 15–28, 2013.

[80] E. C. Yusko, J. M. Johnson, S. Majd, P. Prangkio, R. C. Rollings, J. Li, J. Yang, and M. Mayer, "Controlling protein translocation through nanopores with bio-inspired fluid walls," *Nat. Nanotechnol.*, vol. 6, no. 4, pp. 253–260, 2011.

[81] G. Stober, L. J. Steinbock, and U. F. Keyser, "Modeling of colloidal transport in capillaries," *J. Appl. Phys.*, vol. 105, no. 8, p. 084702, 2009.

[82] L. J. Steinbock, O. Otto, C. Chimerel, J. Gornall, and U. F. Keyser, "Detecting DNA folding with nanocapillaries," *Nano Lett.*, vol. 10, no. 7, pp. 2493–2497, 2010.

[83] N. A. W. Bell and U. F. Keyser, "Digitally encoded DNA nanostructures for multiplexed, single-molecule protein sensing with nanopores," *Nat. Nanotechnol.*, vol. 11, no. 7, pp. 645–651, 2016.

[84] P. Novak, C. Li, A. I. Shevchuk, R. Stepanyan, M. Caldwell, S. Hughes, T. G. Smart, J. Gorelik, V. P. Ostanin, M. J. Lab, G. W. J. Moss, G. I. Frolenkov, D. Klenerman, and Y. E. Korchev, "Nanoscale live-cell imaging using hopping probe ion conductance microscopy," *Nat. Methods*, vol. 6, no. 12, pp. 935–935, 2009.

[85] D. Momotenko, A. Page, M. Adobes-Vidal, and P. R. Unwin, "Write–Read 3D Patterning with a Dual-Channel Nanopipette," *ACS Nano*, vol. 10, no. 9, pp. 8871–8878, 2016.

[86] P. Actis, M. M. Maalouf, H. J. Kim, A. Lohith, B. Vilozny, R. A. Seger, and N. Pourmand, "Compartmental Genomics in Living Cells Revealed by Single-Cell Nanobiopsy," *ACS Nano*, vol. 8, no. 1, pp. 546–553, 2014.

[87] N. J. Penington, "Advanced Micropipette Techniques for Cell Physiology. IBRO Handbook Series: Methods In The Neurosciences, Volume 9," *J. Neurosci. Methods*, vol. 22, no. 1, pp. 88–89, 1987.

[88] L. J. Steinbock, R. D. Bulushev, S. Krishnan, C. Raillon, and A. Radenovic, "DNA translocation through low-noise glass nanopores," *ACS Nano*, vol. 7, no. 12, pp. 11255–11262, 2013.

[89] S. W. Kowalczyk, D. B. Wells, A. Aksimentiev, and C. Dekker, "Slowing down DNA translocation through a nanopore in lithium chloride . Slowing down DNA translocation through a nanopore in lithium chloride," *Nano Lett.*, pp. 1–5, 2012.

[90] L. J. Steinbock, S. Krishnan, R. D. Bulushev, S. Borgeaud, M. Blokesch, L. Feletti, and A. Radenovic, "Probing the size of proteins with glass nanopores," *Nanoscale*, vol. 6, no. 23, pp. 14380–7, 2014.

[91] W. Li, N. A. W. Bell, S. Hernández-Ainsa, V. V. Thacker, A. M. Thackray, R. Bujdoso, and U. F. Keyser, "Single Protein Molecule Detection by Glass Nanopores," *ACS Nano*, vol. 7, no. 5, pp. 4129–4134, 2013.

[92] N. A. W. Bell and U. F. Keyser, "Specific protein detection using designed DNA carriers and nanopores," *J. Am. Chem. Soc.*, vol. 137, no. 5, pp. 2035–2041, 2015.

[93] X. Lin, A. P. Ivanov, and J. B. Edel, "Selective single molecule nanopore sensing of proteins using DNA aptamer-functionalised gold nanoparticles," *Chem. Sci.*, vol. 8, no. 5, pp. 3905–3912, 2017.

[94] P. Nuttall, K. Lee, P. Ciccarella, M. Carminati, G. Ferrari, K. B. Kim, and T. Albrecht, "Single-Molecule Studies of Unlabeled Full-Length p53 Protein Binding to DNA," *J. Phys. Chem. B*, vol. 120, no. 9, pp. 2106–2114, 2016.

[95] P. Actis, A. C. Mak, and N. Pourmand, "Functionalized nanopipettes: Toward label-free, single cell biosensors," *Bioanal. Rev.*, vol. 1, no. 2, pp. 177–185, 2010.

[96] S. Hernández-Ainsa, N. A. W. Bell, V. V. Thacker, K. Göpfrich, K. Misiunas, M. E. Fuentes-Perez, F. Moreno-Herrero, and U. F. Keyser, "DNA Origami Nanopores for Controlling DNA Translocation," *ACS Nano*, vol. 7, no. 7, pp. 6024–6030, 2013.

[97] R. Wei, T. G. Martin, U. Rant, and H. Dietz, "DNA Origami Gatekeepers for Solid-State Nanopores," *Angew. Chemie Int. Ed.*, vol. 51, no. 20, pp. 4864–4867, 2012.

[98] S. Hernandez-Ainsa and U. F. Keyser, "DNA origami nanopores: developments, challenges and perspectives," *Nanoscale*, vol. 6, no. 23, pp. 14121–14132, 2014.

[99] P. Hansma, B. Drake, O. Marti, S. Gould, and C. Prater, "The scanning ion-conductance microscope," *Science*, vol. 243, no. 4891, pp. 641–643, 1989.

[100] A. J. Bard, F. R. F. Fan, J. Kwak, and O. Lev, "Scanning electrochemical microscopy. Introduction and principles," *Anal. Chem.*, vol. 61, no. 2, pp. 132–138, 1989.

[101] C.-C. Chen, Y. Zhou, and L. A. Baker, "Scanning Ion Conductance Microscopy," *Annu. Rev. Anal. Chem.*, vol. 5, no. 1, pp. 207–228, 2012.

[102] D. Polcari, P. Dauphin-Ducharme, and J. Mauzeroll, "Scanning Electrochemical Microscopy: A Comprehensive Review of Experimental Parameters from 1989 to 2015," *Chem. Rev.*, vol. 116, no. 22, pp. 13234–13278, 2016.

[103] A. P. Suryavanshi and M. F. Yu, "Probe-based electrochemical fabrication of free-standing Cu nanowire array," *Appl. Phys. Lett.*, vol. 88, no. 8, pp. 8–11, 2006.

[104] A. P. Suryavanshi and M.-F. Yu, "Electrochemical fountain pen nanofabrication of vertically grown platinum nanowires," *Nanotechnology*, vol. 18, no. 10, p. 105305, 2007.

[105] S. Ito and F. Iwata, "Nanometer-Scale Deposition of Metal Plating Using a Nanopipette Probe in Liquid Condition," *Jpn. J. Appl. Phys.*, vol. 50, no. 8, p. 08LB15, 2011.

[106] F. Iwata, S. Nagami, Y. Sumiya, and A. Sasaki, "Nanometre-scale deposition of colloidal Au particles using electrophoresis in a nanopipette probe," *Nanotechnology*, vol. 18, p. 105301, 2007.

[107] Y. Takahashi, A. I. Shevchuk, P. Novak, Y. Zhang, N. Ebejer, J. V. MacPherson, P. R. Unwin, A. J. Pollard, D. Roy, C. A. Clifford, H. Shiku, T. Matsue, D. Klenerman, and Y. E. Korchev, "Multifunctional nanoprobes for nanoscale chemical imaging and localized chemical delivery at surfaces and interfaces," *Angew. Chemie - Int. Ed.*, vol. 50, no. 41, pp. 9638–9642, 2011.

[108] B. Babakinejad, P. Jönsson, A. López Córdoba, P. Actis, P. Novak, Y. Takahashi, A. Shevchuk, U. Anand, P. Anand, A. Drews, A. Ferrer-Montiel, D. Klenerman, and Y. E. Korchev, "Local Delivery of Molecules from a Nanopipette for Quantitative Receptor Mapping on Live Cells," *Anal. Chem.*, vol. 85, no. 19, pp. 9333–9342, 2013.

[109] R. Singhal, Z. Orynbayeva, R. V. Kalyana Sundaram, J. J. Niu, S. Bhattacharyya, E. a. Vitol, M. G. Schrlau, E. S. Papazoglou, G. Friedman, and Y. Gogotsi, "Multifunctional carbon-nanotube cellular endoscopes.," *Nat. Nanotechnol.*, vol. 6, no. 1, pp. 57–64, 2011.

[110] Y. Kraytsberg, E. Kudryavtseva, A. C. McKee, C. Geula, N. W. Kowall, and K. Khrapko, "Mitochondrial DNA deletions are abundant and cause functional impairment in aged human substantia nigra neurons," *Nat. Genet.*, vol. 38, no. 5, pp. 518–520, 2006.

[111] R. M. M. Smeets, U. F. Keyser, D. Krapf, M.-Y. Wu, N. H. Dekker, and C. Dekker, "Salt Dependence of Ion Transport and DNA Translocation through Solid-State Nanopores," *Nano Lett.*, vol. 6, no. 1, pp. 89–95, 2006.

[112] M. Wanunu, "Nanopores: A journey towards DNA sequencing," *Phys. Life Rev.*, vol. 9, no. 2, pp. 125–158, 2012.

[113] J. B. Edel and T. Albrecht, *Engineered nanopores for bioanalytical applications*. Elsevier, 2013.

[114] F. H. J. Van Der Heyden, D. Stein, and C. Dekker, "Streaming currents in a single nanofluidic channel," *Phys. Rev. Lett.*, vol. 95, no. 11, pp. 9–12, 2005.

[115] D. P. Hoogerheide, S. Garaj, and J. A. Golovchenko, "Probing surface charge fluctuations with solid-state nanopores," *Phys. Rev. Lett.*, vol. 102, no. 25, pp. 5–8, 2009.

[116] R. B. Schoch, J. Han, and P. Renaud, "Transport phenomena in nanofluidics," *Rev. Mod. Phys.*, vol. 80, no. 3, pp. 839–883, 2008.

[117] A. Plecis, R. B. Schoch, and P. Renaud, "Ionic transport phenomena in nanofluidics: Experimental and theoretical study of the exclusion-enrichment effect on a chip," *Nano Lett.*, vol. 5, no. 6, pp. 1147–1155, 2005.

[118] C. Wei, A. J. Bard, and S. W. Feldberg, "Current Rectification at Quartz Nanopipet Electrodes," *Anal. Chem.*, vol. 69, no. 22, pp. 4627–4633, 1997.

[119] C. Rischel and H. Flyvbjerg, "Comment on "Fabrication of a Synthetic Nanopore Ion Pump"," *Phys. Rev. Lett.*, vol. 91, no. 17, p. 179801, 2003.

[120] M. v. Smoluchowski, "Grundriß der Koagulationskinetik kolloider Lösungen," *Kolloid-Zeitschrift*, vol. 21, no. 3, pp. 98–104, 1917.

[121] M. Muthukumar, "Mechanism of DNA Transport Through Pores," *Annu. Rev. Biophys. Biomol. Struct.*, vol. 36, no. 1, pp. 435–450, 2007.

[122] R. M. M. Smeets, U. F. Keyser, N. H. Dekker, and C. Dekker, "Noise in solid-state nanopores," *Proc. Natl. Acad. Sci.*, vol. 105, no. 2, pp. 417–421, 2008.

.

Chapter 2

Nanobridge

The results of this chapter are published in the following paper:

- *P. Cadinu, B. Paulose Nadappuram, D. J. Lee, J. Y. Y. Sze, G. Campolo, Y. Zhang, A. Shevchuk, S. Ladame, T. Albrecht, Y. Korchev, A. P. Ivanov, and J. B. Edel, "Single Molecule Trapping and Sensing Using Dual Nanopores Separated by a Zeptoliter Nanobridge", Nano Letters, 2017 [1]*

2.1 Introduction

In recent years nanopore sensing has emerged as one of the most promising single molecule techniques capable of detecting [2, 3] and even delivering [4] a variety of biological molecules and particles. This is in part due to the simple working mechanism, based on recording changes in the ionic current through a nanometric aperture that separates two reservoirs filled with electrolyte solutions. However, despite being successfully demonstrated for a broad range of applications [5–7], among which nucleic acid sequencing is definitely the most important [8]), the next step to enhance both biological and solid state nanopores sensing capabilities requires to sharpen the control over molecular transport.

This requirement is particularly relevant when detecting small molecules. For instance, short nucleic acid fragments such as microRNAs (single-stranded RNA molecules, 20-25 nucleotide long), which are gaining prominence due to their potential diagnostic capabilities, are exceptionally challenging to detect because of their high translocation velocity. Depending mainly on the pore size, material and voltage applied, translocation speed can be as high as 50000 nucleotides m s^{-1} [9] leading to a poor SNR. Another class of much more challenging small molecules to detect are proteins. This is in part due to their heterogeneous charge, multiple conformations, diffusion rates and non-specific interaction with nanopore walls.

Often only a small fraction of all proteins crossing the pore are detected. For example, based on simulation analysis and theoretical calculations, it has been demonstrated that for sub-100 kDa protein through solid-state nanopores with diameters >10 nm, as small as 0.1% of all proteins transported though the nanopore are detected [10, 11]. These findings, which reflect an insufficient temporal resolution, strongly limited nanopore performances. It required that experiments had to be carried out at higher analyte concentration (>nM) therefore precluding its efficient usage with clinical samples where, for example, the concentration of biologically relevant proteins range from 10^{-16} to 10^{-12} M [12, 13].

Considering the tremendous impact that enhancing temporal resolution would have on next generation nanopore sensing, a lot of effort has been placed towards finding robust solutions applicable to solid state nanopores (and even for biological nanopores, albeit it is not the focus of this thesis). In the first instance strategies have involved development of high bandwidth low noise amplifiers [14–17] capable of recording signals as fast as 5 MHz; however, most of the research focused on the more challenging, perhaps more powerful task of actively tuning the transport of analytes through pore. Apart from the straightforward method of lowering the voltage applied [18, 19], which decelerates molecules but at the not negligible cost of lowered SNR and capture rates, several approaches, acting on different nanopore key parameters, were developed:

- *Viscosity and electrolyte solution.* The viscosity of the electrolyte solution was fine-tuned by adding, for instance glycerol [19] to potassium chloride; alternative electrolyte solutions included glutamate [20], lithium chloride [21], sodium chloride [21], ionic liquids [22]. The last one appeared to be extremely effective on slowing down analytes: single nucleotide events were detected and recorded in the sub-ms regime. Reduced capture rate (although analyte concentration were in the μM to mM range), moderate decrease in SNR, impossibility of distinguishing between single nucleotide and 30 bases oligo are still issues to be addressed. In addition, the system has yet to be demonstrated for proteins. This is not trivial considering that proteins are much more sensitive to the environment they are surrounded by and therefore they degrade more rapidly in comparison to nucleic acids (e.g. solubility, folding and unfolding are key processes that ionic liquid might influence).

- *Geometry, shape and material.* Nanopore shape, geometry [23, 24] and materials (e.g. graphene [25, 26], Al_2O_3 [27], BN [28], MoS_2 [22]) were selected and adapted to the analyte under investigation. The reduced analyte speed was ascribed to interactions with the pore itself.

- *Temperature and pressure.* A pressure gradient across the aperture was employed to counterbalance the electrophoretic force which is the main responsible of driving the molecule through the pore [29, 30]. Temperature exhibited only a moderate impact on the translocation dynamics [19].

- *pH.* pH of the electrolyte solution was selected to be as close as possible to the isoelectric point (pI) of the analyte under investigation (e.g. protein). In this way, the net charge on the protein surface was minimized, the electrophoretic force acting on the protein was weaker and the translocation velocity was therefore lowered [31].

- *Mechanical forces.* Nanopore setups were used in conjunction with optical [32, 33] and magnetic tweezers [34] to exert full control over translocating molecule. Although effective, the use of these methods implied exstensive labelling of the analyte and their efficacy was restricted only to long nucleic acid sequences but not on short oligonucleotides or small proteins.

- *Chemical modification.* The nanopore aperture was chemically functionalized to improve the nanopore sensitivity of particular molecules [35]. For instance, by coating the nanochannel with aptamers, the nanopore becomes extremely sensitive towards a specific protein. Therefore the ionic current modulations will be governed by protein-aptamer interactions.

- *Ionic Field Effect Transistor.* Gated nanostructures allow direct field effect control over the charges inside the nanochannel. Therefore, through a gate bias it was possible to regulate the transport of the analyte across the pore by modulating the electrostatic interactions with the pore [36]. Albeit only demonstrated for long DNA strands and high voltage applied, this technique will be revisited and an easy to fabricate solution will be presented in a separate chapter of this thesis.

Aside from the abovementioned compatibility issue with the solution employed as in the case of ionic liquids, most of these techniques are only moderately effective and translocation velocity is reduced by no more than an order of magnitude. However, they present severe limitations which affect fundamental nanopore sensing parameters. The SNR (current blockades are decreased or noise level performances worsened as in 2D materials or chemical modifications), distribution profiles of both current blockade and dwell time are extremely broadened, detection efficiency and limit of detection are worsened[37]. On top of it, more often than not, most solutions only work for targeted analytes (e.g. chemical modification), therefore developing a simple and universal method capable of slowing and controlling the transport is still an open quest.

In this chapter, we propose a novel detection platform which, on top of being easy to fabricate, addresses many of the above challenges by confining individual molecules in an electrolyte nanobridge formed across two nanopores, separated by a 20 nm gap, which are located at the tip of a dual barrel nanopipette. The electrolyte bridge formation has been documented firstly by Rodolfa [38, 39] for controllable deposition of biomolecules with nanopipettes on a functionalized surface which then was followed by similar works [40–45], however, in the case in question the bridge consists of a zeptolitre volume (10^{-21} litre!) which is much smaller then what previous studies have reported. The physical operation mechanism is also different from a conventional nanopore: a bias is applied between the two barrels of the nanopipettes filled with electrolyte solution and the analyte is driven from one nanopore to the other across the bridge. During this process, the analyte is temporarily confined in space. This, in turns, produces a slowdown of the molecule of up to 3 orders of magnitude compared to conventional nanopore setups. This new configuration, that from now onwards will be referred to as nanobridge configuration, was demonstrated with a broad range of analytes such as dsDNA, ssDNA, and proteins showing in all cases enhanced SNR performances ($\approx 500\%$) while still operating at physiological conditions with analyte concentration in the pM range.

2.2 Experimental procedures

2.2.1 Nanopore setup

Ionic current recordings

The ionic current was measured by applying a voltage bias across a pair of Ag/AgCl electrodes (0.125 mm diameter, GoodFellow U.K.). Depending on the configuration the electrodes were placed differently: in nanobridge and dual pore configuration, one electrode was inserted in each of the two nanopipette barrels; conventional, one electrode was placed in one barrel of the nanopipette while the other electrode was placed in the bath (please refer to *Nanopipette sensing configuration* for a detailed description). The analog data were low-pass filtered using the built-in 4 pole Bessel filter and digitized at 100 kHz (or 50 kHz for current-voltage characteristics) using Digidata 1440A data-acquisition module (Molecular Devices, USA). Data was acquired using Clampex Data Acquisition Module (Molecular Devices, USA). In order to shield electromagnetic radiation the nanopore set up, comprising the amplifier head stage, was embedded into a Faraday cage located on top of an optical table to further isolate the system from unwanted vibrations.

Nanopipette fabrication

Nanopipettes were fabricated using a P-2000 laser puller (Sutter Instrument Co, USA) from quartz theta capillaries (QF120-90-7.5 Sutter Instrument, USA) with an outer diameter of 1.2 mm. The inner diameter, which measured 0.9 mm, is divided into two chambers insulated by a septum of thickness 0.15 mm (the capillary cross section appear to be theta shaped). The former retains its shape also after the capillary has been laser-pulled. Capillaries were plasma cleaned (Harrick Plasma cleaner PDC-001, USA) for 15 minutes prior to pulling. Nanopipettes with two different pore diameters ($15-50$ nm and $50-100$ nm) were fabricated according to the following protocols:

	Heating	Filament	Velocity	Delay	Pulling
Line 1	850	4	30	160	80
Line 2	860	3	20	140	160

Table 2.1 Nanopipette pulling protocol 1. Pore diameter: $15-30nm$

	Heating	Filament	Velocity	Delay	Pulling
Line 1	840	4	30	160	80
Line 2	870	3	20	140	160

Table 2.2 Nanopipette pulling protocol 2. Pore diameter: $50-100nm$

Notably these protocols are puller dependent thus different pullers might result in different nanopipette size although the parameters used are the same. When pulling this type of nanopipette it is fundamental that the septum is aligned parallel to the horizon. In this way the laser irradiates uniformly the capillary leading to symmetric pores. Finally, nanopipettes were stored in closed, dust-free, boxes for no more than a week after pulling.

Nanopipettes were functionalized with silane at the back hand to avoid the possibility of any electrolyte bridge between the 2 barrels. The back of the nanopipette was exposed to the fumes of Trichloro(1H,1H,2H,2H-perfluorooctyl)silane (Cat.Num.448931-10G, Sigma Aldrich) for 5 seconds, enough to create an hydrophobic film. The procedure was carried out in a fume hood and nanopipettes were then immediately used for recordings.

Imaging characterization

Scanning Electron Microscopy (SEM) images were performed on a Leo Gemini 1525 (Carl Zeiss AG, Germany) high resolution field emission gun scanning electron microscope. Samples were sputter coated with 10 nm of Chromium (Q150 Sputter Coater, Quorum

Technologies, UK) before imaging to reduce charge accumulation and improve the image quality.

Transmission electron microscope images were acquired with JEM-2100F TEM (Jeol, USA). Samples were sputter coated with 10 nm of Chromium (Q150 Sputter Coater, Quorum Technologies, UK) before imaging to ensure electrical conductivity. TEM acquisitions were performed by Bernice Akpinar, Department of Materials, Imperial College London.

2.2.2 Nanopipette sensing configuration

Upon filling each barrel with electrolyte solution using a 35G Microfil Syringe Needle (World Precision Instruments, USA), nanopipettes were checked for unwanted air bubbles. To do so a negative pressure was applied to both barrels using a polyethilene tube connected to a syringe; as a result expanding air bubbles were guided away from the nanopore tip. A second technique utilized to evacuate bubbles consists in gently shaking the nanopipette by employing a pair of tweezers with the corrugated tip.
As illustrated in **Figure 2.1** nanopipettes were used in three different configurations:

- **Conventional.** The nanopipette is dipped in a glass vial containing an electrolyte bath. the reference electrode is placed in the bath and the working electrode is placed inside one of the barrels.

- **Dual pore.** Similar to conventional configuration, the nanopipette is dipped in electrolyte bath but the difference lies onto the electrode configuration: the two electrodes are inserted one in each barrel.

- **Nanobridge.** One electrode is inserted in each barrel and the electric circuit is closed by the nanoscale electrolyte bridge located at the tip of the pipette. No bath is required for this configuration.

To perform all the experiments Ag/AgCl electrodes were chosen because of their non-polarizabile nature hence the potential drop occurring at the electrode/solution interfaces can be considered negligible [46]. A silver wire (0.125 mm diameter, Goodfellow Cambridge Ltd, UK) was electroplated in 1 M potassium chloride solution employing a potentiostat (Reference 600 potentiostat, Gamry Instruments, USA) and a Ag wire as reference electrode. The flow of a current caused the deposition of AgCl at the *anode* ($Ag_{(s)} + Cl^{-}_{(aq)} \rightleftharpoons AgCl_{(s)} + e^{-}$) and the reduction of hydrogen ions at the *cathode* ($2H^{+}_{(aq)} + 2e^{-} \rightleftharpoons H_{2(g)}$).

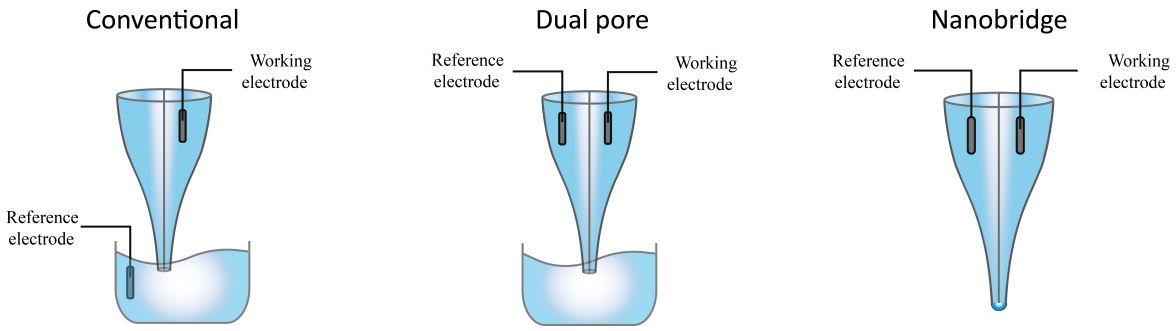

Fig. 2.1 Schematic of the different nanopore sensing configurations: conventional on the left, dual pore configuration in the middle, and nanobridge on the right. They are characterized by the way electrodes are arranged and by the presence or absence (as in nanobridge) of an electrolyte bath in which nanopipettes are dipped in. In **Nanobridge configuration** a dual barrel pipette has one electrode per barrel and an electrolyte bridge is formed at the tip. In **dual pore configuration**. A dual barrel pipette having one electrode per barrel is dipped in an electrolyte bath with the same ionic strength. In **conventional configuration** where one electrode is inserted in one barrel and the other one is located in the bath. It should be noted that in this case the second barrel does not play any active role in the recordings.

2.2.3 Fluorescence Spectroscopy: basic theory

Fluorescence is a form of luminescence where light is emitted from a molecule as a result of optically-induced electronic excited states. The processes that occur between absorption and emission of light are normally described with Jablonski diagrams [47], named after Prof. Alexander Jablonski who is considered as the father of fluorescence spectroscopy. The basic theory of fluorescence spectroscopy is illustrated using a simplified Jablonski diagram where the ground and first electronic energy states are depicted by S_0 and S_1 respectively (a number of vibrational levels are associated to each of these energy levels).

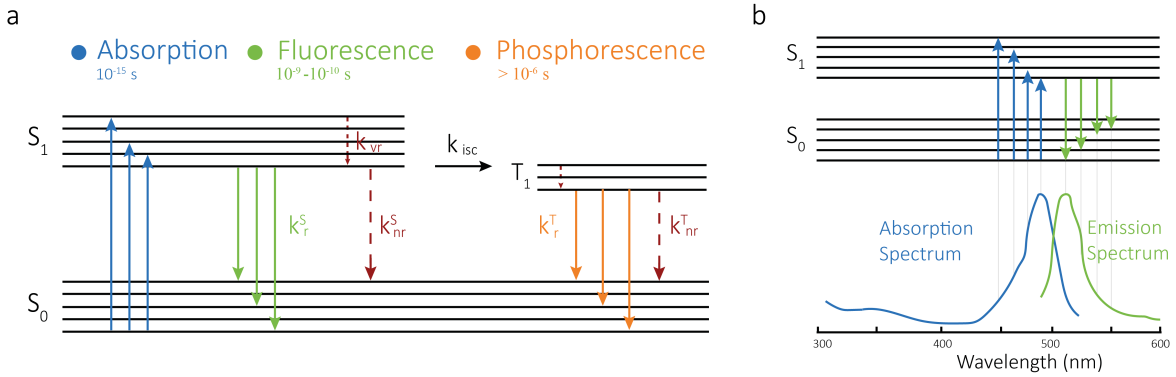

Fig. 2.2 Basic theory of fluorescence spectroscopy. (a) A simplified Jablonski diagram showing the energy levels of a molecule and the transitions between them; radiative transitions (absorption, fluorescence and phosphorescence) are indicated with solid blue, green and orange lines respectively while non-radiative transitions (internal conversion and vibrational relaxation) are indicated with dashed lines. k_r^S is the rate of fluorescence emission. k_{nr}^S is the rate of non-radiative transition from S_1 to S_0. k_{vr} is the rate for vibrational relaxation. k_{isc} is the rate of intersystem crossing from S_1 to T_1. k_r^T is rate of phosphorescence emission. k_{nr}^T is the rate of non-radiative transition from T_1 to S_0. (b) Showing the relation between absorption and emission spectral characteristics and the corresponding energetic levels. Each vertical line in the spectra correlates with the energy of the absorbed photon (arrows pointing up) or with the energy of the emitted photon (arrows pointing down). Figure adapted from [48].

Following the photons absorption, electrons from the ground state S_0 are excited to higher vibrational levels of S_1 according to the photon energy. Electrons rapidly relax from high

vibrational levels to the lowest vibrational levels of S_1 because of two non-radiative processes: internal conversion and vibrational relaxation [47]. Vibrational relaxation is triggered by collisions between the excited molecule with other particles of the system to which energy is transferred. Internal conversion consists of a radiationless transition between energy states having the same spin and it can also occurs between different electronic states ($S_1 \rightarrow S_0$).

Finally fluorescence emission occurs when the electron from S_1 relaxes to a vibrational level located in the ground state S_0 emitting a photon of the corresponding energy difference. In addition there is a further pathway that occurs after intersystem crossing: this process is caused by the overlap between electronic states of different multiplicity meaning transition from single to triplet state $S_1 \rightarrow T_1$. After vibrational relaxation to the lower level of T_1, radiative transitions to S_0 with a photon emission can occur. The former is defined as phosphorescence and its probability, or emission rate, is much smaller than fluorescence because of transitions from triplet states to singlet states are forbidden ($T_1 \rightarrow S_0$) [49].

Jablonski diagrams reflect the spectral characteristics related to absorption and emission of energy by a fluorophore (**Figure 2.2 b**). Due to energy losses (e.g.vibrational relaxation and other non-radiative processes) emitted photons have lower energy (higher wavelength) than the absorbed ones. This phenomenon is reflected in the spectral characteristics where the distance between the peak of the absorption spectrum and the peak of the emission spectrum is named Stokes shift after G.G. Stokes observed it first.

Fluorophores are characterized by the quantum yield and the fluorescence lifetime. The quantum yield is the ratio of photons emitted to the number of photons absorbed and it is given by:

$$Q = \frac{k_r}{k_r + k_{nr}} \tag{2.1}$$

where k_r and k_{nr} are the fluorescence emissive rate constant and the nonradiative rate constant of the fluorophore. The fluorescence lifetime is the average time that the fluorophore spends in the excited state prior returning to its ground state. It is described as following:

$$\tau = \frac{1}{k_r + k_{nr}} \tag{2.2}$$

2.2.4 Fluorescence sensing setup

The schematic of the setup used to perform fluorescence detection is shown in **Figure 2.3**. A IX71 inverted microscope (Olympus, USA) was used in epifluorescence configuration. The excitation light generated by a **continous-wave solid-state laser** (λ_{ex}=488 nm, Sapphire 488LP, Coherent, USA) was focused on the sample through a 60x water immersion **objective lens** (UPLSAPO 60XW, Olympus, USA) having a Numerical Aperture (N.A.) equal to 1.2

and working distance (WD) of 0.28 mm. The fluorescence emitted by the sample was then focused onto electron multiplying Charge Coupled Device (emCCD) camera detector by the same objective. A controller unit (ProScan II, Prior Scientific) was used to precisely control the **motorized stage** (H1117, Prior Scientific, USA) and the z-axis focus motor ensuring accurate sample position with step of 40 nm minimum. A custom **dichroic dual band filter**

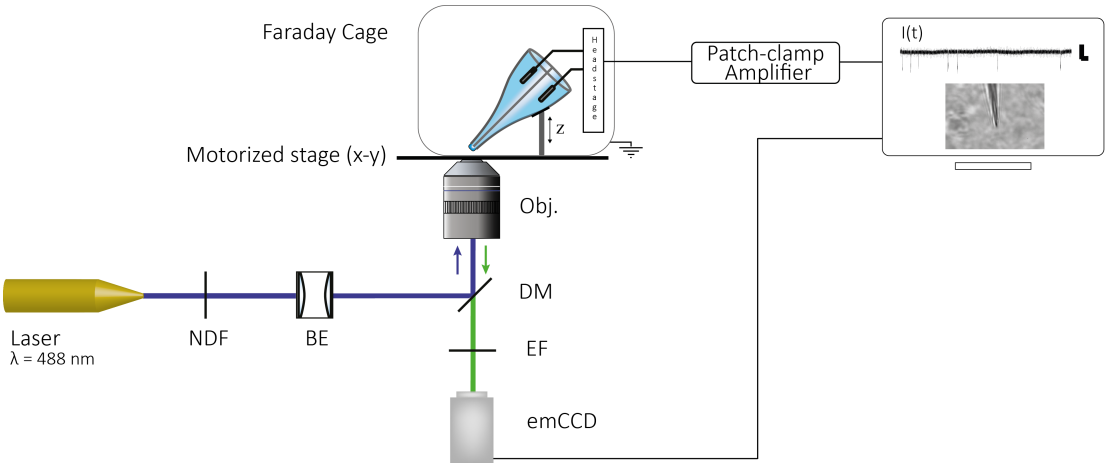

Fig. 2.3 Optical-electrical setup employed for detection of dsDNA fluorescently tagged molecules translocating in nanobridge configuration. The excitation source was a continuous-wave solid-state laser (λ = 488 nm, Sapphire 488LP, Coherent, USA). A Neutral Density Filter (NDF) was employed to reduce the regulate the laser power and Beam Expander (BE, Thorlbas, BE02-05-A) was employed to entirely fill the back aperture of the objective. The former was a 60x water immersion objective lens (UPLSAPO 60XW, Olympus, USA) having a Numerical Aperture (NA) of 1.2 and working distance (WD) of 0.28 mm. The emitted light from the tip of the nanopipette was collected back through the same objective, transmitted through the dichroic mirror (DM), a long pass Emission Filter (EF, HQ540/80M, Chroma, USA) and finally collected by the emCCD camera (iXon Ultra 897, Andor Technologies, UK). A x-y motorized stage (H1117, Prior Scientific, USA) was used to accurately position the sample. In addition the nanopipette was mounted on a single-axis miniature translational stage (DT12, ThorLabs, USA) which was used to control the z position. Ionic current recordings were performed with a pair of Ag/AgCl electrodes inserted into each barrel and connected to the head stage of a patch clamp amplifier (A-M 2400, A-M Systems, USA). A Faraday cage was used to shield electromagnetic noise. The analogue signal coming from the amplifier head stage was filtered (built-in 4 pole Bessel low pass filter) and digitalized using a Data Acquisition Card (NI-USB 6259, National Instrument, USA). WinWCP Strathclyde Electrophysiology software was employed to record electrical traces and apply potentials. Adapted with permission from [1]. Copyright 2017 American Chemical Society.

(Chroma Technology, USA) was used to isolate the laser excitation source ($\lambda_{ex} = 488nm$) from the emitted fluorescence light.

A **beam expander** (BE02-05-A, ThorLabs, USA) was employed to improve the NA of the system by increasing the diameter of the collimated laser beam in such a way that the output beam filled the back entrance of the objective.

A set of **absorptive neutral density filters** (NEK01, ThorLabs, USA) was mounted on a wheel with the purpose of attenuating the laser power. Selectable Optical Densities (OD) ranges from 0.1 to 4 hence the transmittance is given by $T = 10^{-OD}$.

An **electron multiplying Charge Coupled Device (emCCD)** was used as imaging detector (iXon Ultra 897, Andor Technologies, UK). Compared to traditional CCD cameras, an emCCD delivers high sensitivity with high speed. CCD camera suffers from slow readout due to the limited bandwidth. The emCCD utilises an electron multiplying structure (called

gain register) which enables charges (thus collected photons) to be amplified on the sensor before it is read out and transferred to the following amplification stage. In this case the read out noise does not limit the sensitivity because the signal has been already amplified and hence the camera maintains high sensitivity despite the fast acquisition. This type of camera is extremely useful in single molecule measurements due to the limited amount of photons to be recorded and the fast time-scale required in biological applications. In the specific case, the iXon Ultra 897 has a detector of 512x512 pixels (each pixel measures 16 μm x 16 μm) with a readout velocity of 56 fps at full frame(equivalent to 1 frame every 17.8 ms) or 595 fps (frames per second) with 128x128 pixels cropped sensing mode. The dark noise, resulting from thermally generated electrons, is minimized by an active cooling system that mantains the sensor at -60 degrees Celsius. The quantum efficiency, which represents the ability of a incident photon to be absorbed and generate an electron, is above 90%.

Electrical sensing

For the optical detection a dual barrel nanopipette used in nanobridge configuration was clamped to a single-axis miniature translational stage (DT12, ThorLabs, USA) used to manually approach the nanopipette within the objective working distance. The translational stage was placed on top of a universal sample holder (H473XR, Prior Scientific USA). A pair of Ag/AgCl electrodes were inserted in the nanopipettes and connected to the headstage of a patch clamp amplifier (A-M 2400, A-M Systems, USA) which was used to apply a differential voltage. In order to shield electromagnetic radiation, the universal sample holder, onto which the nanopipette and the head stage were mounted, was enclosed in a Faraday cage. The analogue signal coming from the amplifier head stage signal was filtered by an integrated 4th order Bessel low pass filter and then digitalized using a Data Acquisition Card (NI-USB 6259, National Instrument, USA). All traces were recorded with WinWCP Strathclyde Electrophysiology Software freely distributed by University of Strathclyde Glasgow.

2.2.5 Data Analysis

The analysis of single molecule events contained in the recorded ionic current traces were performed using a custom written MATLAB software developed by Prof. Joshua B. Edel (Chemistry Department, Imperial College). The main steps of the algorithm are listed below (**Figure 2.4**):

1. **Data input and resampling.** The input file, either .abf or .wcp format, are loaded and if necessary can be resampled. As in the case of acquisitions performed in nanobridge configuration, the actual information spans a much smaller frequency range

than the one used in conventional configuration. This is due to DNA translocations being significantly slower in time. One key advantage of having the information encompassing a smaller bandwidth range is the possibility of filtering out the high frequency components and thus achieving higher SNR values.

2. **Baseline correction.** The script proceeds to perform a baseline correction of the ionic current trace according to an asymmetric least square smoothing algorithm [50]. Two parameters, which are manually tuned according to each specific dataset, allow the user to have a smooth and faithful fitting of the original baseline. Visual inspection of baseline correction is sufficient to obtain a good set of parameters.

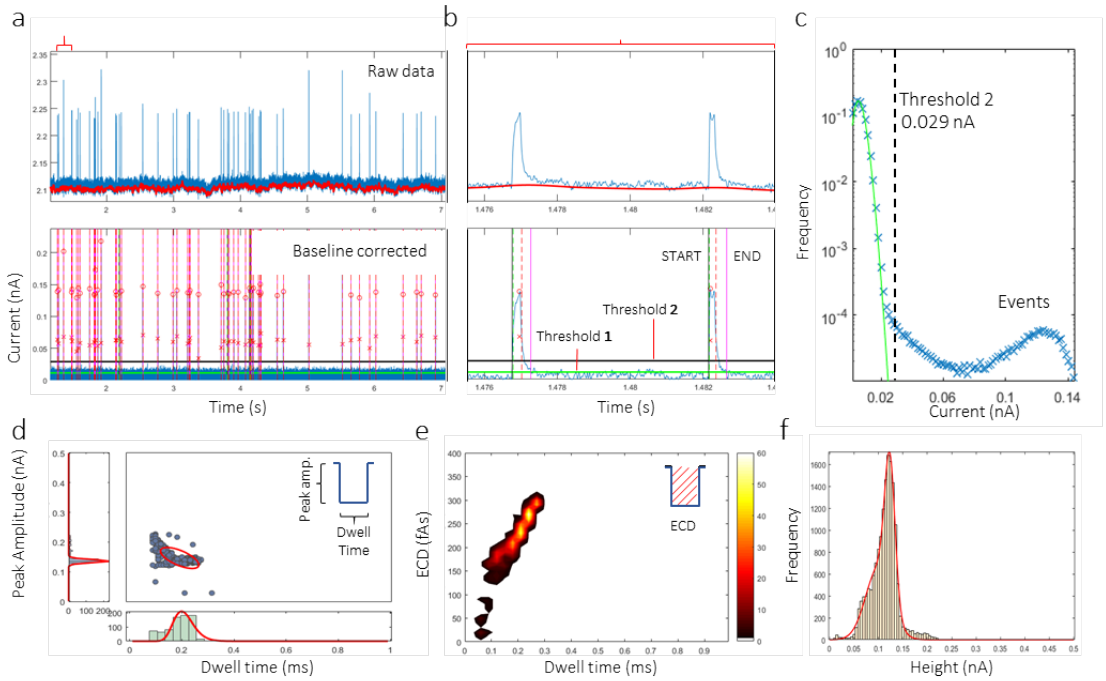

Fig. 2.4 Data analysis performed on 10 kbp DNA translocation data acquired on single barrel nanopipette in conventional configuration at -600 mV (400 pM DNA was initially placed inside the pipette). Event detection consisted on (a) Baseline identification (top) and baseline correction (bottom) performed with an asymmetric least square smoothing algorithm as highlihghted by the red line. Any current modulation above the threshold 2 (black line) was considered an event. As shown in the detail in (b), the start and end of each event corresponded to the first and last data above the threshold 1 (green line). (c) Shows an histogram of the baseline-corrected ionic current trace. The open pore current was fitted with the Poisson probability distribution function (green solid line) and threshold 2 was calculated to be 6 times the variance of the background signal (0.029 nA). Statistics of the detected event: (d) peak current/dwell time scatter plot, (e) equivalent charge density/ dwell time density map (f) peak current histogram.

3. **Single molecule event discrimination.** An all point histogram of the current trace is calculated; a Poisson probability distribution function is used to fit the part of the graph belonging to the baseline current (also called open pore current because recorded when no analyte occupies the pore). Deviations in the ionic current greater than 5 times

the variance of the Poisson distribution, from the baseline current, is considered as an event. The start and the end of each event corresponds to the first (or last) data point which is above the background noise signal.

4. **Statistics and data representation.** For each event the software computes the event duration (dwell time), the mean and max peak amplitude and the discrete integral of the current blockade over the duration of the event. This last quantity is termed Equivalent Charge Deficit (ECD) or alternatively 'Event Charge Deficit' and it represents the amount of charge that would have passed across the pore without the molecule obstructing part of the ionic current flow. The ECD depends mainly on the size of the analyte and not on conformations that the molecule can assume during the translocation process. Finally scatter plots and relative histograms are generated and fitted. Notably, dwell time distributions were fitted according to the Ling-Ling model [51]: first-passage probability density function (PDF), based on Schrödinger first-passage time theory which yields information about velocity and diffusion of the DNA within the nanopore while peak current distributions were fitted with a Gaussian PDF.

2.2.6 Scanning Ion Conductance Microscopy

The height of the nanobridge at the tip of the nanopipette will be measured by using a Scanning Electrochemical Cell Microscopy which is a direct derivation of the Scanning Ion Conductance Microscopy (SICM). Therefore the basic principles of this SICM will be briefly described next.

Principles of operation

SICM is a scanning probe technique that was originally developed to image non conductive surfaces [52]. The mechanism of operation is based on the ion current flow between an electrode located within a nanopipette filled with electrolyte and another electrode located in the electrolytic bath containing the sample to be scanned. The ion current, which is a function of the tip-surface separation, is used as a feedback to maintain the tip-sample distance in such a way that topographical information can be extracted [53]. The ion current is generated as a result of a bias applied between the electrodes (typically Ag/AgCl) and dominated by the total resistance of the nanopipette R_T according to the following equation [54]:

$$I = \frac{V}{R_p + R_{ac}} \tag{2.3}$$

where R_p is the nanopipette resistance and R_{ac} is the access resistance between the nanopipette entrance and the sample surface. Both resistances can be described mathematically as following:

$$R_p = \frac{h}{\kappa\pi r_p r_i}; R_{ac} \approx \frac{\frac{3}{2}\ln\frac{r_0}{r_i}}{\kappa\pi d}; \tag{2.4}$$

where h, r_i, r_p are geometrical parameters of the nanopipette(tip length, inner radius of the tip opening, inner radius of the tip base), κ is the electrolyte conductivity and d is the distance between the tip and the surface.

The nanopipette is typically mounted onto a piezoelectric positioner. The former is an active element of the feedback mechanism which, on top of being responsible for moving the nanopipette over the x-y plane, provides accurate control of the tip-sample distance. Three methods of feedback have been established for SICM: the *nonmodulated mode*, *distance-modulated mode* and *hopping mode* [53]. In the nonmodulated mode a constant potential is applied between the electrodes and the feedback provides a constant tip-sample distance based on the dc-current. However, while following the sample contour, the response of the feedback might not be quick enough to avoid tip-sample collisions especially in cases where the surface present high aspect ratio features. Things are improved in distance-modulated mode where an ac component is added on top of the dc component; the ac is utilised as control feedback signal to maintain a constant tip-surface distance. In this case stability is improved because the system is not susceptible to changes in the ion current that are not in phase with the ac modulation frequency [55]. Samples with high roughness or with high aspect ratio features are still problematic for both non-modulated mode and distance modulated mode. This issue is addressed in hopping feedback control mode. In this case, the SICM probe vertically approaches the surface until ion current charges and it is pulled away. It is therefore possible to image very irregular surfaces without damaging the tip. A prescan at low resolution is performed to have a first estimation of the surface roughness which is then followed by a more accurate scan [56].

SICM setup

A dual barrel pipette in nanobridge configuration was filled 100 mM KCl solution (buffered with 10 mM Tris 1 mM EDTA, pH 8.0). Ag/AgCl electrodes were then inserted into each of the barrels to establish electrical contact. The nanopipette was mounted onto a single axis (z) piezoelectric positioner (P-753-3CD, Physik Instrumente, DE) perpendicular to a quartz substrate to control the position of the nanopipette during the approach. The quartz substrate surface was silanized to minimize nanobridge electrolyte adsorption to the quartz surface. A custom written software (developed by Prof. Yuri Korchev and colleagues in the Dept. of

Medicine, Imperial College London) was used to approach the nanopipette in hopping mode and a constant bias was applied between the Ag/AgCl electrodes to induce an ion current (IDc) between the barrels, across the electrolyte bridge. This IDc was measured and recorded by using MultiClamp 700B amplifier (Molecular Devices, USA) with a digitizer (Digidata 1550, Molecular Devices). The magnitude of IDc was used as a feedback signal to detect contact between the droplet meniscus and the surface and to control the separation between the tip of the nanopipette and the surface.

2.2.7 Nanobridge Experimental Conditions

In nanobridge configuration (see **Figure 2.1**), the pipette is firstly silanized at its back and then filled with electrolyte solution. A Ag/AgCl electrode is inserted in each barrel of a double barrel nanopipette and then connected to the headstage amplifier (Multiclamp 700b, Molecular Devices). In this way the electric circuit is closed by the nanoscale electrolyte bridge located at the tip of the pipette. No bath is required for this configuration and the pipette is clamped to an adjustable holder which leaves the tip and thus the bridge exposed to air. Notably the pipette and the headstage amplifier are placed inside a Faraday cage (connected to ground) which in turns is positioned on top of an optical table. Both the optical table and the Faraday cage are used to shield unwanted noise or vibrations from the recordings. Notably, inside the recording chamber temperature and humidity were not regulated (same as the lab environment) however, as it will be detailed later, the droplet was stable and the recordings were not affected.

2.2.8 Reagents and Sample Preparation

dsDNA

10 kbp, 5 kbp dsDNA 500 mg/ml and 1 kbp dsDNA ladder 500 mg/ml were purchased from New England Biolabs (USA). 1.5 kbp, 500 bp, 200 bp No Limits individual DNA fragments with a stock concentration of 500 mg/ml were purchased from Thermo Scientific (USA). All solutions were prepared in 100 mM KCl, 10 mM Tris 1 mM EDTA, pH 8.0 (Catalog #T9285, Sigma Aldrich, USA). Solutions were prepared fresh by serial dilution and used the same day. Fluorescently labelled DNA samples for imaging were prepared by incubating 250 pM 10 kbp DNA solution in 10 mM Tris 1 mM EDTA with YOYO-1 (Molecular Probes, USA) at a ratio of five base pairs per YOYO-1 molecule.

ssDNA linearization

Linearization of m13mp18 ssDNA was performed by Jasmine Sze, Chemistry department, Imperial College London. The single stranded DNA m13mp18 7.2 kb was purchased from (NEB Hitchin, UK) and is naturally circular. A linear scaffold was required in order to perform translocation experiments. The linear version was made by hybridising a 22 and 23 base oligonucleotide to allow the cutting of SpHI and SnaBI (NEB Hitchin, UK) restriction site respectively. Circular M13 was mixed with 10x molar excess of each oligonucleotide at 90°C and annealed at 65°C in a buffer containing 10 mM Tris-HCL, 1mM EDTA and 5 mM $MgCl_2$ at pH 8 before cooling to 25°C. 1 of SphI and 2 of SnaBI (10000 units/mL) and (5000 units/ mL) respectively were then added to the DNA mixture and incubated overnight at 37°C. The linearized M13 were purified using a QIAquick miniprep kit (Qiagen, CA USA) and the enzymes and excess unbound nucleotides were removed by PCR clean-up gel extraction (Macherey-Nagel, Germany). The linearized M13 were then run in 0.8% gel and 5.5 V/cm for visualisation.

2.3 Results and discussion

The fabrication of the dual nanopore platform was implemented via laser pulling of theta capillaries according to 2 different protocols (see Experimentals). While both protocols gave rise to two reproducible adjacent pores localized at the tip of the nanopipette and separated by 20 nm gap of insulating septum, the difference laid in the pore dimensions. Protocol 1 resulted in nanopores of 20 to 30 nm in diameter (**Figure 2.5 a-d**) whereas protocol 2 resulted in much larger pores, 50 to 100 nm as measured from SEM and TEM (this will be characterized later in the chapter). Notably the pore shape was approximated to a full circle albeit its shape was closer to a truncated circle.

The nanoscale bridge was initially characterized by comparing the current-voltage characteristics (IV) in three different configurations: (i) Conventional configuration where on electrode is placed in the bath while the other electrode is in one of the barrel (ii) Dual pore configuration one electrode is inserted in each barrel and the nanopipette tip is immersed in a bath with same electrolyte and (iii) nanobridge configuration where electrodes are positioned in different barrels but the nanopipette tip is in air (**Figure 2.5 b**). Electrical characterization was carried out by filling each pipette barrel with 100 mM KCl buffered in TE and using a pair of Ag/AgCl electrodes to apply a potential. With nanopipettes pulled with protocol 1 (small apertures), at 100 mM KCl in configuration (i) the conductance was $G_1 = 4.75 \pm 0.52$ nS and $G_2 = 4.45 \pm 0.43$ nS for barrel 1 and barrel 2 respectively (**Figure 2.7 a**). The conductance was measured over the linear range $\pm$ 100 mV. In addition IVs

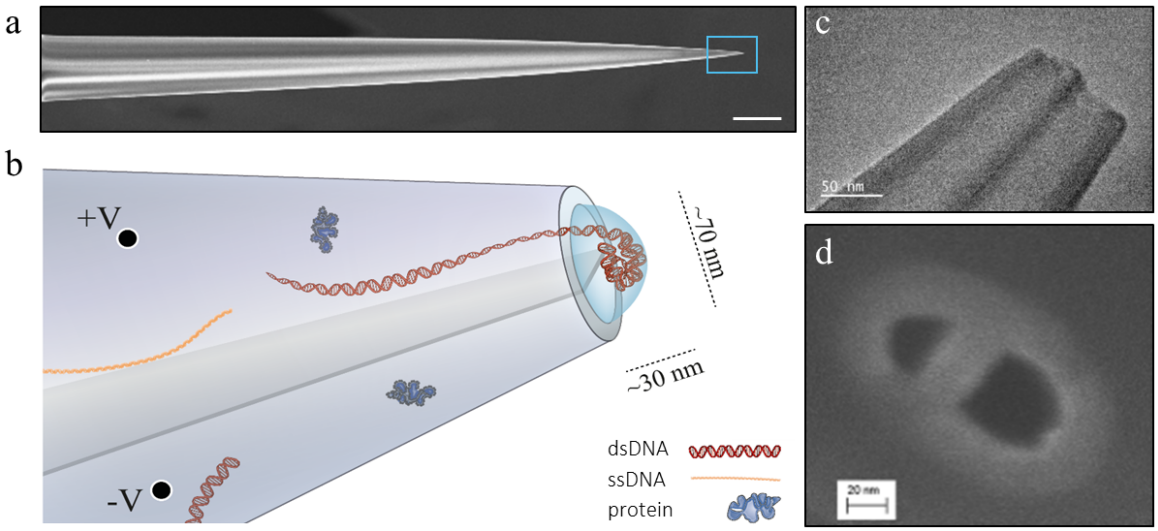

Fig. 2.5 Nanobridge schematics and optical characterization. SEM of the dual barrel nanopipette visualized laterally, scale bar 10um. (b) Schematic representation of the nanoelectrolyte bridge formation at the tip of the nanopipette.(c) TEM and (d) SEM of the tip of nanopipette pulled with protocol 1. Scale bars(c) 50nm, (d) 20nm. Adapted with permission from [1]. Copyright 2017 American Chemical Society.

showed a negative rectification($|I_{-600mv}/I_{+600mv}| = 1.56 \pm 0.08$) which was consistent with negatively charged glass nanopores previously reported at this ionic strength and pH [26, 57]. In fact the negative surface charge present on the quartz nanopipette leads to permselectivity behaviour of the pore (e.g. enhanced Cl^- ion selectivity) [58–60]. In dual pore configuration (ii) IVs were linear over the entire recorded voltage range $\pm$600 mV and the conductance measured of 2.20 ± 0.22 nS which was roughly half of the value measured in (i). This fact was attributed to the introduction of the second pore which increased the total resistance of the system; in the equivalent electrical circuit the conductance of the two nanopores in series $\frac{1}{G_{Tot}} = \frac{1}{G_1} + \frac{1}{G_2} = 2.3$ nS well approximates the value measured in (ii) (2.20 ± 0.22 nS). The absence of rectification in this mode of operation, was ascribed to the enhanced Cl^- selectivity showed by both nanopores, which resulted in an overall loss of rectification.

Interestingly, in nanobridge configuration IV curves revealed a quasi-sigmoidal behaviour with a conductance of 2.04 ± 0.13 nS as measured in the linear region ($\pm$200 mV). One phenomena that can help to understand the non-linear behaviour, observed in nanobridge at voltage higher than 100 mV, was electrowetting. Electrowetting involves the use of an electric field to alter the surface tension of a solid-liquid interface [61]. For instance a water droplet spreads onto a surface if an electric field is present hence both shape and contact angle are affected [62]. This phenomenon applies both at the macroscale and at the nanoscale [63, 64]. This could also be the case in nanobridge where the electric field present in the electrolyte bridge might affect its shape by pulling it towards the tip of the nanopipette as a result of changed surface tension and hence contact angle.

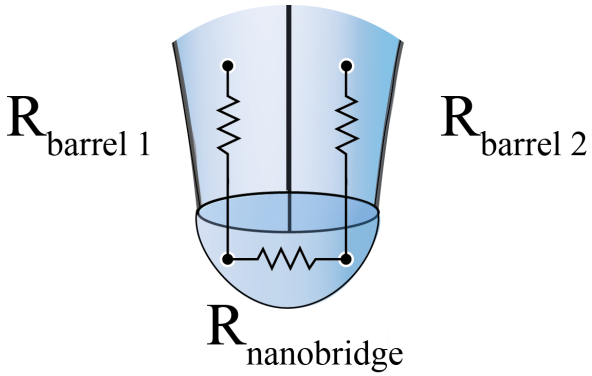

Fig. 2.6 Diagram of the equivalent electrical circuit of the dual barrel nanopipette operating in nanobridge configuration. A simple electrical model, which does not take into account capacitive effects, describes the dual barrel nanopipettes operating in nanobridge configuration as three resistors connected in series: $R_{barrel1}$ and $R_{barrel2}$ represent the two nanopores whereas $R_{nanobridge}$ represent the contribute of the nanofluidic bridge across the two barrels. Therefore the overall resistance of the system is given by $R_{tot} = R_{barrel1} + R_{barrel2} + R_{nanobridge}$

These results indicated that the electrolyte nanobridge accounted on average for up to 11% of the total conductance, although higher values up to 27% has been observed. The remaining conductance was almost equally split between the nanopores in each barrel. A simple electrical model described the nanobridge connected as a third resistor in series to the other two nanopores, therefore the overall resistance of the system was given by $R_{tot} = R_{barrel1} + R_{barrel2} + R_{nanobridge}$). According to this model $R_{nanobridge} = 55M\Omega$, $R_{barrel1} \approx R_{barrel2} \approx 490M\Omega$. This also implied that as little as 11% of the voltage applied dropped within the nanobridge.

Conductance dependence on salt concentration was investigated in nanobridge configuration (**Figure 2.7 b**). The IVs conserved a sigmoidal behaviour and the conductance values followed a linear trend with respect the salt concentration in the range 5 mM and 400 mM KCl at pH 8.0. This result was similar to what has been reported for conventional configuration (i) with glass nanopipettes and solid state nanopores operating in similar conditions [65] perhaps suggesting that, in this salt regime, droplet formation and shape were not affected by the salt concentration. At salt concentration above 400 mM (up to 1 M) this scenario was not true anymore. A consistent percentage of nanopipettes exhibited no ionic current or extremely unstable and noisy one. Most probably at high salt concentration the electrolyte bridge formation and stability were less successful and salt crystals were a source of pore blocking and current noise.

Looking at the power spectral densities for nanobridge configuration and conventional configuration revealed that nanobridge had better noise characteristics both in the low and high frequency regime, compared to conventional configuration. This is most probably the result of decreased device capacitance (the overall device capacitance affects proportionally both the dielectric noise and the input capacitance noise [66]).

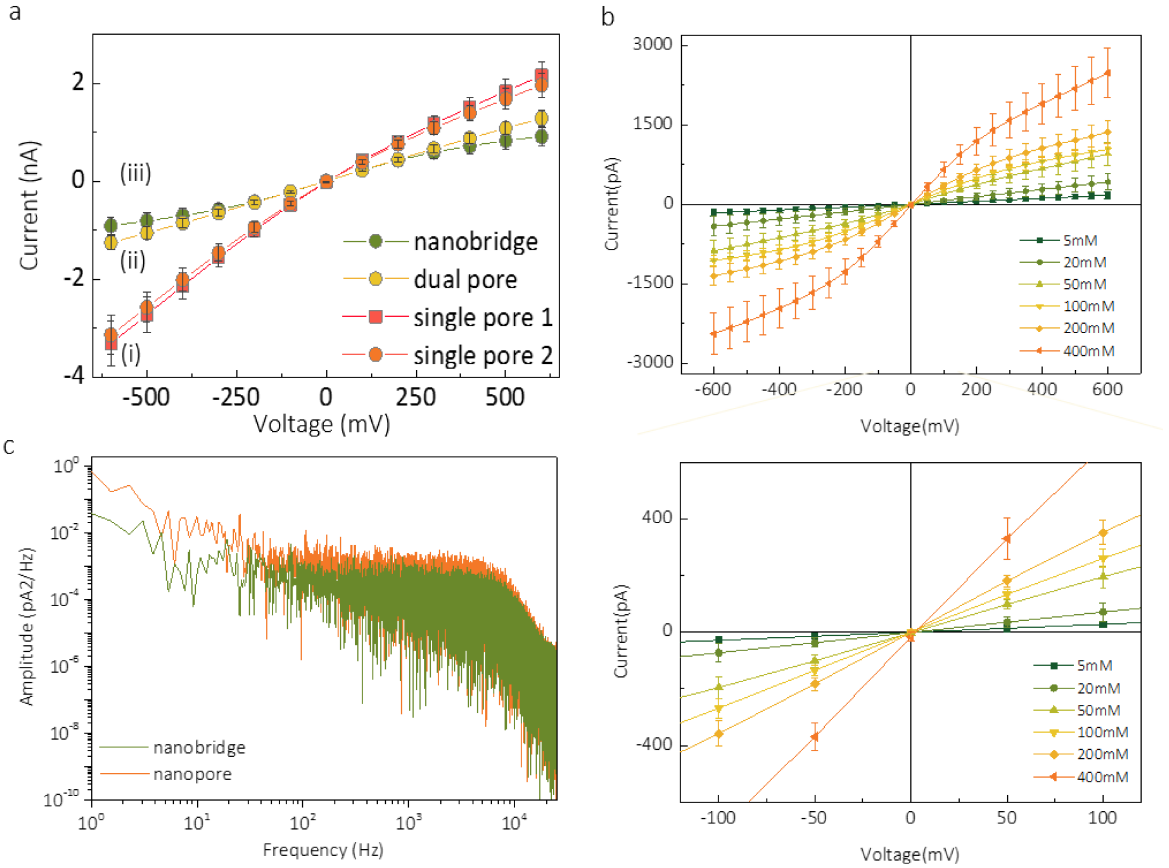

Fig. 2.7 Nanobridge electrical characterization.(a) Current–voltage characteristics of dual barrels nanopipettes measured in nanobridge configuration, conventional configuration and dual pore configuration at 100 mM KCl. (b)Top showing current voltage characteristics for different nanopipettes at KCl concentration of 0.005, 0.02, 0.05, 0.1, 0.2 and 0.4 M as indicated. All IVs show a sigmoidal characteristic which was observed more pronounced at higher ionic strength. Notably above 0.1 M KCl the number of working devices decreased up until 1 M KCl where vast majority of devices failed to produce any IV. In general it was observed a much noisier and unstable ionic current. This fact can be explained with a much higher probability of salt crystal formation at tip of the nanopipette when the ionic strength is high. In turns these crystal might alter substantially, if not blocking completely, the ion flow between the barrels. Bottom showing a zoom of the IV characteristics at different salt concentration between ±100 mV where they displayed a linear behaviour. (c) Noise analysis showing power spectral densities of nanopipettes in conventional and nanobridge configuration, under a negative 300 mV voltage bias at 100 mM KCl. Both signals were filtered at 5 kHz (via Axpotach) and nanobridge showed superior performances in the low-medium frequency regime. Adapted with permission from [1]. Copyright 2017 American Chemical Society.

2.3.1 Estimating the electrolyte bridge volume

Characterization performed with SEM, TEM as well as with current-voltage characteristics at various KCl concentration allowed us to confirm the existence of the bridge and to provide initial estimation of nanobridge dimensions. However, there was no information about the height of the bridge. Estimating the height of the fluidic bridge, therefore the total nanobridge volume, was an essential piece of the puzzle towards understanding this new configuration and its possible use in single molecule sensing. The height of the nanobridge was measured by performing a series of approaches onto an surface utilising a scanning probe microscope with full feedback control (schematic shown in **Figure 2.3**). The idea originates from scanning droplet techniques [67] applied to electrochemical measurements where, a liquid droplet connects the end of the nanopipette probe with the an electrochemical active surface [68]. For instance, in the case of scanning electrochemical cell microscopy (SECCM), a dual barrel nanopipette filled with aqueous electrolytic solution acts as the probe. The ionic current measured between the quasi-reference counter electrodes, inserted in each of the two barrels, serves as a feedback signal for positioning the probe, and thus the droplet, in contact with the surface and maintaining it at a constant probe-surface distance [69, 70].

To estimate the electrolyte bridge a similar setup was adopted: a nanopipette, mounted onto a piezo-stage, was operated in nanobridge configuration and the ionic current was monitored when approaching perpendicularly the nanopipette, hence the electrolyte bridge, towards a silanized glass surface. Changes in the ionic current, due to physical interaction with the surface (as for SICM), were then correlated to changes in the droplet dimensions [52, 54]. **Figure 2.8 a** illustrates the main steps for this experiment i) A stable ionic current I_0 was recorded when the droplet was distant from the surface. Upon contacting (ii) the ionic current immediately decreased (iii) reflecting a change in the bridge dimensions. It should be noted that for practical reasons (e.g. roughness of both substrate and pipette tip) the ionic current was never completely blocked (except in few, almost ideal cases), therefore to estimate the surface contact point, represented by the local minima in the measured ionic current (iv), the pipette was lowered until it came into contact and then physically crashed against the surface. At this point the ionic current suddenly increased due to the increased pore diameter and the approach process was stopped. As a result of multiple approaches the droplet height, which was defined to be the difference between initial (ii) and full surface contact was measured to be 30 ± 5 nm. Based on the SEM and TEM images we knew that the tip profile was semi-ellipsoidal with the major and the minor axes measured $x = 21 \pm 2$ nm and $y = 48 \pm 2$ nm. Considering the height just measured, the overall nanobridge volume was calculated to be 63 ± 19 zL (10^{-21} litre). Notably, this value is derived from approximating the shape of the fluidic nanobridge to a perfect droplet sitting on top the nanopipette however

this might not be case always the case. The wetting process could not only involve the tip but also the outside walls of the nanopipette. In that case, the overall nanobridge volume would be larger but this would not be necessarily visible on SICM type of experiments. Therefore a more extensive work should be conducted on the nature of the nanobridge by using techniques such as Cryo-Electron Microscopy which would allow for a direct and a more precise type of measurement.

After having assessed the bridge dimension, the attention was focused on exploring if biomolecules could effectively be transported and eventually being confined within this zeptolitre bridge when going from one barrel to the other. Towards this goal, experiments consisting of optical translocations of 10 kbp DNA labelled with a fluorophore were carried out (**Figure 2.8 b-c**). The selected dye was YOYO-1 (Life Technologies Molecular Probes, USA) due to its absorbency peak at 491 nm which was extremely close to the laser excitation wavelength (488 nm). YOYO-1 is a bis-intercalator dye with a binding site size of about 4 bp/dye [71, 72]. The high association constant along with a strong fluorescence enhancement upon binding to dsDNA (high SNR) made YOYO-1 extremely attractive for DNA studies. Although being already reported in nanopore works for electro-optical detection of dsDNA [73], it should be noted that intercalating dyes are known to negatively impact both the mechanical and structural properties of DNA [74]. Considering our study, an increase in DNA bending rigidity and DNA persistence length would perhaps affect the translocation and confinement process. However the matter persists to be controversial and recent works performed with magnetic tweezers found that the persistence length of dsDNA (about 50nm) was independent of the amount of bound YOYO-1 and also that the DNA bending rigidity seemed not to be affected by the presence of the fluorophore [72].

As it has been described in the experimental section, a dual barrel nanopipette used in nanobridge configuration was mounted onto a manually actuated translational stage and positioned within the working distance of the 60x objective of an inverted microscope used in epifluorescence configuration equipped with a emCCD for fluorescence detection. To diminish scattered light and avoid overheating the nanopipette tip, the laser power was attenuated using the O.D. filter (the transmission power was $\frac{1}{10}$ of the full power). The emCCD parameters were set to "Speed and Sensitivity" mode which implied high pre-amplifier gain and high secondary amplifier gain with an exposure time set to 100 ms. The long exposure time was selected due to the long DNA translocation duration (a more detailed study on dsDNA translocations will be given in the following section of this chapter); the high exposure time was also used to collect sufficient amount of photons to detect a single event above the noise floor. Both barrels were filled with 250 pM 10 kbp DNA in 100 mM KCl buffered in TE at pH 8.0. Upon the application of a voltage bias (through the A-M 2400),

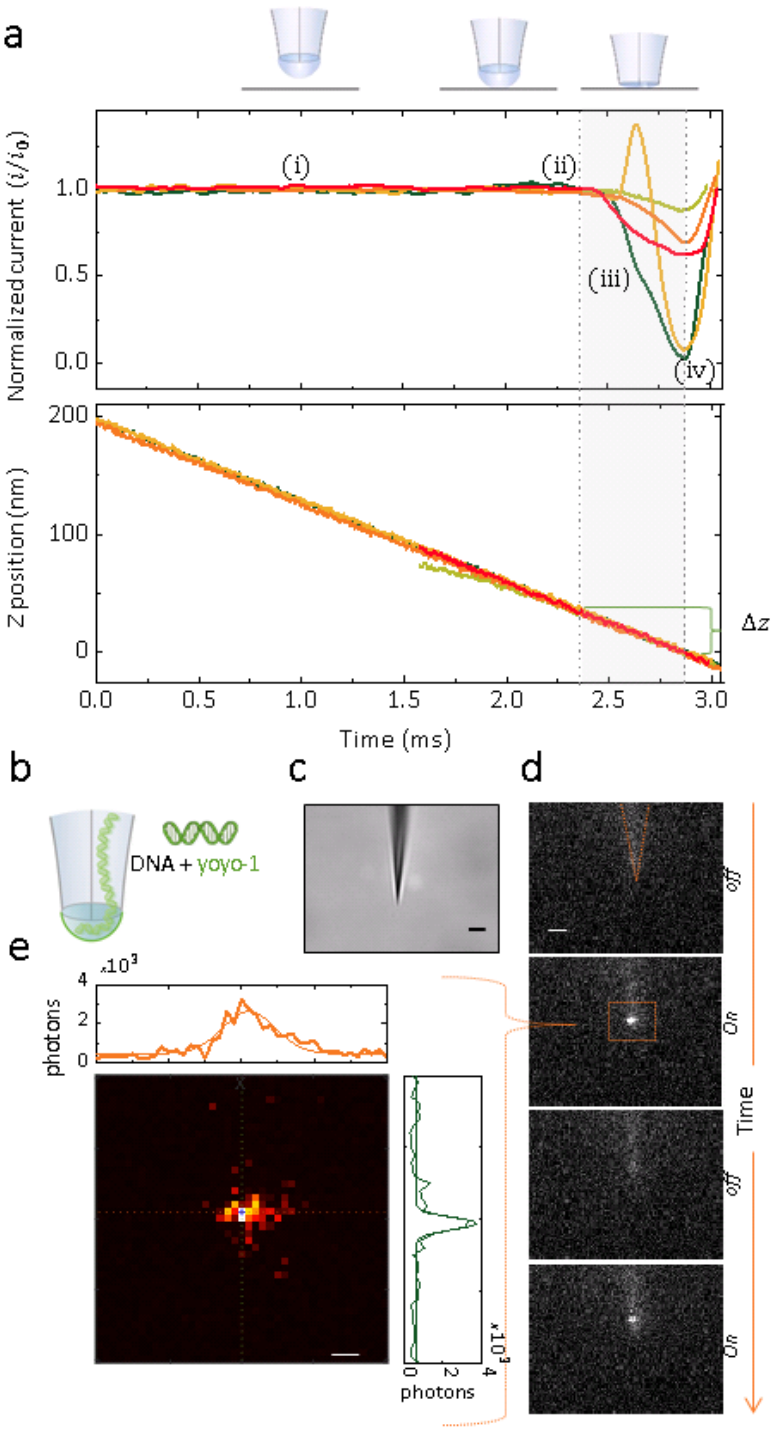

Fig. 2.8 Electrolyte bridge characterization. (a) The height of the nanobridge at the tip of the nanopipette was measured by using a SECCM with ionic current feedback. Both nanopipette barrels were filled with 100 mM KCl solution, was mounted in a piezo-stage perpendicularly to a silanized glass surface. The ionic current (top panel) was recorded with along with the Z-position (bottom panel) of the piezo-stage. During approach the current remained unchanged (i) and decreases when contact between the nanobridge and with the glass substrate occurs (ii). The tip is lowered until the tip is in contact with the substrate (iii) and then crashes into the glass substrate, breaking the tip and increasing its diameter and hence the ionic current (iv). Note that the current in all cases cannot be completely shut off due to surface conductivity and non-ideal surface contact. The nanobridge height (Δz), defined as the difference between the initial nanobridge to surface contact (i) and tip to surface contact (iv), was measured to be $30 \pm 5nm$. (b) Schematic of optical fluorescence detection used to confirm molecular confinement and DNA transport via the electrolyte nanobridge. 10kbp DNA stained with YOYO-1 was used in 100mM KCl solution buffered with 10mM Tris 1mM EDTA pH 8.0. (c) Bright field of the nanopipette (scale bar shows 5μm). (d) Fluorescence images recorded with an emCCD camera (100ms exposure time) showing that upon the application of a bias (300mV), a fluorescent spot, owing to DNA translocation, was detected at the tip of the nanopipette. (scale bar shows 5μm). (e) A close-up of a representative DNA optical translocation showing the fluorescent profile along x-y axis. Measurements were diffraction limited therefore, despite the DNA being confined the fluorescence appeared bigger than the bridge. (scale bar shows 1μm). Reprinted with permission from [1]. Copyright 2017 American Chemical Society.

translocations were recorded electrically and then visualized optically with the emCCD camera in the form of a blinking spot at the tip of nanopipette (**Figure 2.8 d**) while no optical or electrical event was recorded when there the voltage applied was 0 mV. The electrical trace was only used to confirm the correct functioning of the device (e.g. ionic current value along with DNA translocation events). The recorded fluorescence spot (which a representative example is shown in **Figure 2.8 e**), showed an asymmetric but gaussian profile along the two directions with its size being well above the diffraction limit. It is important to make some practical considerations about these recordings:

- Exposure time. In light of the long exposure time, the recorded spot might be the sum of part of even the whole DNA threading process.
- Diffraction limit. Recorded fluorescence signals are subjected to the diffraction limit.
- Refractive index mismatch. A light ray is always refracted at the glass-medium interface. In this case photons, either coming from the excitation source or the emitted photons, had to go through different media carrying different refractive index: Water of the objective, glass coverslip, air. In the first instance index mismatch affects negatively the spatial resolution because of optical aberrations. Secondly, whenever light is refracted some light is also reflected thus the overall intensity decreases [75].
- Salt concentration. Ionic conditions could potentially alter the stability of YOYO-1 binding.The electrolyte solution used for the DNA experiment was potassium chloride at 100mM concentration. Collisional quenching between the chloride ions and the fluorescent dyes (YOYO-1) arising from electron transfer affects the fluorescence intensity [76]. Stern-Volmer equation described a linear relation between the collisional quenching and the concentration of the quencher [48]:

$$\frac{F_0}{F} = 1 + K_{sv}[Q] \tag{2.5}$$

Where F_0 is the rate of fluorescence without the quencher, F is the rate of fluorescence with the quencher, K_{sv} is the Stern-Volmer quenching constant and $[Q]$ is the concentration of the quencher. From the previous equation is clear that the lower the salt concentration the smaller the quenching effect and the higher the fluorescence signal however an extremely low salt concentration would have made the electrical detection of single DNA events extremely challenging because of the small signal they produced thus salt concentration of 100mM appeared to be a good trade-off between electrical and optical detection.

The considerations raised above, limited but did not prevent to confirm some key experimental points. Firstly, the blinking spot at the tip of the nanopipette suggested that dsDNA was effectively translocated through nanobridge confirming the more extensive study based on electrical detection only (Section: *dsDNA detection*). Secondly molecules did not accumulate neither at the tip in correspondence of the electrolyte bridge, nor upstream in the barrel but they translocated from one barrel to the other. Accumulation of molecules would have caused an instability in the electrical trace due to ionic current decrease over the time. Optically, even taking photobleaching into account, accumulation would have translated into a continuous growing of the intensity signal.

Electrolyte bridge stability

The fluidic bridge size was not a precondition for stability. As shown in **Figure 2.9 a,b**, the ionic current baseline was stable over the time: initially the mean current (at 200 mV voltage applied) was measured to be 497 ± 1 pA while after 50 minutes of continuous recording the baseline was measured to be 505 ± 1 pA which corresponded to a variation of 1.6 %. The rms value was 1.12 pA. This result indicated that evaporation was not a dominant factor in the fluidic bridge. The reason of this stability resided in the capillary force which continuously acted to replenish any evaporated solution at the tip. To further confirm the marginal role played by evaporation it was carried out another type of experiment: ionic currents were compared when the nanopipette, assembled in nanobridge configuration, was in air and when the tip was immersed in FC70 which is a fluorinated oil (**Figure 2.9 c**). The former was not miscible with the aqueous phase in the nanoscale bridge therefore it prevented evaporation to take place. Results showed nearly identical IV characteristics before and after the nanopipette was immersed in the oil bath (**Figure 2.9 d**).

2.4 Single molecule confinement

To assess the role of molecular confinement in the detection process, experiments, involving different lengths of dsDNA, were carried out in the three different configurations: nanobridge, dual pore and conventional.

Before presenting the results it is important to distinguish nanobridge arrangement from other nanopore architectures with internal cavities which have been previously reported [77, 11, 78]. Most importantly, none of these architecture could be approximated to neither the uniqueness of nanobridge geometry that has two pore distanced by 10-20 nm nor to the level of confinement expressed in this work. For instance nanocavities "sandwiched" between two pores were used as nanoreactors to monitor chemical reactions at single molecule level

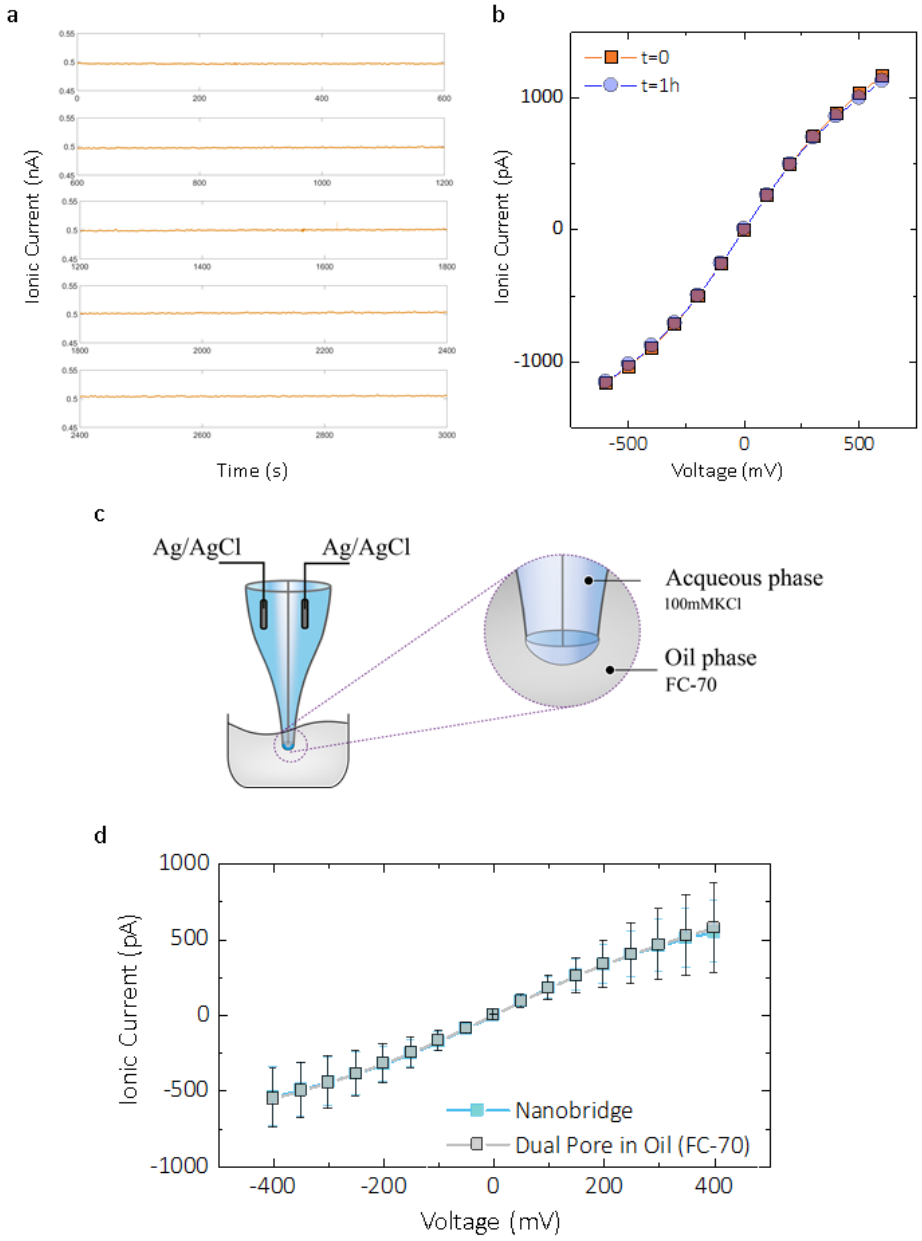

Fig. 2.9 Nanobridge stability. (a) An ionic current time trace is shown using 100 mM KCl and recorded at 200 mV applied bias. The trace has been resampled at 1kHz for visualization purposes. Importantly the open pore current was exceptionally stable over long time periods. For example, at time t=0 the mean current was 497 ± 1 pA; after 50 minutes of continuous recording the baseline slightly increased to 505 ± 1 pA which corresponded to a variation of 1.6 %. This result shows that nanobridge configuration was not affected by evaporation which would result in much larger fluctuations and instability in the signal due to salt crystal formation at the tip of the nanopipette. (b) I-V characterization before and after use show minimal observable change in the ionic current. (c) Schematic of nanobridge stability control experiments were performed using an an immiscible fluorinated oil (FC-70). IVs were measured for nanobridge configuration in air and immersed in oil, where electrolyte evaporation is unlikely to occur. (d) I-V characterization for both the nanobridge configuration in air and the nanobridge immersed in oil showing minimal deviation and indicating that under the experimental conditions used, electrolyte is efficiently replenished at the nanopipette tip and evaporation has negligible effect on the open-pore current. All experiments were performed in 100 mM KCl and recorded using a Multiclamp 700B (Molecular Devices, USA). Adapted with permission from [1]. Copyright 2017 American Chemical Society.

[79], to study the electrophoretic time of flight of DNA molecules [78] or alternatively to measure escape times of nanoparticles and DNA as a function of entropic cavity barrier [11]. Compared to the systems above, nanobridge operated in a substantially different regime: the radius of the confining volume ($R_{confine}$) was equal or smaller than the radius of gyration (R_g) of the molecule (e.g. dsDNA) that was confined.

Pud et al [80] presented a planar dual nanopore architecture where a membrane with pore-to-pore distance ranged between 250 nm and 1 μm. Aside from the presence of two apertures in the same membrane, this configuration operated in a absolutely different manner compared to nanobridge: a ssDNA molecule was threaded simultaneously in both pores resulting in a mechanical trapping. The electrophoretic force acting in both pores but in opposite directions hinder the molecule, as described by the authors, in a sort of "tug of war". This approach did not allow for controllable single molecule confinement due to the lack of a physical confining volume, as opposed to what is described in this work. In addition, this "tug of war" was limited to less than 1%, therefore only a small fraction of the observed events was trapped while all others threaded through a single pore in a classical fashion [80].

2.4.1 Confinement mechanism

Compared to the conventional nanopore scenario, the mechanism of DNA transport across the nanobridge appeared to be completely different [81]. While optical recordings were useful to confirm that DNA effectively moved from barrel to the other passing across the bridge, electrical recordings helped to clarify the overall picture unveiling how it behaved in such ultraconfined space.

As shown in **Figure 2.10 a**, the translocation mechanism envisioned for nanobridge consisted of three steps: (i) a DNA molecule was electrophoretically transported at the mouth of the pore due to the applied voltage. (ii) The electrolyte bridge expanded as a result of the DNA threading in. At this point DNA was fully recoiled ($R_{droplet} < R_g$) and finally (iii) it threaded into the second barrel.

Upon DNA threading in the nanoscale bridge, a correspondent monoexponential decay with time constant τ was recorded in the ionic current (**Figure 2.10 b**). This decay was linearly dependent on the DNA size (0.34 $\pm$ 0.10 ms, 0.75 $\pm$ 0.21 ms, 1.40 $\pm$ 0.46 ms for 1.5 kbp, 5 kbp and 10 kbp DNA respectively) and almost independent on the voltage applied (**Figure 2.10 c,d**). The correlation between DNA size and *tau* was explained with the increase in the total nanobridge volume generated by the DNA insertion. In addition the measured τ values were on the same time-scale with the Zimm relaxation time[1] [78]

[1]The Zimm relaxation time is a model used to study the relaxation process of a polymer chain such as DNA after stretching.

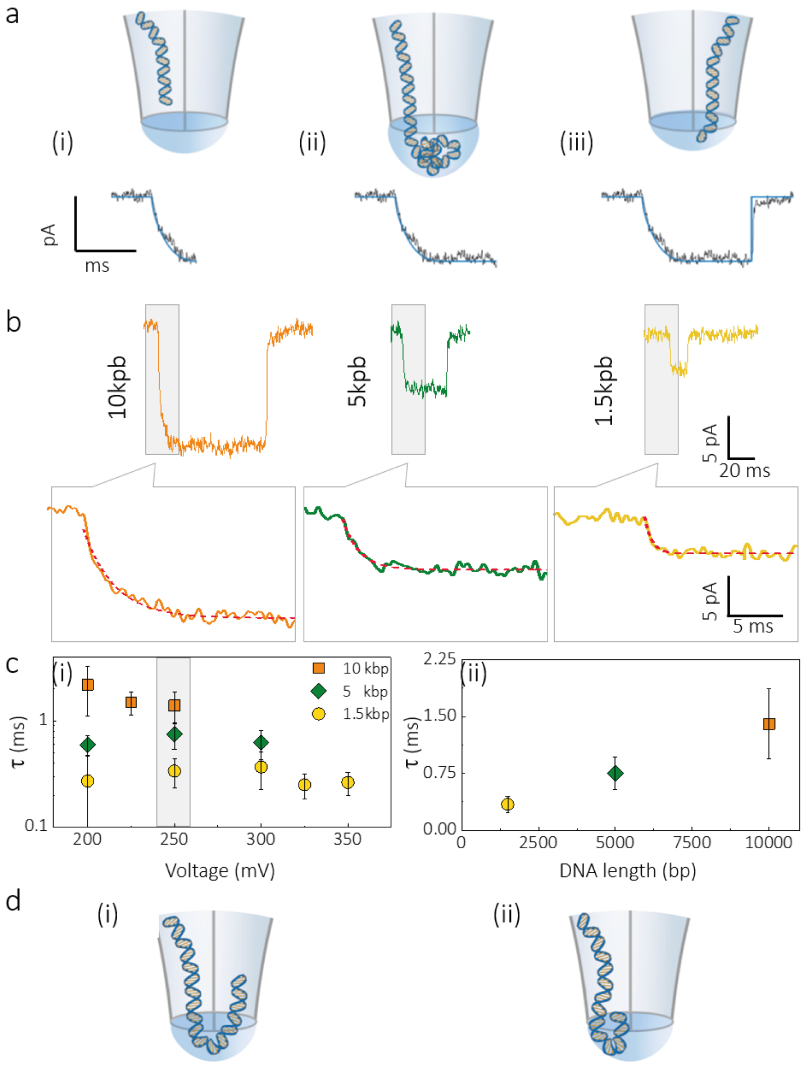

Fig. 2.10 Translocation mechanism of dsDNA in nanobridge configuration. (a) Schematic of the threading process: i) the dsDNA molecule is threaded inside the nanobridge leading to its expansion. The threading process results in the ionic current exhibiting a mono-exponential decay with time constant τ. ii) The DNA recoils inside the bridge. As the DNA in the droplet is predominately governed by Brownian motion, the duration of the blockade is governed by the time it takes the DNA to rearrange and become inserted and finally (iii) threads into the second barrel. (b) Examples of 10 kbp, 5 kbp and 1.5 kbp DNA translocation events recorded in nanobridge configuration in 100 mM KCl. The onset of each translocation event was fit with a mono-exponential decay function. (c) Dependence of threading time τ on voltage applied (left panel) for 10 kbp, 5 kbp and 1.5 kbp DNA. Threading time dependence on DNA length for events recorded at 250 mV (right panel). (d) Alternative translocation mechanisms where (i) the DNA bridges the two barrels and (ii) it enters the nanoffluidic bridge partially folded. Adapted with permission from [1]. Copyright 2017 American Chemical Society.

but much smaller than the overall translocation time therefore it was legitimate to consider the DNA as fully recoiled inside the nanobridge. This result was also in good agreement with the optical recordings where a transient fluorescent spot was localized at the tip of the nanopipette.

The threading out step followed a different dynamic, from the threading in step. As a result of recoiling inside the nanobridge, both DNA ends were somehow trapped and distanced from the second aperture. The recoiling process was assumed to be stochastic and DNA had no preferential direction or configuration once inside the nanobridge. Therefore, despite the presence of a weak electric field ($\approx 11\%$ of the total voltage dropped inside the bridge as described in the Characterization paragraph of this chapter), the DNA, which was mainly driven by Brownian motion, would struggle to find its way out. In other words, in the attempt of rearranging its configuration and orientation to leave the DNA molecule spent a prolonged amount of time inside the nanobridge. From the ionic current perspective these corresponded to a long dwell time which was in good agreement with our experimental observations (**Figure 2.13**).

In our discussion we proposed one model that could explain the experimental results on DNA translocation across the nanobridge. Notably, some of the hypothesis lack of direct experimental evidences. In particular, the increase of the overall nanobridge volume as a result of DNA insertion and the DNA recoiling (partial or total) upon translocation in the nanofluidic bridge are essential part of the model that have not being verified yet. Therefore, as shown in **Figure 2.10 d**, we cannot completely ruled out the possibility of other translocation mechanisms where, for example, the DNA molecule bridges both barrels simultaneously upon threading. Despite the rigidity of dsDNA (and its associated persistence length which, for this ionic conditions was approximately $\approx$ 50nm [82]), the DNA chain could make a "U-turn" inside the fluidic bridge (e.g. bridging both barrels). Due to the DNA coiling/recoiling process on one mechanism and the pronounced DNA-bending on the other, both of them are energetically unfavourable. It is not straightforward to establish which one has the lowest energy barrier. Perhaps, one mechanism might be more favourable with long polymer chains while the other is more suitable with shorter DNA strains. In the future it would be interesting to perform experiments using DNA chains equipped with a protrusion such as DNA-protein complex, DNA-apatmer complex or alternatively nicked dsDNA; in this way the secondary level generated by the protusion in the ionic current signature could be used to unravel step-by-step the translocation process.

2.4.2 dsDNA detection: a comparison between nanobridge, dual pore and conventional nanopore configuration

DNA translocation experiments were performed in the three configurations as shown **Figure 2.11** (ionic current traces recorded for 5 kbp DNA in 100 mM KCl, TE buffer at pH 8.0) and nanobridge revealed some key advantages: enhanced temporal resolution, improved SNR, the possibilty of discriminating DNA fragments of different sizes by peak currents alone, low noise electrical recordings.

In both conventional configuration and dual pore configuration the passage of DNA molecule through the pore resulted in ionic current increase, or current enhancement, as reported in literature for similar DNA in similar conditions [4, 83]. For 5 kbp DNA recorded in 100 mM KCl at 250 mV voltage applied, dwell times were measured to be 0.13 ± 0.03 ms and 0.19 ± 0.08 ms for conventional and dual pore respectively. These values were comparable to the one reported in literature for the same DNA size detected with quartz single barrel nanopipettes [4]). Notably, the same device, but arranged in nanobridge configuration, gave rise to events detected up to 100 ms, resulting in a slowdown factor up to 3 order of magnitude as shown in **Figure 2.13 a**. It should be noted that a decrease in ionic current, also called current depletion, was observed within the nanobridge configuration which suggested a decrease in the flux of ions across bridge followed by a decrease in conductance.

A similar effect applied for other DNA fragments such as 10 kbp, 1.5 kbp, 500 bp and 200 bp. The former, 200 bp fragments, went completely undetected in conventional configuration due to their fast translocation velocity and poor SNR, however in nanobridge events were detected with dwell times as long as 20 ms (**Figure 2.13 a**).

The voltage dependence on peak current for dsDNA detected in nanobridge configuration is shown in **Figure 2.13 b**. The peak current increased proportionally with the voltage applied similarly to what was observed for dual pore and conventional configuration. In the case of 1.5kbp DNA, the peak current, as determined by Gaussian fittings, increased from 9.94 ± 0.82 pA at 250 mV to 20.16 ± 0.92 pA at 350 mV. The SNR was calculated according to the following equation[84]:

$$SNR = \frac{\mid \Delta I \mid}{I_{noise,rms}} \tag{2.6}$$

where $\mid \Delta I \mid$ is absolute current change of the single DNA event and $I_{noise,rms}$ is the square root of the integral of current power spectral densities $I_{Noise,rms} = \int_0^{\Delta\nu} Sdf$, where $\Delta\nu$ is the bandwidth and S the current spectral density. As shown in **Figure 2.13 c**, in case of

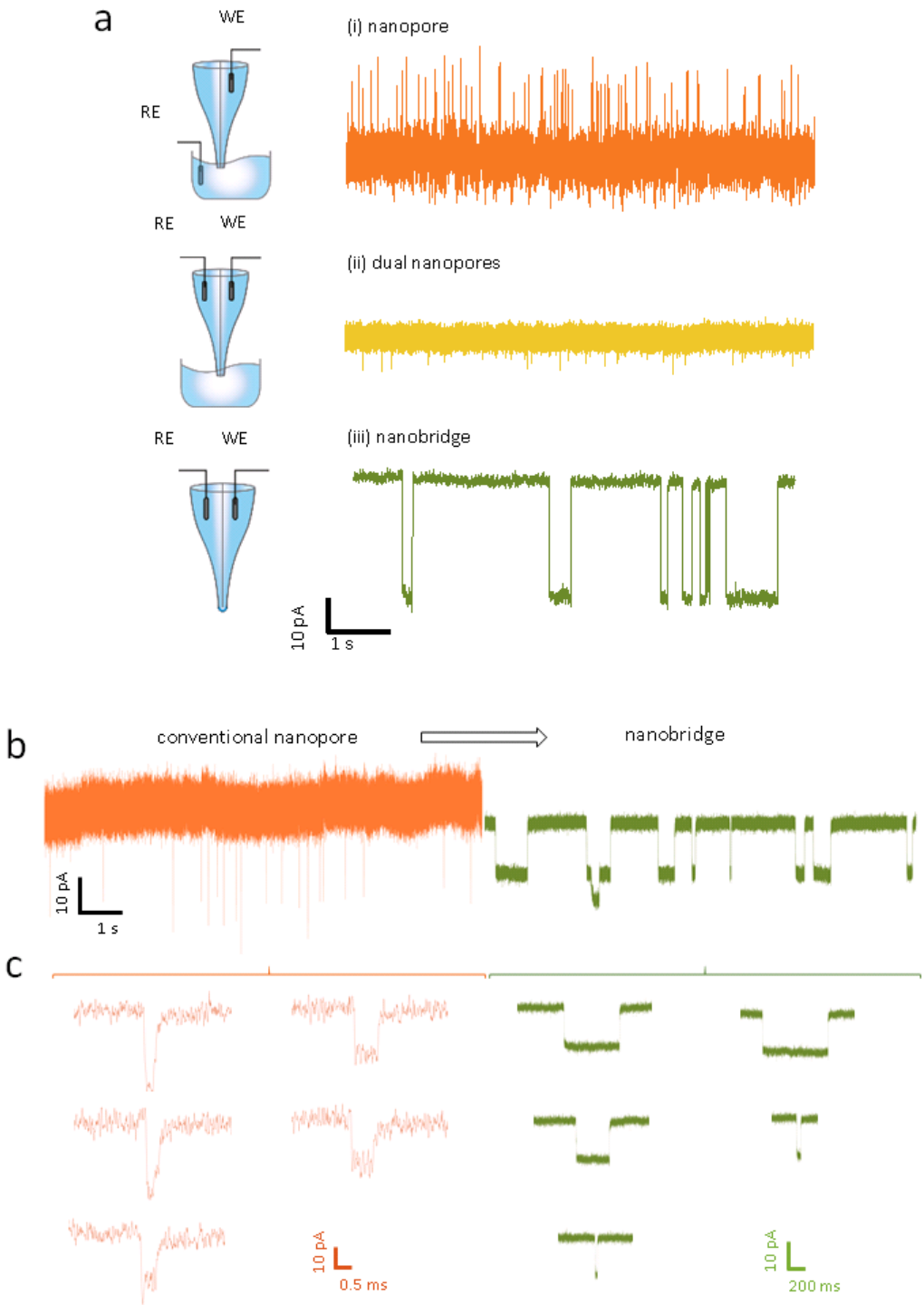

Fig. 2.11 (a) Ionic current recordings of 5 kbp DNA translocations in 100 mM KCl buffered in 10 mM Tris 1 mM EDTA at 350 mV voltage applied, performed in conventional, dual pore and nanobridge configuration as illustrated in the schematic on the left. (b) Ionic current recordings of 10kbp translocations performed in nanobridge and conventional configuration (Acquisition rate: 100 ksample/s). In this case, the conventional approach consisted of a single barrel nanopipette dipped in 100 mM KCl bath and DNA translocations were performed from the pipette to the bath. DNA concentration was set to 400 pM. The signal was analog filtered at 10 kHz via the amplifier. In nanobridge configuration DNA (200 pM) the ionic current signal was resampled at 10 kHz. Looking at single events recorded in nanobridge(c), a clear slowdown of the molecule along with an improved SNR is clearly visible. Adapted with permission from [1]. Copyright 2017 American Chemical Society.

5kbp DNA the measured SNR in nanobridge configuration was 543 % higher than the one measured, for the same molecule and same device, in conventional configuration.

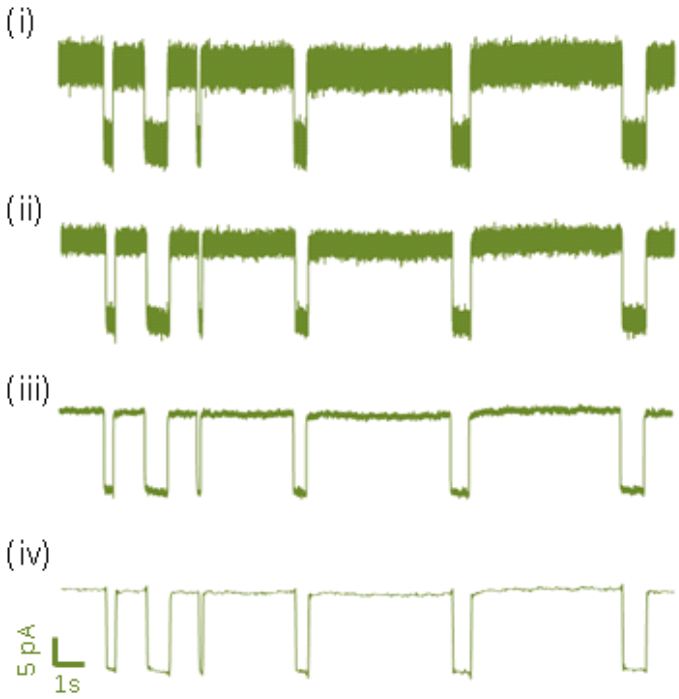

Fig. 2.12 SNR and bandwidth in nanobridge. Due to long translocation times, when operating in nanobridge configuration, high bandwidth recordings were not necessary. Current-time traces can be resampled with a significant SNR improvement at no cost to the amount of information being obtained. This advantage is clearly visible in the representative example shown here where ionic current traces recorded in nanobridge configuration of 200 pM 10 kbp DNA in 100 mM KCl were resampled at (i) 100 kHz, (ii) 10 kHz, (iii) 1 kHz and (iv) 100 Hz. Reprinted with permission from [1]. Copyright 2017 American Chemical Society.

The improved SNR scenario was attributed to the better noise profile and to the long translocation time. In particular, due to the long dwell times, high bandwidth recordings were not required and in principle, the current-time trace could either be recorded using a lower bandwidth or, as done in this work, resampled. In both cases, according to Equation 2.6 and consistent with our findings, it resulted in a better SNR. This significant advantage came at no cost to the information being obtained as shown in **Figure 2.12** where a current-time traces of 10 kbp DNA in 100 mM KCl was resampled at different frequencies (100 KHz, 10 KHz, 1 KHz and 100 Hz). While the event shape was conserved, the SNR improved dramatically.

Longer dwell times was not the only surprising property observed, in fact, nanobridge configuration showed an high ability in discriminating DNA fragments of different lengths based solely on peak current. For dsDNA lengths ranging from 200 bp to 10 kbp, the peak current had a very narrow Gaussian distribution with a full width half maximum (FWHM) calculated to be as small as 2.5 pA **(Figure 2.13a,c)**. For instance the mean peak current

for 5 kbp DNA was 17.17 $\pm$ 0.96 pA in nanobridge configuration compared to 17.96 $\pm$ 2.12 pA measured in conventional configuration at an applied bias of 250 mv. A similar narrow distribution was observed for 10 kbp (24.59 $\pm$ 0.92 pA) 1.5 kbp (9.94 $\pm$ 0.82 pA) 500 bp (7.46 $\pm$ 0.44 pA) and 200 bp (3.42 $\pm$ 0.34 pA). Generally one of the most important side effects of other techniques employed to slowdown DNA molecules, especially the ones that take advantage of viscosity gradients in the electrolyte solution, is the spread in both time and current distributions. This effect affects the resolution of the system, limiting the possibility of resolving species of different sizes. In contrast, nanobridge showed an opposite behaviour: due to the narrow distribution profiles DNA molecules of different lengths were discriminated based solely on peak current values. In conventional configuration, resolution accuracy, hence discrimination of different analytes would require calculation of the event charge deficit (ECD) [85] by integration of the translocation events over time however this technique is only efficient if analyte velocity is well above the cut-off frequency of the amplifier (typically 10 kHz) which, most of the time, is not the case.

In addition, as it will described in the following paragraphs of this chapter, the mean peak current for each fragment size was closely related to square of the radius of gyration indicating that the peak current is proportional to the cross-sectional area of the DNA blocking the nanobridge.

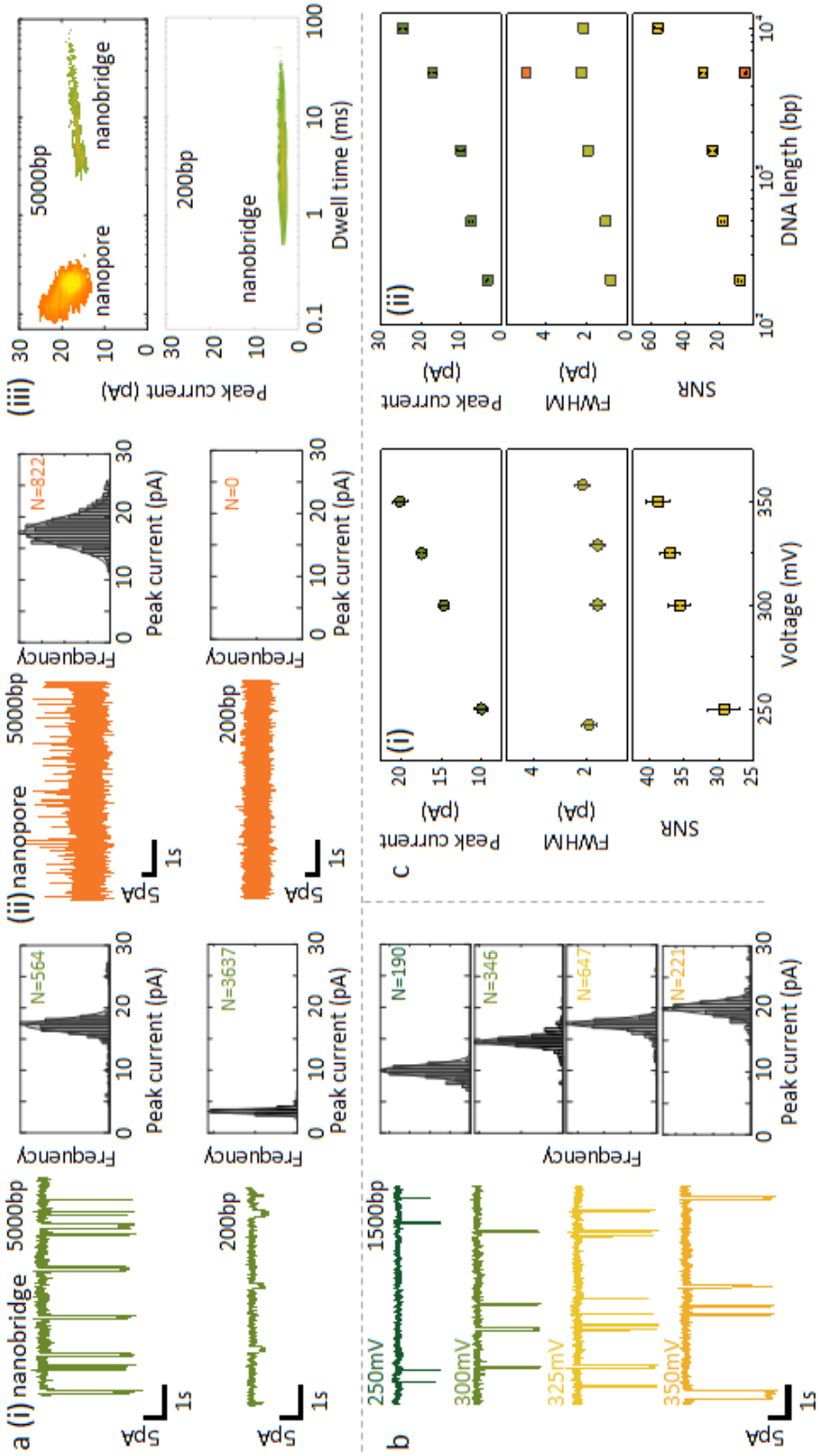

Fig. 2.13 dsDNA detection: nanobridge configuration vs conventional configuration.

Caption Figure 2.13 (a) (i) Trace recorded for 5 kb dsDNA top and 200 bp bottom (both baseline corrected) in Nanobridge configuration at 250 mV. The Gaussian fitting in the histogram reports a current amplitude of 17.17 ± 0.96 pA and 3.42±0.34 pA respectively. (ii) Trace recorded for 5 kb dsDNA top and 200 bp bottom (both baseline corrected) in conventional configuration at 250 mV voltage applied. In this case vents were only detected for 5 kbp with a current amplitude of 17.65 ± 2.11 pA. (iii) Scatter plots showing the dwell time distribution for 5 kbp (top) and 200 bp (bottom). For 5 kbp events were detected below 0.2 ms in conventional configuration while they were distributed up to 100 ms in nanobridge configuration showing a slowing factor of almost 1000. For both length events were broadly distributed in time but tightly distributed in current. This was not true in conventional configuration where the cluster appeared to be broadly distributed along the current axis. (b) Voltage dependence on current amplitude in Nanobridge configuration. (i) Traces, baseline adjusted, showing events detected for 1500 bp at 250 mV (top), 300 mV, 325 mV, 350 mV (bottom). Histograms for current amplitude of the different voltage revealed an increasing trend which is common to conventional configuration: 9.94 ± 0.82 pA at 250 mV, 14.62 ± 0.68 pA at 300 mV, 17.43 ± 0.68 pA at 325 mV, 20.16 ± 0.92 pA at 350 mV. (ii) Shows no voltage dependence for FWHM, meaning that current distribution were not broadening upon a higher voltage applied as shown in conventional configuration. Current drop exhibited a linear trend vs voltage applied. (iii) shows that SNR increased with the voltage applied passing from 9.7 at 250 mV to 16.7 at 350 mV meaning not only that not only the current drop increased but also that noise levels were still modest at higher voltages. (c) Showing Nanobridge configuration performances for dsDNA lengths ranging from 200 bp to 10 kbp. (i) showing that current drop increased from 3.42 ± 0.34 pA for 200 bp to 24.59 ± 0.92 pA for 10 kbp at 250 mV voltage applied(fit). (ii) Shows DNA length dependence on SNR revealing a linear trend for Nanobridge. For 5 kbp the SNR in Nanobridge was almost 3 times bigger than when calculated in conventional configuration (15.32 compared to 5.45). (iii) Shows DNA length dependence on FWHM. Reprinted with permission from [1]. Copyright 2017 American Chemical Society.

2.4.3 Voltage dependence

For solid state nanopores, translocation times of DNA molecules strongly depend on the voltage applied. According to two different theories, dsDNA translocation times were either inversely proportional to the transmembrane voltage as $\sim 1/V$ [86, 87] or, as in the second case, exhibited an exponential decay dependence on the applied voltage ($\sim e^{-V}$) [86, 18, 88, 87]; however, both models predicted a decrease in dwell times when increasing the potential difference across the nanopore.

In **conventional configuration** experimental data matched theoretical predictions and previously reported data [4]. As shown in **Figure 2.14**, for 5 kbp DNA the peak current increased linearly from 13.81 ± 1.76 pA at 200 mV to 40.46 ± 1.76 pA at 600 mV while dwell times decreased from 0.11 ± 0.03 ms at 200 mV to 0.11 ± 0.03 ms at 600 mV. At higher voltages, dwell time distributions appeared plateauing at 0.1 ms while in reality this was related to the amplifier rather than to a biophysical process. Considering that data was acquired at 100 kHz sampling frequency and filtered at 5 kHz, using a 4-pole Bessel filter, it meant that only events equal or longer than ≈ 0.2 ms were detected while all others not.

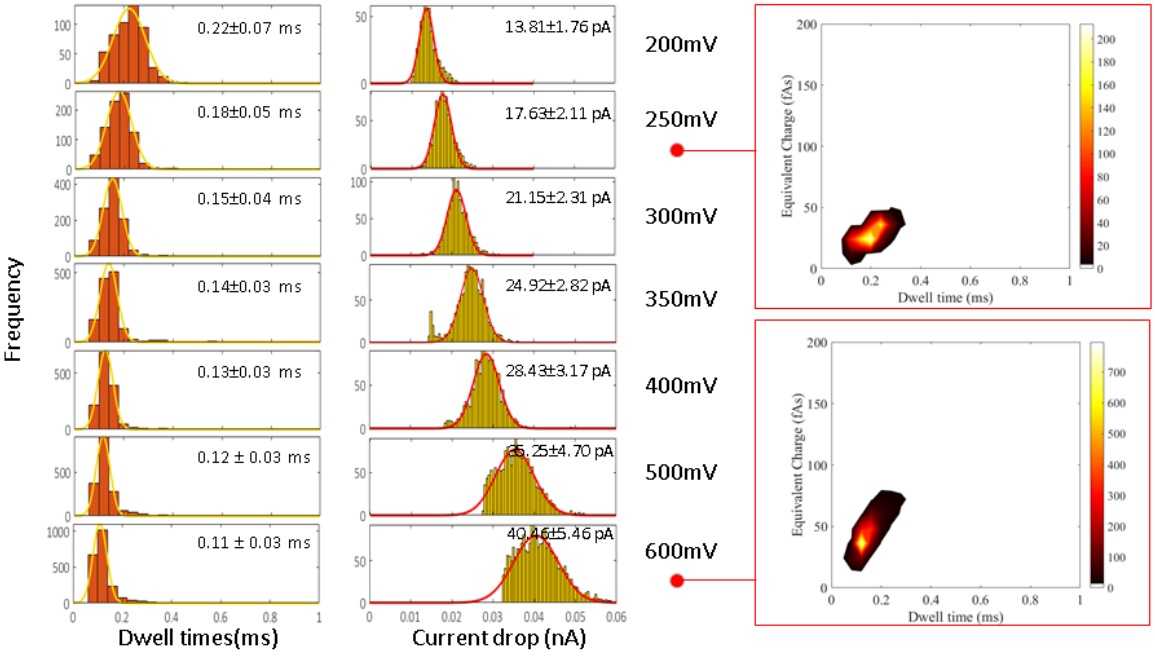

Fig. 2.14 Translocation of 5 kbp DNA in conventional configuration. Translocation analysis of 400 pM 5 kbp DNA in conventional configuration at 100 mM KCl in 10 mM Tris 1 mM EDTA at pH 8.0. Showing dwell times (left column), current drop(middle column) and ECD (right column) for voltage applied ranging from 300 mV to 600 mV. Reprinted with permission from [1]. Copyright 2017 American Chemical Society.

In **dual pore configuration**, it was observed a similar tendency where, dwell times decreased and current drop increased with the voltage applied (**Figure 2.15**). The peak current were smaller than the one recorded in conventional configuration however this was explained with the introduction of the second pore in the system (as described in the equation 1.8). As for translocation speed, conventional and dual pore configuration showed similar values for 5 kbp DNA at 400 mV applied bias: 14.2 ± 0.4 mm s^{-1} and 8.9 ± 0.7 mm s^{-1} respectively. Those values were in good agreement with the literature [89]. The fact that dwell times were comparable to the one obtained in conventional configuration indicated that, even in dual pore configuration, DNA molecules were threaded from the pipette directly to

the bath. It confirmed that the scenario where the DNA molecule rethreaded into the second barrel was highly improbable considering the high velocity with which DNA, after threading, was pushed away from the tip.

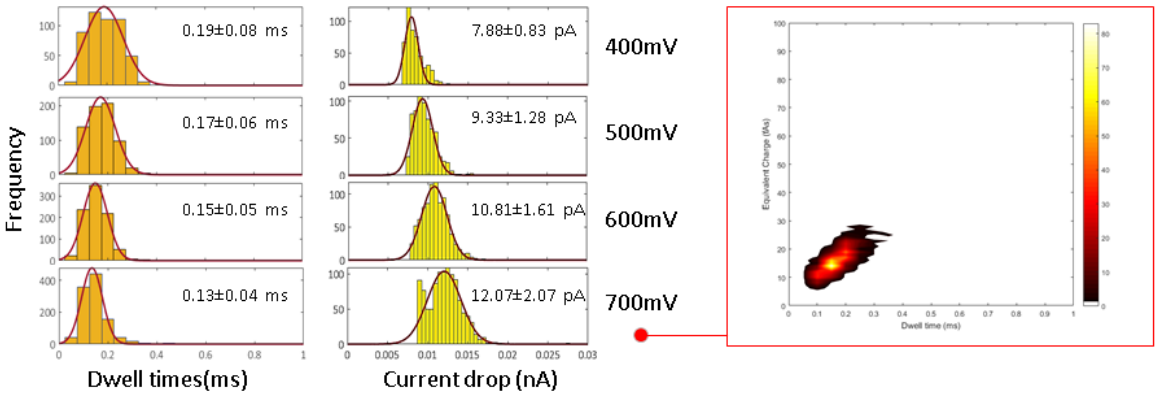

Fig. 2.15 Translocation of 5 kbp DNA in dual pore configuration. Dwell time, current drop and ECD for different voltage applied for 400 pM 5 kpb DNA in dual pore configuration at 100 mM KCl in 10 mM Tris 1 mM EDTA at pH 8.0. Reprinted with permission from [1]. Copyright 2017 American Chemical Society.

The voltage dependence data acquired in **nanobridge configuration** pictured a substantially different landscape. As described previously described the peak current increased proportionally with the voltage applied. For instance, for 1.5 kbp DNA recorded in 100 mM KCl, the current increased from 9.94±0.82 pA at 250 mV to 20.16 ± 0.92 pA at 350 mV (**Figure 2.13 b**). However, the interesting finding concerned the dwell time: when the applied voltage was increased, DNA fragments, irrespective of size, were subjected to an even more pronounced slowing down **Figure 2.16 a**.

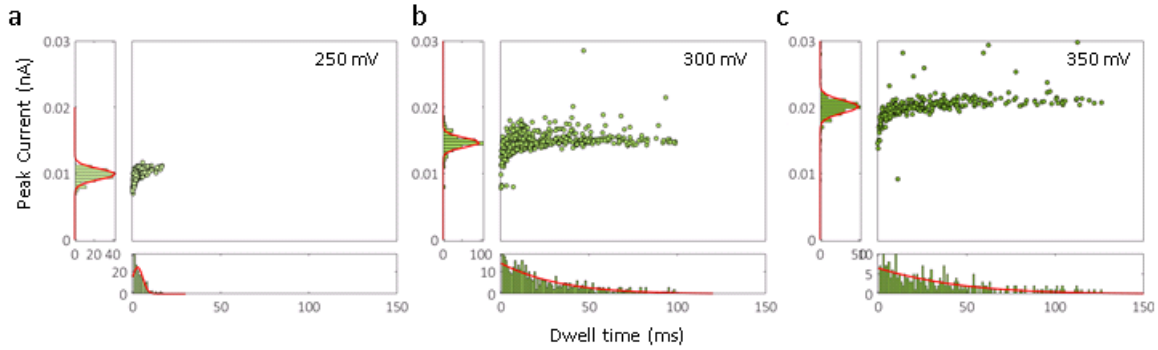

Fig. 2.16 Voltage dependence in nanobridge configuration. Scatter plots of 1500 kbp DNA translocation recorded in nanobridge configuration at 100 mM KCl at (a) 250 mV, (b) 300 mV and (c) 350 mV voltage applied.

For example for 1.5 kbp DNA events were detected up to 20 ms at 250 mV, which increased to approximately 120 ms at 350 mV voltage applied (**Figure 2.16 c**). The corollary

of this more pronounced single molecule trap was an enhanced SNR (**Figure 2.13 c**), however the FWHM remained constant reflecting the tight distribution.

A potential explanations for this distinctively different behaviour was related to a sort of crowding and compacting effect that DNA experience when it is in close proximity with the nanopore/droplet interface. In addition, varying the potential will result in different electroosmotic flow which in turns will influence the degree of molecular confinement and forces applied to the DNA inside the droplet.

In case of longer DNA fragments such as 10 kbp DNA, the longer dwell time was accompanied with the emergence of discrete multistep in the ionic current blockade (**Figure 2.17 a,b**). Secondary steps, which were also observed for 5 kbp DNA and 1.5 kbp DNA, were recorded within the event duration without a preferred position or evident pattern (Altought, qualitatively the vast majority were observed distant from the beginning or the end of the event). The frequency of these events was marginally related to the voltage applied: in fact it was observed that at higher voltage these secondary level were more evident (in terms of peak current) and numerous.

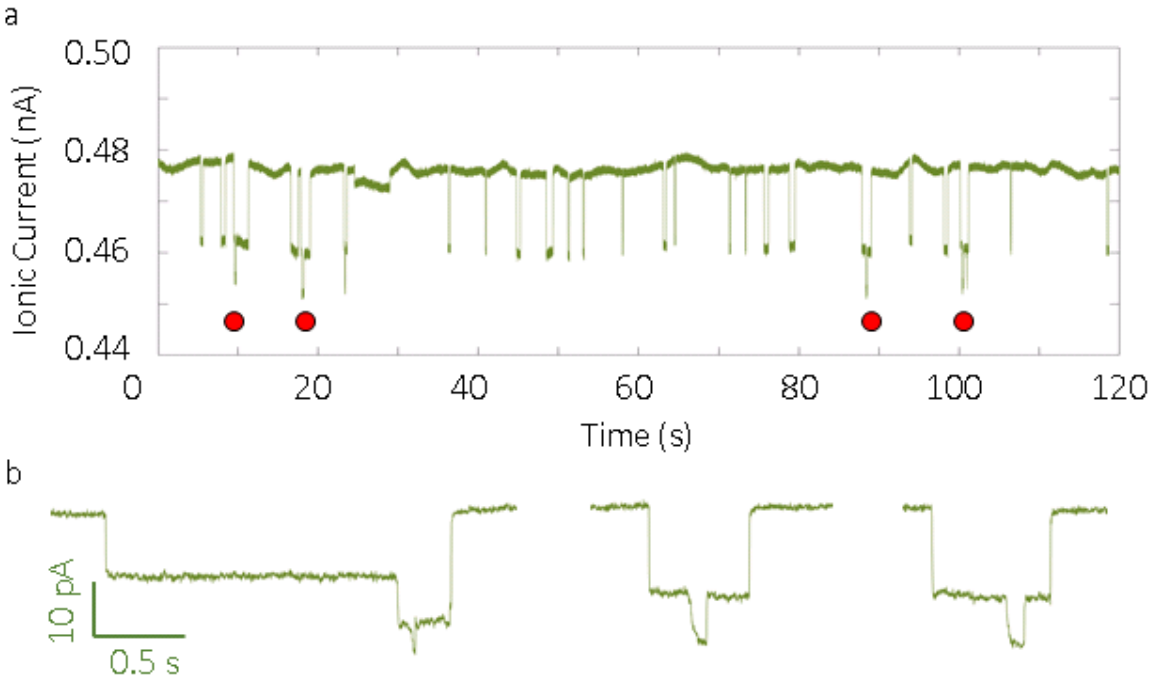

Fig. 2.17 Multistep ionic current signature for 10 kbp DNA translocation performed in nanobridge configuration. (a) Both barrels were filled with 200 pM 10 kbp in 100 mM KCl at 225 mV of voltage applied (traces were resampled at 1 kHz for visualisation). It was observed that a minority of the DNA translocation events presented a multistep ionic current signature rather than a single step (as observed in the vast majority). These secondary steps did not manifest a preferred position within the event (b).

One might assume, as documented by previous studies [90], that these secondary steps were associated to specific DNA conformations, called knots, that DNA assumed while

threading through the pore; however the data acquired thus far was not conclusive to draw a picture of this specific phenomenon.

2.4.4 The role of nanopore dimensions on DNA transport in nanobridge configuration

To investigate how and if the pores size, hence the nanobridge, affects the transport properties, DNA translocation experiments were carried out on nanopipettes pulled with the second protocol which produced pores with diameters ranging between 50 and 100 nm (**Figure 2.18 a-e**).

The profile of the tip remained ellipsoidal, however in in the vast majority of cases the apertures where asymmetric with one pore considerably bigger than the other. The electrical characterization performed in different configurations (**Figure 2.18 f**) and at different salt concentration (**Figure 2.18 g**) matched with the one observed for smaller nanopipettes. At 100 mM KCl, the IV displayed a sigmoidal behaviour (G = 9.16 $\pm$ 0.15 nS) whereas in dual pore and in conventional the IV was observed to be linear ($G_{dual\,pore}$= 11.50 $\pm$ 0.01 nS) and in the conventional approach almost linear with a marginal rectification ($G_{barrel1}$= 22.85 $\pm$ 0.52 nS and $G_{barrel2}$= 23.73 $\pm$ 0.13 nS). The decreased rectification ratio recorded in standard configuration was compatible with a bigger aperture where, generally surface charges played a minor role in the ionic current flow. As expected $1\ G_{barrel1} + 1\ G_{barrel2} = 1\ G_{dual\,pore} \sim$ 87 MΩ. Therefore the contribution of the fluidic bridge was equal to $\sim$ 22 MΩ which corresponded to $\sim$ 22 % of the total resistance of the system. This value was much higher than the one recorded for the smaller nanopipette where it was calculated to be $\sim$ 11 %. In this case, one can therefore assume that, the aspect ratio of the droplet (height vs area) diminished, in other words the droplet spread over a larger area (nanopore apertures) forming more a 2D film rather than sphere.

Figure 2.19 shows a representative current trace of single-molecule detection of 10 kbp DNA in nanobridge configuration at 100 mM KCl salt concentration. Generally, the baseline current was slightly less stable than the ones recorded with smaller pores and they exhibited low frequency (below 1 Hz), low amplitude($\sim$ 10 pA) fluctuations.

The overall behaviour of these larger nanopipettes was similar to what we observed for nanopipettes pulled using protocol 1. In fact, despite the larger pore size, the duration of DNA translocations appeared to be still remarkably long, with events being detected as slow as 500 ms at 150 mV voltage applied. Current blockades followed a linear trend with the voltage applied passing from 1.97 ± 0.33 pA at 100 mV to 12.27 ± 0.79 pA at 175 mV (**Figure 2.19 c-e**) and in addition events were detected in depletion, as with smaller pores. Control

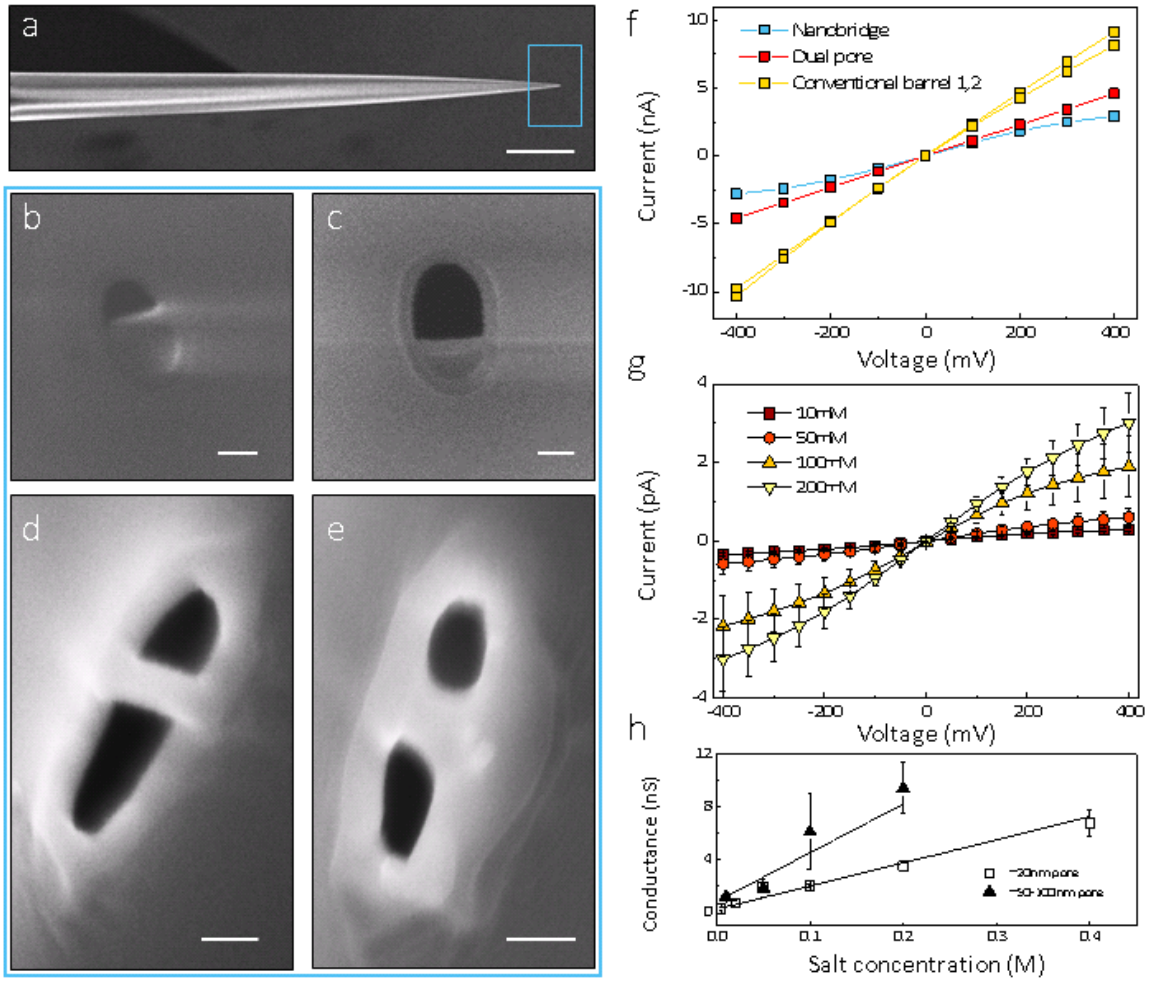

Fig. 2.18 Characterization of nanopipettes having pore diameters between 50 nm and 100 nm. (a) SEM micrographs a dual barrel nanopipette visualized laterally and (b)-(e) top view of the aperture of different nanopipettes showing the asymmetry between the two apertures. (f) Current–voltage characteristics of a dual barrel nanopipttes measured in nanobridge configuration, conventional configuration and dual pore configuration at 100 mM KCl. (g) IVs performed in nanobridge configuration at salt concentration ranging from from 10 mM to 200 mM kCl. (g) Conductance dependence versus salt concentration for nanopipettes pulled with protocol 1 and protocol 2 and characterized in nanobridge configuration. In both cases it was observed a linear dependence (R^2 = 0.83, R^2 = 0.95).Scale bars: (a) 10 μm (b),(c) 50 nm (d) (e) 100 nm.

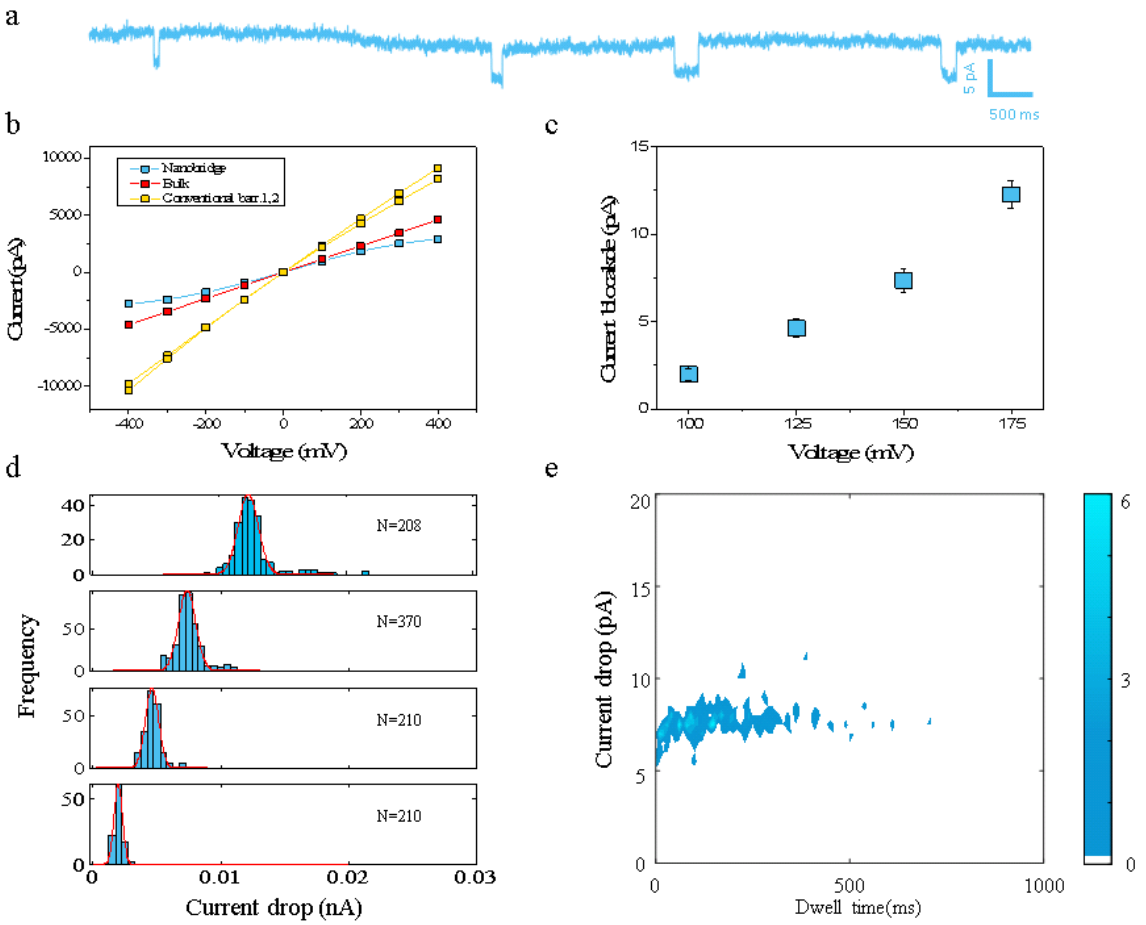

Fig. 2.19 dsDNA translocations in nanobridge configuration using nanopipettes having pore diameter of 50 nm to 100 nm. (a)Ionic current recording in nanobridge configuration of 10 kbp DNA translocation at 100 mM KCl at 150 mV voltage applied. Trace was resampled at 1 kHz.(b)Current voltage characterization of the nanopipette in nanobridge, bulk and conventional configuration. (c) Voltage dependence of current blockade for 20 pM 10 kbp DNA in 100 mM KCl 10 mM Tris 1 mM EDTA . (d) Corresponding histograms for each voltage.(e) Scatter plot of current drop as a function of dwell time for 10 kbp detected in nanobridge configuration at 150 mV.

experiments were also carried out in dual pore and conventional configuration showing that DNA translocated in the sun-ms regime with voltage applied ranging from 100 mV to 600 mV. Due the large pore size, the peak current and the SNR was remarkably small; however this was not surprising because, according to theory [91], the ionic current blockade scales with the pore size.

2.4.5 Fragments sizing

Interestingly, in nanobridge configuration, such a well defined narrow peak current distribution, allowed DNA species to be identified not only from the absolute value of the current but also by looking at the integrated area of the region bounded by each recorded event or, in other words, at the integrated current profile (**Figure 2.20**).

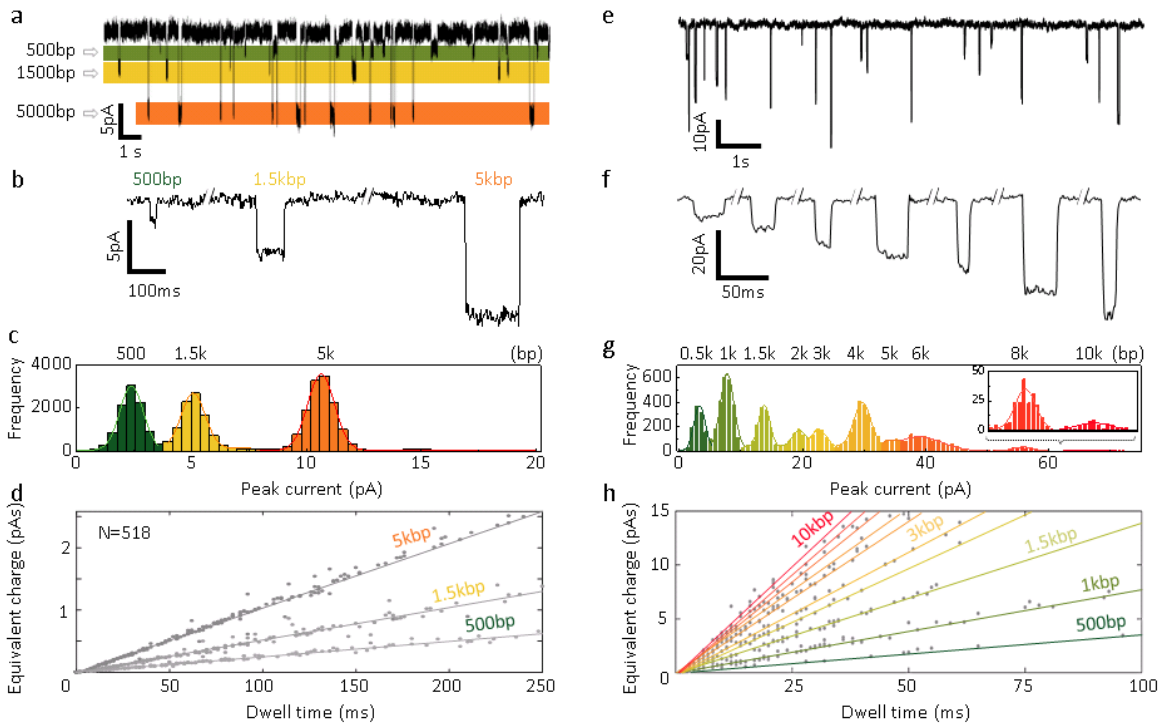

Fig. 2.20 Detection of mixed dsDNA sample in the nanobridge configuration. (a) Translocation signals of a sample containing 500 bp, 1.5 kbp, 5 kbp at a concentration of 100 pM each in 100 mM KCl buffered in TE (pH8.0) at 200 mV. (b) Representative current blockade traces of 500 bp, 1.5 kbp, 5 kbp DNA. (c) Peak current histogram for a mixture containing 500 bp,1.5 kbp, 5 kbp. The mean peak current was obtained via Gaussian fitting (2.4 $\pm$ 0.5 pA for 500 bp, 5.1 $\pm$ 0.5 pA for 1.5 kbp and 10.7 $\pm$ 0.6 pA for 5 kbp). (d) Equivalent charge plot was used to identify the different DNA population and was shown to be linear dependent on dwell time. The calculated slopes were 2.5 pA for 500 bp, 5.2 pA for 1.5 kbp and 10.3 pA for 5 kbp. (e) Translocation signal of 1 kbp DNA ladder, containing 10 DNA fragments (500 bp, 1.5 kbp, 2 kbp, 3 kbp, 5 kbp, 6 kbp, 8 kbp and 10 kbp) at a total concentration of 100 pM in 100 mM KCl buffered in TE (pH 8.0) at 350 mV. Adapted with permission from [1]. Copyright 2017 American Chemical Society.

It is important to distinguish between the integrated current profile and the equivalent charge deficit (ECD), whose values, in conventional nanopore experiments, are related to the

amount of charges carried by a specific analyte [85] while in nanobridge configuration broadly dispersed dwell time distributions do not allow for a similar interpretation. Remarkably, in nanobridge configuration, the integrated event profile were distributed along a straight line therefore by using a least square fitting algorithm it was possible to distinguish different DNA species within the sample. For example, in the case of 500 bp, 1.5 kbp, 5 kbp DNA sample, the slopes of the three fittings were calculated to be 2.48 pA for 500 bp, 5.19 pA for 1.5 kbp and 10.31 pA for 5 kbp. These values were in good agreement with the ones obtained in **Figure 2.20 c**. In addition these experiments highlighted another difference with the conventional nanopore approach where the ECD was generally clustered (**Figure 2.14**) rather than being dispersed as observed in nanobridge configuration. A more complex DNA sample displayed similar results. As shown in **Figure 2.20 e-h**, 1 kbp DNA ladder sample consisting of 10 dsDNA fragments was employed (sizes: 500 bp, 1 kbp, 1.5 kbp, 2 kbp, 3 kbp, 4 kpb, 5 kbp, 6 kbp, 8 kbp, 10 kbp) and the peak current distribution revealed 10 distinct peaks. In this case, fragments had different concentrations and this was reflected on the different frequencies of each peak as shown in the histogram.

Interestingly it was observed that mean peak current of each fragment size scaled up with the radius of gyration squared (R_g^2). The former is defined as the average squared distance of any point in the polymer (DNA in this case) from its center of mass. R_g was calculated according to a simplified model which defines the mean square end-to-end distance in an ideal polymer as [92, 93]:

$$< R^2 >= p^2 N \tag{2.7}$$

where p is the persistence length (at 100 mM KCl, $\approx$ 50 nm [82], which is equivalent to $\approx$ 147 bases for dsDNA) and N represents the number of segments of length p that compose the entire chain. The ratio between the end-to-end distance and the radius of gyration is given by:

$$R_g^2 = \frac{< R^2 >}{6} \tag{2.8}$$

As an example, R_g was calculated to be 90 nm for 1.5 kbp, 164 nm for 5 kbp and 233 nm for 10 kbp. It was interesting to look at the peak current and conductance distributions for dsDNA data acquired (in nanobridge configuration) with different nanopipettes through the course of this study. As shown in **Figure 2.21 a,b**, the values of both peak current and conductance appeared to scale with the radius of gyration squared. Notably, in the analysis the self-avoidance nature of DNA was taken into account. In this case R_g scales as $\sim N^{3/5}$ (R_g $\sim N^{1/2}$ without self-avoidance) where the factor 3/5 is also called the Flory scaling exponent [94]. From a biophysical perspective, it reinforced the idea that molecules were most likely confined in the nanobridge when translocating from one barrel to the other, because the peak

current was proportional to the cross sectional area of the DNA blocking the nanobridge electrolyte.

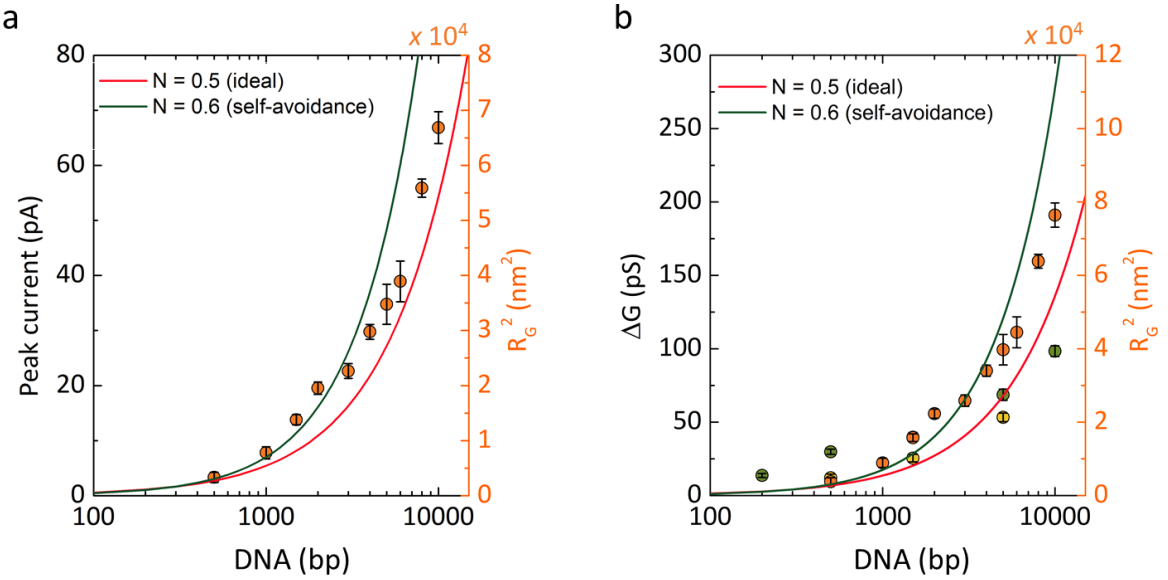

Fig. 2.21 Relation between radius of gyration and (a) peak current distribution, (b) conductance distribution for dsDNA fragments ranging from 200 bp to 10 kbp. The radius of gyration was calculated considering the DNA equal to an ideal polymer (red line) and also considering its self-avoidance nature (dark green line). Reprinted with permission from [1]. Copyright 2017 American Chemical Society.

2.4.6 Sensing ssDNA and proteins

The novel sensing approach proposed in this chapter was extended to other analytes: experiments were carried out with ssDNA and $\alpha - synuclein$ which is a small protein (14.5 kD, hydrodynamic diameter 1.7 – 2.2 nm). Viral ssDNA M13mp18, about 7.2kb long, was linearised before being used for detection (for details refer to the experimental section). ssDNA was firstly characterized using a conventional approach. **Figure 2.22 a** shows a representative ionic current trace recorded at 400mV in 100mM KCl. The biphasic behaviour of the ionic current, where it initially decreases and then increases **Figure 2.22 b**, was in well agreement with the reported literature [95, 87].

The measured dwell time was below 0.5 ms for the entire range of applied voltages (300-600 mV); for instance, at 300 mV it measured 0.05 ± 0.02 ms (**Figure 2.22**). The current amplitude distributions were broadly spread between 20 pA and 80 pA at 300 mV. This result was not entirely surprising, because, as reported in literature, the ssDNA Mp13mp18 is an heteropolymer, therefore, opposite to an homopolymer, it presents a large number of possible intramolecular interactions [95]. In turns, these interactions, give rise to a multitude of differently coiled ssDNA structures that must partially or completely unravel when going through nanobridge resulting in broad distribution peak.

In nanobridge, the temporal resolution of M13 appeared to be markedly increased as shown in ionic current trace in **Figure 2.23 a-b**. Events as slow as 700 ms were detected however the vast majority clustered around a window comprised between 1 and 40 ms (**Figure 2.23 c**).

Notably the peak current distributions were spread and not as sharp as the ones observed for dsDNA of similar sizes. This was particularly evident when looking at the single event: clear multistep current levels were observed in the vast majority of cases (**Figure 2.23 b**). As explained above, this behaviour could be partly explained with the multiple conformation that ssDNA can assume. In addition it was not observed an exponential decay in the ionic current upon threading. The much faster transition was considered consistent with lower values for the Zimm relaxation time of ssDNA compared with that of dsDNA [96]. This effect takes into account that ssDNA is much more flexible than dsDNA: the persistence length of ssDNA at 100 mM KCl is considered about 2 nm [97]. Therefore, it is reasonable to consider that the translocation mechanism for such flexible chains might be different from the one envisioned for dsDNA and multistep events might be a direct consequence of this.

Finally, nanobridge configuration was used to detect $\alpha - synuclein$. The former is thought to play a key role in neurodegenerative diseases such as Parkinson. However the main reason

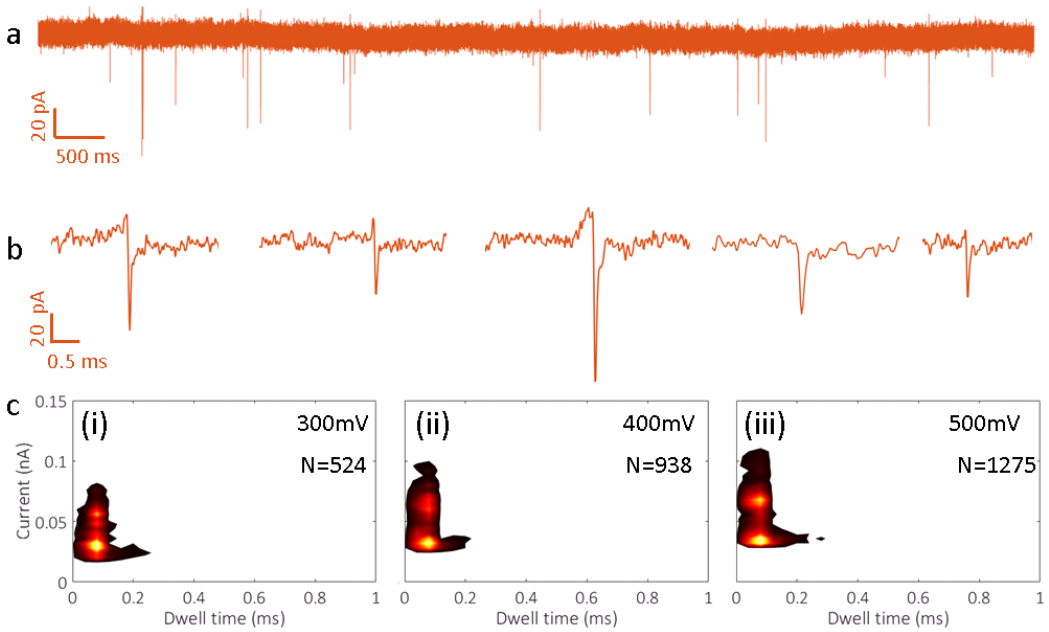

Fig. 2.22 Detection of ssDNA in conventional configuration. (a) Ionic current trace showing M13 ssDNA translocations performed in conventional configuration at 100 mM KCl 10 Tris 1 mM EDTA pH8 at 400 mV voltage applied. ssDNA concentration was 100 pM. (b) Examples of single events at 400 mV voltage applied. In contrast with nanobridge events threaded through the pore at high velocity with sub-ms dwell times. The biphasic behaviour was in good agreement with what has been previously reported for the same molecule in similar ionic strength[95]. (c) showing scatter plots of ssDNA at i) 300 mV ii) 400 mV and iii) 500 mV voltage applied. Adapted with permission from [1]. Copyright 2017 American Chemical Society.

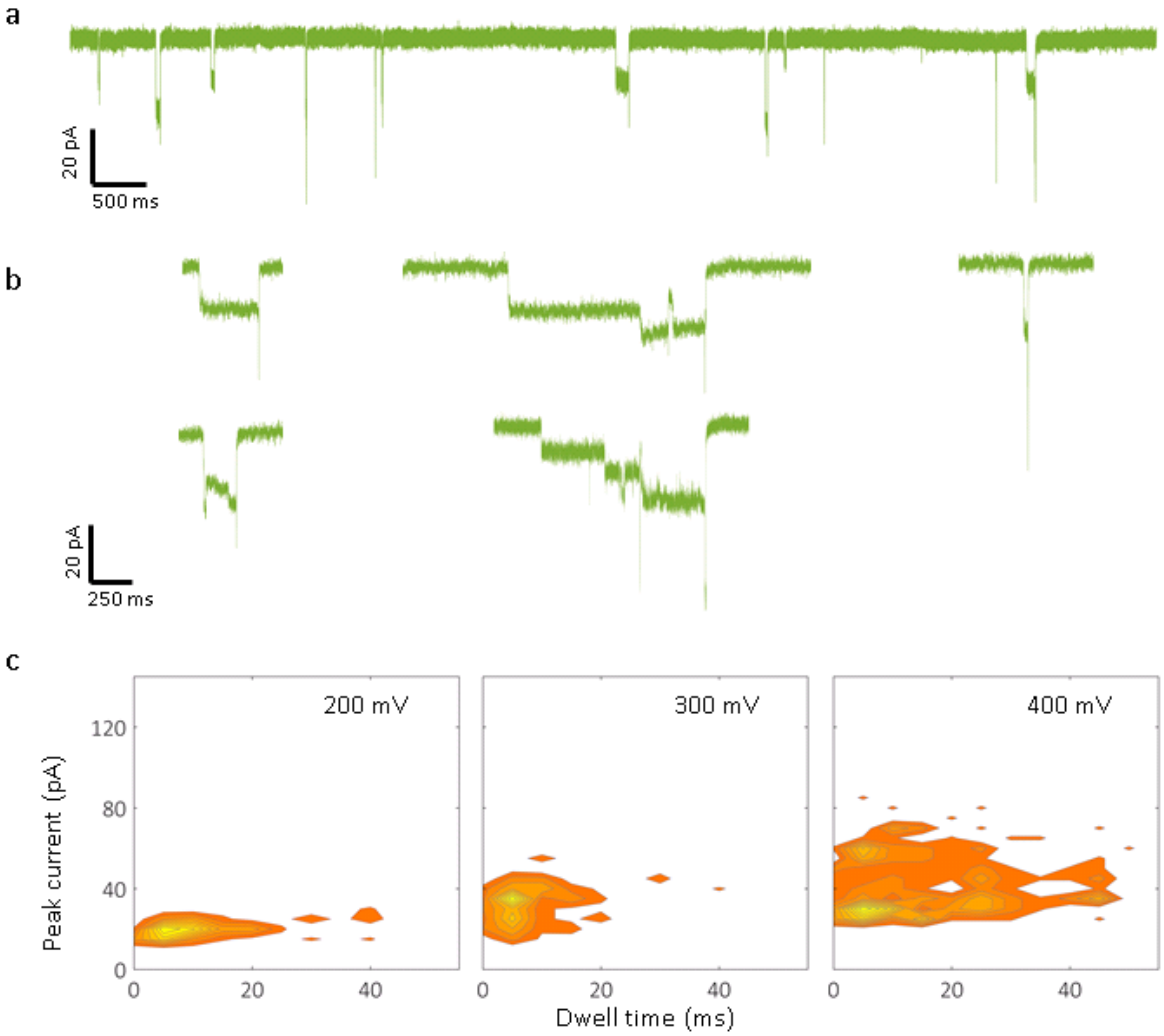

Fig. 2.23 Detection of ssDNA in nanobridge configuration. (a) Ionic current trace showing M13 ssDNA translocations performed in nanobridge configuration at 100 mM KCl 10 Tris 1 mM EDTA pH 8.0 at 400 mV voltage applied. ssDNA concentration was 100 pM. Even for ssDNA the dwell times were considerably slower than in conventional configuration however the current blockade showed multi step levels. (b) Examples of single events where it is possible to see clear, discrete current levels. Notably this multistep behaviour was not dependent on the voltage applied, in fact it was observed at 200 mV and 300 mV. (c) Current-dwell time contour plots are shown for voltages of 200 mV, 300 mV, and 400 mV respectively. Similar to dsDNA, the dwell times increase with voltage. Events as slow as 40 ms could be detected which is substantially slower than in a conventional nanopore configuration. Adapted with permission from [1].

for its choice as a benchmark for nanobridges was due to its size which made the analyte extremely challenging to be detected. If nanopore-based solutions to improve the range of concentration and length of nucleic acid detection were substantially ameliorated over the last 10 years, the same cannot be said for protein detection which lagged far behind in terms on technological advances. Fast translocation times with event rates significantly lower than predicted from the Smoluchowski equation, represent an impervious obstacle for conventional nanopore.

In particular, as shown in **Figure 1.6** the translocation mechanism can be split in two phases: the capture of the analyte and its translocation across the pore. Initially the analyte is freely diffusing in the solution however, when its random walk brings it in close proximity to the pore (within the capture volume having radius r), the analyte is subjected to a high electric field and it is electrodynamically translocated through the pore to the opposite chamber. Interestingly, the Smoluchowski rate equation gives the rate at which a specific analyte arrive at the pore entrance due to free diffusion; if the measured event rate is considerably lower than the this prediction it is reasonable to assume that the a fraction of analyte pass the pore undetected. These problems are normally compensated by using very high protein concentration 10's – 100's nM. However as illustrated in the ionic current trace in **Figure 2.24** we showed that it was possible detecting $\alpha - synuclein$ at sub-nm concentration (700 pM) in 100 mM KCl. Events were detected between 0.1 – 0.75 ms at 600 mV while the peak current was well defined with a mean of 30 ± 3 pA with a SNR of 11.5 ± 1.1. These numbers represented a remarkable slowdown especially when considering alternative slowdown strategies which, as in the case of high ionic strength LiCl (normally 4M!), are not ideal for biological analytes (on top of having detrimental impact on the event rate).

2.5 Conclusions

In this chapter, we have presented a novel detection method for solid state nanopores based on dual barrel nanopipette. We showed that this method, called nanobridge, allowed us to tune the analyte transport by confining single molecules within a zeptolitre volume located at the tip of the nanopipette. In this way molecules can be slowed down by several orders of magnitude compared to conventional nanopores. In the first part of this chapter nanobridge was characterized by looking at the ionic current stability over the time, salt concentration dependence, noise characteristics, pore size dependence as well as estimating the fluidic bridge dimensions via SEM, TEM and scanning probe microscopy.

In the second part, we focused on studying dsDNA transport in nanobridge and comparing it to conventional approaches. By using a broad range of dsDNA fragments we demonstrated

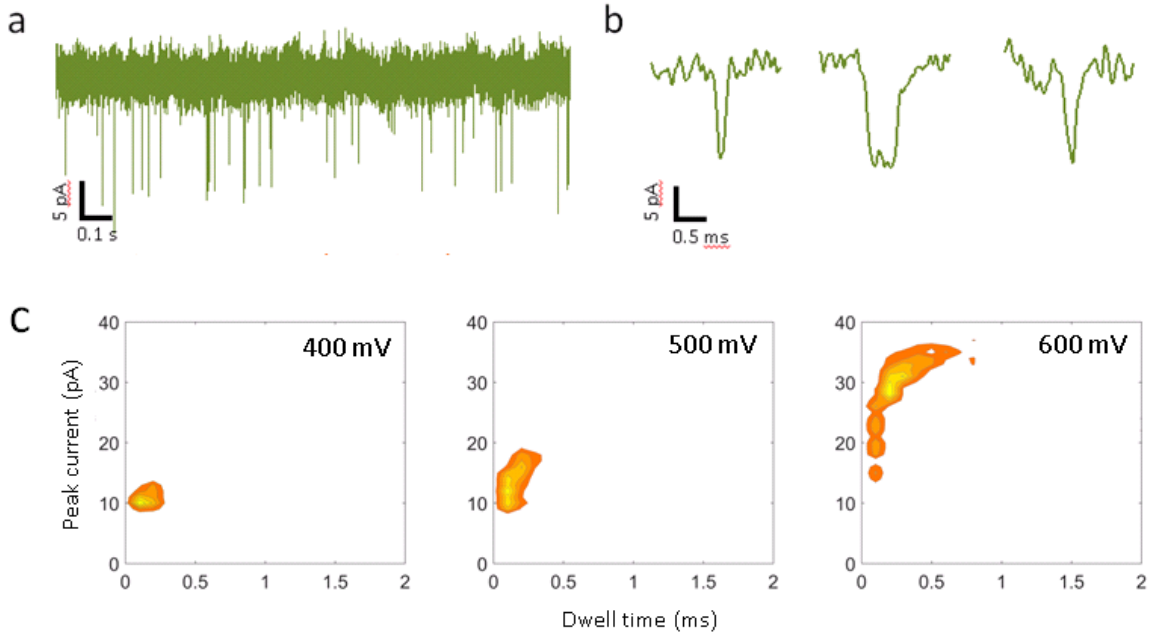

Fig. 2.24 Detection of $\alpha-synuclein$ in nanobridge configuration. (a) Current-time trace for monomeric $\alpha-synuclein$ for a concentration of 700 pM in 100 mM KCl and recorded at an applied bias of 400 mV. (b) Showing representative example of single events. (c) Current-dwell time contour plots are shown for voltages of 400 mV, 500 mV, and 600 mV respectively. This data was acquired by Giulia Campolo (Chemistry department, Imperial College London). Adapted with permission from [1]. Copyright 2017 American Chemical Society.

that in nanobridge, as opposed to conventional nanopores setups, the translocation peak currents displayed tighter distributions with lower FWHM values and significantly enhanced SNR (up to 5.4 fold) on top of severely decelerating the molecule when translocating (up to 3 orders of magnitudes). This represents a remarkable improvement over existing nanopore methods that reduce translocation speed by regulating electrolyte viscosity, electrophoretic force, pressure, which often result in broad current/dwell time distributions and lower SNR and as a result prevent the discrimination of multiple analytes in complex samples. In contrast we showed that in nanobridges DNA size profiling can be performed by either measuring the current amplitude or alternatively, as in the case of multiple DNA populations, by analysing the equivalent charge/dwell time distributions. In addition, due to the limited bandwidth required for the nanobridge to operate, it was possible to use sampling rates as low as 1 kHz. This advantage had a twofold implication: on one hand it resulted in very low noise profile (for the benefit of the SNR), but it also opened up the possibility of using cheaper and portable amplifier.

Finally, nanobridge setup was tested with different analytes such as ssDNA and proteins. The broad range of dimensions and conformations, the high translocation velocity, along with non-uniform surface charge make protein detection particularly challenging to nanopores

sensors. In contrast, we showed that nanobridge detection adapts well to this task, allowing to confine and detect proteins as small as few nanometers.

References

[1] P. Cadinu, B. Paulose Nadappuram, D. J. Lee, J. Y. Y. Sze, G. Campolo, Y. Zhang, A. Shevchuk, S. Ladame, T. Albrecht, Y. Korchev, A. P. Ivanov, and J. B. Edel, "Single Molecule Trapping and Sensing Using Dual Nanopores Separated by a Zeptoliter Nanobridge," *Nano Lett.*, no. ii, p. acs.nanolett.7b03196, 2017.

[2] J. J. Kasianowicz, E. Brandin, D. Branton, and D. W. Deamer, "Characterization of individual polynucleotide molecules using a membrane channel," *Proc. Natl. Acad. Sci. U. S. A.*, vol. 93, no. 24, pp. 13770–3, 1996.

[3] B. N. Miles, A. P. Ivanov, K. a. Wilson, F. Doğan, D. Japrung, and J. B. Edel, "Single molecule sensing with solid-state nanopores: novel materials, methods, and applications," *Chem. Soc. Rev.*, vol. 42, no. 1, pp. 15–28, 2013.

[4] A. P. Ivanov, P. Actis, P. Jönsson, D. Klenerman, Y. Korchev, and J. B. Edel, "On-demand delivery of single DNA molecules using nanopipets," *ACS Nano*, vol. 9, no. 4, pp. 3587–3594, 2015.

[5] K. J. Freedman, L. M. Otto, A. P. Ivanov, A. Barik, S.-H. Oh, and J. B. Edel, "Nanopore sensing at ultra-low concentrations using single-molecule dielectrophoretic trapping," *Nat. Commun.*, vol. 7, p. 10217, 2016.

[6] X. Lin, A. P. Ivanov, and J. B. Edel, "Selective single molecule nanopore sensing of proteins using DNA aptamer-functionalised gold nanoparticles," *Chem. Sci.*, vol. 8, no. 5, pp. 3905–3912, 2017.

[7] W. Shi, A. K. Friedman, and L. A. Baker, "Nanopore Sensing," *Anal. Chem.*, vol. 89, no. 1, pp. 157–188, 2017.

[8] J. Clarke, H.-c. Wu, L. Jayasinghe, A. Patel, S. Reid, and H. Bayley, "Continuous base identification for single-molecule nanopore DNA sequencing.," *Nat. Nanotechnol.*, vol. 4, no. 4, pp. 265–270, 2009.

[9] B. M. Venkatesan and R. Bashir, "Nanopore sensors for nucleic acid analysis," *Nat. Nanotechnol.*, vol. 6, no. 10, pp. 615–624, 2011.

[10] C. Plesa, S. W. Kowalczyk, R. Zinsmeester, A. Y. Grosberg, Y. Rabin, and C. Dekker, "Fast Translocation of Proteins through Solid State Nanopores," *Nano Lett.*, vol. 13, pp. 658–663, feb 2013.

[11] D. Pedone, M. Langecker, G. Abstreiter, and U. Rant, "A pore-cavity-pore device to trap and investigate single nanoparticles and DNA molecules in a femtoliter compartment: Confined diffusion and narrow escape," *Nano Lett.*, vol. 11, no. 4, pp. 1561–1567, 2011.

[12] J. J. Gooding and K. Gaus, "Single-Molecule Sensors: Challenges and Opportunities for Quantitative Analysis," *Angew. Chemie Int. Ed.*, vol. 55, no. 38, pp. 11354–11366, 2016.

[13] D. M. Rissin, C. W. Kan, T. G. Campbell, S. C. Howes, D. R. Fournier, L. Song, T. Piech, P. P. Patel, L. Chang, A. J. Rivnak, E. P. Ferrell, J. D. Randall, G. K. Provuncher, D. R. Walt, and D. C. Duffy, "Single-molecule enzyme-linked immunosorbent assay detects serum proteins at subfemtomolar concentrations," *Nat. Biotechnol.*, vol. 28, no. 6, pp. 595–599, 2010.

[14] J. K. Rosenstein, M. Wanunu, C. a. Merchant, M. Drndic, and K. L. Shepard, "Integrated nanopore sensing platform with sub-microsecond temporal resolution," *Nat. Methods*, vol. 9, no. 5, pp. 487–492, 2012.

[15] J. Larkin, R. Y. Henley, M. Muthukumar, J. K. Rosenstein, and M. Wanunu, "High-bandwidth protein analysis using solid-state nanopores," *Biophys. J.*, vol. 106, no. 3, pp. 696–704, 2014.

[16] S. Shekar, D. J. Niedzwiecki, C.-C. Chien, P. Ong, D. A. Fleischer, J. Lin, J. K. Rosenstein, M. Drndic, and K. L. Shepard, "Measurement of DNA translocation dynamics in a solid-state nanopore at 100-ns temporal resolution," *Nano Lett.*, p. acs.nanolett.6b01661, 2016.

[17] R. L. Fraccari, P. Ciccarella, A. Bahrami, M. Carminati, G. Ferrari, and T. Albrecht, "High-speed detection of DNA Translocation in Nanopipettes," *Nanoscale*, pp. 1–20, 2016.

[18] M. Wanunu, J. Sutin, B. McNally, A. Chow, and A. Meller, "DNA Translocation Governed by Interactions with Solid-State Nanopores," *Biophys. J.*, vol. 95, no. 10, pp. 4716–4725, 2008.

[19] D. Fologea, J. Uplinger, B. Thomas, D. S. McNabb, and J. Li, "Slowing DNA translocation in a solid-state nanopore," *Nano Lett.*, vol. 5, no. 9, pp. 1734–1737, 2005.

[20] C. Plesa, N. van Loo, and C. Dekker, "DNA nanopore translocation in glutamate solutions," *Nanoscale*, vol. 7, no. 32, pp. 13605–13609, 2015.

[21] S. W. Kowalczyk, D. B. Wells, A. Aksimentiev, and C. Dekker, "Slowing down DNA translocation through a nanopore in lithium chloride . Slowing down DNA translocation through a nanopore in lithium chloride," *Nano Lett.*, pp. 1–5, 2012.

[22] J. Feng, K. Liu, R. D. Bulushev, S. Khlybov, D. Dumcenco, A. Kis, and A. Radenovic, "Identification of single nucleotides in MoS2 nanopores," *Nat. Nanotechnol.*, vol. 10, no. 12, pp. 1070–1076, 2015.

[23] R. Akahori, T. Haga, T. Hatano, I. Yanagi, T. Ohura, H. Hamamura, T. Iwasaki, T. Yokoi, and T. Anazawa, "Slowing single-stranded DNA translocation through a solid-state nanopore by decreasing the nanopore diameter," *Nanotechnology*, vol. 25, no. 27, p. 275501, 2014.

[24] P. Chen, T. Mitsui, D. B. Farmer, J. Golovchenko, R. G. Gordon, and D. Branton, "Atomic Layer Deposition to Fine-Tune the Surface Properties and Diameters of Fabricated Nanopores," *Nano Lett.*, vol. 4, no. 7, pp. 1333–1337, 2004.

[25] S. Banerjee, J. Wilson, J. Shim, M. Shankla, E. a. Corbin, A. Aksimentiev, and R. Bashir, "Slowing DNA Transport Using Graphene-DNA Interactions," *Adv. Funct. Mater.*, vol. 25, no. 6, pp. 936–946, 2015.

[26] C. R. Crick, J. Y. Y. Sze, M. Rosillo-Lopez, C. G. Salzmann, and J. B. Edel, "Selectively Sized Graphene-Based Nanopores for in Situ Single Molecule Sensing," *ACS Appl. Mater. Interfaces*, vol. 7, no. 32, pp. 18188–18194, 2015.

[27] B. M. Venkatesan, A. B. Shah, J.-M. Zuo, and R. Bashir, "DNA Sensing Using Nanocrystalline Surface-Enhanced Al 2 O 3 Nanopore Sensors," *Adv. Funct. Mater.*, vol. 20, no. 8, pp. 1266–1275, 2010.

[28] S. Liu, B. Lu, Q. Zhao, J. Li, T. Gao, Y. Chen, Y. Zhang, Z. Liu, Z. Fan, F. Yang, L. You, and D. Yu, "Boron nitride nanopores: Highly sensitive DNA single-molecule detectors," *Adv. Mater.*, vol. 25, no. 33, pp. 4549–4554, 2013.

[29] B. Lu, D. P. Hoogerheide, Q. Zhao, H. Zhang, Z. Tang, D. Yu, and J. A. Golovchenko, "Pressure-controlled motion of single polymers through solid- state nanopores," *Nano Lett.*, vol. 13, no. 7, pp. 3048–3052, 2013.

[30] H. Zhang, Q. Zhao, Z. Tang, S. Liu, Q. Li, Z. Fan, F. Yang, L. You, X. Li, J. Zhang, and D. Yu, "Slowing Down DNA Translocation Through Solid-State Nanopores by Pressure," *Small*, vol. 9, no. 24, pp. 4112–4117, 2013.

[31] M. Firnkes, D. Pedone, J. Knezevic, M. Döblinger, and U. Rant, "Electrically facilitated translocations of proteins through silicon nitride nanopores: Conjoint and competitive action of diffusion, electrophoresis, and electroosmosis," *Nano Lett.*, vol. 10, no. 6, pp. 2162–2167, 2010.

[32] U. F. Keyser, B. N. Koeleman, S. van Dorp, D. Krapf, R. M. M. Smeets, S. G. Lemay, N. H. Dekker, and C. Dekker, "Direct force measurements on DNA in a solid-state nanopore," *Nat. Phys.*, vol. 2, no. 7, pp. 473–477, 2006.

[33] R. D. Bulushev, S. Marion, and A. Radenovic, "Relevance of the Drag Force during Controlled Translocation of a DNA–Protein Complex through a Glass Nanocapillary," *Nano Lett.*, vol. 15, no. 10, pp. 7118–7125, 2015.

[34] H. Peng and X. S. Ling, "Reverse DNA translocation through a solid-state nanopore by magnetic tweezers.," *Nanotechnology*, vol. 20, no. 18, p. 185101, 2009.

[35] S. M. Iqbal, D. Akin, and R. Bashir, "Solid-state nanopore channels with DNA selectivity," *Nat. Nanotechnol.*, vol. 2, no. 4, pp. 243–248, 2007.

[36] Y. Liu and L. Yobas, "Slowing DNA Translocation in a Nanofluidic Field-Effect Transistor," *ACS Nano*, vol. 10, no. 4, pp. 3985–3994, 2016.

[37] S. Carson and M. Wanunu, "Challenges in DNA motion control and sequence readout using nanopore devices," *Nanotechnology*, vol. 26, no. 7, pp. 1–14, 2015.

[38] K. T. Rodolfa, A. Bruckbauer, D. Zhou, Y. E. Korchev, and D. Klenerman, "Two-Component Graded Deposition of Biomolecules with a Double-Barreled Nanopipette," *Angew. Chemie Int. Ed.*, vol. 44, no. 42, pp. 6854–6859, 2005.

[39] K. T. Rodolfa, A. Bruckbauer, D. Zhou, A. I. Schevchuk, Y. E. Korchev, and D. Klenerman, "Nanoscale pipetting for controlled chemistry in small arrayed water droplets using a double-barrel pipet," *Nano Lett.*, vol. 6, no. 2, pp. 252–257, 2006.

[40] J. T. Kim, S. K. Seol, J. Pyo, J. S. Lee, J. H. Je, and G. Margaritondo, "Three-dimensional writing of conducting polymer nanowire arrays by meniscus-guided polymerization," *Adv. Mater.*, vol. 23, no. 17, pp. 1968–1970, 2011.

[41] J. Hu and M.-F. Yu, "Meniscus-Confined Three-Dimensional Electrodeposition for Direct Writing of Wire Bonds," *Science*, vol. 329, no. 5989, pp. 313–316, 2010.

[42] C. Laslau, D. E. Williams, and J. Travas-Sejdic, "The application of nanopipettes to conducting polymer fabrication, imaging and electrochemical characterization," *Prog. Polym. Sci.*, vol. 37, no. 9, pp. 1177–1191, 2012.

[43] S. C. S. Lai, P. V. Dudin, J. V. MacPherson, and P. R. Unwin, "Visualizing zeptomole (electro)catalysis at single nanoparticles within an ensemble," *J. Am. Chem. Soc.*, vol. 133, no. 28, pp. 10744–10747, 2011.

[44] D. Yang, L. Han, Y. Yang, L.-B. Zhao, C. Zong, Y.-F. Huang, D. Zhan, and Z.-Q. Tian, "Solid-State Redox Solutions: Microfabrication and Electrochemistry," *Angew. Chemie Int. Ed.*, vol. 50, no. 37, pp. 8679–8682, 2011.

[45] M. A. O'Connell, M. E. Snowden, K. McKelvey, F. Gayet, I. Shirley, D. M. Haddleton, and P. R. Unwin, "Positionable vertical microfluidic cell based on electromigration in a theta pipet," *Langmuir*, vol. 30, no. 33, pp. 10011–10018, 2014.

[46] E. Sakmann, Bert, Neher, *Single-Channel Recording*. Boston, MA: Springer US, 1995.

[47] A. Jabłoński, "Über den Mechanismus der Photolumineszenz von Farbstoffphosphoren," *Zeitschrift für Phys.*, vol. 94, no. 1-2, pp. 38–46, 1935.

[48] J. R. Lakowicz, *Principles of Fluorescence Spectroscopy*. Boston, MA: Springer US, 2006.

[49] J. W. Lichtman and J. A. Conchello, "Fluorescence microscopy," *Nat. Methods*, vol. 2, no. 12, pp. 910–919, 2005.

[50] P. H. C. Eilers and H. F. M. Boelens, "Baseline correction with asymmetric least squares smoothing," *Leiden Univ. Med. Cent. Rep.*, vol. 1, p. 1, 2005.

[51] D. Y. Ling and X. S. Ling, "On the distribution of DNA translocation times in solid-state nanopores: an analysis using Schrödinger's first-passage-time theory," *J. Phys. Condens. Matter*, vol. 25, no. 37, p. 375102, 2013.

[52] P. Hansma, B. Drake, O. Marti, S. Gould, and C. Prater, "The scanning ion-conductance microscope," *Science*, vol. 243, no. 4891, pp. 641–643, 1989.

[53] C.-C. Chen, Y. Zhou, and L. A. Baker, "Scanning Ion Conductance Microscopy," *Annu. Rev. Anal. Chem.*, vol. 5, no. 1, pp. 207–228, 2012.

[54] Y. E. Korchev, C. L. Bashford, M. Milovanovic, I. Vodyanoy, and M. J. Lab, "Scanning ion conductance microscopy of living cells.," *Biophys. J.*, vol. 73, no. 2, pp. 653–658, 1997.

[55] C. Li, N. Johnson, V. Ostanin, A. Shevchuk, L. Ying, Y. Korchev, and D. Klenerman, "High resolution imaging using scanning ion conductance microscopy with improved distance feedback control," *Prog. Nat. Sci.*, vol. 18, no. 6, pp. 671–677, 2008.

[56] P. Novak, C. Li, A. I. Shevchuk, R. Stepanyan, M. Caldwell, S. Hughes, T. G. Smart, J. Gorelik, V. P. Ostanin, M. J. Lab, G. W. J. Moss, G. I. Frolenkov, D. Klenerman, and Y. E. Korchev, "Nanoscale live-cell imaging using hopping probe ion conductance microscopy," *Nat. Methods*, vol. 6, no. 12, pp. 935–935, 2009.

[57] N. Sa and L. Baker, "Experiment and Simulation of Ion Transport through Nanopipettes of Well-Defined Conical Geometry," *J. Electrochem. Soc.*, vol. 160, no. 6, pp. H376–H381, 2013.

[58] C. Wei, A. J. Bard, and S. W. Feldberg, "Current Rectification at Quartz Nanopipet Electrodes," *Anal. Chem.*, vol. 69, no. 22, pp. 4627–4633, 1997.

[59] R. B. Schoch, J. Han, and P. Renaud, "Transport phenomena in nanofluidics," *Rev. Mod. Phys.*, vol. 80, no. 3, pp. 839–883, 2008.

[60] N. Laohakunakorn and U. F. Keyser, "Electroosmotic flow rectification in conical nanopores," *Nanotechnology*, vol. 26, no. 27, p. 275202, 2015.

[61] H.-c. Chang and L. Y. Yeo, "Electrokinetically driven microfluidics and nanofluidics," *Int. J. Bifurc. Chaos*, p. 544, 2008.

[62] L. Yeo and J. Friend, "Electrowetting, Applications," in *Encycl. Microfluid. Nanofluidics*, vol. 1, pp. 606–615, Boston, MA: Springer US, 2008.

[63] F. Mugele, a. Klingner, J. Buehrle, D. Steinhauser, and S. Herminghaus, "Electrowetting: a convenient way to switchable wettability patterns," *J. Phys. Condens. Matter*, vol. 17, no. 9, pp. S559–S576, 2005.

[64] C. D. Daub, D. Bratko, K. Leung, and A. Luzar, "Electrowetting at the Nanoscale," *J. Phys. Chem. C*, vol. 111, no. 2, pp. 505–509, 2007.

[65] R. M. M. Smeets, U. F. Keyser, D. Krapf, M.-Y. Wu, N. H. Dekker, and C. Dekker, "Salt Dependence of Ion Transport and DNA Translocation through Solid-State Nanopores," *Nano Lett.*, vol. 6, no. 1, pp. 89–95, 2006.

[66] V. Tabard-Cossa, "Chapter 3 - Instrumentation for Low-Noise High-Bandwidth Nanopore Recording," in *Eng. Nanopores Bioanal. Appl.* (J. B. Edel and T. Albrecht, eds.), Micro and Nano Technologies, pp. 59–93, Oxford: William Andrew Publishing, 2013.

[67] M. M. Lohrengel, A. Moehring, and M. Pilaski, "Electrochemical surface analysis with the scanning droplet cell," *Fresenius. J. Anal. Chem.*, vol. 367, no. 4, pp. 334–339, 2000.

[68] N. Ebejer, M. Schnippering, A. W. Colburn, M. A. Edwards, and P. R. Unwin, "Localized high resolution electrochemistry and multifunctional imaging: Scanning electrochemical cell microscopy," *Anal. Chem.*, vol. 82, no. 22, pp. 9141–9145, 2010.

[69] N. Ebejer, A. G. Güell, S. C. Lai, K. McKelvey, M. E. Snowden, and P. R. Unwin, "Scanning Electrochemical Cell Microscopy: A Versatile Technique for Nanoscale Electrochemistry and Functional Imaging," *Annu. Rev. Anal. Chem.*, vol. 6, no. 1, pp. 329–351, 2013.

[70] P. B. Nadappuram, K. McKelvey, J. C. Byers, A. G. Güell, A. W. Colburn, R. A. Lazenby, and P. R. Unwin, "Quad-Barrel Multifunctional Electrochemical and Ion Conductance Probe for Voltammetric Analysis and Imaging," *Anal. Chem.*, vol. 87, no. 7, pp. 3566–3573, 2015.

[71] C. Carlsson, M. Jonsson, and B. Akerman, "Double Bands in Dna Gel-Electrophoresis Caused By Bis- Intercalating Dyes," *Nucleic Acids Res.*, vol. 23, no. 13, pp. 2413–2420, 1995.

[72] K. Günther, M. Mertig, and R. Seidel, "Mechanical and structural properties of YOYO-1 complexed DNA," *Nucleic Acids Res.*, vol. 38, no. 19, pp. 6526–6532, 2010.

[73] W. H. Pitchford, H.-J. Kim, A. P. Ivanov, H.-M. Kim, J.-S. Yu, R. J. Leatherbarrow, T. Albrecht, K.-B. Kim, and J. B. Edel, "Synchronized Optical and Electronic Detection of Biomolecules Using a Low Noise Nanopore Platform," *ACS Nano*, vol. 9, no. 2, pp. 1740–1748, 2015.

[74] D. E. Smith, T. T. Perkins, and S. Chu, "Dynamical Scaling of DNA Diffusion Coefficients," *Macromolecules*, vol. 29, no. 4, pp. 1372–1373, 1996.

[75] A. Egner and S. W. Hell, *Aberrations in Confocal and Multi-Photon Fluorescence Microscopy Induced by Refractive Index Mismatch*, pp. 404–413. Boston, MA: Springer US, 2006.

[76] S. Jayaraman and A. S. Verkman, "Quenching mechanism of quinolinium-type chloride-sensitive fluorescent indicators," *Biophys. Chem.*, vol. 85, no. 1, pp. 49–57, 2000.

[77] Z. D. Harms, K. B. Mogensen, P. S. Nunes, K. Zhou, B. W. Hildenbrand, I. Mitra, Z. Tan, A. Zlotnick, J. P. Kutter, and S. C. Jacobson, "Nanofluidic Devices with Two Pores in Series for Resistive-Pulse Sensing of Single Virus Capsids," *Anal. Chem.*, vol. 83, no. 24, pp. 9573–9578, 2011.

[78] M. Langecker, D. Pedone, F. C. Simmel, and U. Rant, "Electrophoretic Time-of-Flight Measurements of Single DNA Molecules with Two Stacked Nanopores," *Nano Lett.*, vol. 11, no. 11, pp. 5002–5007, 2011.

[79] X. Liu, M. Mihovilovic Skanata, and D. Stein, "Entropic cages for trapping DNA near a nanopore.," *Nat. Commun.*, vol. 6, p. 6222, 2015.

[80] S. Pud, S.-H. Chao, M. Belkin, D. Verschueren, T. Huijben, C. van Engelenburg, C. Dekker, and A. Aksimentiev, "Mechanical Trapping of DNA in a Double-Nanopore System," *Nano Lett.*, vol. 16, no. 12, pp. 8021–8028, 2016.

[81] M. Muthukumar, "Mechanism of DNA Transport Through Pores," *Annu. Rev. Biophys. Biomol. Struct.*, vol. 36, no. 1, pp. 435–450, 2007.

[82] J. R. Wenner, M. C. Williams, I. Rouzina, and V. A. Bloomfield, "Salt Dependence of the Elasticity and Overstretching Transition of Single DNA Molecules," *Biophys. J.*, vol. 82, no. 6, pp. 3160–3169, 2002.

[83] R. M. M. Smeets, U. F. Keyser, M. Y. Wu, N. H. Dekker, and C. Dekker, "Nanobubbles in Solid-State Nanopores," *Phys. Rev. Lett.*, vol. 97, no. 8, p. 088101, 2006.

[84] R. M. M. Smeets, U. F. Keyser, N. H. Dekker, and C. Dekker, "Noise in solid-state nanopores," *Proc. Natl. Acad. Sci.*, vol. 105, no. 2, pp. 417–421, 2008.

[85] N. A. W. Bell, M. Muthukumar, and U. F. Keyser, "Translocation frequency of double-stranded DNA through a solid-state nanopore," *Phys. Rev. E*, vol. 93, p. 022401, feb 2016.

[86] L. Brun, M. Pastoriza-Gallego, G. Oukhaled, J. Mathé, L. Bacri, L. Auvray, and J. Pelta, "Dynamics of Polyelectrolyte Transport through a Protein Channel as a Function of Applied Voltage," *Phys. Rev. Lett.*, vol. 100, no. 15, p. 158302, 2008.

[87] S. W. Kowalczyk and C. Dekker, "Measurement of the docking time of a DNA molecule onto a solid-state nanopore," *Nano Lett.*, vol. 12, no. 8, pp. 4159–4163, 2012.

[88] M. Wanunu, "Nanopores: A journey towards DNA sequencing," *Phys. Life Rev.*, vol. 9, no. 2, pp. 125–158, 2012.

[89] J. Y. Y. Sze, S. Kumar, A. P. Ivanov, S.-H. Oh, and J. B. Edel, "Fine tuning of nanopipettes using atomic layer deposition for single molecule sensing," *Analyst*, vol. 140, no. 14, pp. 4828–4834, 2015.

[90] C. Plesa, D. Verschueren, S. Pud, J. van der Torre, J. W. Ruitenberg, M. J. Witteveen, M. P. Jonsson, A. Y. Grosberg, Y. Rabin, and C. Dekker, "Direct observation of DNA knots using a solid-state nanopore," *Nat. Nanotechnol.*, vol. 11, no. 8, pp. 1–6, 2016.

[91] L. J. Steinbock, J. F. Steinbock, and A. Radenovic, "Controllable Shrinking and Shaping of Glass Nanocapillaries under Electron Irradiation," *Nano Lett.*, vol. 13, no. 4, pp. 1717–1723, 2013.

[92] M. K. Liu and J. C. Giddings, "Separation and Measurement of Diffusion-Coefficients of Linear and Circular Dnas by Flow Field-Flow Fractionation," *Macromolecules*, vol. 26, no. 14, pp. 3576–3588, 1993.

[93] P. J. Flory, *Principles of Polymer Chemistry*. Baker lectures 1948, Cornell University Press, 1953.

[94] D. E. Smith, T. T. Perkins, and S. Chu, "Dynamical Scaling of DNA Diffusion Coefficients," *Macromolecules*, vol. 29, no. 4, pp. 1372–1373, 1996.

[95] S. W. Kowalczyk, M. W. Tuijtel, S. P. Donkers, and C. Dekker, "Unraveling single-stranded DNA in a solid-state nanopore," *Nano Lett.*, vol. 10, no. 4, pp. 1414–1420, 2010.

[96] N. Douville, D. Huh, and S. Takayama, "DNA linearization through confinement in nanofluidic channels," *Anal. Bioanal. Chem.*, vol. 391, no. 7, pp. 2395–2409, 2008.

[97] B. Tinland, A. Pluen, J. Sturm, G. Weill, and I. C. Sadron-cnrs universite, "Persistence Length of Single-Stranded DNA," *Macromolecules*, vol. 30, no. 9, pp. 5763–5765, 1997.

Chapter 3

DEP-nanotweezer: a tool for single molecule and single cell manipulation

3.1 Introduction

Single molecule detection and single molecule manipulation are two sides of the same coin. In contrast with ensemble measurements, in which signals are robust (proportional to the number of molecules), for single molecule methods particles exhibit fast dynamics and the measured signal appears to be random and stochastic, due to high fluctuations in magnitude. Therefore improving the amount of information that one can extract from a single molecule depends on, inevitably, through how well one can control, spatially and temporally, that specific molecule [1]. Governing single entity dynamics has important implications: the first one has to do with the time that it spends in the detection area; often single molecule kinetics are on a much faster timescale than the measurement time resulting in a loss of information [2, 3]. However, by temporarily confining the particle in a small probe volume, for example, it is possible to overcome bandwidth problems associated with detection. Notably, detection speed and sensitivity are inversely related in most detectors. The second important implication is linked with the diffusion mechanism which single molecule experiments are affected by. In most cases, molecules reach the detection volume, which for a typical single molecule experiment is on the order of femtoliters, by diffusion [1]. The time required for this process to happen depends on the analyte concentration which for single molecule experiments is never higher than a few nM; this means that if a population of molecules has to be explored at single molecule level, the measurement time will likely be unsuitably long. It is clear that being able to actively bring particles closer to the detection

area would drastically reduce the measurement time necessary to build up a statistically relevant dataset, allowing detection in highly diluted samples.

The precise control of biological particles, such as cells, viruses, proteins, DNA molecules, in terms of spatio temporal position and also in terms of quantity of particles, has attracted great interest from the scientific community and various methods have been proposed, including the use of electromagnetic traps (optical tweezers [4]), magnetic forces (magnetic tweezers [5]), mechanical forces (atomic force microscopy), electrical forces and microfluidics [6]. As summarized in Table 3.1, each of these techniques presents advantages and disadvantages which are mainly associated with the low throughput of techniques such as optical, magnetic tweezers and near-field approaches (scanning tunneling microscopy and AFM), as well as the necessity for molecule labelling and possible photodamange of the sample (e.g. with optical tweezers). Microfluidics, on the other hand, can provide a high throughput, and manufacturing and device operation are generally reliable and easy. Its precision in handling a particle, however, is not comparable with that which can be offered by other techniques [7].

Methods	**Controllability**	**Operation**	**Efficiency**	**Cost**	**Damage**
Optical	strong	hard	low	high	slight
Microfluidic	weak	easy	high	low	little
Mechanical	strong	hard	low	low	large
Magnetic	strong	hard	low	low	slight
Electrical fields	strong	easy	high	low	slight

Table 3.1 Comparison of different methods employed to control particles at the nanoscale [8].

In contrast, strong controllability, relatively easy operation due to the lack of any sophisticated equipment, high throughput and limited sample damage make electric fields an ideal candidate for biomolecule manipulation [8]. In particular the focus of the present work stems on dielectrophoresis (DEP) which is a technique to manipulate polarizable objects using electric field gradients. There are several excellent reviews that focus on DEP-based methods to manipulate nucleic acids and proteins [27, 17, 20]. These solutions show that it is possible to trap molecules, albeit with some limitations: the high voltages required for operation, generation of heat and limited flexibility. They cannot easily be integrated with other techniques, either single molecule or common molecular biological techniques such as new generation sequencing machines, enzymatic assays (ELISA) or quantitative polymerase chain reaction (PCR). In addition, more often than not they are based on micro-nano architectures which are cleanroom fabricated and thus time-consuming, expensive and difficult to scale up production volumes.

Here we propose a novel device we call nanotweezers, based on dual barrel quartz nanopipettes, which addresses the aforementioned challenges, allowing DEP based single molecule manipulation. The tip of the nanopipette, where two nanometric carbon electrodes are located, acts as an ultra precise electrical handle. Depending on parameters such as polarizability, frequency and voltage applied, it is capable of selectively trapping molecules in a confined volume surrounding the tip and subsequently manipulating them (**Figure 3.1**). In addition, the high aspect ratio of the nanopipette shape, makes them not only easy to fabricate - since this does not require a cleanroom - but also easy to be manually handled while still operating at the nanoscale.

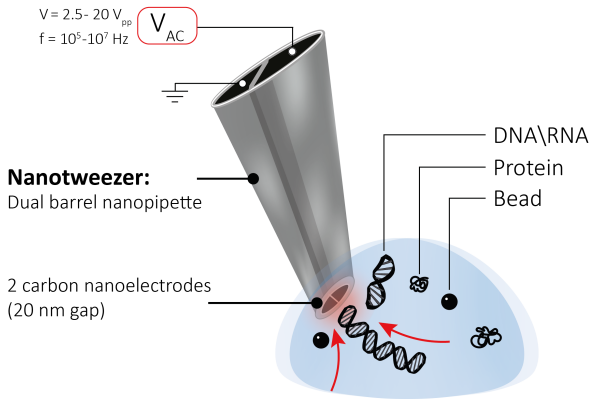

Fig. 3.1 DEP-Nanotweezer: a graphical concept. The nanotweezer consists of a quartz dual barrel nanopipette equipped with 2 carbon nanoelectrodes separated by 20 nm gap at its apex. DEP-nanotweezer is essentially a nano-handle and the working principle is based around dielectrophoresis. By applying an alternate electric field between the electrodes it is possible to exert a force on an object (e.g. DNA, proteins, polysterene beads etc.) and subsequently trap them in a confined volume surrounding the apex.

Most single-molecule studies are performed in a simple scenario in which one or more purified components - DNA or proteins, for example - are used at a time. Nanotweezers aim to bridge another gap and incorporate ideas from a vibrant research field at the edge between biology and nanotechnology: single cell nanobiopsy, a non-invasive interrogation of cells with unprecedented spatial and temporal resolution.

Stochastic gene and protein expression at the single cell level [9] has clearly demonstrated that conventional assays designed for large cell populations (thousands to millions of cells at a time) mask and dilute, in a sea of averages, relevant alterations that occur in a small subset of cells. In addition to the limits of detection, the real Achilles heel of these commercially available assays is the destructive reading of cellular content to acquire information, which requires cell suspension and lysis. Therefore, limitations in the field of cell biology can arise not only from the intricate processes under investigation, but also from of a lack of research tools capable of continuously monitoring, sampling and manipulating individual cells without altering molecular parameters (e.g. cell biophysical features and gene expression profile).

The state of the art for single cell biopsy includes fluid force microscopy [10], nanostraw architectures [11], carbon nanotube probes [12] and glass nanopipettes [13] (**Figure 3.2**). In general, techniques for long-term monitoring of single cells must be non-invasive, capable of manipulating from femtoliter volumes to single sub-cellular constituents (e.g. organelles, mitochondria, DNA), must preserve cell viability and allow for easy automation and integration of the extracted materials for further analysis.

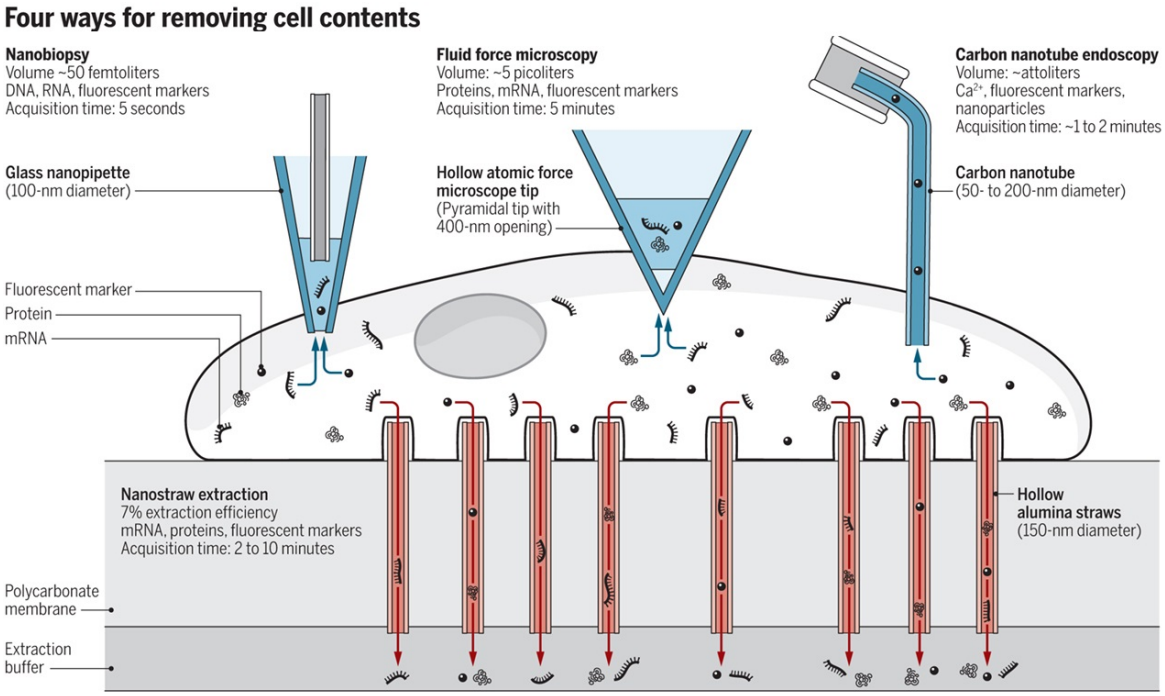

Fig. 3.2 Methods of extracting contents of living cells. Fluid force microscopy consists of an atomic force microscope equipped with pyramidal microfluidic probes that can penetrate the cell membrane and withdraw picoliters of intracellular material by applying a negative pressure at the tip [10, 14]. Molecules were successfully extracted from both nucleus and cytoplasm and later analyzed with qPCR, enzyme assays and electron microscopy. Post-extraction cellular viability was 82% and cells were monitored up to 5 days after the experiment. **Nanostraw** extraction process consisted of continuous sampling of biomolecules from a subset of cells by using hollow, polymeric nanoneedles with a high aspect ration, onto which cells were seeded on a polymeric substrate. These nanoneedles, or nanostraws, have a diameter of about 150 nm. Sampling was performed by temporarily electroporating the cells; the extraction efficiency was calculated to be approximately 7% and the withdrawn material was finally used to map mRNA expression levels [11]. **Carbon nanotubes** have been employed to develop a nanometric endoscope. A multiwalled carbon nanotube of 50-200 nm in diameter, and 50μm in length is glued to the end of a glass pipette. Applications include aspiration of cytosolic Ca^{2+}-labelled and nanoparticles down to attoliter volumes, with the possibility of performing in situ electrochemistry and SERS analysis using gold-coated carbon nanotube tips [12]. **Quartz nanopipettes**, with diameters of $\approx$ 100 nm, have been used to extract up to $\approx$ 50 femtoliters of intracellular material. Nanopipettes, combined with scanning ion conductance microscopy, allow precise targeting of organelles within the cell. Extraction is performed via electrowetting: nanopipettes, filled with an immiscible organic solvent (dichloroethane), create a liquid-liquid interface between the nanopipette aperture and the aqueous cellular phase. The application of a voltage perturbs this interface causing the aqueous phase to flow inside the nanopipette. The extracted material was used to perform mRNA profiling of single cells [13]. Reprinted with permission from [15]. Copyright (2017) American Association for the Advancement of Science.

Although single cell biopsy techniques have proved to be promising, all the methods proposed rely on aspiration as the only way of extracting and manipulating cells. The main limits of these approaches are the limited control on what is aspired and in which cellular compartment, and the poor integration with other techniques. In contrast nanotweezers

represent a robust choice to interact with cells in a non-destructive manner, handling small volumes, and displaying excellent integration with existing molecular biology assay; instead of using nanopipettes as femto to attoliter-syringes [16, 17], in this chapter, nanopipettes are employed as a scalpel to actively exert a force on specific entities inside the cell by using the dielectrophoretic force.

3.2 Experimental procedures

3.2.1 Nanopipette fabrication

Nanopipettes were fabricated using a P-2000 laser puller (Sutter Instrument Co) from quartz double-barrel capillaries (Friedrich & dimmock, USA) with an outer diameter of 1.2 mm and an overall inner diameter of 0.9 mm, which comprises two chambers separated by an insulating quartz septum which retains its shape after the pulling process. Capillaries were plasma cleaned (Harrick Plasma cleaner PDC-001, USA) for at least 15 minutes prior to pulling. Nanopipettes were pulled according to the following protocol:

	Heating	Filament	Velocity	Delay	Pulling
Line 1	850	4	30	160	80
Line 2	860	3	20	140	160

Table 3.2 Nanopipette pulling protocol

3.2.2 Setup for fabrication of carbon electrodes

Utilising the setup illustrated in **Figure 3.3 a**, it was possible to fabricate electrodes via butane deposition starting from freshly pulled theta quartz nanopipettes. Firstly nanopipettes were mounted in a one-axis moveable holder and the back-end was connected, via a rubber tube, to a butane canister (Campingaz, USA). The tip of the nanopipette was moved to the opening of a quartz, single barrel capillary placed on the opposite side. This second capillary was connected to an argon cylinder and provided argon flow at the tip of the theta nanopipette. Both argon and butane were regulated by gas flow meters. A gas blow torch (RS Components, UK) was used to heat the tip of the nanopipette for 30 s leading to pyrolytic deposition of carbon from butane as shown in **Figure 3.3 b**. Through this process, both barrels of the nanopipette were filled with carbon. Electrical contact was then established by inserting a copper wire through the back-end of the nanopipette's barrel to make contact with the carbon layers.

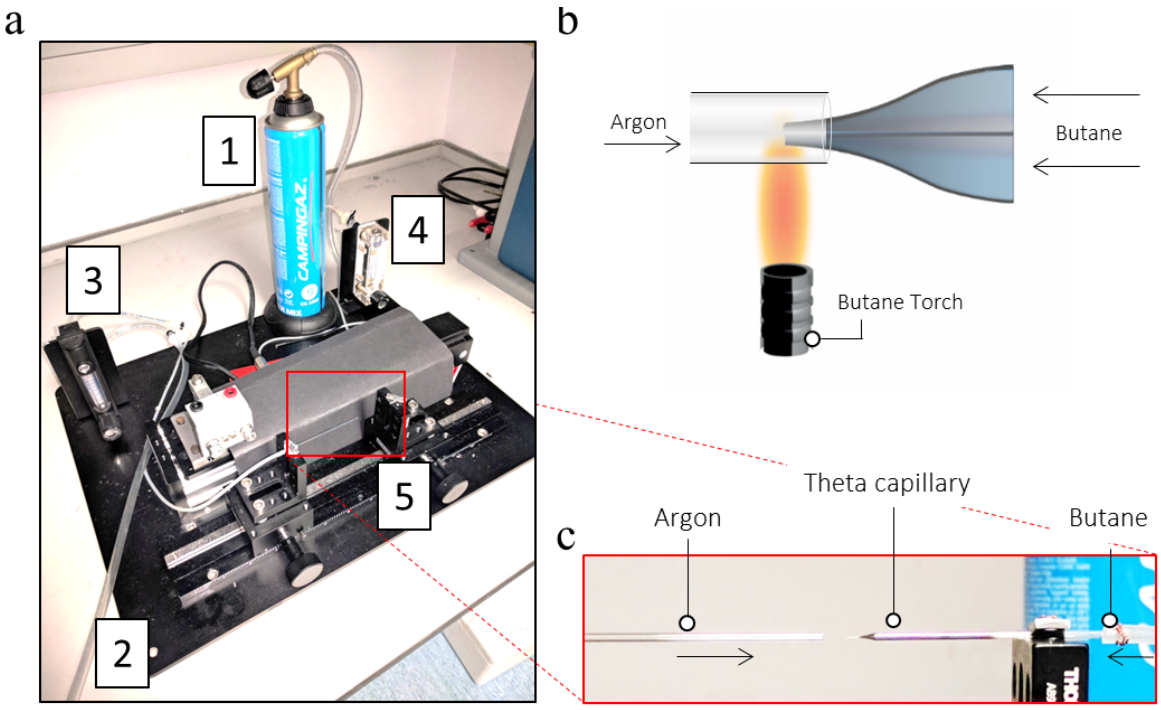

Fig. 3.3 DEP-nanotweezer fabrication setup. (a) Illustration showing the carbon electrode fabrication setup composed by 1) Butane Canister, 2) tube supplying argon gas from an argon cylinder (BOC, UK), 3), 4) gas flow meters and 5) nanopipette holder. b) Cartoon showing the deposition process: a pulled nanopipette was fixed onto a holder and connected via a tube with a butane canister. The nanopipette was then approached to a quartz pipette, positioned opposite it, into which argon gas was fed. The tip of the nanopipette was heated with a butane torch resulting in pyrolytic deposition of carbon from butane. c) Detail showing the nanopipette and quartz capillary.

3.2.3 Laboratory setup

The experimental setup used for this study is illustrated in **Figure 3.4 a,b**. A nanopipette was mounted onto a micromanipulator placed on top of an inverted microscope (IX71, Olympus, USA) which was used in epifluorescence configuration to perform fluorescence recordings. DEP signals were applied to the nanopipette via a function generator which was connected to the copper wires inserted in each barrel of the carbon-coated nanopipette.

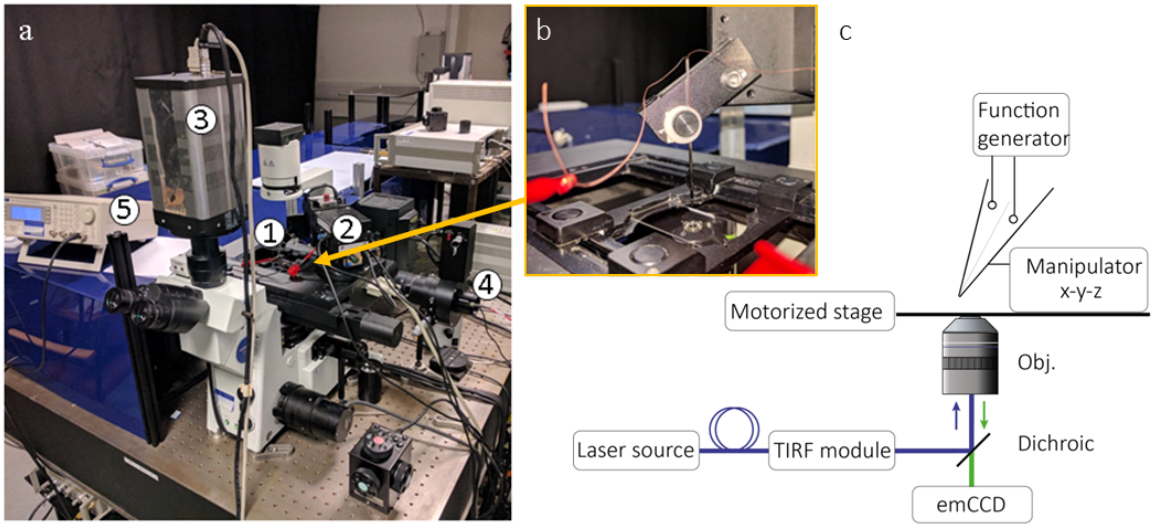

Fig. 3.4 Fluorescence setup. (a) A custom made setup was built on top of an inverted microscope, Olympus IX71. A laser (Melles Griot Laser Group, USA) with excitation at 488 nm was fiber coupled to a TIRF module (1) located on the back aperture of the microscope. A 498 nm dichroic mirror reflected the incoming light towards the sample, where a 60x objective (UPLSAPO 60XW, Olympus, USA) was employed to both illuminate the sample and collect the emitted fluorescence which was sensed by an emCCD camera (2) (Photometrics Cascade II, USA). The nanotweezer was mounted on a micromanipulator (3) (PatchStar Micromanipulator, Scientifica, UK). The nanotweezer was connected to the function generator (TG2000, TTi, UK) via a BNC to hook clips (RS, UK). (b) Showing the nanotweezers vertically mounted on the micromanipulator. Two copper wires were inserted in each barrel to connect the carbon electrodes to the function generator. (c) Schematic of the optical setup.

- **Light source** An argon–krypton mixed gas tunable laser (Melles Griot Laser Group, USA) was used for excitation at 488 nm. The laser was fiber-coupled and connected to a total internal reflection (TIRF) module. For all experiments the illumination angle was kept at 90 degrees, perpendicular to the surface. A 498 nm dichroic mirror reflected the laser-light towards the sample, where a 60x water immersion objective (UPLSAPO 60XW, Olympus, USA, with an NA value of 1.2 and WD of 0.28mmm) was used in epifluorescence mode to both illuminate the sample and collect the emitted fluourescence.

- **Detector** The optical set-up was equipped with an emCCD as an imaging detector which collected the light being transmitted through the dichroic mirror. The camera, a

Photometrics Cascade II (USA) operating at $-80°$C provided low dark noise performance. The detector was composed of 512x512 imaging pixels of 16 x 16-μm with a quantum efficiency of $\approx 92\%$. The software used to acquired the videos was Micromanager 2.0 (Open source software initially developed at University of California San Francisco).

- **Stage** The micromanipulator was positioned on top of a motorized xyz-stage (Prior Scientific, USA) equipped with a controller unit (Proscan II, Prior Scientific).

- **Micromanipulator**. A PatchStar micromanipulator (Scientifica, UK) was used to precisely move the nanopipette. The Patchstar was equipped with 3 motorized axes capable of 20 mm of movement in each axis and down to 20 nm resolution across its range of travel. Stability was ensured to be less than one micron of drift in two hours. Each axis was controllable, either manually, via three wheel-controllers, or via the dedicated PC software LinLab (Scientifica, UK).

- **Function generator**. A TG2000 (TTi, UK) was used to apply a specific voltage to the nanopipette. The function generator provided 0.001 Hz to 20 MHz frequency range with up 1 mHz resolution. The amplitude varied between 5 mV and 20 V_{pp}. The function generator was connected to the nanopipette via a BNC to dual hook clips (RS, UK).

3.2.4 Materials

Lambda DNA (48.5 kbp), along with 10 kbp and 5 kbp DNA samples, in a stock concentration of 500 mg ml^{-1}, were purchased from New England Biolabs (USA). Solutions were prepared in 1 mM KCl and buffered in 10 mM Tris 1 mM EDTA, pH 8.0 (Cat. Num. T9285, Sigma Aldrich, USA). All DNA solutions were prepared fresh by serial dilution and used for experiments the same day. For fluorescence imaging, 10 kbp dsDNA was incubated for 45 minutes with YOYO-1 (Molecular Probes, USA) at a ratio of five base pairs per molecule for 45 minutes.

Fluorescent beads (FluoSpheres Carboxylate-Modified Microspheres, 0.1 μm, Cat. Num. F88000, Invitrogen, USA) with a mean diameter of 100 nm were used for characterizing the carbon-coated nanopipettes. Absorption and emission maxima were 505 nm and 515 nm, respectively. A working solution of approximately 3.63 x 10^4 beads/ml was used. This corresponds to a 10000 fold dilution of the stock solution. Dilutions were performed in deionized water (minimum 18 MΩ as measured from the water purification system).

HPLC purified ssDNA labelled with Atto488 (Atto488-GGTTGGTGTGGTTGGAGGTCGC CGCCC) was purchased from IBA Lifesciences (Germany). HPLC purified ssDNA labelled with Cy3 (Cy3-TGAGGGTGGGTAGGGTGGGTAA-SH) was purchased from Sigma-Aldrich (Germany). Streptavidin DyLight 488 conjugate was purchased from ThermoScientific (USA).

qPCR amplification was performed using a Stratagene Mx3005P qPCR (Agilent Technologies) and dedicated optically clear qPCR tube (Agilent Technologies). Primer3 online software (http://bioinfo.ut.ee/primer3-0.4.0/) was used to design the qPCR primer pairs. β-Actin primers: ACTACCTCATGAAGATCCTC (forward), CTAGAAGCATTTGCGGTGGACGATGG (reverse). λ-DNA primers: CAAACTGCGCAACTCGTGAA (forward), GACAGGCGAATCGCAATCAC (reverse). In both cases primers were purchased from Applied Biosystems (UK). qPCR was performed using qPCR master mix (iTaq™ Universal SYBR® Green Supermix, BIO-RAD, USA). A thermal cycling protocol was programmed according to instructions provided by the manufacturer (BIO-RAD, USA).

3.2.5 Fluorescence spectra

The following figure depicts the fluorescence spectra of the main fluorophores used for this work:

	$\lambda_{ex}(nm)$	$\lambda_{em}(nm)$
Fluospheres	540	560
Dylight	493	518
YOYO-1	491	509
Cy3	554	568
Atto 488	500	520

Table 3.3 Maximum absoprtion and emission fluorescence wavelengths for the main fluorophores presented used in this work.

3.2.6 Cell culture

Bone osteosarcoma U2OS cells (obtained from London Research Institute, Cancer Research UK) were grown in low glucose phenol red-free Dulbecco's modified Eagle medium containing 10% fetal bovine serum at 37°C with 10% CO_2 in humidified air. Cells were kept continuously under confluence before being split twice a week. Contamination was avoided by regularly performing mycoplasma tests.

Cells were seeded on chambered coverglass (ca. 2 x 10^4, 300 μl, 0.8 cm^2) for $6-24$h, then the media was replaced with fresh phenol red free media, containing DAOTA-M2 (20

μM, 300 μl) for 24 hrs [18] for 15 minutes. Cell culturing was performed by Dr. Jorge Garcia Gonzalez in collaboration with Prof. Ramon Vilar (Chemistry Department, Imperial College).

Primary human pulmonary artery endothelial cells (HPAEC) were obtained from Promocell, cultured at 37oC, 5% CO2 in EGM-2 media (Promocell) and used between passages 4-10. HPAEC were seeded into an 8 well μ-Slide (IBIDI) at a density of 20000 cells/200μl and left to incubate for 24 hrs (Procedure performed by Alex Ainscough, Medicine Department, Imperial College)).

3.3 Theory

When a particle is placed in an electric field it experiences a force which is given by [19]:

$$\vec{F}_{elect} = q\vec{E} + (\vec{p}\nabla)\vec{E} + \frac{1}{6}\nabla(\vec{Q}\nabla\vec{E}) + ... \tag{3.1}$$

The first term, $\vec{F} = q\vec{E}$, describes the coulombic interaction between a particle with charge q and the electric field $\vec{E}$. Electrophoretic phenomena resulting from this force, vanishes in case the net charge of the particle is zero or in the presence of an alternating field whose time average is zero. In contrast, dielectrophoresis (DEP), described by the additional terms in the expression above, arises from the interaction of dielectric polarization components (e.g. dipoles $\vec{p}$, quadrupoles $\vec{Q}$) induced by a spatially non-uniform electric field ($\nabla\vec{E} \neq 0$). In the simplest case, the dielectrophoretic force between a particle's dipole and the spatial gradient of the electric field is given by [20]:

$$\vec{F}_{DEP} = (p \cdot \nabla)\vec{E} \tag{3.2}$$

where p represents the particle's dipole and $\nabla\vec{E}$ the gradient of the electric field. As shown in **Figure 3.5**, the electric field polarizes the particle (which can even be electrically neutral) by generating an effective dipole moment; the inhomogeneous electric field subsequently exercises a net force on the dipole hence moving the particle.
The general expression for the induced dipole moment p of a dielectric particle of volume V is given by:

$$\vec{p} = \alpha V\vec{E} \tag{3.3}$$

α is the induced polarizability per unit volume. In this case it is assumed that the particle is isotropically, homogeneously and linearly polarizable. The physical origin and the different

kinds of polarizability are presented in the following section assuming a variable electric field of frequency f and phase ϕ,

$$\vec{E} = \vec{E}\cos(2\pi ft + \phi) \tag{3.4}$$

and combining the equations 3.2, 3.3 and 3.4 we can express the dielectrophoretic force as follows:

$$\vec{F}_{DEP} = \frac{1}{2}\alpha V \nabla |\vec{E}|^2 \cos^2(2\pi ft + \phi) \tag{3.5}$$

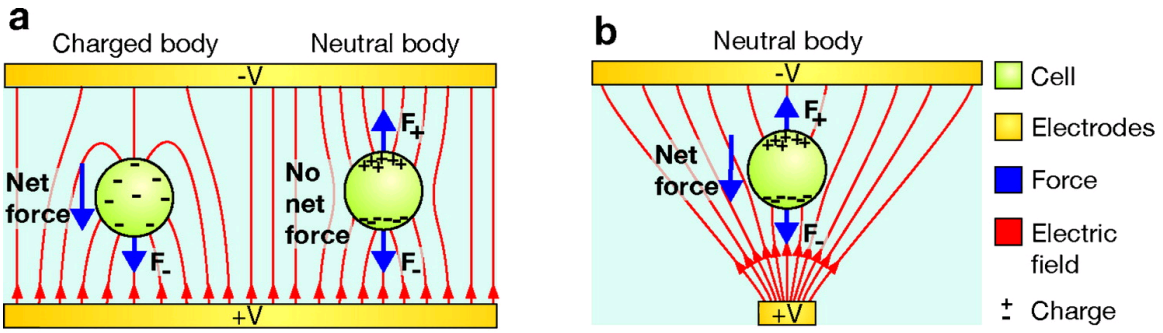

Fig. 3.5 Electrophoretic versus dielectrophoretic forces. (a) Charged and neutral particles immersed in a uniform electric field. (b) A neutral particle in a non-homogneous electric field. Adapted from [20]

The latter (Eq. 3.5) can be further rearranged in a purely space-dependent component and a time dependent component:

$$\vec{F}_{DEP} = \frac{1}{4}\alpha V \nabla |\vec{E}|^2 (1 + \cos(4\pi ft + 2\phi)) \tag{3.6}$$

Assuming that the electric field oscillates at frequencies higher than 50 kHz (which is the case for this study), the cosine term in 3.6 becomes negligible and the $\vec{F}_{DEP}$ average over time is given by:

$$\langle \vec{F}_{dep} \rangle = \frac{1}{4}\alpha V \nabla |\vec{E}|^2 \tag{3.7}$$

3.3.1 Physical origin of polarization

Polarization describes how charges located in a dielectric object respond to an externally applied electric field. There are different types of polarization: electronic, ionic, dipolar, interfacial and counterion polarization.

- **Electronic polarization** α_e, also called atomic polarization, is caused by an asymmetric distribution of the electronic cloud surrounding the positive nucleus as a result of an electric field.
- **Ionic polarization** α_i arises from the polarization of ions. In particular, it happens in solid materials with ionic bonding, such as NaCl. These dipoles get cancelled due to symmetry of the crystal, however under the influence of an external electric field, ions are slightly displaced from their equilibrium position, resulting in a net dipole.
- **Dipolar or orientation polarization** α_d arises from molecules such as water which, due to an asymmetric distribution of electrons in the molecule, have a permanent dipole. Molecular dipoles tend to be aligned in the direction of the applied electric field. If the latter is not present, molecules, hence dipoles, are randomly distributed.
- **Interfacial polarization**, also known as space-charge polarization α_s is caused by an external electric field which induces the orientation and accumulation of charges across the interface between two different materials (e.g. electrode-material interface).
- **Counterion polarization** α_c arises from the response of the counterions surrounding a molecule to an externally applied electric field.

In general, the polarization density can be expressed as $\vec{P} = N\alpha\vec{E}$, where N is the number of dipoles per unit volume and α is defined as the polarizability. For the different types of polarization, the following applies:

$$\alpha_e < \alpha_i < \alpha_d < \alpha_s, \alpha_c \tag{3.8}$$

In contrast, the time required for an electron, an atom or a molecule to respond to an external electric field will follow the inverse trend. For instance, a latex bead will respond slower than an atom.

3.3.2 Maxwell-Wagner polarization model: the case of polystyrene beads

The polarizability α is a key parameter when it comes to predict the DEP force acting on a given object. Towards this end, the Maxwell-Wagner interfacial polarization model, a commonly used model for describing the polarizability of dielectric particles, can be used to derive a complete expression for the DEP acting on polystyrene beads immersed in an aqueous solution. Firstly, most polystyrene beads display a charge on their surface, usually negative, arising from surface modification (e.g. with carboxyl groups). Therefore in solution,

counterions such as K^+, Na^+, Cl^-, OH^- accumulate in different layers around the surface of a particle shielding negative charges. This interface, called the electrical double layer, has been described in depth in section 1.4. Briefly, the ionic condition (e.g. ion concentration) and the bead's geometry determine the extension of the double layer which is normally described, using the Debye-Henkel approximation [21], in terms of Debye screening length λ_D. Under a variable electric field it is assumed that counterions continuously re-arrange around the particle in an attempt to respond to an electric field. The response time is also known as the relaxation time. In this model, charges are assumed to be strongly attracted by the surface and thus move along the surface only, not radially.

It is demonstrated that for uniform spheres within a sinusoidal electric field $\vec{E}(r,t)$, the induced dipole is equivalent to [20]:

$$\vec{p}(r) = 4\pi\varepsilon_m R^3 CM(\omega)\vec{E}(r) \tag{3.9}$$

where R is the radius of the particle, ε_m is the complex permittivity of the medium the particle is immersed in, which is given by $\varepsilon_m = \varepsilon + \sigma/(j\omega)$, ε is the permittivity and σ is the conductivity of the medium, j = $\sqrt{-1}$ and $CM(\omega)$ is the Clausius-Mossotti (CM) factor which takes into account the polarization difference between the particle and the surrounding medium.

Combining equation 3.2 and 3.9 leads to a time-average DEP force given by:

$$\langle F_{dep}(r)\rangle = \pi\varepsilon_m R^3 Re[CM(\omega)]\nabla|\vec{E}(r)|^2 \tag{3.10}$$

Examining the expression above, it is clear that the sign of the CM factor governs the overall behaviour of the particle. In general, if the relative polarizability of the particle is greater than that of the medium, which means $Re[CM(\omega)] > 0$, results in the force directed up the field gradient. This condition is known as positive DEP or pDEP. In contrast if the particle is less polarizable than the medium, $Re[CM(\omega)] < 0$, the force is directed down the gradient of the electric field. This second condition is known as negative DEP or nDEP.
The general expression for the CM factor is given by:

$$CM(\omega) = \frac{\varepsilon_p - \varepsilon_m}{\varepsilon_p + 2\varepsilon_m} \tag{3.11}$$

where ε_p and ε_m are the complex permittivity of medium and particle respectively. CM factor has a value varying between -0.5 and 1 as shown in the **Figure 3.6**. Notably, evaluation of the CM factor is far from trivial because objects, especially biological entities such as cells,

organelles, nucleic acids and proteins, constitute inhomogeneous dielectric materials and have complex geometries.

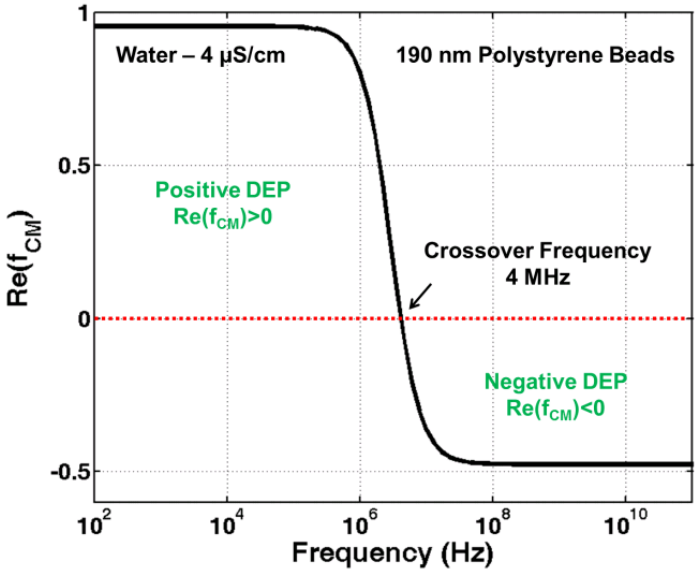

Fig. 3.6 Clausius-Mossotti (CM) factor plot for 190 nm polystyrene beads in water (conductivity: 4 μS/cm). Reproduced with permission from [22].

Notably, among the scientific community there is no general consensus on a specific polarization mechanism which is able to explain polarization properties at different frequencies and for different types of molecule. Currently, interfacial polarization models such as the Maxwell-Wagner [23] are used to describe DEP force in polysterene beads, while counterion fluctuation polarization models are used for biomolecules such as DNA [24].

3.3.3 Considerations when calculating the DEP force

Firstly, the overall DEP force acting on a particle is frequency dependent. In fact, the dielectric and permittivity values, which are embedded in the CM factor, vary with the frequency of the applied electric field.

A second observation is that DEP force can be tuned by not only varying the frequency but also by varying the values of conductivity and permittivity. These key parameters are easy to adjust: either by varying the ionic strength of the buffer solution or, as in the case of permittivity, by adding molecules with a large dipole moment, such as organic carbonates or urea [25] to the existing buffer.

Special attention should also be paid to the gradient term $\nabla\vec{E}^2$ of the equation 3.10 which hides one of the most explored, and sensitive, parameters, the geometry of the electrodes used. This defines the shape and strength of the electric field used to manipulate particles. In

the literature, a range of different approaches have been reported including planar electrodes [26, 27], 3D electrode designs [28, 29], and electrodes integrated within or external to a lab-on-a-chip . [20]. When comparing between them, a number of interconnected characteristics need to be taken into account:

- **Force generated and power required.** DEP forces scale with V^2/L^3, therefore the distance between the electrodes influences the magnitude of the generated force as well as the voltage required to handle or separate a particle. Placing the electrodes as close as possible generates higher forces at even lower applied voltages.
- **Joule heating.** Joule dissipation from the electrodes scales as $\Delta T \approx L^2|E|^2$ [30]. The smaller the system the lower the heat dissipation.
- **Biocompatibility.** The DEP device should be biologically compatible; therefore, materials employed to fabricate the electrodes can easily degrade or interact non-specifically with the sample. This point is also related to the Joule heating. Biological systems are extremely sensitive to any rise in temperature (e.g. protein denaturation).
- **Fabrication.** Depending on the complexity, fabrication processes are not time or cost-efficient therefore limiting the scalability of the technology.

3.4 Results and discussion

3.4.1 Nanopipettes fabrication and characterization

Nanopipettes were fabricated with very high success rates (> 90% of more than 200 made) according to a well established protocol (see Experimental section for details). Our approach was inspired by similar methods established to fabricate probes for scanning electrochemical microscopes [31], albeit in our case with much smaller overall diameter. Briefly, a theta quartz capillary, consisting of two barrels separated by an insulating septum, was plasma cleaned for approximately 15 minutes and then heated and drawn to a fine tip by pulling, using a P2000 laser puller (Sutter, USA). **Figure 3.7a-f** shows bright field and electron microscope micrographs of the apex of a typical nanopipette which consisted of semi-elliptical geometry where two nanometric apertures were separated by a gap of 20 nm. In general the effective diameter of each barrel ranged between 20 nm and 50 nm, leading to an overall probe radius of around 100 nm. The size of the apertures was controlled by the initial pulling parameters which ensured high reproducibility. Finally carbon electrodes were fabricated via pyrolytic deposition of carbon from butane. This step was performed in argon atmosphere

employing a manually controlled butane torch and a custom-made setup to control gas flow (See experimentals section). After the deposition step, both barrels were filled from end to end with carbon, resulting in two nanoelectrodes with almost perfect 2D planar interface. It was observed that a reduction in the butane flow rate generated recessed carbon electrodes which had an irregular pocket extending inside the barrel. In the vast majority of cases the electrodes were symmetrical, as confirmed by $Ru(NH_3)_6Cl_3$ electrochemical characterization using linear sweep voltammetry (**Figure 3.7 i**). By applying a negative bias to the carbon electrode, $Ru(NH_3)_6Cl_3$ was reduced and the generated current was related to the electrode size [32] according to the following expression [33]:

$$r = \frac{i_{ss}}{4.64nFDC} \tag{3.12}$$

where r is the radius of the electrode, i_{ss} is the steady-state reduction current, n is the number of the electron transferred during the reduction (i.e., 1) F is the Faraday's constant, D is the diffusion coefficient of $Ru(NH_3)_6Cl_3$ in 100 mM KCl (8.5 10^{-10} m^2s^{-1} [34]) and C is the concentration of $Ru(NH_3)_6Cl_3$ (1 mM). These numbers lead to an overall electrode diameter of approximately 41 nm which was in good agreement with the SEM and TEM micrographs.

The small electrode active area and the small separation gap (< 20 nm) are key aspects when dealing with dielectrophoresis. As described earlier, F_{DEP} scales as $\sim V^2/L^3$ where L is the characteristic length of the system (e.g. the distance between the electrodes). It is clear that strong DEP force can be generated either by applying high voltage between the electrodes (which implies higher $|\vec{E}|$) or alternatively by scaling down the distance between them, hence increasing $\nabla|\vec{E}|^2$. However high voltage results in heat generation, electrochemical reactions and gas formation at the electrode interface therfore solutions with small electrode gaps such as the nanotweezer are preferred.

The first practical implication was that our dual carbon probe, as it will be shown in the following paragraphs of this chapter, operated in a low voltage regime (1-20 V_{pp}, peak-to-peak Voltage) because it is possible to generate very high forces without applying high voltages. Therefore our nanotweezers were low power devices and did not require a dedicated high voltage amplifier. This was in contrast with most common DEP architectures reported in literature, whereby hundreds of V [35], or even kV [36], were applied to drive objects, cells or biomolecules. In addition, although fabrication of electrodes with sub-20 nm gaps have been previously reported (bow-tie like structures [37, 38] or carbon nanotube based platforms [39], for example), they rely on lithographic cleanroom processes which are slow and expensive compared to the method proposed here.

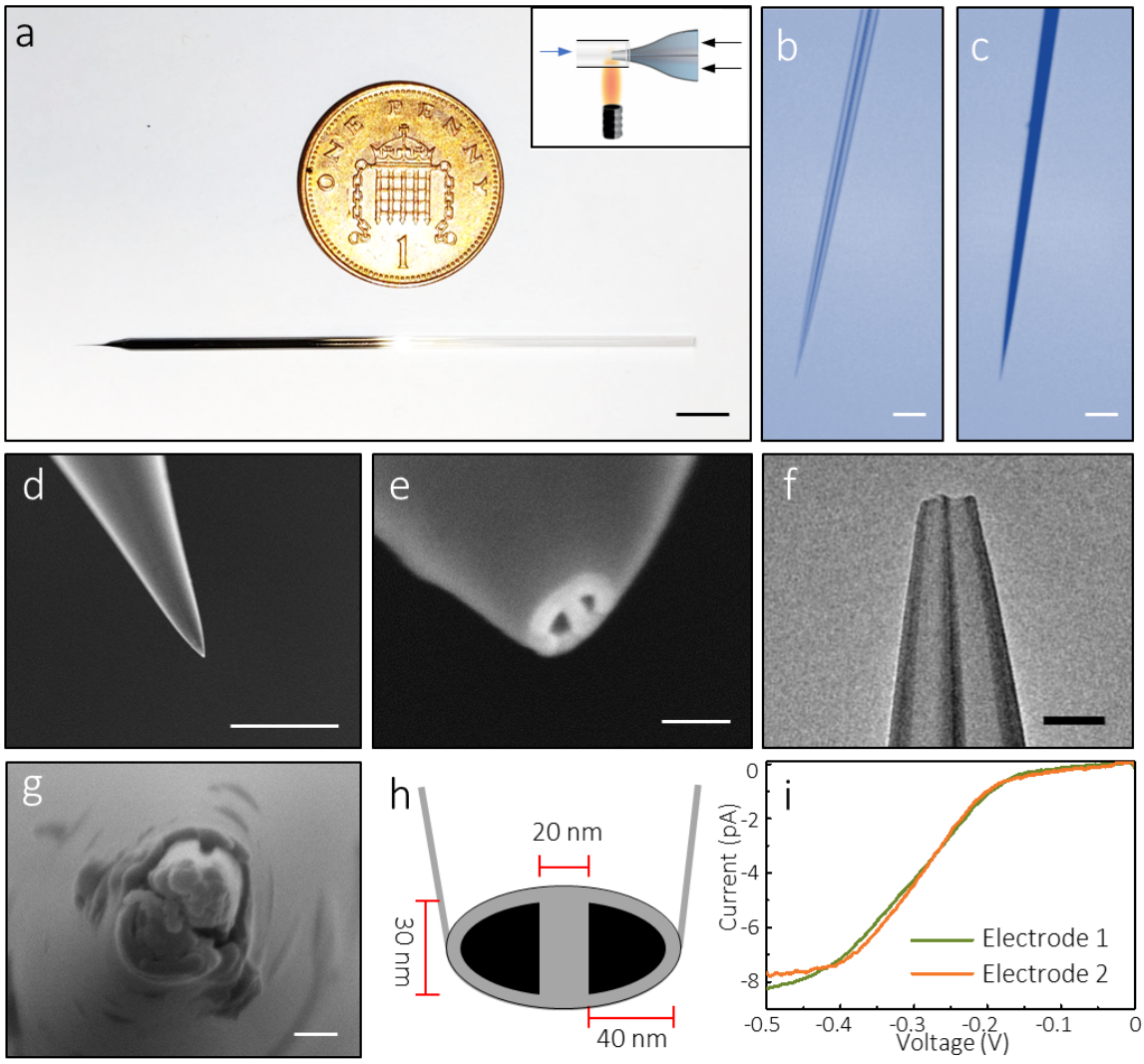

Fig. 3.7 Nanotweezer fabrication and characterization. (a) Nanotweezer overall dimension compared to a Penny. The black colour reflects the carbon being deposited inside both barrels (inset: schematic showing the fabrication of carbon electrode via pyrolytic deposition of carbon from butane via a manually controlled butane torch). (b), (c) showing bright field images of a dual barrel nanopipette before and after the carbon deposition respectively. (d), (e), (f) SEM and TEM micrographs of a bare dual barrel nanopipettes. (g) and (h) SEM micrograph and schematic of the carbon deposited dual barrel nanopipette. (i) Linear sweep voltammogram of the carbon deposited electrodes of a representative nanopipette performed with 1 mM $Ru(NH_3)_6Cl_3$ in 100 mM KCl using Ag/AgCl electrode. Electrode diameter was estimated to be about 41 nm (assuming a disk-shape geometry). In addition, the curves revealed almost symmetrical electrode areas. Scale bars: (a) 5 mm, (b), (c) 100 μm, (d), (f) 100 nm. TEM images were performed by Bernice Akpinar, Materials Department, Imperial College London.

3.4.2 Modelling of dielectrophoretic fields

A theoretical approach was used to gain an accurate estimate of the electric field distribution around the tip of the nanopipette when immersed in solutions with different conductivities. Finite element method (FEM) modelling was performed using COMSOL Multiphysics. As determined by SEM, the profile of the nanopipette was modelled as an ellipse with an external diameter of 100 nm, with a 20 nm outer glass wall thickness and a 20 nm gap between the electrodes.

The goal was to evaluate the strength of the electric field intensity gradient, $\nabla|\vec{E}|^2$, which is directly related to the $\vec{F}_{DEP}$. Simulations were performed with a solution conductivity of 14.6 mS/m (corresponding to 1 mM KCl) and 20 V_{pp} at a frequency of 1 MHz applied between the electrodes. Plots of $|\log_{10}\nabla|\vec{E}|^2|$ surrounding the nanopipette where extracted from the simulation and they revealed that the electric field gradient, therefore the force, was highly localized within 100 nm radius from the tip (**Figure 3.8 a**).

In general, to trap a particle floating in solution, it is necessary to overcome the Brownian motion, which fora particle of radius R is given by:

$$F_{thermal} = \frac{k_B T_R}{2R} \tag{3.13}$$

where k_B is the Boltzmann constant and T_R is room temperature (298.15 K). For instance, based on this equation, it has been calculated that for a 10 kbp DNA molecule the force required to overcome the thermal motion is 9.92 fN [24] which corresponds to $|\log_{10}\nabla|\vec{E}|^2| = 10^{16.4}V^2m^{-3}$. In the specific conditions we simulated, the trapping volume extends ≈ 450 nm from the electrodes (**Figure 3.8 b**) with the force decaying exponentially with the distance from the tip. It should be noted that the trapping volume can be tuned by varying the voltage applied, the frequency or alternatively the solution conductivity. [4]

This model was extremely useful for estimating the DEP induced temperature changes caused by power dissipation in the form of Joule heating. Two cases were analyzed: low solution conductivity (14.6 mS/m) and high solution conductivity (1 S/m). In the first case, the temperature profile around the tip of the nanopipette showed a constant behaviour along the radial axis. It was estimated a maximum temperature increase of less than 0.5 K above T_R in the proximity of the tip therefore heat dissipation in low salt conductivity was considered negligible.

The second scenario, with high medium conductivity, was useful to provide an estimate of Joule dissipation when the nanotweezer was operating in a comparable environment, in terms of salt concentration, to the cellular one. An estimate of the rise in temperature was sought

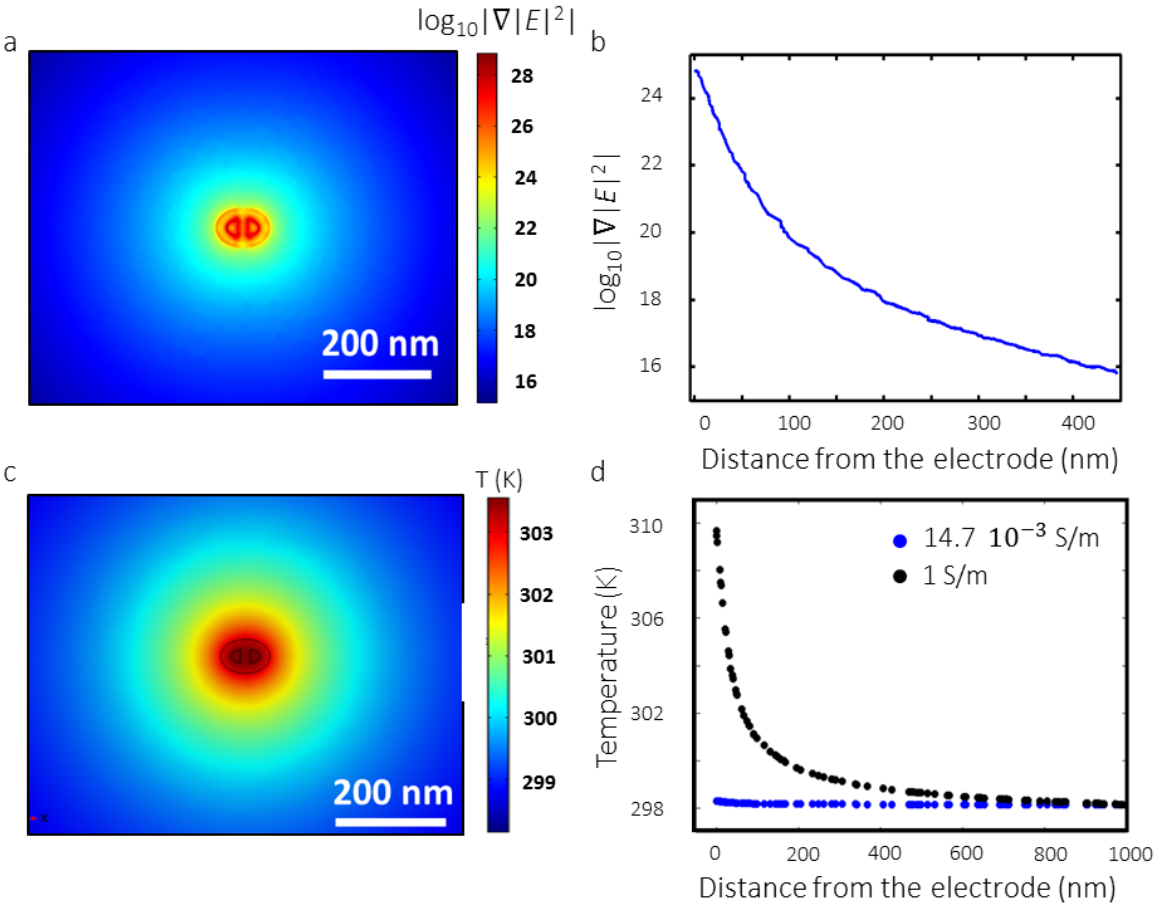

Fig. 3.8 FEM nanotweezer modelling. Nanotweezers Comsol simulations showing (a) logarithm of the gradient of $\nabla|\vec{E}|^2$, which is proportional to the DEP force, when 10 V_{pp} at 1 MHz was applied. The nanotweezer is immersed in solution with a conductance of 14.6 mS. The figure shows a frontal view, as if the nanotweezer were extruded out of the page. (b) Dependence of log $\nabla|\vec{E}|^2$ on the distance from the nanotweezer. Notably distance = 0 nm corresponds the outer walls of the nanopipette. (c),(d) showing the temperature dependence simulations. Simulations were performed by Avijit Barik (University of Minnesota).

for the case in which the nanotweezer was inserted and operated inside a cell. As shown in **Figure 3.8 c,d**, the temperature increase was 12 K above T_R, however it was localized within the first few nanometres (1-5 nm) from the tip. Following an exponential drop from the tip in the radial direction, at a distance of 100 nm the temperature was marginally higher (2 K) than that measured in the bulk solution.

It is important to note that temperature excursions have been proven to affect cellular phenotype, however the exact threshold needed to trigger a cellular response is still a matter of debate. Nonetheless these data demonstrated that the small electrode area minimized and confined such temperature excursion, therefore limiting any cellular response and preserving the cell integrity [20].

3.4.3 Characterization using fluorescence beads

Characterization of the DEP trapping kinetics was performed using polystyrene fluorescence spheres of 100 nm in diameter (Fluospheres, Invitrogen, USA). Polystyrene beads were diluted in DI water (10^4 times lower than the stock concentration). 40 μl of the diluted solution was spotted onto a rectangular cover glass (VWR scientific, USA) and positioned on the microscope holder of the fluorescence microscopy setup described in **Figure 3.4**. The nanotweezer, which was fixed to the micromanipultor (Scientifica, UK), was vertically moved towards the surface of the coverslip in the direction of the spotted solution **Figure 3.9 a**. To ensure electrical contact with the carbon electrodes, a pair of copper wires (0.25 mm diameter, GoodFellows, UK) were inserted, one per barrel, at the back-end of the nanopipette while on the other side the wires were connected to the function generator. The former allowed us to control the DEP force by applying an AC square wave voltage signal of a specified magnitude and frequency between the electrodes. Finally an emCCD camera (Photometrics Cascade II, USA) was utilized to capture the fluorescence signals that were later analysed using a custom written Matlab (Mathworks) script and ImageJ software.

The working principle of the nanotweezer is illustrated in the schematic in **Figure 3.9b**: initially, DEP was off (meaning no voltage applied between the electrodes) and particle dynamics were governed by the Brownian motion. As soon as DEP was turned on particles were attracted towards the tip of the nanotweezers resulting in fluorescence intensity build-up due to particle accumulation. For simplicity, in the schematic it was the case of positive DEP was assumed, where particles were attracted towards the tip, however attraction or repulsion was a function of the electric field frequency and dielectric properties of the medium and the analyte as described in paragraph 3.3.2.

Initially the relation between DEP force and electric field frequency was investigated. To do so, experiments were performed by applying an AC signal of 10 V_{pp} at frequencies varying

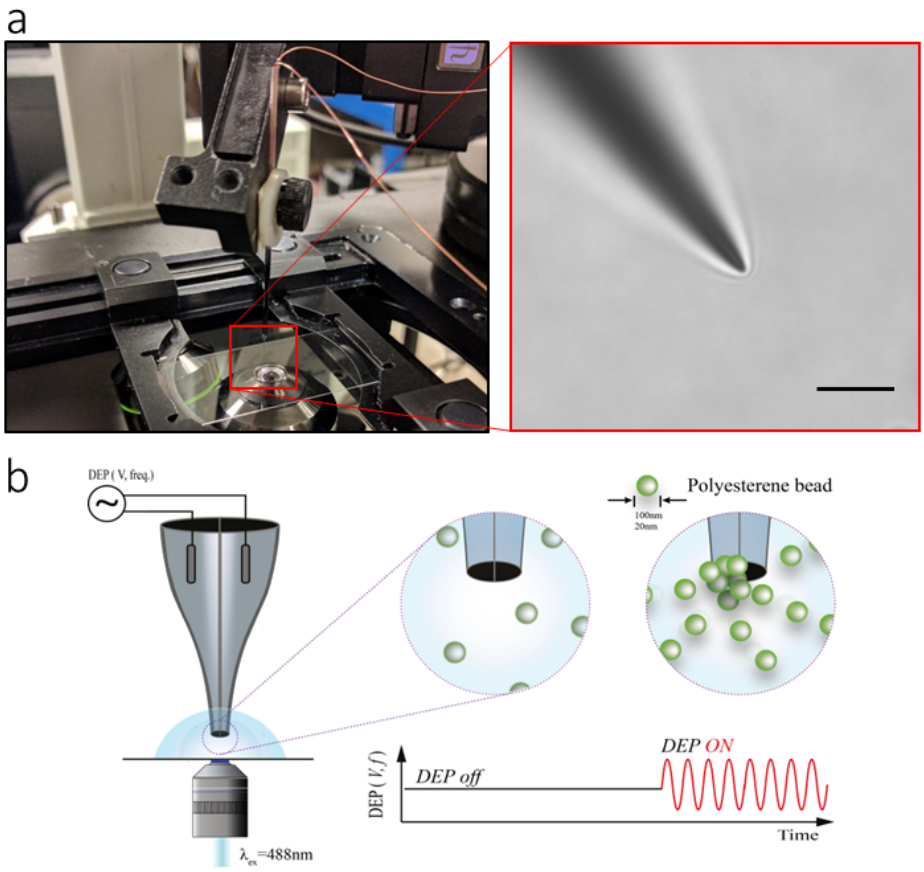

Fig. 3.9 Schematic and setup used for trapping 100 nm polystyrene beads. (a) Showing the setup with a nanopipette, mounted on a micromanipulator, being approached perpendicularly to the glass coverslip where the sample solution was spotted. The zoom shows a bright field image of the nanotweezers immersed in solution. (b) Showing the schematic of the DEP-nanotweezers working principle. In the presence of an AC field applied between the electrodes of the nanotweezers, 100 nm fluorescence beads were attracted towards the tip resulting in fluorescence intensity build-up by particle accumulation. Scale bar 10 μm.

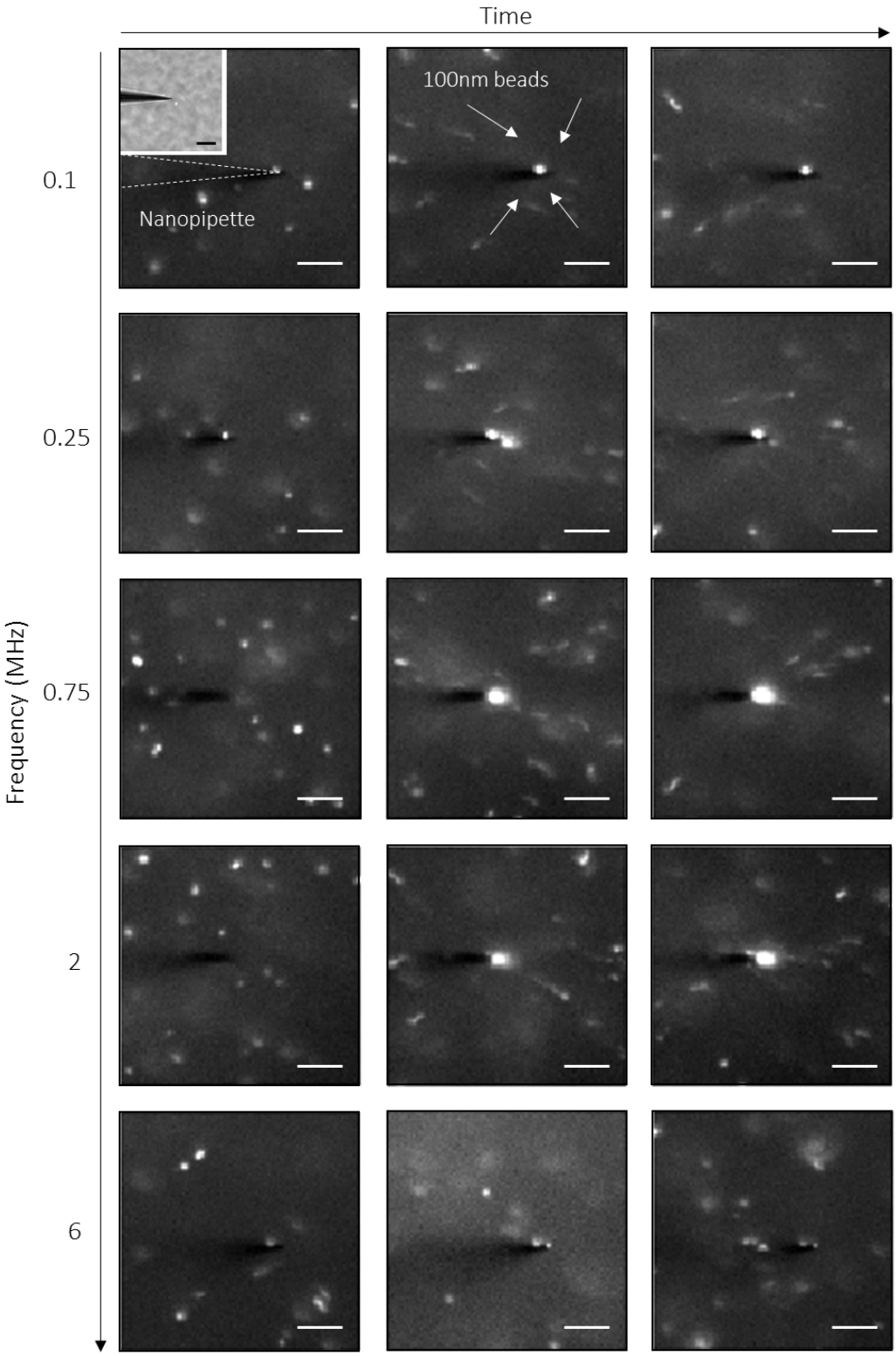

Fig. 3.10 Frequency dependence of 100 nm polystyrene beads. Showing fluorescence images captured with the emCCD at different time points for different frequencies (100 kHz, 250 kHz, 750 kHz, 2 MHz, 6 MHz) at 10 V_{pp} voltage applied. The timelapse showed how DEP force generated by the nanotweezer was strongly dependent on the frequency applied. The inset in the first image shows a bright field image of the nanopipette. Scale bars 5μm for the fluorescence images and 10μm for the inset

between 100 kHz and 7 Mhz. Unlike previous studies [40] where sub-Hz AC voltage signals were used to study dielectrophoretic properties of DNA molecules in quartz nanopipettes, the frequency utilised in this work ranged from 50 kHz to 10 MHz, and electrode polarization as well as electro-osmotic effects could be considered negligible.

Figure 3.10 shows fluorescent images of the nanotweezer tip captured at different time points (t=0 s, t=3 s and t=6 s) and for different DEP frequencies: 100 kHz, 250 kHz, 750 kHz, 2 MHz and 6 MHz. Beads, initially freely diffusing in media, accumulated around the tip as a result of DEP activation; the former was turned on at t = 0 s. As expected, the fluorescence was a function of the frequency: for instance at 1 Mhz, 750 kHz and 500 kHz, a strong fluorescent intensity was observed whereas at f > 4 Mhz no significant change from the background value was recorded. This fact was directly related to the CM factor which represented the frequency dependent component in the $\vec{F}_{DEP}$ expression. From the theory we know that the value of the CM factor, which governs the overall sign of the $\vec{F}_{DEP}$, determines if a particle is either attracted towards an electrode (pDEP) or is repelled (nDEP). For particles of similar size in solutions of similar ionic strength (190 nm in diameter polystyrene spheres in DI water), it has been reported that the frequency at which $\vec{F}_{DEP}$ switches from being repulsive to attractive is 4 MHz [22] (**Figure 3.6**). The value of this frequency, also know as the transition frequency, is consistent with our results: pDEP was observed for frequencies within 100 kHz < f < 2 MHz while nDEP was observed above 4 MHz (**Figure 3.11 a**).

Notably, the trapping process was fully reversible, hence in the absence of an electric field, when $\vec{F}_{DEP} = 0$, particles were immediately released from the tip. Interestingly, the time required to trap the first bead varied within the pDEP range. For instance, at f = 750 kHz and f = 1 Mhz with 10 V_{pp} applied (the frequencies at which the fluorescence intensity response was measured to be highest), the first bead was trapped within less than 34.8 ms (the minimum readout time of the emCCD). From the recordings it was observed that a fluorescence spot localized at the tip of the nanopipette was recorded in the first frame immediately after DEP activation.

To further characterize the nanotweezers, experiments were carried out at different voltages with a fixed frequency. Based on the results presented earlier, an AC signal of 750 kHz was chosen (pDEP), with the voltage varying between 5 V_{pp} and 20 V_{pp}. Due to the accumulation of beads in a volume around the tip, fluorescence intensity was averaged over an area of 11x11 pixels which corresponded to 2.93 x 2.93 μm surrounding the apex of the nanotweezers.

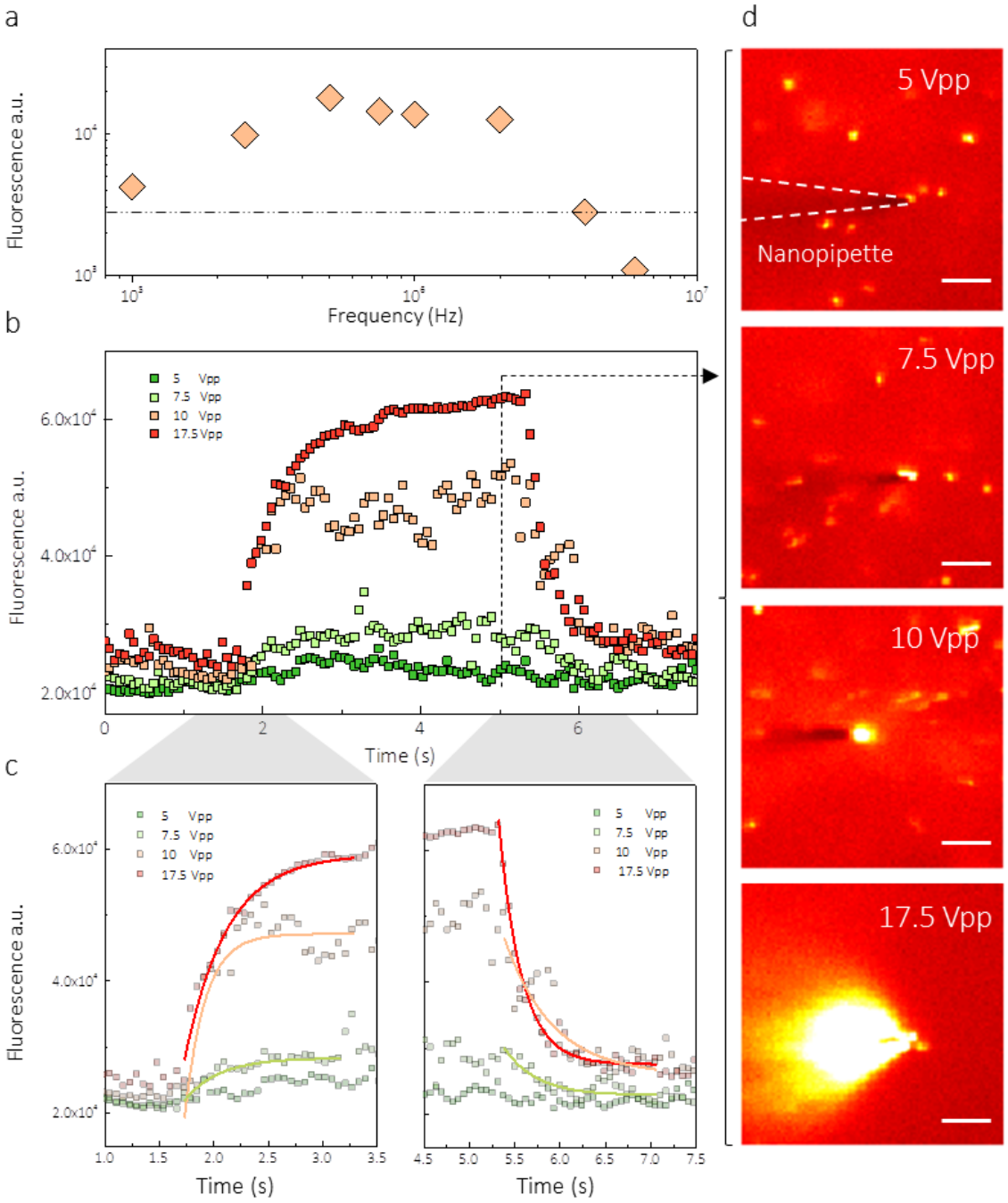

Fig. 3.11 Voltage and frequency dependence of 100 nm polystyrene beads. (a) Showing the frequency response of polystyrene beads when a fixed voltage (10 V_{pp}) was applied at the nanotweezers electrodes. The fluorescence intensity was calculated averaging over an area of 11x11 pixels around the tip 3 s after DEP was activated. This area corresponded to 2.93 x 2.93 μm. (b) Showing the voltage response of 100 nm beads at a fixed frequency (750 MHz). (c) DEP time constants for different applied voltages (17.5 V_{pp},10 V_{pp}, 7.5 V_{pp}). The activation or suppression of DEP results in fluorescence signals exhibiting a mono-exponential type of behaviour with a time constant τ. When DEP was turned on: $\tau = 0.39 \pm 0.03$ s at 17.5 V_{pp}, $\tau = 0.19 \pm 0.04$ s at 10 V_{pp} and $\tau = 0.32 \pm 0.06$ s at 7.5 V_{pp}. When DEP was turned off $\tau = 0.25 \pm 0.02$ s at 17.5 V_{pp}, $\tau = 0.52 \pm 0.17$ s at 10 V_{pp} and $\tau = 0.35 \pm 0.10$ s at 7.5 V_{pp}. (d) Fluorescence images of polystyrene beads for different applied voltages (5, 7.5, 10, 17.5 V_{pp}) at 750 kHz.

Figure 3.11 b illustrates how the magnitude of the electric field influenced the $\vec{F}_{DEP}$. In fact by increasing the voltage applied, thus the overall $\vec{F}_{DEP}$, the number of beads being trapped around the tip considerably increased, as did the fluorescence signal. Voltage is also related to the trapping volume: the stronger the electric field the longer the distance over which particles are subjected to DEP force. It was observed that at 750Khz the distance at which DEP force acting on particles overcame the Brownian motion was $\approx 4\ \mu m$ at $5V_{pp}$ and $\approx 40\mu m$ at $17.5V_{pp}$ respectively. This was quite remarkable since, despite the nanometric size of the electrodes, the nanotweezers were able to exert a force over such a long distance range.

As part of the characterization, the overall system response time was evaluated. In order to do this, we considered the variation of the fluorescence signal over time as a function of DEP status (e.g. active or inactive). As shown in **Figure 3.11 c,d** upon DEP activation the fluorescence signals exhibited a mono-exponential behaviour, with time constant τ (**Figure 3.11 c**) followed by a plateau. The former suggested that the trapping volume reached full capacity and no more beads could be captured and held within it. The meaning of the trapping constant τ was therefore related to how long would it take for this step to happen. For instance, τ was calculated to be 0.39 ± 0.03 s, 0.19 ± 0.04 s, 0.32 ± 0.06 s at 17.5 V_{pp}, 10 V_{pp} and 7.5 V_{pp} respectively. A similar approach was applied when DEP was turned off and particles diffused away from the tip resulting in a fluorescence decay. In this case $\tau = 0.25 \pm 0.02$ s at 17.5 V_{pp}, $\tau = 0.52 \pm 0.17$ s at 10 V_{pp} and $\tau = 0.35 \pm 0.10$ s at 7.5 V_{pp}.

Notably, variable electric fields triggered secondary forces such as electrothermal flow (ETF) . ETF refers to the fluid motion due to spatial variation of electrical properties (permittivity and conductivity) of the medium, induced by temperature gradients caused by Joule heating, which itself arises from the presence of an AC field. It has been demonstrated that, as a result of conductivity and permittivity gradients generated by the temperature gradient, an electrothermal force whose time average is given by [41]:

$$F_{ETF} = \frac{1}{2} Re[(\frac{\nabla\sigma}{\sigma} - \frac{\nabla\varepsilon}{\varepsilon})E_0 \frac{\varepsilon E_0}{1 + (\omega\frac{\varepsilon}{\sigma})^2}] + \frac{1}{2}|E_0|^2\nabla\varepsilon \tag{3.14}$$

where σ and ε are the conductivity and permittivity, E_0 the magnitude of the applied electric field, and ω the angular frequency.

It is important to note that, in the trapping process, ETF force competed against $\vec{F}_{dep}$: the presence of ETF flow facilitated molecules to escape from the trapping volume. In addition, by increasing the voltage, ETF component becomes even more prominent (the theory predicts that the heat generation is proportional to σV^2). Qualitatively, we observed a similar scenario where for instance below 10 V_{pp} (f = 750 kHz), particles were attracted towards the tip of

the nanopipette following radial trajectories, while increasing the voltage to 17.5 V_{pp} we observed particles which followed toroidal-like trajectories depicting vortices. This agreed with previously reported works [42] where microvortices were ascribed to ETF induced by DEP. ETF showed an important positive aspect: it produced an enhancement in the number of particles being actively transported into the trapping volume. In general, particles entered the trapping volume by diffusion only, whereas with ETF, especially at high voltages, there was an increase in the capture volume.

3.4.4 Single molecule manipulation

We have characterized the frequency and voltage response of the nanotweezers showing that they can be used to locally enhance the concentration of particles. However the desired function of the nanontweezers was the manipulation of single molecules, and here we show that it was indeed possible to trap and manipulate one particle at a time.

This was achieved by decreasing the applied voltage (V = 2.5 V_{pp}, f = 750 kHz) which in turn decreased the F_{DEP} to the point that the force was sufficient to trap a single particle. An example of manipulation was demonstrated by using 100 nm fluorescent beads suspended in DI water (100 nm, Fluosphere Yellow-Green, Invitrogen, USA). Bead concentration was further diluted from the previous experiments (10^6 times from stock solution) to avoid overlap of fluorescent signals and facilitate particle tracking. Particle tracking was carried out using Fiji software and previously reported algorithms [43]. The setup employed, in addition to the nanopipette approach adopted ($\approx 40\ \mu l$ solution spotted onto a glass coverslip), was exactly the same as the one mentioned in the previous characterisation experiments.

Figure 3.12 a illustrates the steps involved in trapping and manipulating a single particle: (i) Initially, DEP was inactive, and as expected particle dynamics were governed by Brownian motion. (ii) DEP was turned on and after a specified time, t, a particle was trapped at the tip of the nanotweezer. In contrast with the previous tests, where the first bead was trapped within tens of milliseconds, in this case the time required to trap the first bead was significantly longer: in the representative case shown in **Figure 3.12 b** was 29 s. This was justified by a smaller trapping volume as a result of lower voltage applied as well as a lower concentration. The probability of a particle diffusing into the trapping volume at any given time was a function of the particle concentration (iii) By utilising the micromanipulator, the nanotweezers were moved within the camera's field of view and the bead was observed to remain at the tip, as illustrated in **Figure 3.12 c**. (iv) Finally, when DEP was turned off the particle diffused away indicating that tip-bead interaction was purely based on DEP and not on other non-specific surface-bead interactions. This was a clear advantage over other techniques used to control single particles, for instance AFM, where non-specific interaction, especially

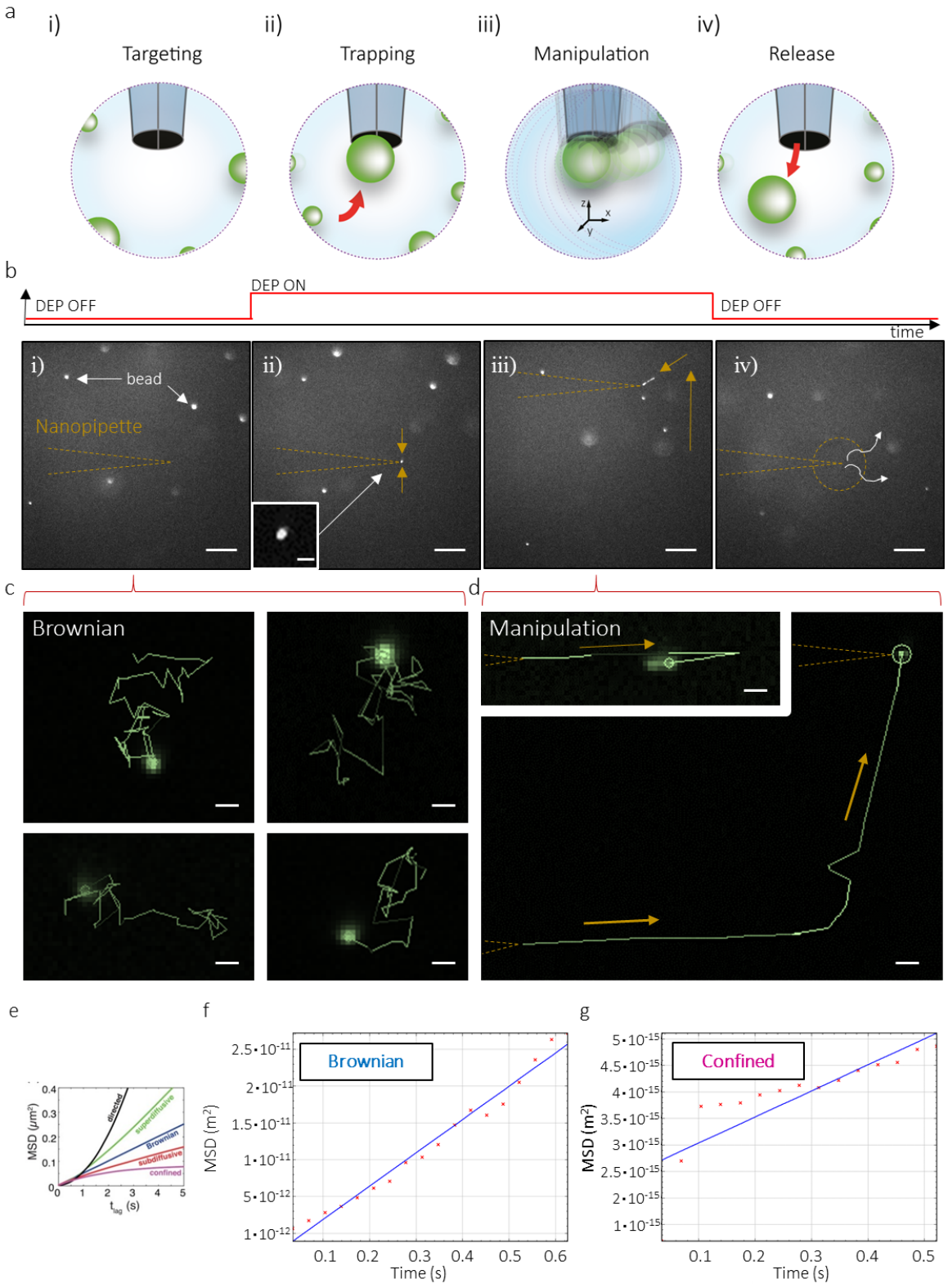

Fig. 3.12 Trapping and manovreuing a single 100 nm bead. (a) Schematics describing the main steps involved during manipulation of single entities with the nanotweezer. i) Target a specific particle that floating in solution and move the nanotweezer in close proximity by using the micromanipulator or alternatively wait for a particle to diffuse close-by; ii) Trap the particle by turning on the DEP (frequency and voltage applied depend on the particle characteristics); iii) manipulation: with the DEP still on, one can use the micromanipulator to move the pipette around and the particle will follow; iv) Release: by turning off the DEP, the trapped particle is released in solution and it quickly diffuse away. (b) Showing the manipulation of a single 100 nm fluorescence bead immersed in a solution of 1 mM KCl. The trapping was performed by applying a low voltage (V = 2.5 V_{pp} at f = 750 kHz). (c)-(g) Showing the trajectories and MSD of particles free to diffuse in solution subjected to Brownian motion and particles being manipulated with the nanotweezer. (e) Classification of particle tracks in different diffusion conditions. In case of Brownian motion the MSD grows linearly with the lag-time whereas when the particle is confined, as in the case of particles trapped at the tip of nanopiette, the diffusion process displays a non-linear relationship to time. Therefore unlike Brownian diffusion, the MSD tends to plateau over the time [ref]. Scale bars: (b) 10 μm , inset 1 μm, (c), (d) 5 μm.

with biomolecules presents an issue. In addition, nanotweezers can operate over the spatial range of the micromanipulator, measured cm, while still conserving a high resolution (40 nm here, according to the manufacturer's specifications). Further precision could be gained if necessary by mounting on a piezo-stage similar to those used in current SICM or SECCM setups [44].

A dedicated plug-in for Fiji software called MOSAIC was used to perform particle tracking analysis and subsequently extract information such as the mean square displacement (MSD). The MSD analysis is among the most used approaches in single-particle tracking and it describes the average extent of space explored by a particle as a function of the time-lag Δt. In the case of a particle having 2 degrees of freedom the MSD is defined as:

$$\langle \Delta r^2 \rangle = 4D\Delta t \tag{3.15}$$

where D is diffusion coefficient.

Evaluating the MSD allowed us to evaluate the beads' diffusion coefficient value which can be related to the regimes in which the particles are operating. In fact the plots of the MSD as a function of the time lag for a single particle trajectory in 2D subjected to Brownian motion show a linear behaviour. Anomalous diffusion, which is classified into sub or superdiffusion, displays power-law behaviour with the value of the exponent scaling accordingly. Directed motion, corresponding to the superimposition of Brownian and ballistic motion such as fluid flow, is described by a quadratic scaling. Confined motion shows a characteristic plateau whose value is proportional to the confinement area. [45].

The diffusion coefficient extracted from 203 trajectories of beads floating in solution according to equation 3.15 was $7.72 * 10^{-11} \pm 6.00 * 10^{-10} m^2/s$. This value was consistent with the maximum theoretical value which is $4.4 * 10^{-12} m^2/s$. The former was calculated according to the the Einstein-Stokes equation which can be used for isotropic, non-hindered diffusion of a spherical particle as in the case presented here.

$$D = \frac{k_b T}{3\pi\mu d} \tag{3.16}$$

where k_B is the Boltzmann's constant, T is the temperature, μ is the dynamic viscosity and d is the diameter of the particle.

The particle captured via DEP at the tip of nanotweezer remained highly confined over time: Δx = 0.77 pixels $\approx$ 204 nm, Δy = 0.94 pixels $\approx$ 250 nm which was determined by Gaussian fittings over the bead location (it is important to note that these numbers, as well as all the recordings performed in this work, are subjected to the well known diffraction limit which strongly limit the optical resolution!). Nonetheless, the calculated MSD, rather than

increasing linearly with the time lag, tended to plateau, and the diffusion coefficient was almost 3 orders of magnitude lower ($10^{-15} m^2/s$) than for free beads. This further confirmed that the trapped particle was strongly spatially confined over time.

3.4.5 Manipulating DNA

Nanotweezers were successfully employed to manipulate DNA molecules. Experiments were initially conducted using 10 kbp DNA molecules suspended in 1 mM KCl solution buffered with 10 mM Tris and 1 mM EDTA at pH 8.0. DNA molecules were stained with YOYO-1 intercalator dye and the nanotweezers were vertically approached towards the glass coverslip where 20- 40 μl of solution was spotted (**Figure 3.13 a**).

Qualitatively, the nanotweezers operated in a similar manner to that described for manipulating beads: when DEP was not active, DNA molecules were only subjected to Brownian motion, whereas when the DEP was turned on, a fluorescence spot was localized at the tip of the nanopipette. As the electric field was kept on the fluorescence region around the tip would grow further in size owing to an accumulation of DNA molecules at the tip. As for the beads, DNA behaviour upon DEP was frequency dependent. To study this phenomenon, frequencies varying between 100 kHz and 6 MHz at 20 V_{pp} were applied to the carbon electrodes. As shown in the **Figure 3.13 b**, the highest fluorescence intensity, and therefore the strongest $\vec{F}_{DEP}$, was recorded at 1.5 MHz, however between 750 kHz and 2 MHz $\vec{F}_{DEP}$ was still considerable. At frequencies above 2 MHz, the fluorescence intensity in response to applied DEP dropped significantly. For instance, at 4 and 5 MHz, the analysis revealed that there was not significant trapping of DNA molecules around the tip. These results were in good agreement with previously reported works which employed the same DNA fragment in similar low conductivity solutions [24]: maximum DEP was localized at f = 1 MHz whereas at high frequencies they also recorded a net decrease in trapping efficiency. The minimum voltage at which trapping was observed was 5 V_{pp}. As illustrated in **Figure 3.13 c,d**, increasing the voltage applied thus, the DEP force, resulted in more DNA molecules being captured and the profile of the tip showed a brighter and larger spot (f = 2 MHz, $0 < V_{pp} < 10$, DNA concentration: 2 pM).

To further investigate the manipulation of DNA with nanotweezers, a series of consecutive trapping and release experiments were carried out using 100 pM 10 kbp DNA in 1 mM KCl. A time lapse of one example with the correspondent fluorescent profile is shown in **Figure 3.13 e-f** where 20 V_{pp} and f = 1 MHz was applied to the electrodes and DNA was localized around the tip. When the bias was switched off, molecules were almost instantaneously released and the fluorescence returned to the baseline level within $\sim$ 700 ms.

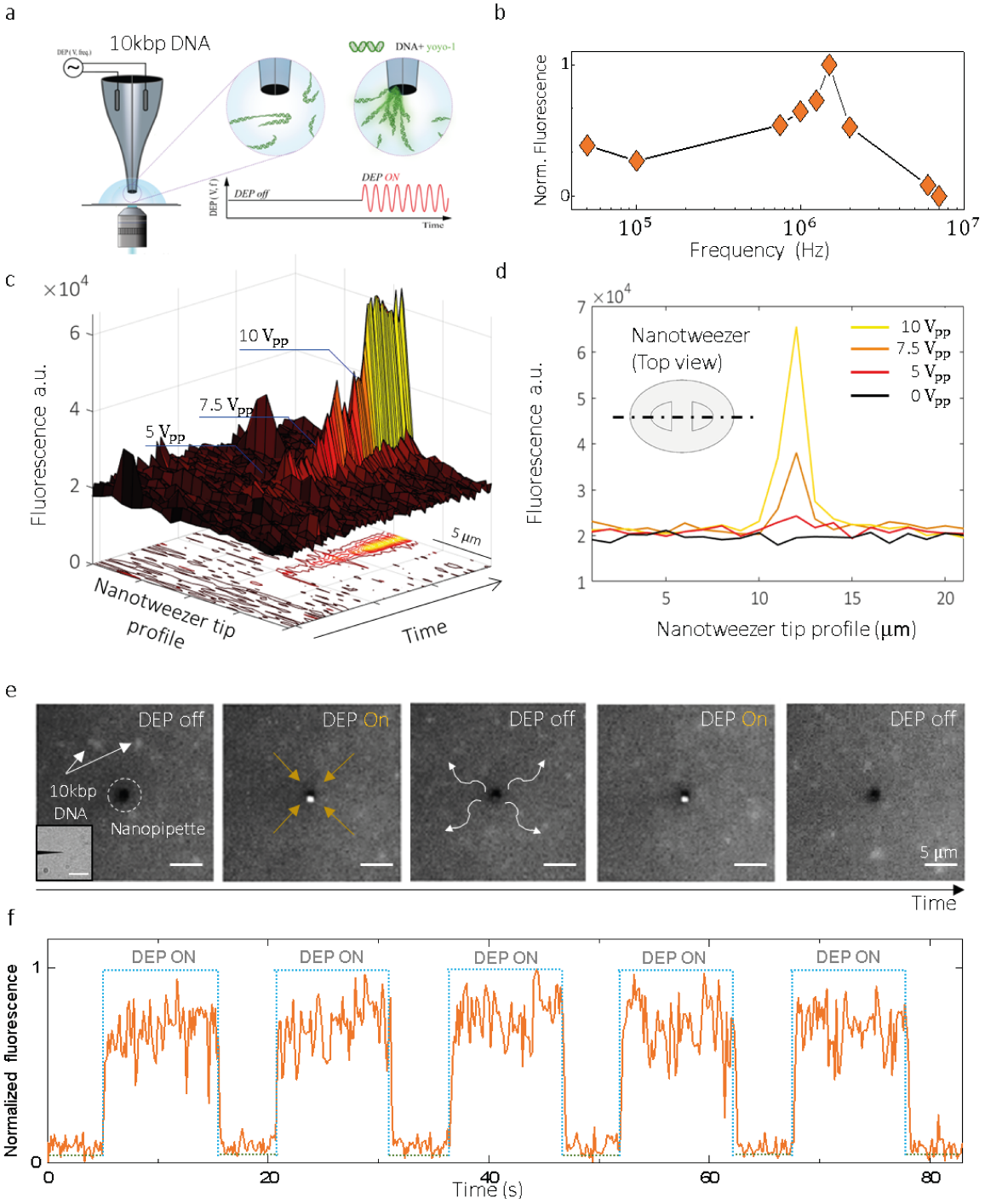

Fig. 3.13 Trapping 10 kbp DNA with the nanotweezer. (a) Showing the nanotweezers schematic employed to trap 10 kbp DNA molecules labelled with YOYO-1. (b) Normalized fluorescent intensity recorded at the tip of the nanotweezer as a function of the frequency applied, at a fixed voltage applied of 20 V_{pp} (DNA concentration was 100 pM and the solution employed was 1 mM KCl.). The peak frequency was observed at 1.5 MHz. (c)(d) Voltage dependence. Showing the evolution of the fluorescence intensity profile over the time when 0 V_{pp}, 5 V_{pp}, 7.5 V_{pp} and 10 V_{pp} at f = 2 MHz was applied to the nanotweezer. The solution consisted of 2 pM 10 kbp DNA in 1 mM KCl. (e) Showing the fluorescence intensity over the time and the fluorescence image of the nanotweezers captured when a series of consecutive trapping and release experiments was performed at 1 MHz, 20 V_{pp} voltage applied using a solution of 100 pM 10 kbp DNA in 1 mM KCl. When DEP was turned on, DNA was immediately trapped at the tip of the nanotweezers and subsequently released when DEP was switched off. The inset shows the bright field image of the nanopipette. (f) Fluorescence intensity-time plot of a typical trapping experiment where, by turning DEP on and off, 10 kbp DNA molecules were trapped and released. (Scale bars: (e) 5 μm and inset 50 μm.

Non-specific binding of DNA (> 10 pM) to the tip was not observed, except when high concentrations of DNA were tested and DEP was on for a prolonged amount of time. However, this could have been induced by DNA molecules being wrapped around the tip rather then sticking to the surface. 10 kbp DNA is about 3 μm long and its radius of gyration 230 nm. Normally, quick bursts of high frequencies (5-10 MHz) at high voltage (20 V_{pp}) were sufficient to successfully remove any loosely bound molecule. Since this was an uncommon problem we did not thoroughly investigate non-specific binding.

Interestingly we were able to manipulate one DNA molecule at the time. The key point was to reduce the DEP force so that it was sufficient to capture a single molecule (**Figure 3.14 a,b**). In principle this could be achieved by either lowering the bias or by operating at a frequency which is slightly off from the response peak ($\sim$ 1 MHz for 10 kbp). The second scenario was chosen: f = 2 MHz, 10 V_{pp} with a solution of 2 pM 10 kbp DNA in 1 mM KCl. As illustrated in **Figure 3.14 c, d**, these conditions were sufficient to trap one DNA molecule within $\approx$200 ms after it entered the DEP capture volume. The molecule was subsequently released after DEP was turned off. Understanding the polarizability is conditio sine qua non to predict how DNA molecules can be manipulated using dielectrophoresis. Although the general DEP theoretical framework has been described in *section 3.3*, some considerations of DNA polarization are fundamental for a better understanding of the experimental results.

DNA polarizability depends, as for the beads, on parameters such as the permittivity and conductivity of the solution in which DNA is immersed in, the frequency of the applied electric field and temperature. The main difference lies in the model used to calculate polarizability. In fact, the interfacial polarization model (Maxwell-Wagner), which is based on the CM factor, and which has been used to describe the polarizability of dielectric particles, is not appropriate to describe the response of DNA molecules. For instance the Maxwell-Wagner model still cannot fully explain the frequency dependence of the polarizability [46]. In general counterion fluctuation (CIF) polarization model is adopted. Specifically CIF takes into account the fact that DNA charges (deriving from its phosphate backbone) are fixed and the polarizability is mainly governed by counterion redistribution around the DNA. An electric double layer, especially at low concentrations (1mM KCl) as in our case, have been demonstrated to dominate.

According to the Mandel-Manning-Oosawa model, which is one of the most adopted CIF models, each DNA molecule in solution is assumed to be formed by N segments of length L_S. The DNA is surrounded by counterions which are free to move within each segment and also between different segments [47] in response to an external electric field. The generalized

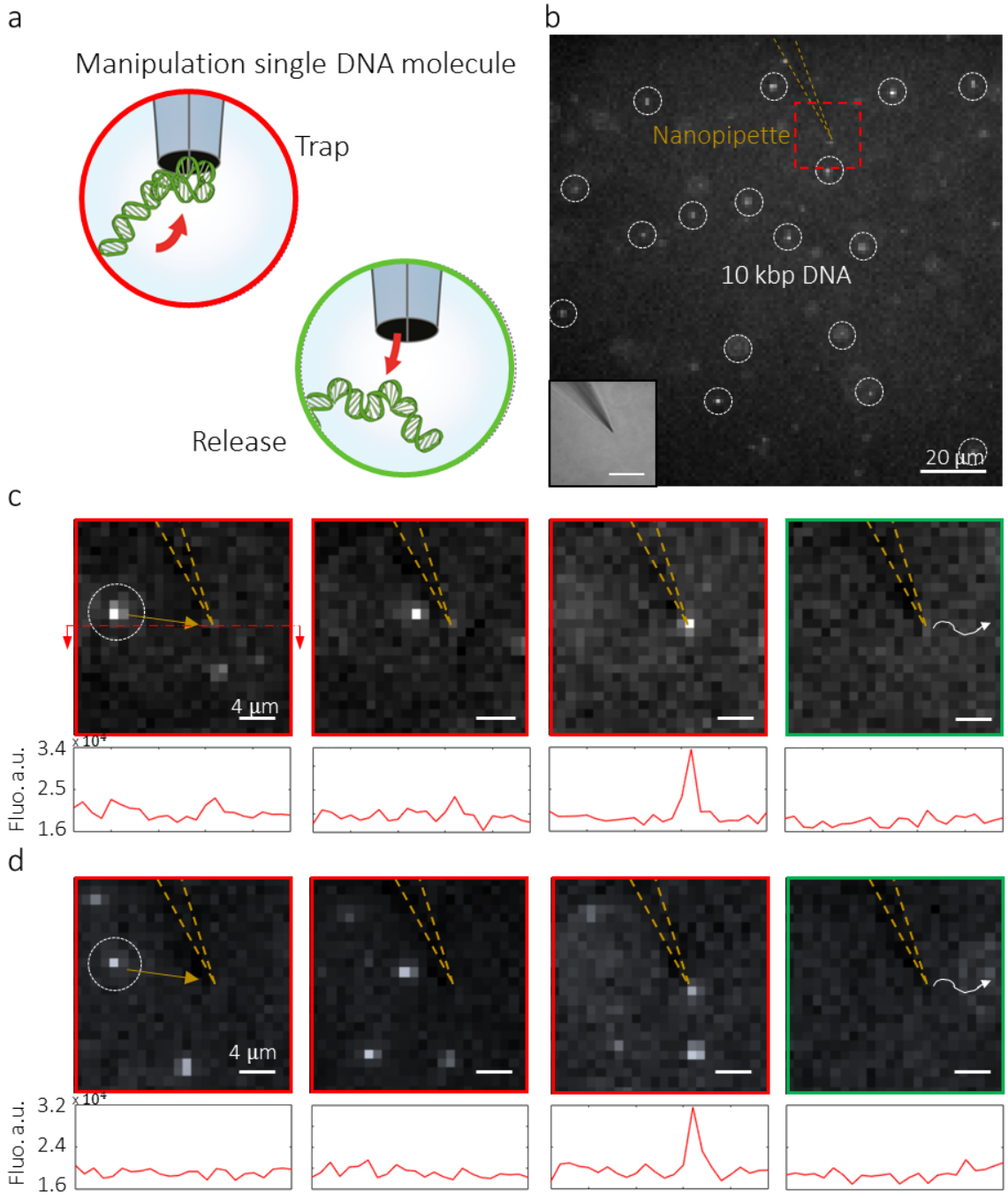

Fig. 3.14 10 kbp DNA single molecule manipulation. (a) Showing the colour-coded cartoon of a single DNA molecule being DEP-trapped (red) with the nanotweezer and subsequently released (green). (b) Fluorescence image of 2 pM 10 kbp molecules (highlighted with dashed circles) in 1 mM KCl solution. (inset: nanotweezer bright field image).(c)(d) Fluorescence images showing single 10 kbp DNA molecule trapping (f = 2 MHz, 10 V_{pp}). The orange dashed line represents the nanotweezer position. Scale bars: (b) 20 μm (inset: 20 μm), (c),(d) 4 μm.

expression for the polarizability per subunit length L_S is given by [48]:

$$\alpha_s = \frac{z^2 q^2 L_S^2 n_{cc} A}{12 k_B T} \tag{3.17}$$

where z is the ion valency, q is electronic charge, $n_c c$ is the number of condensed counterions, which represents the first layer of counterions located in close proximity to the DNA, A is a dimensionless factor that takes into account the stability of the ionic phase and also the electrostatic repulsion between the phosphate backbone charges, and $k_B T$ is the Boltzmann temperature. The polarization for the entire DNA molecule can be obtained by multiplying α_s by the number of segments L_s that the molecule is formed of. Thus, $\alpha_{tot} = \alpha_s \frac{L_{DNA}}{L_s}$. Finally the DEP force acting on DNA can be expressed as in Equation 3.7 as: $\vec{F}_{DEP} = \alpha_{tot} \vec{\nabla} |\vec{E}|^2$. It is worthy noting that even counterion fluctuation models do not provide a full picture of the mechanisms involved in DNA polarization or the dependence of the dielectrophoretic response on the DNA length and structure. DEP and biomolecules remain an active area of research [46].

The case of $\lambda - DNA$

After having investigated DNA with 10 kbp, attention was shifted to longer strands. Experiments were conducted with 48.5 kbp λ DNA. The KCl ionic strength was kept at 1 mM, buffered in TE at pH 8.0 and DNA concentration was set to 10 pM. Similar to the method applied to 10 kbp, λ DNA was stained with YOYO-1 intercalator dye (dye to base ratio of 1:5).

In contrast with what we have observed for 10 kbp, the experimental results showed that the manipulation of λ DNA was more efficient at higher frequencies. As shown in **Figure 3.15 a,b**, the maximum fluorescence intensity was recorded between 2 and 4 Mhz for a 10 V_{pp} applied voltage. At lower frequencies, 100 kHz < f < 2 MHz, DNA was still subjected to a trapping force, however its intensity was not enough to hold the molecule at the tip. At f > 2 MHz DNA experienced nDEP, hence molecules were actively repelled from the tip's surroundings. There is no general consensus for the transition from positive to negative DEP for λ-DNA: reported values varied from 60 kHz [49] to 880 kHz [50]. Our result tends to be aligned towards the former. It is important to note that a rigorous comparison was not possible due to the different buffer conductivity (16 mS/m here, while in [50] this was 2 mS/m) which was suggested to affect the crossover frequency [51]. In addition, electro-osmotic flow, which is also dependent on the DEP system architectures, may be partly responsible for the discrepancies in reported crossover frequencies [50]. Despite the size difference (λ DNA was significantly larger than the previously tested 10 kbp DNA,

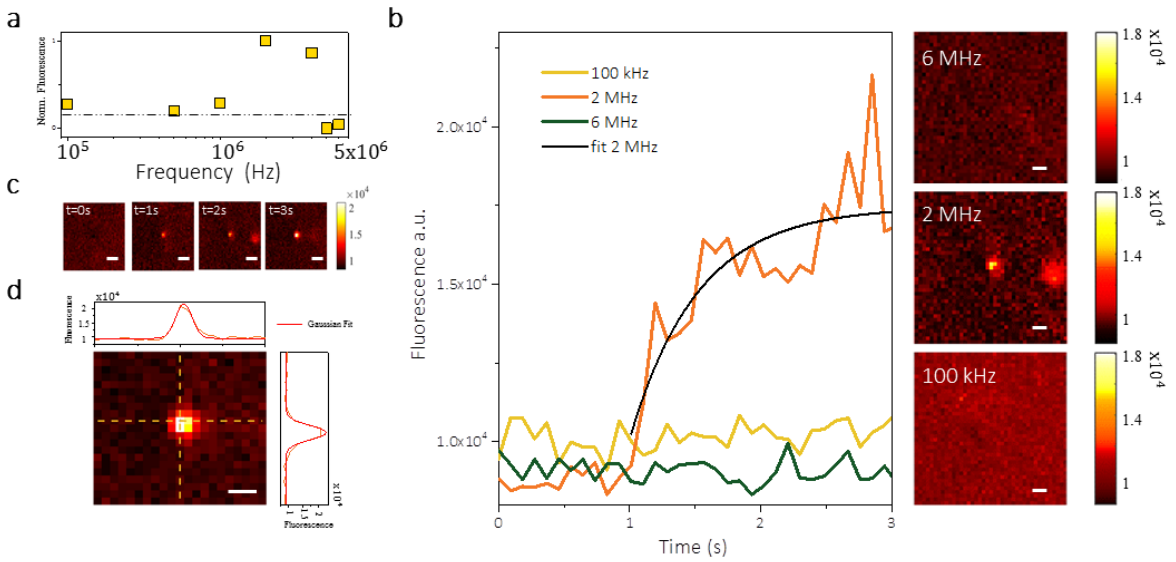

Fig. 3.15 Trapping λ-DNA with the nanotweezer. Nanotweezers were used to trap 48.5 kbp λ DNA dispersed in 1 mM KCl solution (DNA concentration = 10 pM). (a) shows the fluorescence intensity variation at the tip of the nanotweezers as a result of AC electric field with different frequencies, and a fixed magnitude (10 V_{pp}) applied between the electrodes. The dashed line represents baseline fluorescence intensity, demonstrating that no variation was recorded when an electric field was applied. (b) Evolution of the fluorescence intensity profile over time for different frequencies at 10 V_{pp}. (c) Fluorescence images showing how the fluorescence spot at the nanotweezer's tip broadened when 10 V_{pp} at 2 MHz was applied between the electrodes. (d) Gaussian profile of the fluorescence spot shown in D for $t = 3s$. The calculated FWHM was 587 ± 33 nm along the x-axis and 611±26 nm along the y-axis. Scale bars: (b), (d) 1 μm, (c) 2 μm

and the radius of gyration of λ DNA is ∼ 0.73 μm [52]), the trapping response time was fast and comparable with 10 kbp; for instance at 2 MHz $\tau = 0.52 \pm 0.16$ s (Figure 3.15 B). As shown in the time dependent analysis (**Figure 3.15 c**) where DEP was set at 2 MHz and $10V_{pp}$, the profile of the fluorescence spot at the tip of the nanotweezer expanded over time due to the increasing number of molecules being trapped. The spot showed a gaussian shape with a full width half maximum of 587 ± 33 nm along the x-axis and 611 ± 26 nm along y-axis. (**Figure 3.15 d**).

As demonstrated for polystyrene beads and 10 kbp DNA, even for λ-DNA nanotweezers were successful in manipulating one molecule at the time (in this case the sample concentration was as low as 100 fM). As shown in **Figure 3.16 a**, a λ-DNA entering the capture volume was captured within 0.5 s and released after about 6 s. Notably, during this time, as suggested by the fluorescent intensity profile, no other molecule was trapped and the slight fluorescent decay was ascribed to photobleaching **Figure 3.16 b**. In addition, the molecule remained clamped to the tip even when the nanotweezer was moved in space with the micromanipulator.

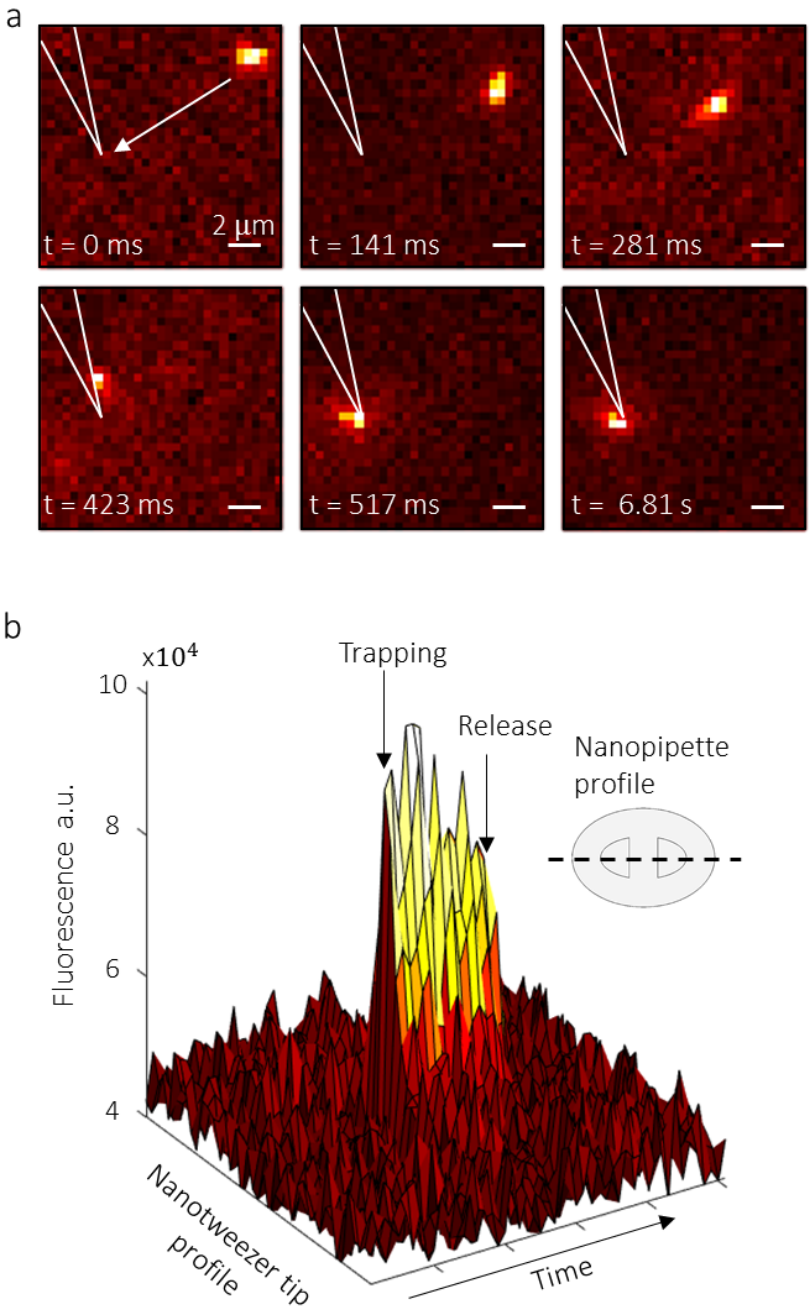

Fig. 3.16 Single λ-DNA molecule manipulation. (a) Time lapse of fluorescence images showing a λ-DNA molecule being captured at the tip of the nanotweezer (λ-DNA concentration of 100 fM in 1 mM KCl. DEP trapping condition: f = 6 MHz, 15 V_{pp}). (b) Evolution of the fluorescence tip profile over the time. The fluorescence peak represent the DNA molecule held at the tip (in this case approximately 7 s although it is an arbitrary value) before being released by turning off the voltage applied. Notably the fluorescence over slightly decays over the time as a result of continuous photobleaching. Scale bars: (a) 4 μm.

Trapping small molecules: short ssDNA and proteins

The $\vec{F}_{DEP}$ acting on a particle depends on its size ($\sim R^3$, where R is the radius of the particle, Equation 3.10) and on the gradient of the square of the magnitude of the electric field. Therefore for small biomolecules such as short oligonucleotides (e.g. mRNA, or DNA) and proteins with low molecular weight (10-100 kDa), manipulation becomes a challenging task due to $\vec{F}_{DEP}$ being weak. In addition, thermal forces which are inversely proportional to the particle dimension ($F_{th} \sim 1/R$), tends to dominate within this regime. This is also the reason why the vast majority of existing DEP architectures are focused on long DNA fragments or relatively large proteins (>50 kDa) [53], whereas in our case, due to the small gap between the carbon electrodes of the nanotweezers, the strong electric field allowed us to trap proteins as small as few nanometres.

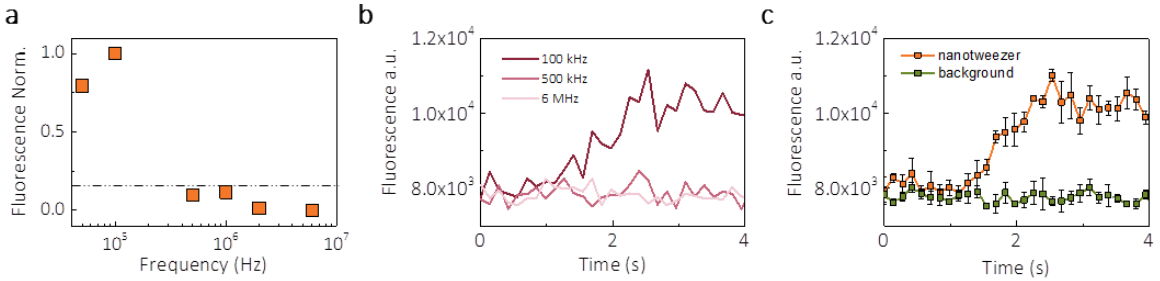

Fig. 3.17 Trapping short ssDNA-Atto488. Nanotweezers were used to trap 22-mer ssDNA labelled with Atto 488 and dispersed in 1 mM KCl solution (DNA concentration = 100 pM). (a) shows the fluorescence intensity variation at the tip of the nanotweezers as a result of AC electric field with different frequency at 20 V_{pp}. The dashed line represents baseline fluorescence intensity, therefore no variation is recorded when an electric field is applied. (b) Evolution of the fluorescence intensity profile over the time when DEP is applied at f = 100 kHz, 500 kHz and 6 MHz frequencies at 20 V_{pp}. (c) Comparison of the background fluorescence signal with the one recorded at the apex of the nanopipette when 100 kHz and 20 V_{pp} where applied. The calculated SNR was 17.6 $\pm$ 1.6.

Experiments were initially carried out using a 27-mer long ssDNA labelled with Atto488 and diluted to 100 pM in 1 mM KCl TE solution at pH 8.0. As shown in **Figure 3.17 a,b**, successful trapping was observed at 100 kHz or lower. In contrast with results observed for λ-DNA and 10 kbp DNA, for this short sequence, there was no detectable increase in fluorescence intensity around the nanotweezers at f > 100 kHz confirming that dielectrophoretic force greatly depends on the length of the DNA molecule [36]. Due to the presence of only a single fluorophore per molecule, the overall fluorescence signal at the tip of nanotweezer was weaker than in the previous experiments however the SNR calculated between the signal at the tip and the background was 17.6 $\pm$ 1.6 (**Figure 3.17** c).

Experiments were confirmed using another short ssDNA molecule: 22 nucleotides long labelled with Cy3 (**Figure 3.18**). It is important to note that DEP trapping of short DNA fragments have previously been investigated. An interesting example is of a glass nanopipette, similar to the one utilized to manufacture the nanotweezers but with only one barrel, employed to trap 40-mer DNA at very low voltage: 0.5-4 V and f = 0.5 Hz [40]. The

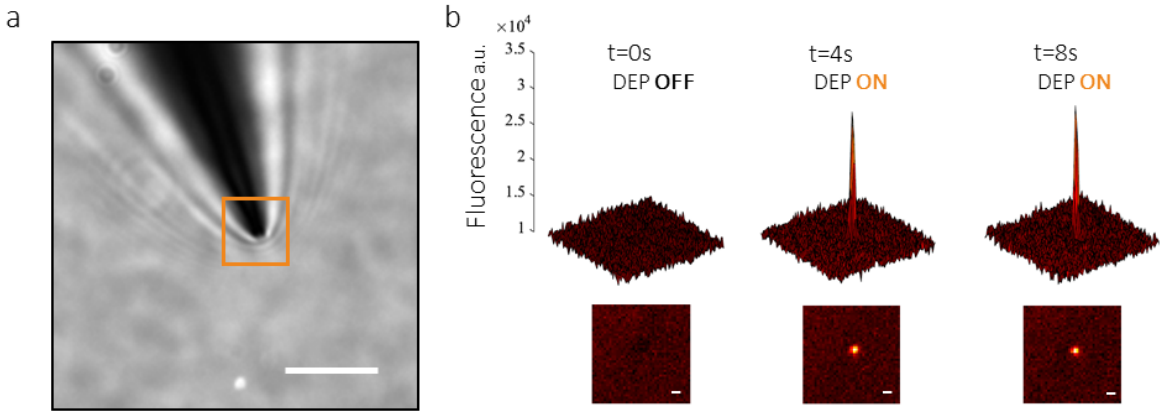

Fig. 3.18 Trapping short ssDNA-Cy3. (a) Bright field image showing nanotweezers dipped in 1 mM KCl buffered in TE containing 100 pM 22-mer DNA labelled with Cy3. (b) Evolution of the fluorescence intensity of the tip at different time points for 20 V_{pp} and f = 100 kHz. Scale bars (a) 10 μm and (b) 1 μm for the 2D images while the 3D plots correspond to an area of 16 x 16 μm

nanopipette was filled with ionic buffer containing the DNA. As a result of a voltage applied, a high field gradient was localized in the proximity of the nanopipette aperture leading to DNA entrapment around that area. This system was elegant, with its only weakness from the viewpoint of a nanotweezer application being that the DNA was concentrated inside and not outside the nanopipette, making any further manipulation more complicated compared to the solution hereby proposed.

Nanotweezers have also demonstrated their capabilities in manipulating proteins. The first protein utilized was Streptavidin labelled with Dylight. Streptavidin could be considered as a relatively large protein with a molecular weight of 52.8 kDa and a diameter of 5 nm. For the experiments, a solution of 100 pM streptavidin diluted in 1 mM KCl, 10 mM TE, pH 8.0, was employed. Importantly, as a result of DEP trapping experiments, it was observed that quite often proteins exhibited a partial irreversible non-specific binding to the tip of the nanopipette resulting in a residual fluorescence at the tip even after DEP was turned off. Despite this drawback it was still possible to perform experiments and explain the results obtained.

As shown in **Figure 3.19 a** pDEP was observed at 100 kHz with 20 V_{pp} voltage applied whereas at higher frequencies (500 kHz < f < 6 Mhz), similar to what we reported for short oligonucleotides, no fluorescence activity was noted. These findings were consistent with other published works [54] where they report DEP trapping of streptavidin at 10 kHz.

If theoretical models predicting DNA behaviour under the influence of a variable electric field are incomplete, models capable of predicting protein behaviour are even less advanced [55]. The main reason for this is that proteins exhibit complex structures; as an example, consider the charges arising from amino acid chains on a protein; these lead to charged surface patches which will respond differently to an applied electric field.

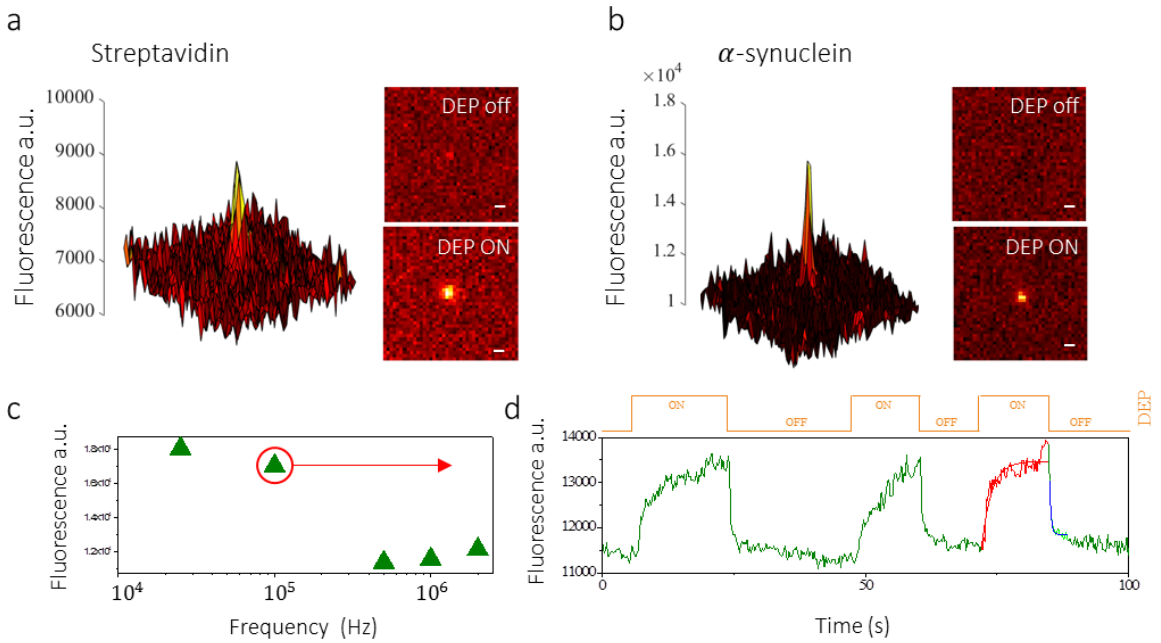

Fig. 3.19 Nanotweezer operating with small proteins. Showing the fluoresence intensity profile when Streptavidin (a) or monomeric *alpha*-synuclein molecules were trapped at the nanotweezers tip. In both cases the solution employed consisted of 1 mM KCl buffered in TE; the concentration was set to 100 pM and 200 pM for Streptavidin and *alpha*-synuclein respectively (DEP parameters: 100 kHz, 20 V_{pp} for both cases) (c) Frequency response of monomeric *alpha*-synuclein at 100 kHz 20 V_{pp} voltage applied. (d) Trapping and release experiments performed with *alpha*-synuclein at 100 kHz and 20 V_{pp} voltage applied. Scale bars: 1μm

To further extend the capabilities of nanotweezers, a smaller protein was investigated: $\alpha - synuclein$ (the protein and its labelling were kindly performed in Dr.Gabriele Kamischi Schierle's lab, Cambridge University). $\alpha - synuclein$ is a highly biologically relevant protein which is thought to be related to neurodegenerative processes leading to Parkinson's disease and dementia with Lewy bodies [56]. However our attention towards this protein was given by its extremely small dimension ($\approx 14\ kDa$) along with the lack of fixed structures, which makes its manipulation and even its detection with current tools, particularly challenging.

Under the same ionic solution, we recorded pDEP at 50 kHz and 100 kHz (**Figure 3.19 b**) while at 500 kHz, 1 MHz, and 2 MHz, no signal was detected (**Figure 3.19** c). As for Streptavidin, the applied voltage was 20 V_{pp}. Lower voltages did not generate sufficient force to trap this specific protein. A series of trap and release experiments were carried out at 100 kHz, 20 V_{pp}. The response time during the trapping step calculated to be $\tau = 1.31$ s while for the release step, a much faster time constant was observed $\tau = 0.29$ s (**Figure 3.19 d**).

3.4.6 DNA trapping, extraction and analysis

In the previous paragraphs we demonstrated that the nanotweezers presented here can easily manipulate nucleic acids and proteins of various dimensions. Is it possible to transfer the

trapped material out of the solution and, more importantly, are these trapped biomolecules still viable and functional for analysis and study?

To answer these fundamental questions a series of experiments was conducted using $\lambda - DNA$ as the target molecule: nanotweezers were utilized to trap DNA molecules which were then extracted from the solution and amplified via quantitative real-time PCR (qPCR). For the former, SYBR green I dye chemistry was used: during the PCR, DNA polymerase amplified the target sequence which generates the PCR products. SYBR green I is an intercalating dye (λ_{Ex} = 497 nm, λ_{Em} = 520 nm) which binds to double-stranded DNA. As the PCR progresses, more DNA products are created, therefore more Green I dyes bind to DNA resulting in an increase fluorescence intensity which is proportionate to the amount of PCR product produced. The reason why $\lambda - DNA$ was initially chosen to perform these experiments was extremely simple: in contrast with other commercially available DNA samples whose sequences were not publicly available due to confidentiality (e.g. 10 kbp sample from NEB, USA), the $\lambda - DNA$ sequence was well known. Forward and reverse primers consisted of 20 nucleotides, with a melting temperature of 59.97°C for both of them, with no Gs or Cs repeated. High specificity was ensured by using the open source software Blast: these primer pairs were unique and therefore could bind to other places in the $\lambda - DNA$ except that which they were designed for.

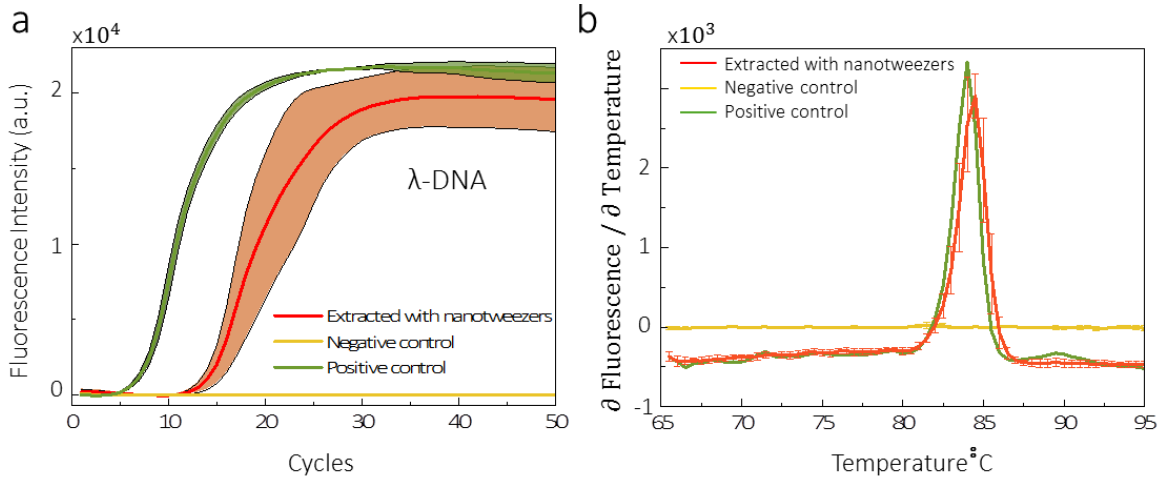

Fig. 3.20 PCR amplification of $\lambda - DNA$ trapped and extracted via nanotweezer. (a) Fluorescence intensity, due to DNA molecules accumulating at the tip of a nanopipette as a result of pDEP (4 Mhz, 10 V_{pp}). (a) qPCR targeting $\lambda - DNA$. Nanotweezer indicated λ-DNA which was obtained via nanotweezer trapping and then transferred in a PCR tube containing PCR master mix along with forward and reverse primers. Positive control indicates 5 ng of λ-DNA pipetted into the PCR tube along with the PCR master mix and forward and reverse primers. In the negative control, λ-DNA was substituted with water. (b) Comparison between qPCR amplification curves generated from DNA samples pre-stained with or without YOYO-1. Samples were extracted using the nanotweezer method and later transferred into PCR tubes.

10 pM λ-DNA (without YOYO-1 although experiments were successful also using DNA stained with YOYO-1) was prepared in a solution containing 1 mM KCl buffered at pH 8.0.

Based on the previous experiments pDEP was applied using 10 V_{pp} and the fluorescence intensity, due to DNA molecules accumulating at the tip of the nanopipette, was monitored over time. In this case the DEP was applied for a longer time to ensure the saturation of the trapping volume with DNA molecules. It was observed that this happened within few seconds (< 10 s).

The extraction process was straightforward: while DEP was still active, the nanotweezers, and therefore the trapped molecules at its tip, were lifted up and out of the solution using the micromanipulator. The nanotweezers were then disconnected from the function generator and unlocked from the micromanipulator holder so that they could be handled manually for the next step. The λ-DNA located at the tip was transferred into the qPCR tube by inserting the nanotweezer into the PCR-tube containing 5 μl of 10 mM Tris-HCl (pH 8.5) and breaking the very end of the nanotweezer inside the solution. To this 10 μL of qPCR master mix, 1 μL each of the forward and reverse primers were added and the total the volume was made up to 20 μL with 10 mM Tris-HCl (pH 8.5).

Figure 3.20 a shows the real time amplification plot recorded using the qPCR machine. The protocol used consisted of an initial denaturation cycle of 95 °C applied for 5 min and 50 PCR cycles performed (denaturation at 95 °C for 15 s, annealing/extension at 60 °C for 60 s).

The real time amplification plot in **Figure 3.20 a** demonstrated that nanotweezers were able to extract biomolecules and that those biomolecules were still viable, as demonstrated by their successful amplification (it is important to mention that amplification does not necessarily ensure DNA viability; only by sequencing the amplified PCR material one can understand if the amplification is the result of a false positive or not). Notably the average quantification cycle (C_q) of 9 distinct extracted samples measured 14, however it varied considerably from C_q = 11 to C_q = 21. These values reflected the different DNA starting concentration which in turn was dependent on the different amounts of DNA being trapped and extracted by the nanotweezers. Positive controls consisted of a qPCR with 5 ng of λ-DNA (manually pipetted in) along with the PCR master mix and forward/reverse primers. In this case, due to the high concentration, C_q = 5. The negative control, which contained DI water instead of a DNA sample, did not show any amplification as expected. Melting peak analysis was performed by increasing the temperature at a rate of 0.5 °C/s from 60 to 90 °C, to confirm the validity of PCR. As shown in **Figure 3.20 b** the melting temperature for the amplified product was measured to be 84.06 $\pm$ 0.11 °C. This value was in agreement with that predicted, which was calculated to be $\sim$ 85 °C.

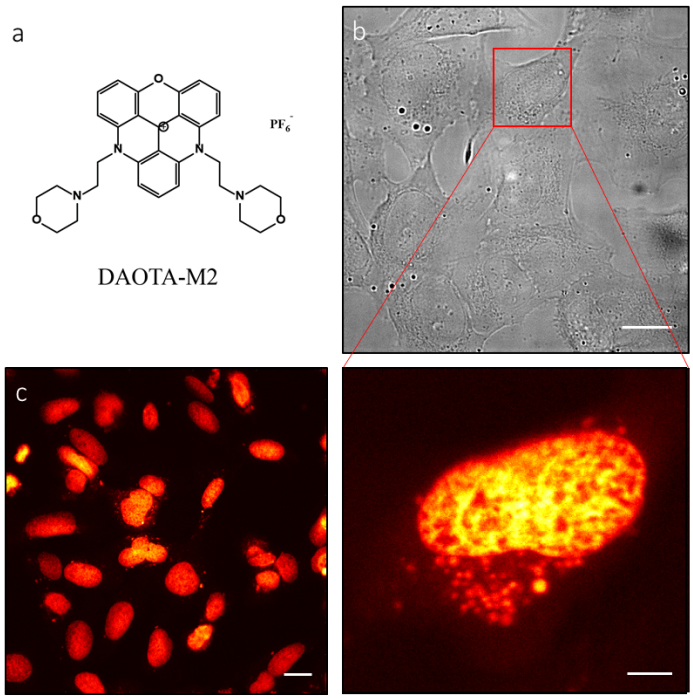

Fig. 3.21 U2OS cells characterization. (a) DAOTA-M2 fluorescence dye structure. DAOTA-M2. (b) Bright field image of U2OS cells treated with DAOTA-M2. (c) Representative confocal image of U2OS cell acquired with a custom-built fluorescence confocal microscope λ_{Ex} = 488 nm. Scale bars: (b) bright field 20 μm, fluorescence 5 μm (c) 20 μm.

3.5 Single cell nanobiopsy: a proof-of-concept study

Here we show that the newly develop nanotweezers were capable of manipulating and eventually extracting molecules from a cell. We showed that it was possible to manipulate the main cellular building blocks, nucleic acids and proteins, down to a few nanometres in size, and therefore verified whether nanotweezers could be used to handle the same molecule but within a more complex environment such as the cellular one. In contrast with conventional technologies such as cell fixation or cell lysis where the genetic profile of the cell at a particular time point is obtained at the price of cell viability, herein we demonstrate that it is possible to extract content from living cells without perturbing their viability.

To perform sub-cellular nanobiopsy, bone osteosarcoma U2OS cells were utilized. Cells were grown according to the protocol described in the experimental section. Cells were first seeded on an 8 well chambered coverglass (ca. 2 x 10^4 cells, 300 μl, 0.8 cm^2) and then treated with a fluorescence dye. The reason for treating the cell with a dye was to be able to track fluorescence changes inside the cell when performing a nanobiopsy. The dye selected for use was DAOTA-M2, a triangulenium derivative (**Figure 3.21 a**). From previous work [18] we knew that DAOTA-M2 targeted DNA and RNA molecules, prevalent in the nucleus of U2OS cells. **Figure 3.21 b,c** show bright field and fluorescence images obtained via a

custom scanning confocal microscope, of U2OS cell's stained with DAOTA-M2 (a pulsed diode laser at λ_{Ex} = 488 nm was used).

The experimental setup was identical to the one utilized and described for the bulk of the previous experiments except for the glass coverslip (used to pipette the solution containing the beads, DNA, protein etc.) which was replaced with an 8-well cell culture slide. **Figure 3.22** illustrates the main steps followed to perform a sub-cellular nanobiopsy. At the beginning of the procedure the nanotweezers were mounted on the micromanipulator holder, perpendicular to the chambered coverglass with both electrodes connected to the function generator.

- **Approach**. The first step consisted of selecting one of the 8 wells and approaching its surface with the nanotweezers, in close proximity to the cells (**Figure 3.21 a**). This action was performed manually, in bright field, by gently lowering the nanopipette with the micromanipulator along the z-axis. The emCCD was used as visual feedback and, at first, low magnitude objectives, such as 4X and 10X, were employed due to their long working distance. By doing so, the nanotweezers were brought within ~ 50 μm of the surface. At this point, we switched to a 60X water immersion objective with a field of view of ≈ 136 μm x 136 μm and a working distance of approximately 200 μm.

- **Penetration**. The nanotweezers were positioned on top of the selected cell, whose integrity was checked beforehand by looking at its shape and its fluorescence signal. By gently lowering the nanotweezers along the vertical axis the cell membrane was pierced. The distance travelled by the nanotweezers was a function of the distance between the tip and the cell.

  To establish the minimum distance that the nanotweezers had to travel in order to pierce the cell membrane we firstly assumed, based on previous work [57] and confirmed with our bright field images and confocal images (**Figure 3.21**), that the cell volume and diameter were ~ 4000 μm^3 and ~ 20 μm, respectively. Secondly, operating in bright field, we estimated the distance between the bottom of the well and the tip which was localized as a dark spot, as shown in **Figure 3.21 d**. It should be noted that this distance represented only an approximation. In fact, determining the tip position with nanometric precision is not possible because of, among other factors, the diffraction limit. Although simple, our approach was effective and rarely did the nanopipette impact against the surface. Nevertheless, the system could be fully automatized by implementing a feedback mechanism during the approach. This would involve monitoring the current across the carbon electrodes when a small bias is applied; upon cell penetration the current should vary and clearly signal the event.

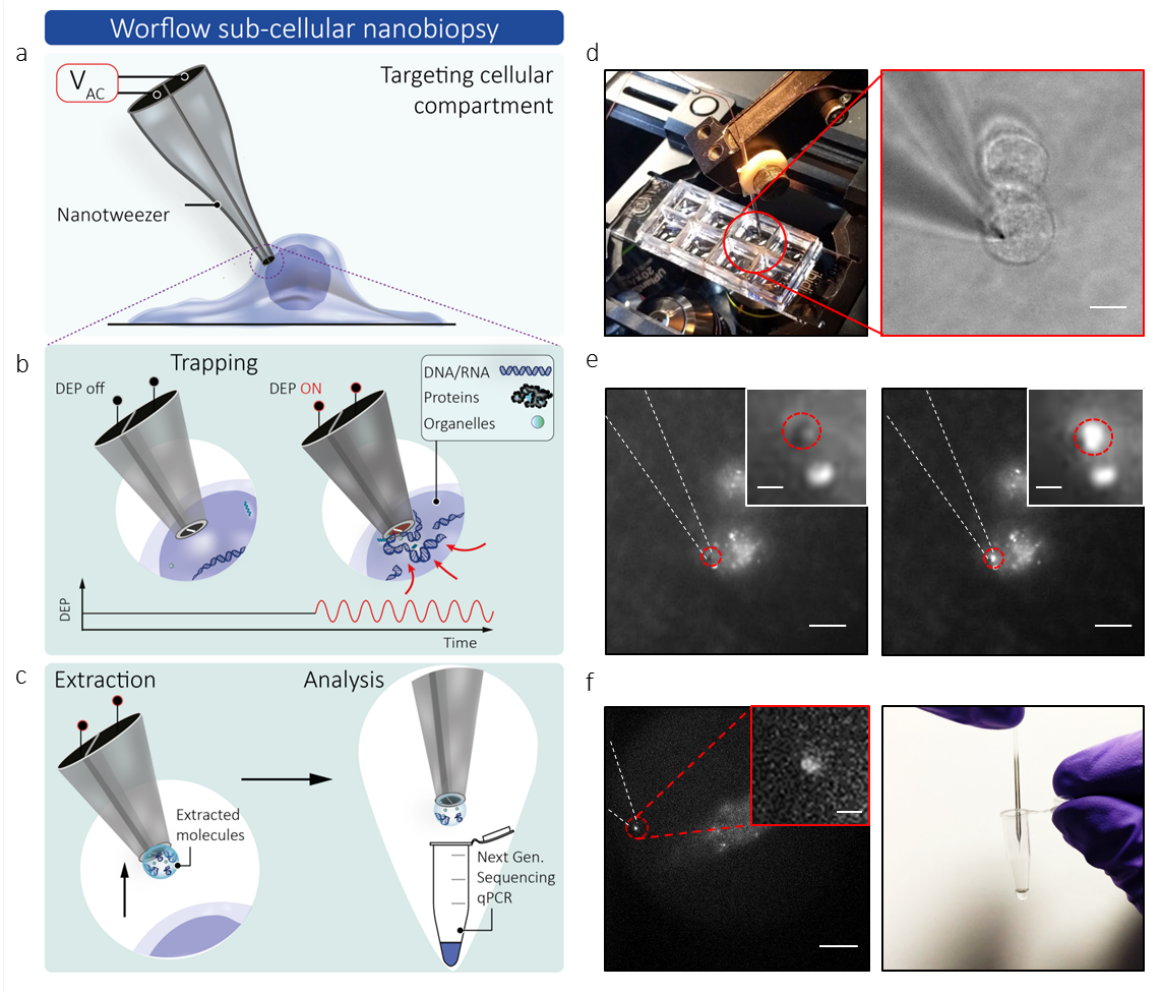

Fig. 3.22 Schematic showing the workflow of sub-cellular nanobiopsy performed with the nanotweezer. The first step consisted of approaching (a) the nanotweezer towards a selected cell and then penetrating its cell membrane as shown in the bright field image (d) (cells were seeded in a chamber coverglass as illustrated in the image on the left). Both actions were performed manually with the help of the micromanipulator (which the nanotweezer was mounted on) and using the emCCD camera as a visual feedback to control the tip position. The second step consisted of activating the DEP (b) and trapping molecules around its tip. As shown in the fluorescence images (e), when DEP was turned on (1 Mhz, 20 V_{pp}), a fluorescence spot was visualized in juxtaposition with the nanotweezer tip, as a result of molecules accumulation. The nanotweezer was vertically withdrawn from the cell (c) and as shown in (f), a fluorescence signal was still detectable at its apex. The final step involved transferring the trapped material into a PCR tube in such a way that further analysis could be carried out. In order to do so, the nanotweezer was first completely lifted up from the chambered coverglass and disconnected from the copper wires; then the nanotweezer was manually inserted into a PCR tube containing 5 μl of 10 mM Tris-HCl (pH 8.5) and the tip was broken inside the solution. Scale bars: (d) 10 μm, (e) 10 μm while insets 2 μm, (f) 20 μm and 5 μm.)

- **Trapping** This operation was performed under fluorescence illumination and DEP was used in a similar manner to that employed when the analyte was in bulk solution: with the nanotweezer located inside the cell, an AC field was applied between the electrodes resulting in a strong $\vec{F}_{DEP}$ at its apex. Molecules in the surrounding volume were trapped, leading to a localized increase in the overall fluorescence intensity. A representative example of this step is illustrated in **Figure 3.22 e**: a DEP signal of 20 V_{pp} at 1 MHz was applied to the nanotweezer, localized inside the cell, resulting in a visible fluorescence spot around its tip.

- **Extraction and analysis** The nanotweezer was then retracted from the cell. While in the cell media, it was observed that the fluorescence spot was still localized at its apex. This suggested that part of the cellular content accumulated beforehand remained trapped after retraction (**Figure 3.22 f**). The nanotweezers were fully withdrawn from the chamber coverglass using the z-axis of the micromanipulator.

  In the final step the trapped material was transferred into a qPCR tube ready for the process described in the previous section: the nanotweezer was manually inserted into a qPCR tube containing 5 μl of 10 mM Tris-HCl (pH 8.5) and breaking the tip inside the solution. Tubes were then stored at -20°C.

Finally we evaluated the viability of the extracted material which represent a fundamental point for any nanobiopsy. qPCR assays were performed to verify the integrity of nucleic acid bound to the nanopipette and possibly the quantity. Compared to other techniques were up to pL of cytoplasm were aspirated, in this case the volume extracted might be much smaller (atto to zeptoliters) and therefore more challenging. The nucleic acid sequence chosen to be amplified belonged to the β actin gene which is a housekeeping gene responsible for expressing actin, a major component of the cytoskeleton.

As illustrated by the real time amplification curves and the corresponding melting temperature profile (**Figure 3.23**) it was possible to amplify the extracted cellular materials. $C_q \approx 28$ while for the negative control $C_q \geq 40$ (forward and reverse primer were designed according to [58]).

Overall, more than 20 nanobiopsy experiments were successfully performed using different cell batches demonstrating the ability of nanotweezers to operate within a cellular environment. pDEP trapping conditions were met for frequencies equal to 100 kHz and 1 MHz with a voltage applied varying from 10 to 20 V_{pp}. As shown in **Figure 3.24 a-f**, cells conserved its shape after being exposed to the electric field. This happened in the vast majority of cases analysed however in some we observed the cell shrinking (irreversible

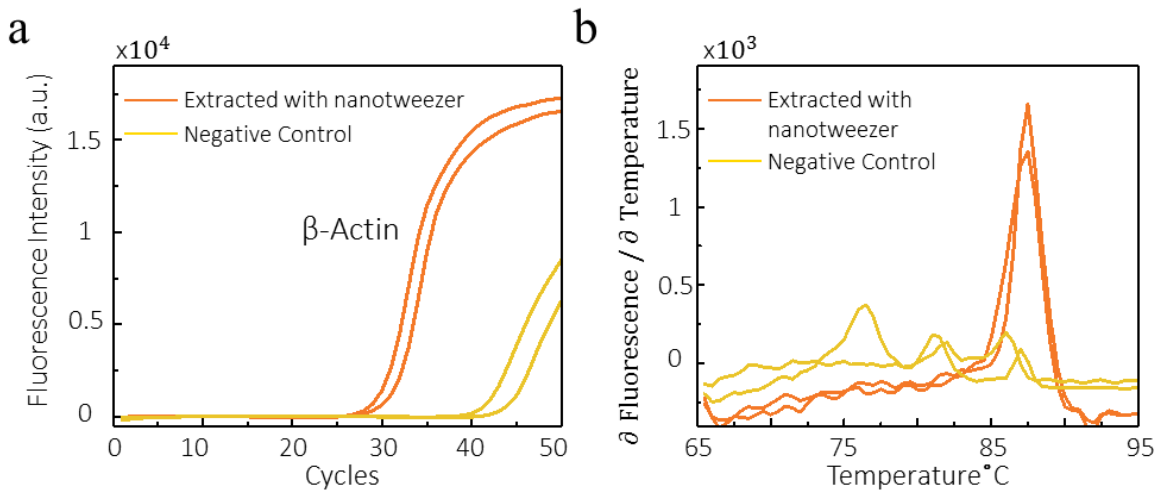

Fig. 3.23 Real time amplification plot (a) and melting temperature profile (b) of DNA encoding β-actin gene extracted with the nanotweezer from U2Os cell. Every curve was generated by a single nanobiopsy performed on different cells. Negative controls consists of addition of

damage). This might be attributed to electrodes with much larger surface area which in turn produced a much more extended electric field resulting in cell deformation (**Figure 3.24 g-i**).

Generally, nanotweezers were considered minimally invasive due to their dimensions. In fact the area of the nanopipette, based on the SEM, was approximately $\approx 0.011\ \mu m^2$. This value was orders of magnitude smaller (0.00088%) than the total surface area of a U2OS cell which, according to previous studies, could be estimated around 1250 μm^2.

When talking about DEP response of a molecule in the cytoplasm one should consider, among many factors, its conductivity; previous work on cytoplasmic conductivity reported $\sigma_{cyto} = 0.31$ S/m for red blood cells and $\sigma_{cyto} = 0.19$ S/m for E.coli cells [59] which are ≈ 1 order of magnitude higher than the one used in bulk experiments ($\sigma_{1mMKCl} = 14.6$ mS/m). A different response in the cell is therefore expected compared to the one we reported for bulk experiments. However even the reported cytoplasmic conductivity values represent only an average of the actual scenario inside the cell which is much more complex and inhomogeneous. An important consequence of the preceding discussion is that the same DEP stimulus inside the cell will generate different responses depending on where the stimulus originated. Ultimately, this is advantageous because it represents another degree of freedom in our system. In fact one can speculate about probing specific molecules in one compartment while not affecting other molecules located in the same compartment or surrounding compartments because of the different DEP response.

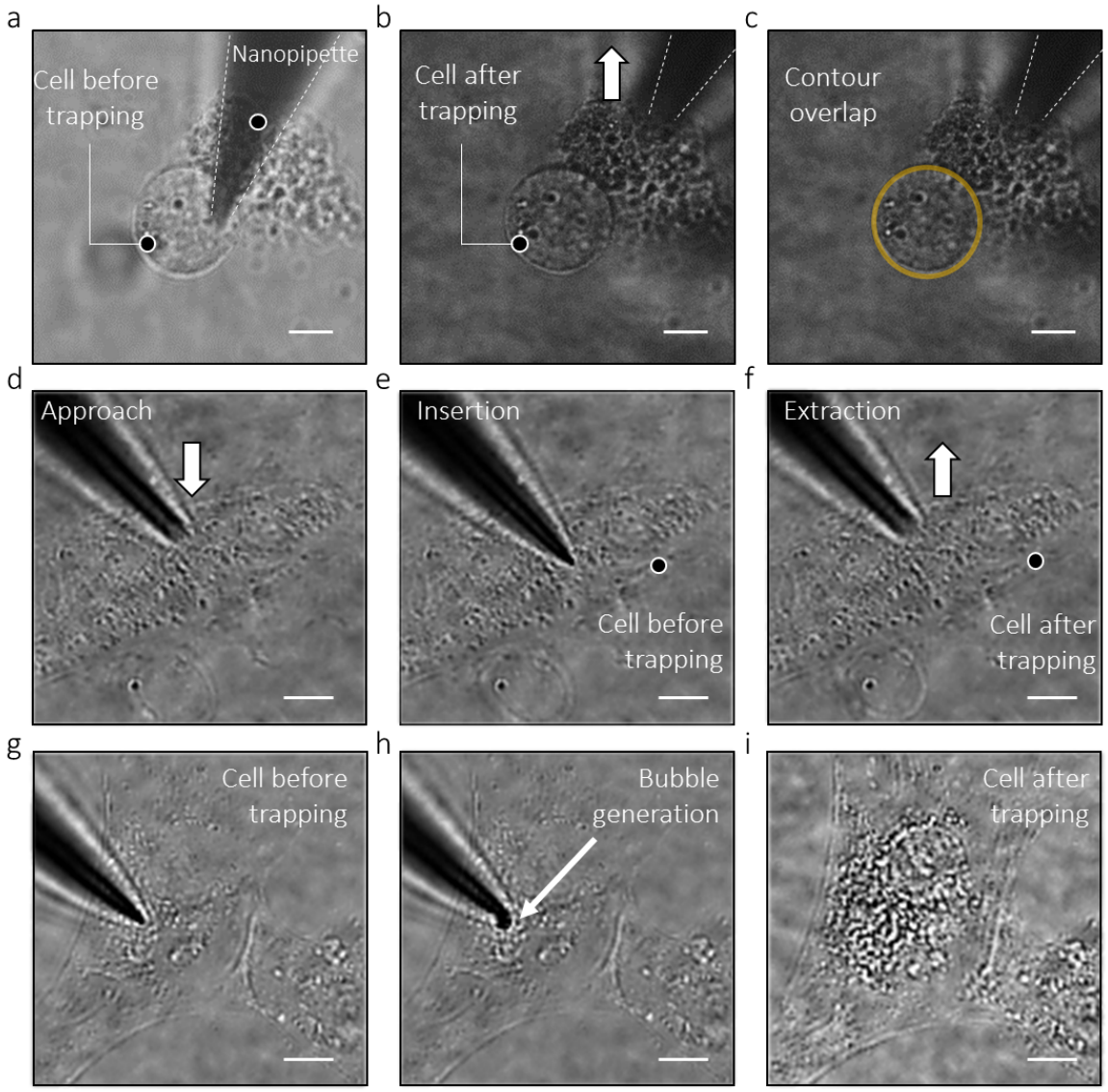

Fig. 3.24 The effect of DEP on cell shape. Bright field images showing (a) U2OS cell before and (b) after DEP performed at 100 kHz-20 V_{pp}. (c) Showing the overlap of the cell before (green shadow) and after DEP was activated. (d-f) Showing a nanobiopsy performed on endothelial cells (HPAEC) at 1 MHz-10 V_{pp}. The cell conserved its shape. In some cases (g-i), under the same conditions (e.g. voltage and frequency), DEP resulted detrimental to the cell shape and to the cell survival. In this cases, following the DEP activation, a gas-bubble was observed in correspondence of the tip of the nanopipette. This might be attributed to "faulty" electrodes which have much larger surface area which in turn produced a much more extended electric field resulting in cell deformation. Scale bars μm10.

3.5.1 Limitations and open challenges

The experiments above described a proof of concept experiment where it was shown that it is possible to concentrate cellular material around the nanopipette and subsequently extract part of it. However it comes with certain limitations and aspects that need to be addressed.

In general, all biological manipulation of cultured cells (e.g. microscopy, flowcytometry etc.) potentially alter the cell's physiology. Electric fields are no exception. The generate a twofold effect: firstly it provokes current flow which causes power dissipation in the form of Joule heating; secondly it has direct interaction with the cell. The latter takes into account interactions with electric fields which already exist in the cell, such as at the cell membrane. DEP-electric field might overlap with transmembrane voltages (which are in the tens of millivolts) hence affecting voltage-sensitive proteins (e.g. voltage-gated ion channels [60]). The first issue, the heating effect, is the main problem that almost all DEP architectures suffer from when it comes to biological material [61]. Joule heating scales with the characteristic length of the electrodes, L, and voltage applied as $\Delta T \approx L^2|E|^2$ [30]. Therefore nanotweezers, because of their nanometric scale, do not generate excessive heat. For instance, when considering a cell conductivity of 1 S/m, DEP at 20 V_{pp} at 1 MHz, simulations performed on our nanotweezer model predicted a maximum increase of about 10 K, in close proximity of the electrodes (approximately 5 nm) then dropping exponentially up to $\approx 2K$ at a distance of 100 nm from the electrode (**Figure 3.8 c,d**). Although limited and localized, this electric field might be detrimental for the cell's survival or it might strongly affect its phenotype. A way of mitigating this effect is by working with cells suspended in a low conductivity buffer: the latter will diffuse inside the plasma membrane reducing cytoplasmic conductivity and therefore heat dissipation. Following from the discussion on the effect of Joule heating, an in vitro study over time, investigating the viability and phenotype of cells after being perturbed by an electric field with different frequencies and magnitude has to be carried out. Ideally, one would like to determine conditions that will affect as few cells as possible (if any at all) and then use those conditions to perform the nanobiopsy.

The second aspect that would be worth investigating is the integrity of the cell membrane's function after nanopipette penetration. Although quartz nanopipettes of similar dimensions ($\approx$100 nm) [13, 62] or even larger ($\approx$ 400 nm) have been used to penetrate the cell, resulting in no discernible damage of the membrane a similar procedure has to be implemented in our case. To verify this, one option is by using a fluorescence microscopy to monitor any disruption in the intracellular Ca^{2+} signalling before, during, and after nanopipette insertion [63]. Calcium ions cannot cross the cell membrane on its own because the cell actively pumps out calcium so that a strong calcium gradient across the membrane is maintained. If the integrity of the membrane is disrupted, calcium ions will leak across the aperture,

equilibrating the inside and outside concentrations. Alternatively one might employ Tripan Blue Solution to assess cell viability using the dye exclusion test: viable cells do not take up Trypan Blue whereas dead cells (or with compromised membrane) do.

The third consideration is about the specificity of trapping and capture. In the experiments above we showed that is possible to trap a range of different analytes both when isolated in solution as well as in cellular environments. In principle, DEP allows to selectively trap a specific molecule by tuning the frequency and thus the dielectric response of that molecule in solution. However, especially inside a cell, achieving such sensitivity is not trivial due to the enormous amount of molecules of similar size and charge being contained in a such a small volume. Therefore it is reasonable to think that at the moment, the trapped material is not of made of a specific analyte but it is rather a mixture of them. In future studies, it would be interesting but also essential to establish the real specificity limits of our platform.

3.6 Conclusions

In conclusion, in this chapter we have presented a new manipulation tool for single molecules, based on dual barrel nanopipettes which allow dielectrophoretical confinement of single molecules in a volume surrounding the nanometric apex. We showed that this device, called nanotweezer, is extremely easy, quick, robust to be fabricated and operated and also cost-efficient (cleanroom facilities are not required). We demonstrated that the closely space nanoelectrodes positioned at the tip of the nanotweezer are capable of generating an intense, but highly confined dielectrophoretic force. We observed that this force can be used to easily manipulate a broad range of analytes such as polystyrene beads, DNA fragments and small proteins down to single molecule level. This is a significant improvement over existing DEP-based devices used to manipulate molecules, which normally require extensive fabrication processes, but also, over other single molecule techniques such as optical tweezers or AFM where analyte labelling, induced-photodamage, or complex apparatus, to name but a few, often represent insurmountable problems.

We demonstrated that nanotweezers were successful in extracting the captured molecules outside the solution. For example we showed λ-DNA being trapped, extracted from the solution and amplified via commercially available qPCR equipments. The impact of these experiments was twofold. Firstly, it proved that DEP-handling was not harmful to biomolecules which remained still viable and ready for further analysis. Secondly, it highlighted the versatility of nanotweezer which could be used in combination with popular molecular biology techniques.

Importantly we extend the method capabilities to the field of minimally invasive sub-cellular nanobiopsy. We demonstrated that nanotweezers, operating in a complex scenario such as the cellular one, were capable of manipulating and consequently extracting cellular content from a targeted cell. The extracted material was shown to be viable to be analyzed with qPCR. Within the sphere of interest of single cell nanosurgery, nanotweezers represent a substantial technological advancement due to their simplicity, rapidity in sample extraction, and flexibility for integration with other techniques: technically, one could operate with the nanotweezers on virtually any microscope (not necessarily fluorescence-based).

As such, the present technology opens the door to a new way of interrogating single cells at specific time points without the necessity of performing cell fixation or alternatively cell lysis; applications might range from fundamental science (e.g. following the protein expression and studying cellular processes) to diagnostics where it could be used to monitor the effectiveness and the mechanism of action of a specific drug over the time.

References

[1] P. Holzmeister, G. P. Acuna, D. Grohmann, and P. Tinnefeld, "Breaking the concentration limit of optical single-molecule detection," *Chem. Soc. Rev.*, vol. 43, no. 4, pp. 1014–1028, 2014.

[2] J. J. Gooding and K. Gaus, "Single-Molecule Sensors: Challenges and Opportunities for Quantitative Analysis," *Angew. Chemie Int. Ed.*, vol. 55, no. 38, pp. 11354–11366, 2016.

[3] T. Ha, "Single-molecule methods leap ahead," *Nat. Methods*, vol. 11, no. 10, pp. 1015–1018, 2014.

[4] U. F. Keyser, B. N. Koeleman, S. van Dorp, D. Krapf, R. M. M. Smeets, S. G. Lemay, N. H. Dekker, and C. Dekker, "Direct force measurements on DNA in a solid-state nanopore," *Nat. Phys.*, vol. 2, no. 7, pp. 473–477, 2006.

[5] A. del Rio, R. Perez-Jimenez, R. Liu, P. Roca-Cusachs, J. M. Fernandez, and M. P. Sheetz, "Stretching Single Talin Rod Molecules Activates Vinculin Binding," *Science*, vol. 323, no. 5914, pp. 638–641, 2009.

[6] S. M. Stavis, J. B. Edel, K. T. Samiee, and H. G. Craighead, "Single molecule studies of quantum dot conjugates in a submicrometer fluidic channel," *Lab Chip*, vol. 5, no. 3, p. 337, 2005.

[7] J. C. Cordova, D. K. Das, H. W. Manning, and M. J. Lang, "Combining single-molecule manipulation and single-molecule detection," *Curr. Opin. Struct. Biol.*, vol. 28, pp. 142–148, 2014.

[8] C. Qian, H. Huang, L. Chen, X. Li, Z. Ge, T. Chen, Z. Yang, and L. Sun, "Dielectrophoresis for bioparticle manipulation," *Int. J. Mol. Sci.*, vol. 15, no. 10, pp. 18281–18309, 2014.

[9] G.-W. Li and X. S. Xie, "Central dogma at the single-molecule level in living cells," *Nature*, vol. 475, no. 7356, pp. 308–315, 2011.

[10] O. Guillaume-Gentil, R. V. Grindberg, R. Kooger, L. Dorwling-Carter, V. Martinez, D. Ossola, M. Pilhofer, T. Zambelli, and J. A. Vorholt, "Tunable Single-Cell Extraction for Molecular Analyses," *Cell*, vol. 166, no. 2, pp. 506–516, 2016.

[11] Y. Cao, M. Hjort, H. Chen, F. Birey, S. A. Leal-Ortiz, C. M. Han, J. G. Santiago, S. P. Paşca, J. C. Wu, and N. A. Melosh, "Nondestructive nanostraw intracellular sampling for longitudinal cell monitoring," *Proc. Natl. Acad. Sci.*, vol. 114, no. 10, pp. E1866–E1874, 2017.

[12] R. Singhal, Z. Orynbayeva, R. V. Kalyana Sundaram, J. J. Niu, S. Bhattacharyya, E. a. Vitol, M. G. Schrlau, E. S. Papazoglou, G. Friedman, and Y. Gogotsi, "Multifunctional

carbon-nanotube cellular endoscopes.," *Nat. Nanotechnol.*, vol. 6, no. 1, pp. 57–64, 2011.

[13] P. Actis, M. M. Maalouf, H. J. Kim, A. Lohith, B. Vilozny, R. A. Seger, and N. Pourmand, "Compartmental Genomics in Living Cells Revealed by Single-Cell Nanobiopsy," *ACS Nano*, vol. 8, no. 1, pp. 546–553, 2014.

[14] A. Meister, M. Gabi, P. Behr, P. Studer, J. Vörös, P. Niedermann, J. Bitterli, J. Polesel-Maris, M. Liley, H. Heinzelmann, and T. Zambelli, "FluidFM: Combining Atomic Force Microscopy and Nanofluidics in a Universal Liquid Delivery System for Single Cell Applications and Beyond," *Nano Lett.*, vol. 9, no. 6, pp. 2501–2507, 2009.

[15] S. G. Higgins and M. M. Stevens, "Extracting the contents of living cells," *Science*, vol. 356, no. 6336, pp. 379–380, 2017.

[16] Y. Nashimoto, Y. Takahashi, Y. Zhou, H. Ito, H. Ida, K. Ino, T. Matsue, and H. Shiku, "Evaluation of mRNA Localization Using Double Barrel Scanning Ion Conductance Microscopy," *ACS Nano*, vol. 10, no. 7, pp. 6915–6922, 2016.

[17] F. O. Laforge, J. Carpino, S. A. Rotenberg, and M. V. Mirkin, "Electrochemical attosyringe," *Proc. Natl. Acad. Sci.*, vol. 104, no. 29, pp. 11895–11900, 2007.

[18] A. Shivalingam, M. A. Izquierdo, A. L. Marois, A. Vyšniauskas, K. Suhling, M. K. Kuimova, and R. Vilar, "The interactions between a small molecule and G-quadruplexes are visualized by fluorescence lifetime imaging microscopy," *Nat. Commun.*, vol. 6, p. 8178, 2015.

[19] X. Wang, X.-B. Wang, and P. R. Gascoyne, "General expressions for dielectrophoretic force and electrorotational torque derived using the Maxwell stress tensor method," *J. Electrostat.*, vol. 39, no. 4, pp. 277–295, 1997.

[20] J. Voldman, "Electrical Forces for Microscale Cell Manipulation," *Annu. Rev. Biomed. Eng.*, vol. 8, no. 1, pp. 425–454, 2006.

[21] R. B. Schoch, J. Han, and P. Renaud, "Transport phenomena in nanofluidics," *Rev. Mod. Phys.*, vol. 80, no. 3, pp. 839–883, 2008.

[22] A. Barik, X. Chen, and S. H. Oh, "Ultralow-Power Electronic Trapping of Nanoparticles with Sub-10 nm Gold Nanogap Electrodes," *Nano Lett.*, vol. 16, no. 10, pp. 6317–6324, 2016.

[23] N. G. Green and H. Morgan, "Dielectrophoretic investigations of sub-micrometre latex spheres," *J. Phys. D. Appl. Phys.*, vol. 30, no. 18, pp. 2626–2633, 1997.

[24] K. J. Freedman, L. M. Otto, A. P. Ivanov, A. Barik, S.-H. Oh, and J. B. Edel, "Nanopore sensing at ultra-low concentrations using single-molecule dielectrophoretic trapping," *Nat. Commun.*, vol. 7, p. 10217, 2016.

[25] W. Michael Arnold, "Positioning and levitation media for the separation of biological cells," *IEEE Trans. Ind. Appl.*, vol. 37, no. 5, pp. 1468–1475, 2001.

[26] B. M. Taff and J. Voldman, "A Scalable Addressable Positive-Dielectrophoretic Cell-Sorting Array," *Anal. Chem.*, vol. 77, no. 24, pp. 7976–7983, 2005.

[27] L. Wang, L. A. Flanagan, N. L. Jeon, E. Monuki, and A. P. Lee, "Dielectrophoresis switching with vertical sidewall electrodes for microfluidic flow cytometry," *Lab Chip*, vol. 7, no. 9, p. 1114, 2007.

[28] R. Martinez-Duarte, R. A. Gorkin III, K. Abi-Samra, and M. J. Madou, "The integration of 3D carbon-electrode dielectrophoresis on a CD-like centrifugal microfluidic platform," *Lab Chip*, vol. 10, no. 8, p. 1030, 2010.

[29] S. Li, M. Li, Y. S. Hui, W. Cao, W. Li, and W. Wen, "A novel method to construct 3D electrodes at the sidewall of microfluidic channel," *Microfluid. Nanofluidics*, vol. 14, no. 3-4, pp. 499–508, 2013.

[30] A. Castellanos, A. Ramos, A. González, N. G. Green, and H. Morgan, "Electrohydrodynamics and dielectrophoresis in microsystems: scaling laws," *J. Phys. D. Appl. Phys.*, vol. 36, no. 20, pp. 2584–2597, 2003.

[31] K. McKelvey, B. P. Nadappuram, P. Actis, Y. Takahashi, Y. E. Korchev, T. Matsue, C. Robinson, and P. R. Unwin, "Fabrication, Characterization, and Functionalization of Dual Carbon Electrodes as Probes for Scanning Electrochemical Microscopy (SECM)," *Anal. Chem.*, vol. 85, no. 15, pp. 7519–7526, 2013.

[32] Y. Fang and J. Leddy, "Cyclic Voltammetric Responses for Inlaid Microdisks with Shields of Thickness Comparable to the Electrode Radius: A Simulation of Reversible Electrode Kinetics," *Anal. Chem.*, vol. 67, no. 7, pp. 1259–1270, 1995.

[33] Z. Yu, T. E. McKnight, M. N. Ericson, A. V. Melechko, M. L. Simpson, and B. Morrison, "Vertically aligned carbon nanofiber arrays record electrophysiological signals from hippocampal slices," *Nano Lett.*, vol. 7, no. 8, pp. 2188–2195, 2007.

[34] C. E. Banks, R. G. Compton, A. C. Fisher, and I. E. Henley, "The transport limited currents at insonated electrodes," *Phys. Chem. Chem. Phys.*, vol. 6, no. 12, p. 3147, 2004.

[35] J. Regtmeier, T. T. Duong, R. Eichhorn, D. Anselmetti, and A. Ros, "Dielectrophoretic Manipulation of DNA: Separation and Polarizability," *Anal. Chem.*, vol. 79, no. 10, pp. 3925–3932, 2007.

[36] C.-F. Chou, J. O. Tegenfeldt, O. Bakajin, S. S. Chan, E. C. Cox, N. Darnton, T. Duke, and R. H. Austin, "Electrodeless Dielectrophoresis of Single- and Double-Stranded DNA," *Biophys. J.*, vol. 83, no. 4, pp. 2170–2179, 2002.

[37] R. Hölzel, N. Calander, Z. Chiragwandi, M. Willander, and F. F. Bier, "Trapping single molecules by dielectrophoresis," *Phys. Rev. Lett.*, vol. 95, no. 12, pp. 18–21, 2005.

[38] D. Porath, A. Bezryadin, S. de Vries, C. Dekker, S. D. Vries, and C. Dekker, "Direct measurement of electrical transport through DNA molecules," *Nature*, vol. 403, no. 6770, pp. 635–638, 2000.

[39] S. Tuukkanen, J. J. Toppari, A. Kuzyk, L. Hirviniemi, V. P. Hytönen, T. Ihalainen, and P. Törmä, "Carbon Nanotubes as Electrodes for Dielectrophoresis of DNA," *Nano Lett.*, vol. 6, no. 7, pp. 1339–1343, 2006.

[40] L. Ying, S. S. White, A. Bruckbauer, L. Meadows, Y. E. Korchev, and D. Klenerman, "Frequency and Voltage Dependence of the Dielectrophoretic Trapping of Short Lengths of DNA and dCTP in a Nanopipette," *Biophys. J.*, vol. 86, no. 2, pp. 1018–1027, 2004.

[41] N. G. Green, A. Ramos, A. González, A. Castellanos, and H. Morgan, "Electrothermally induced fluid flow on microelectrodes," *J. Electrostat.*, vol. 53, no. 2, pp. 71–87, 2001.

[42] A. Kumar, C. Cierpka, S. J. Williams, C. J. Kähler, and S. T. Wereley, "3D3C velocimetry measurements of an electrothermal microvortex using wavefront deformation PTV and a single camera," *Microfluid. Nanofluidics*, vol. 10, no. 2, pp. 355–365, 2011.

[43] I. F. Sbalzarini and P. Koumoutsakos, "Feature point tracking and trajectory analysis for video imaging in cell biology," *J. Struct. Biol.*, vol. 151, no. 2, pp. 182–195, 2005.

[44] N. Ebejer, A. G. Güell, S. C. Lai, K. McKelvey, M. E. Snowden, and P. R. Unwin, "Scanning Electrochemical Cell Microscopy: A Versatile Technique for Nanoscale Electrochemistry and Functional Imaging," *Annu. Rev. Anal. Chem.*, vol. 6, no. 1, pp. 329–351, 2013.

[45] C. Manzo and M. F. Garcia-Parajo, "A review of progress in single particle tracking: from methods to biophysical insights," *Reports Prog. Phys.*, vol. 78, no. 12, p. 124601, 2015.

[46] H. Zhao, "Role of hydrodynamic behavior of DNA molecules in dielectrophoretic polarization under the action of an electric field," *Phys. Rev. E - Stat. Nonlinear, Soft Matter Phys.*, vol. 84, no. 2, pp. 6–11, 2011.

[47] D. Bakewell, I. Ermolina, H. Morgan, J. Milner, and Y. Feldman, "Dielectric relaxation measurements of 12 kbp plasmid DNA," *Biochim. Biophys. Acta - Gene Struct. Expr.*, vol. 1493, pp. 151–158, sep 2000.

[48] S. Bone and C. A. Small, "Dielectric studies of ion fluctuation and chain bending in native DNA," *BBA - Gene Struct. Expr.*, vol. 1260, no. 1, pp. 85–93, 1995.

[49] R. Martinez-Duarte, F. Camacho-Alanis, P. Renaud, and A. Ros, "Dielectrophoresis of lambda-DNA using 3D carbon electrodes," *Electrophoresis*, vol. 34, no. 7, pp. 1113–1122, 2013.

[50] R. Yokokawa, Y. Manta, M. Namura, Y. Takizawa, N. C. H. Le, and S. Sugiyama, "Individual evaluation of DEP, EP and AC-EOF effects on λDNA molecules in a DNA concentrator," *Sensors Actuators, B Chem.*, vol. 143, no. 2, pp. 769–775, 2010.

[51] P. D. Hoffman, P. S. Sarangapani, and Y. Zhu, "Dielectrophoresis and AC-induced assembly in binary colloidal suspensions," *Langmuir*, vol. 24, no. 21, pp. 12164–12171, 2008.

[52] J. Tang, S. L. Levy, D. W. Trahan, J. J. Jones, H. G. Craighead, and P. S. Doyle, "Revisiting the conformation and dynamics of DNA in slitlike confinement," *Macromolecules*, vol. 43, no. 17, pp. 7368–7377, 2010.

[53] A. Nakano and A. Ros, "Protein dielectrophoresis: Advances, challenges, and applications," *Electrophoresis*, vol. 34, no. 7, pp. 1085–1096, 2013.

[54] K. T. Liao and C. F. Chou, "Nanoscale molecular traps and dams for ultrafast protein enrichment in high-conductivity buffers," *J. Am. Chem. Soc.*, vol. 134, no. 21, pp. 8742–8745, 2012.

[55] F. Camacho-Alanis and A. Ros, "Protein dielectrophoresis and the link to dielectric properties," *Stroke*, vol. 7, no. 3, pp. 353–371, 2015.

[56] A. B. Singleton, "-Synuclein Locus Triplication Causes Parkinson's Disease," *Science*, vol. 302, no. 5646, pp. 841–841, 2003.

[57] M. Beck, A. Schmidt, J. Malmstroem, M. Claassen, A. Ori, A. Szymborska, F. Herzog, O. Rinner, J. Ellenberg, and R. Aebersold, "The quantitative proteome of a human cell line.," *Mol. Syst. Biol.*, vol. 7, no. 549, p. 549, 2011.

[58] J. J. Zhu, F. B. Li, J. M. Zhou, Z. C. Liu, X. F. Zhu, and W. M. Liao, "The tumor suppressor p33ING1b enhances taxol-induced apoptosis by p53-dependent pathway in human osteosarcoma U20S cells," *Cancer Biol. Ther.*, vol. 4, no. 1, pp. 39–47, 2005.

[59] S. Park, Y. Zhang, T.-H. Wang, and S. Yang, "Continuous dielectrophoretic bacterial separation and concentration from physiological media of high conductivity," *Lab Chip*, vol. 11, no. 17, p. 2893, 2011.

[60] W. A. Catterall, "Structure and Function of Voltage-Gated Ion Channels," *Annu. Rev. Biochem.*, vol. 64, pp. 493–531, jun 1995.

[61] R. C. Gallo-Villanueva, M. B. Sano, B. H. Lapizco-Encinas, and R. V. Davalos, "Joule heating effects on particle immobilization in insulator-based dielectrophoretic devices," *Electrophoresis*, vol. 35, no. 2-3, pp. 352–361, 2014.

[62] P. Actis, S. Tokar, J. Clausmeyer, B. Babakinejad, S. Mikhaleva, R. Cornut, Y. Takahashi, A. López Córdoba, P. Novak, A. I. Shevchuck, J. A. Dougan, S. G. Kazarian, P. V. Gorelkin, A. S. Erofeev, I. V. Yaminsky, P. R. Unwin, W. Schuhmann, D. Klenerman,

D. A. Rusakov, E. V. Sviderskaya, and Y. E. Korchev, "Electrochemical Nanoprobes for Single-Cell Analysis," *ACS Nano*, vol. 8, no. 1, pp. 875–884, 2014.

[63] A. Demuro, E. Mina, R. Kayed, S. C. Milton, I. Parker, and C. G. Glabe, "Calcium dysregulation and membrane disruption as a ubiquitous neurotoxic mechanism of soluble amyloid oligomers," *J. Biol. Chem.*, vol. 280, no. 17, pp. 17294–17300, 2005.

Chapter 4

Nanopore-FET: a novel fabrication strategy

4.1 Introduction

The analogies between semiconductor materials and electrolyte solutions [1] fuel, since the late fifties, the interest in developing devices capable of actively manipulating different biomolecules within "ionic integrated circuits", which represent the solid state electronics equivalent of integrated circuits. From the pioneering works that established the electrolytic analogy to the p-n junction [2] and the first ionic-liquid channel field-effect transistor (FET) [3] a variety of devices and materials have been proposed leading to the birth of a new field called iontronics.

Various architectures and materials (e.g. silicon, quartz, polydimethylsiloxane, silicon nitride etc.) have been reported [4], however, one of the most promising sub-class of field-effect transistor devices for biosensing are based around nanopores and nanoporous structures. In general such hybrid platforms are extremely versatile because they can manipulate ions or biomolecules (prerogative of FET) and at the same time interrogate them with single molecule resolution in a sub-femtoliter volume (typical of nanopore).

The central element of these field-effect driven nanofluidic architectures is their perms-elective behaviour [3]. Spatial and temporal redistributions of ions and biomolecules (e.g. concentration, depletion and flow) represent the way of implementing logic gates and making them communicating among each other effectively to generate ionic integrated circuits (e.g. moving DNA molecules, proteins and charged species across channels). Nonetheless compared to the electronic counterpart, the ionic circuits building blocks present some intrinsic differences. Firstly, ions carry a charge n, which could be higher than one; secondly, there

is not an equivalent electron-hole recombination process for ions (in the sense that anion and cation do not disappear after they recombine); lastly, ions, compared to electrons (and holes) move much slower due to relatively low mobilities. Despite having a slower response, ion-based circuits, have the tremendous advantage of operating in an aqueous, biocompatible environment.

Although there is an extensive literature about simulated ionic FET and actual working devices [5–9], if we consider field-effect platforms for single molecule detection and manipulation of biomolecules this number shrinks considerably. The main problem is definitely the complexity in fabricating such devices. The standard approach consists on integrating a pair of nanometric electrodes of various nature (tunneling electrodes [10, 11], graphene nanogaps [12], graphene nanoribbons [13]) or alternatively a nanowire [14] onto a conventional SiN_x nanopore membrane. However this fabrication route normally requires multi-step procedures largely based on cleanroom facilities which are costly, time consuming and with a low overall process yield.

In this work we present a new method for fabricating field effect nanofluidic transistors based around quartz nanopipettes which are a sub-class of solid state nanopores. As shown in **Figure 4.1** the 3 electrodes system was implemented in a double barrel nanopipettes setup where one barrel, which has been carbon coated first and gold electroplated after serves as gate electrode to actively regulate the ionic species passing through the open barrel which acts as a standard nanopore sensor. We showed that these new field effect devices, which are easy to fabricate and operate, allowed to sense and regulate the passage of individual DNA molecules similarly to a molecular switch. In addition, we show that this new method allows to simultaneously tune the pore size, consequently improving the signal-to-noise (SNR) of the detected molecules.

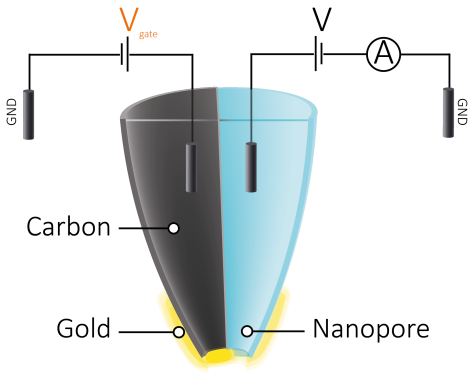

Fig. 4.1 Nanopore-based ionic-FET schematic. The device consists of a dual barrel quartz nanopipette in which one barrel acts as a nanopore channel while the other one acts as a gate electrode and it is responsible for regulating the electric field around the pore entrance. As a result of the fabrication process which involves carbon deposition followed by electrochemical growth of gold, the nanopore aperture is coated with a metal electrode which is independently driven from the open nanochannel.

Overall this novel nanopore-FET fabrication strategy would have a twofold impact in the field: precisely active control over ionic species such as charged biomolecules (e.g. nucleic acids or proteins) as well as investigating the fundamental physico-chemical mechanisms involved in this type of field-effect systems.

4.2 Experimental procedures

4.2.1 Pipette pulling

Dual barrel nanopipettes were fabricated using a P-2000 laser puller (Sutter Instrument, USA) from quartz double-barrel capillaries (Friedrich & Dimmock, USA) with an outer diameter of 1.2 mm and an overall inner diameter of 0.9 mm which comprises two chambers separated by an insulating quartz septum (0.2 mm) which retains its shape after the pulling process. The quartz capillary were 100 mm in length.

Capillaries were plasma cleaned (Harrick Plasma cleaner PDC-001, USA) for at least 15 minutes and subsequently pulled according to the following protocol:

	Heating	Filament	Velocity	Delay	Pulling
Line 1	850	4	30	160	100
Line 2	870	3	20	140	160

Table 4.1 Nanopipette pulling protocol for dual barrel nanopipettes.

4.2.2 Carbon deposition

Dual barrel nanopipettes with a carbon nanoelectrodes were fabricated with the setup described in **Figure 3.3**.

A rubber plug (Blu Tak, Bostik, FRA) located at the back-end of one barrel was used to prevent the butane gas from flowing in both barrels leading to carbon being deposited inside the open barrel only. The procedure adopted was identical to the one described in the previous chapter. Briefly, nanopipettes were mounted onto single-axis moveable holder and the back-end connected, via a rubber tube, to a butane canister. The tip of the nanopipette was aligned to the opening of a quartz, single barrel capillary, placed on the opposite side which provided argon gas flow at the tip of the dual barrel nanopipette. A manually controlled gas blow torch, was used to heat the tip of the nanopipette for approximately 30 s leading to pyrolytic deposition of carbon from butane.

4.2.3 Gold deposition setup

The feedback controlled electrochemical gold deposition was performed using a bipotentiostat (model 760C, CH instrument, USA). The nanopipette was immersed in the gold electroplating solution (ECF 64, Metalor, JPN) with the open barrel being filled with a solution of ammonium sulfite (supporting electrolyte of ECF64). In this way the electroplating was localized outside the nanopipette and the possibility of gold being deposited inside the pipette was further minimized (notably the SEM did not show any carbon being deposited inside the open barrel therefore this possibility should be already low). A copper wire (0.125 mm in diameter, GoodFellow U.K.) was employed to connect the carbon deposited barrel with Working Electrode 1 of the electrochemical station; a silver wire (0.0125mm in diameter, GoodFellow U.K.) was inserted in the open barrel and connected to the Working Electrode 2. A second silver wire dipped in the gold electrochemical bath acted as a Quasi Reference Counter Electrode (QRCE).

A dual channel chronoamperometry protocol was used for the feedback controlled electrochemical gold deposition: one channel, connected to the carbon electrode, was dedicated for the actual deposition and a constant bias of -0.73 V was applied. The second channel, connected to the open barrel, was used to measure the ionic current flow across the pore and therefore monitor in real-time the pore size. This channel was held at -0.1V.

Notably before and after the deposition, IV characteristics of the open barrel were performed using a cyclic voltammetry where the voltage was swiped between -500 mV and 500 mV at a scan rate of 0.05 V/s with a sampling rate of 0.02 V). The conductance, thus the pore size, was calculated over the linear region +100 mV and -100 mV. After the deposition, each nanopipette was rinsed with DI water multiple times. To shield unwanted electromagnetic noise experiments were carried out by placing the nanopipette inside a Faraday cage.

4.2.4 Materials

10 kbp dsDNA 500 mg/ml was purchased from New England Biolabs(USA). DNA translocation experiments were performed in a solution of 100 mM KCl, 10 mM Tris 1 mM EDTA,at pH 8.0.

The gold electroplating solution ECF64 was purchased from Metalor (JPN) and it consisted of 16.5 g/L of $AuNH_4(SO_3)_2$ (8.4 mM of Au), 70 g/L $(NH_4)_2SO_3$ (0.52 mM). The solution appeared semi-bright, with a density of 19.3 g/cm^3, with a pH of ~ 9.

For the electrodeposition experiments, ECF64 stock solution was diluted 1:10 (v/v) in DI water (18.2 MΩ). The freshly prepared solution was used for no longer than a day.

The supporting electrolyte, which the open barrel was filled with, consisted of 0.052 M NH_4AuSO_3 aqueous solution. NH_4AuSO_3 (in powder form) was purchased from Sigma-Aldrich and prepared in ultra pure DI water.

4.2.5 Single molecule recordings

Single molecule recordings were performed using Axopatch 200B in conjunction with a Digidata 1440 (Molecular Devices, USA) or by using MultiClamp 700B amplifier (Molecular Devices, USA) with Digidata 1550 digitizer (Molecular Devices, USA). In both cases the analog data was acquired with Clampex Data Acquisition Module (Molecular Devices, USA), low-pass filtered using the built-in 4 pole Bessel filter (Data acquisition frequency was set to 100 kHz aside from current voltage characteristics which were performed at 50 kHz) and processed with the Matlab script described in Chapter 2.

4.3 Results

4.3.1 Fabrication

The fabrication method consisted of three main steps: nanopipette pulling, carbon coating and electrochemical gold deposition (**Figure 4.2**). Starting from theta quartz capillaries, nanopipettes were laser pulled according to the protocol described in the experimental section. The apex of a typical nanopipette consisted of a semi-elliptical geometry where two nanometric apertures were separated by an insulating quartz septum (20 ± 5 nm). According to the SEM micrographs the effective radii of each nanopore aperture was comprised between 20 to 50 nm leading to an overall tip radius of approximately 100 nm and 50 nm along the long and short axis respectively (**Figure 4.3**).

Carbon deposition

The carbon deposition step was performed, according to a well established procedure [15, 16], using the setup described in **Figure 3.3**. The butane flow was passed in one barrel only by blocking the other with a rubber plug. This method resulted in one nanoelectrode and an open pore placed next to each other at the apex of the nanopipette. Notably no carbon was deposited around or inside the open barrel leading to no change or contamination of the nanopore aperture.

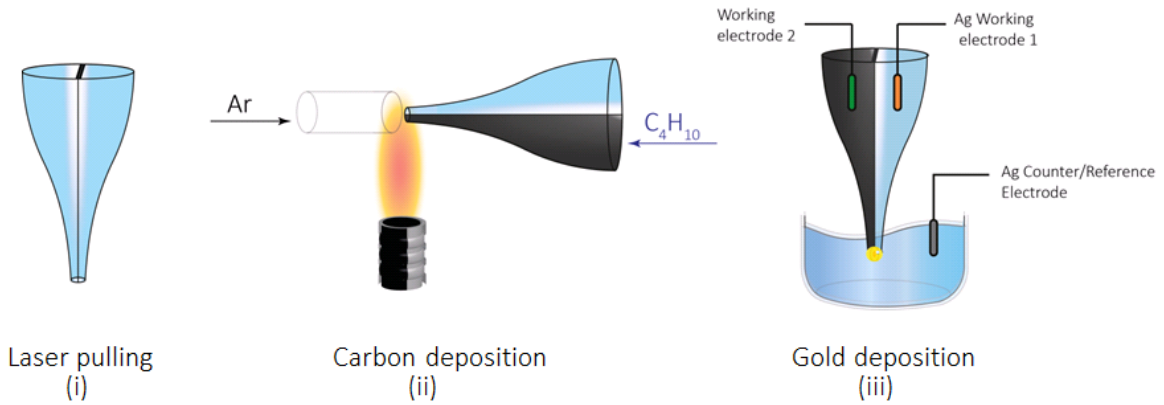

Fig. 4.2 Schematic of naopore-FET fabrication. Showing the three steps necessary to fabricate a nanopore based ionic FET: laser pulling of quartz capillaries; carbon deposition on one of the two nanopipettes barrels and electrochemical deposition of the gold electrode around the tip which serves as gate electrode.

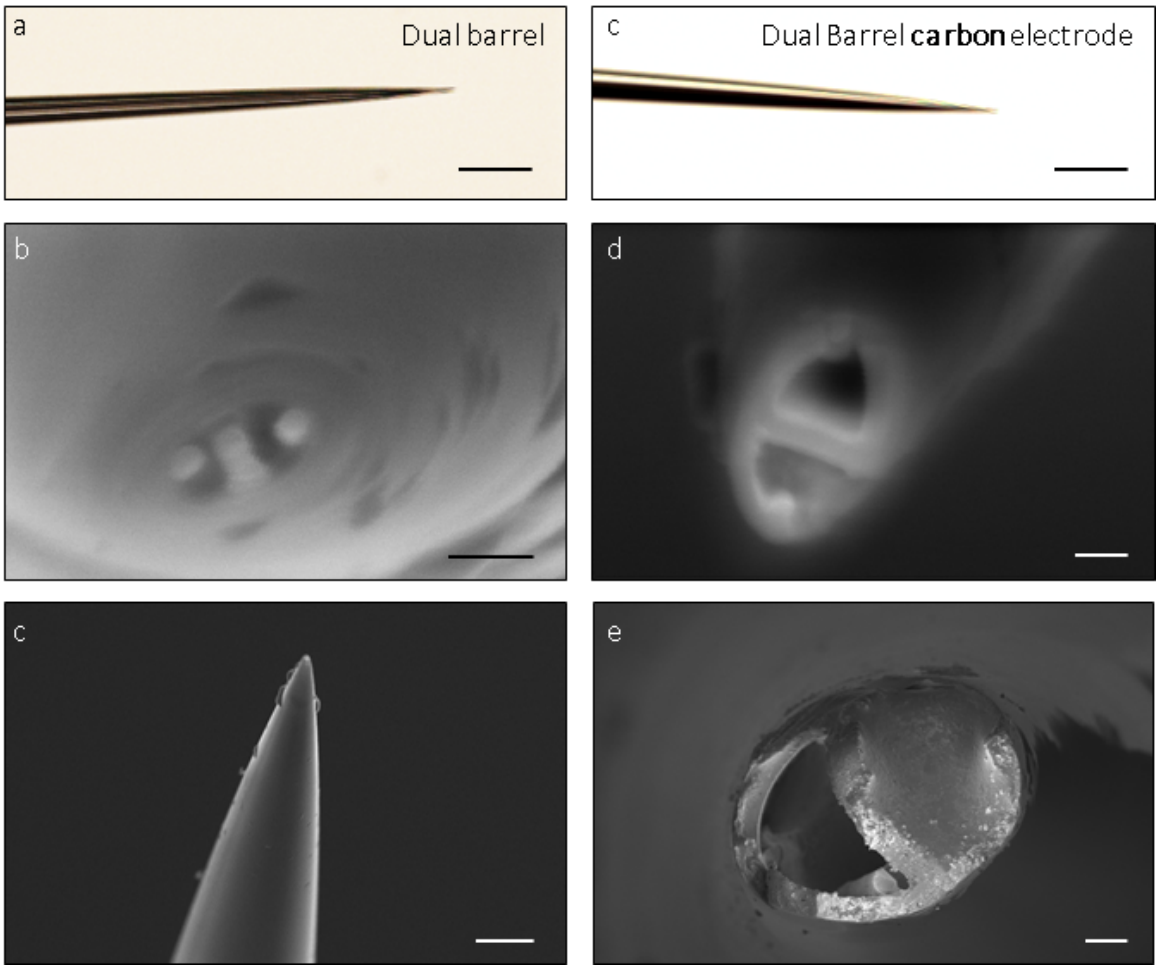

Fig. 4.3 Carbon deposition characterization. Showing bright field and SEM micrographs of dual barrel nanopipette before (a-c) and after carbon deposition (d-e). Scale bars: (a),(d) 20 μm, (b) 100 nm, (c),(f) 10 μm, (e) 50 nm.

Gold deposition

The gate of the fluidic transistor was fabricated via electrodeposition of gold onto the carbon electrode at the tip of the nanopipette. This step was made necessary by the fact that the carbon electrode itself did not show any "gate activity. In other words, applying a bias to the carbon electrode was not sufficient to perturb the ionic current of the open barrel. Perhaps this can be explained by considering the fact that the carbon electrode is positioned on one side of the source-drain fluidic transistor (in an ideal scenario, the gate electrode should surround a narrow source-drain channel so that a small change in the gate potential would immediately perturb the ionic current flow between source and drain channel).

Integration of a third metallic, gating, electrode into a solid-state nanopore device, via electrodeposition, has been previously reported [17, 18], however in the method adopted here, the novelty is represented by the possibility of tuning in real time the pore aperture by continuously monitoring the ionic current flow across the open barrel. In other words, it was implemented a feedback-controlled deposition system. For this step ECF64 solution (Metalor, JPN) was utilized. ECF64 consisted of cyanide free sulphite gold electroplating processes based on the ammonium gold sulphite electrolyte. ECF64 was chosen due to its slow deposition rate [19] which allowed an higher degree of precision when depositing at the nanoscale.

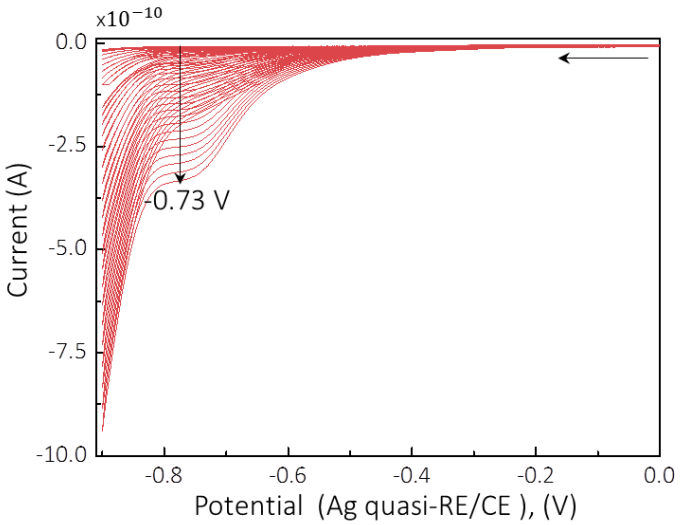

Fig. 4.4 Cyclic voltammograms of ECF64 gold electroplating solution at the carbon nanoelectrode vs. Ag quasi-RE/CE. The scan rate was 50 mV s and the scanning started at 0 V. Gold ions undergo a reduction process at around -0.7 V whereas at -0.9 V oxygen was reduced. The amount of gold deposited increased at every CV cycle resulting in bigger electrode area and therefore larger measured currents (60 cycles shown).

Cyclic voltammetry (CV) was initially used to study the reactions taking place at the carbon electrode surface; in particular it was useful to determine the type of reactions (e.g.

electrodeposition) involved in the system as well as the potential at which they occur. **Figure 4.4** shows a series of cyclic voltammograms of the dual barrel carbon coated nanopipette in ECF 64 solution (diluted in DI water 1:10 v/v) between 0 V and -0.9 V at a scan rate of 0.05 V/s. An Ag electrode wire was used as Ag quasi reference electrode- counter electrode. In agreement with what has been reported in literature [17] ECF64, undergoes a reduction process at ~ 0.75 V. The deposition mechanism is thought to occur most likely through the dissolution of the gold sulphite ions and consequent adsorption of gold ions onto the carbon electrode surface according to the following reactions [17]:

$$[Au(SO_3)_2]^{3-} \rightarrow [Au(SO_3)_2]^{-} + SO_3^{2-} \tag{4.1a}$$

$$[Au(SO_3)_2]^{-} \rightarrow Au^{+}_{ads} + SO_3^{2-} \tag{4.1b}$$

$$Au^{+}_{ads} + e^{-} \rightarrow Au^{0} \tag{4.1c}$$

After every cycle the magnitude of the reduction peak increased suggesting that the nucleation process was taking place and the active area of the electrode was growing over the time. The peak observed at around -0.9 V in the CV was due to oxygen reduction. On pyrolytic graphite electrodes the oxidation process proposed for aqueous alkaline solution like ECF64 is given by [20]:

$$O_2 \rightarrow O_{2(ads)} \tag{4.2a}$$

$$O_{2(ads)} + e^{-} \rightarrow O^{-}_{2(ads)} \tag{4.2b}$$

$$2O^{-}_{2(ads)} + H_2O \rightarrow HO_2^{-} + OH^{-} \tag{4.2c}$$

Notably the assumption of considering the nature of the electrode as largely graphitic was justified by recent works [21, 22] where the Raman spectrum of carbon nanoelectrodes fabricated in similar manner revealed D and G bands at 1367 cm^{-1} and 1576 cm^{-1} respectively (G^1 band was not detected). Such peaks are characteristic of graphitic, disordered type of material.

Having successfully determined the optimal working conditions (e.g. potential and solution concentration) to electrodeposit gold on a carbon electrode, the attention was focused on integrating the procedure in the presence of a nanopore aperture. In other words, incorporating the gold electrode around the open channel preventing the deposition to obstruct the aperture. Although in principle, the open barrel could be metallized by depositing a fixed amount of gold, thus electrodepositing for a fixed amount of time using either cyclic voltammetry or chronoamperometry, a feedback mechanism that allowed real time monitoring of the process was not only preferable but also necessary. Since the pipette

to pipette variability was estimated to be around $10\% - 20\%$ of the measured conductance value, each electrodeposition would have different electrode active area and hence different starting conditions (pore size translates into different carbon electrode area). As a result, the nucleation and subsequently growth of gold deposits will vary from pipette to pipette albeit operating in the same conditions (e.g. solutions, reduction potential, deposition time).

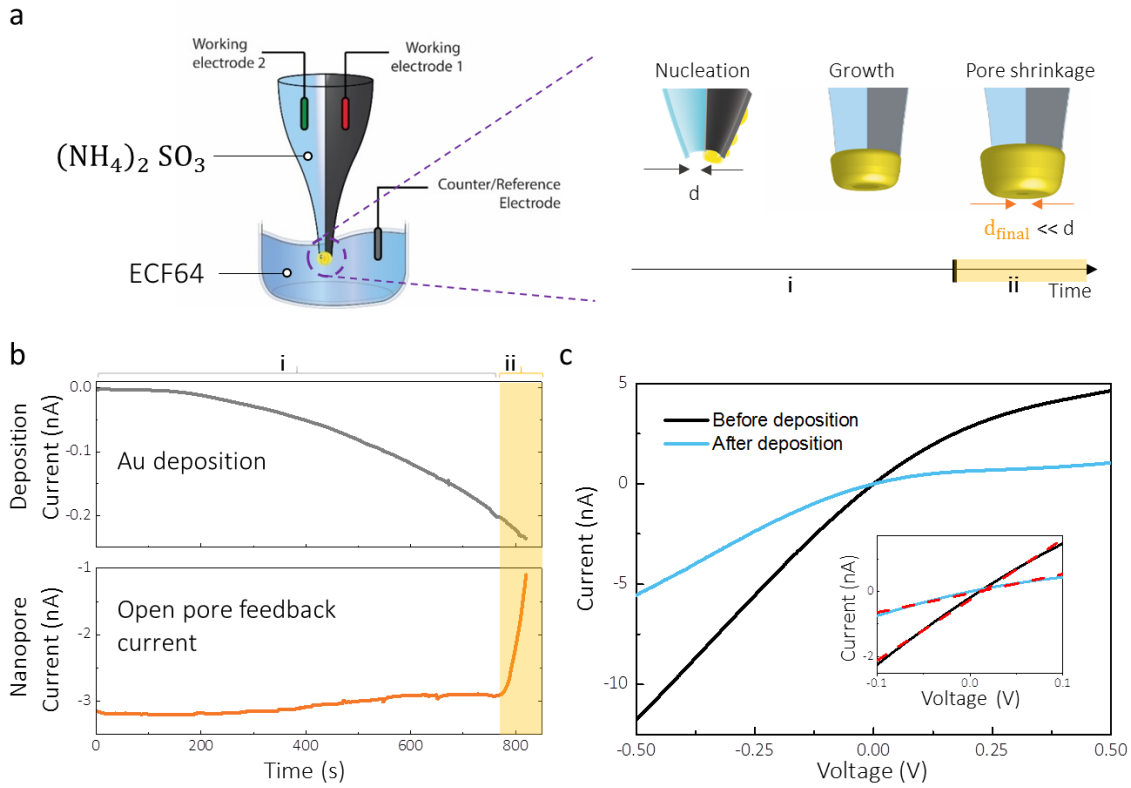

Fig. 4.5 Feedback controlled gold deposition. (a) Showing the schematic of the electrochemical deposition setup. The nanopipette was immersed in a bath containing ECF64 gold plating solution while the open barrel was filled with its supporting electrolyte (0.052 M NH_4AuSO_3). A feedback mechanism was established by using a bipotentiostat and a three electrodes configuration. Two independent WE were used: one Cu electrode, was inserted into the carbon-coated barrel and used for the gold deposition while the second WE consisting of a Ag wire was inserted in the other barrel and used monitor the ionic current flow across the open channel. A common Ag quasi quasi-RE/CE was placed in the bath. The carbon electrode was held at the reduction potential (*sim* -0.75 V) while the electrode in the open barrel was held at -0.1 V. The chronoamperometric traces recorded from the two WE (b) showed 2 distinct phases: in the first one, where nucleation and subsequently gold deposits formation took place, the deposition current increased in absolute value (top panel), while the open pore current remained almost constant (bottom panel). In the second phase, the open pore current decreased significantly as a result of gold material being deposited around the nanopore which eventually lead to a pore shrinkage. The former was particularly evident when comparing the IV characteristics before and after the deposition (c). The inset is showing a zoom of the IV linear region where linear fittings were performed. G = 18.63 $\pm$ 0.07 nS and G = 5.90 $\pm$ 0.06 nS before and after the deposition respectively.

A feedback mechanism was established by using a bipotentiostat and a three electrodes configuration as illustrated in the schematic in **Figure 4.5 a**. Two independent working electrodes (WE) were used: one electrode (consisting of a copper wire) was inserted into the carbon-coated barrel and used for the gold deposition while the second electrode (Ag wire) inserted in the open barrel which was filled with supporting electrolyte and used as

feedback. All electrochemical depositions were performed using a Ag quasi-RE/CE dipped in the ECF64 electrochemical bath.

The main idea consisted on monitoring the ionic current flow across the open channel while gold was electrodeposited on the carbon electrode. The reason why the ionic current flow across the nanopore was monitored is because as a result of the nucleation first, and the subsequent further growth and thickening of the gold layer, the nanopore will start shrinking (the two barrels are separated by a small gap of $\sim$ 20 nm). Therefore, by monitoring the ionic current it is possible not only to avoid pore blocking but to also actively tune it to the desired diameter. Notably, as it will be shown in the optical characterization later in this chapter, the gold growth is not restricted at very end of the pipette tip but it rather extends for several hundreds of nm, forming a sort of globular structure with a nanometric channel embedded on it. The former will have smaller diameter than the initial nanopipette diameter.

A typical feedback-guided deposition is shown in **Figure 4.5 b**. The procedure was performed using i-t chronoamperometry (sampling time was set to 1 s): the deposition potential on the carbon electrode was kept constant at -0.73 V while -0.1 V was applied to the open barrel (notably this potential value was arbitrary however a low voltage was chosen to minimize interferences with the deposition process). The absolute value of the electroplating current gradually increased over the time indicating successful nucleation and progressive expansion of the electrode surface area as a result of the deposition. On the other side the nanopore current remained almost constant for a long period of time ($\sim$ 750 s in the specific case) and it was then followed by a sharp transition where the current magnitude quickly decreased. This sudden variation was due to gold being progressively deposited around the nanopore aperture leading to a modulation in the pore dimension and therefore in the measured current. At this point the deposition was halted.

This reduction in pore size was evident when comparing the IV characteristics acquired between $\pm$ 0.5 V before and after the deposition. As shown in **Figure 4.5 c** the conductance over the linear region $\pm$ 0.1 V was calculated to be 18.63 $\pm$ 0.07 nS 5.90 and $\pm$ 0.06 nS before and after the deposition respectively leading to an overall variation of $\sim$ 70%.

A more careful analysis of the IV revealed the presence of the rectification phenomenon: experimentally the magnitude of the ionic current flow at two biases which are equal in magnitude but opposite in sign did not coincide. Such non-linear behaviour was explained with the ion accumulation-depletion model [23] where the flux of anions (SO_3^{2-}) in one direction differs from flux of cations (NH_4^+) in the other direction as a direct consequence of the charges present on the nanopipette wall. For instance when a positive potential was applied to the Ag electrode inside the nanopipette relative to the Ag electrode placed in the bath, NH_4^+ ions moved from the nanopipette to the bath while SO_3^{2-} moved in the opposite

direction. As a result of the hydroxyl groups present on the surface (ECF64 was an alkaline solution with a pH of $\sim$ 8.0), SO_3^{2-} ions were electrostatically rejected. Therefore SO_3^{2-} were depleted within the first few tens of nanometres of the nanopore channel, leading to an overall decrease of conductivity and hence a decrease in the measured current. In general this phenomenon is more pronounced when the width of the EDL region is comparable with nanopore aperture [24] as in the case documented herein.

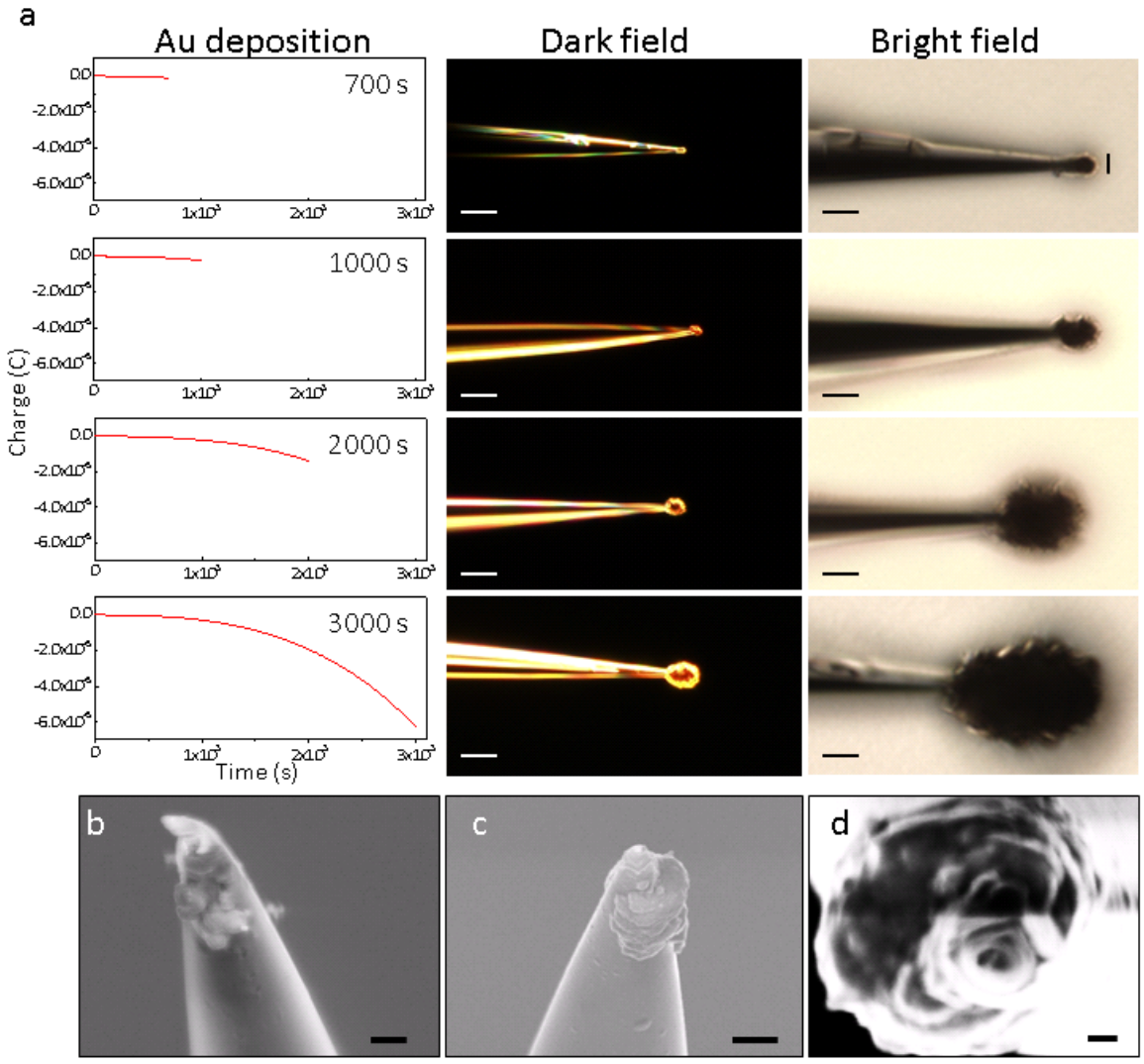

Fig. 4.6 Optical characterization of gold deposited nanopipettes. a) A series of time dependent depositions were used to study how the deposited gold material expanded around the nanopipette tip. b) SEM micrograph of a nanopipette tip deposited for 50 s and c) and d) 400 s. Scale bars: a) dark field 30 μm, bright field 3 μm b,c) 500 nm d) 100nm.

A series of time dependent depositions were used to study how the deposited gold material physically developed on the nanopipette tip. As shown in **Figure 4.6 a** a set of nanopipettes were electrodeposited under the same conditions (e.g. voltage applied and electroplating

solution concentration) for 700 s, 1000 s, 2000 s, 3000 s, subsequently rinsed in DI water and imaged in dark and bright field mode. Gold material appeared to grow around the tip as a blob with an ellipsoidal profile: x-y axis dimensions ranged from $1.5 \pm 0.3\ \mu m$ and $2.5 \pm 0.3\ \mu m$ at 700s to $9 \pm 0.5\ \mu m$ and $12 \pm 0.5\ \mu m$ at 3000s.

The SEM micrographs (**Figure 4.6 c-e**) confirmed that nucleation took place at the very end of the tip followed by the growth of these nucleus generating a more uniform gold blob wrapped around the tip. Only in a later stage, gold was deposited in the proximity of the open pore channel causing its shrinkage. This was in good agreement with the our previous findings where the nanopore ionic current was measured to be constant for a long period of time followed by a sharp transition which represented the point where the electrodeposited material effectively shrunk the pore.

It was observed that the time required for this point varied considerably from pipette to pipette. As illustrated in **Figure 4.7 a**, the segment where nanopore feedback current was measured to be constant ranged from 600 s to 1000 s. This behaviour was totally expected and two main factors were identified as responsible of such a high variability.The first one was the intrinsic pipette to pipette differences in terms of pore size, given by the laser puller which was extremely sensitive to temperature and humidity. The second factor was the carbon deposition step, which could generate carbon electrodes with slightly different active area.

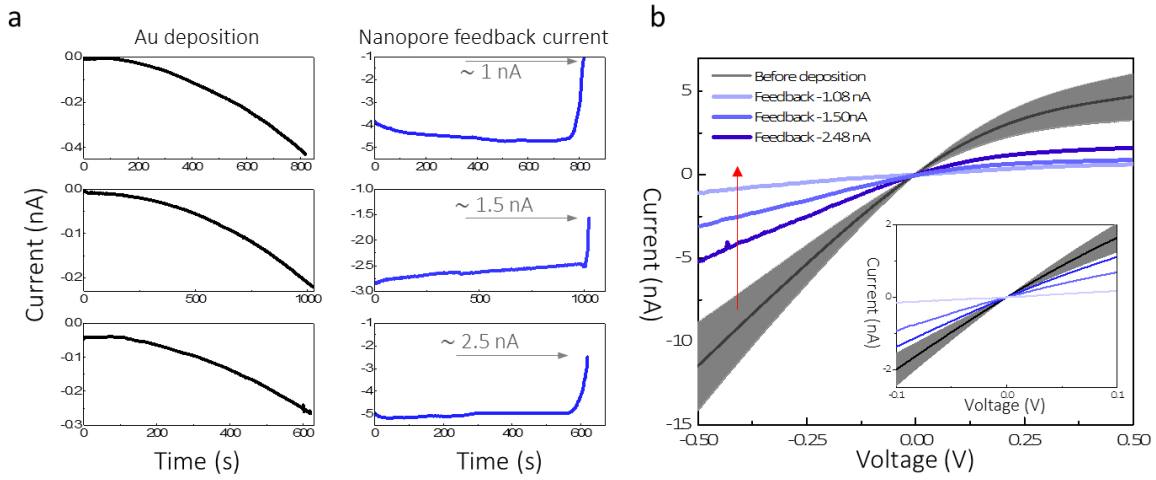

Fig. 4.7 Tuning nanopore size via feedback controlled feedback depositon. (a) Showing the current deposition trace and open pore current feedback for three different nanopipettes. The deposition process was halted at three distinct values of feedback current: ∼ -2.5 nA, ∼ -1.5 nA and ∼ -1 nA. As shown in (b), these values were correlated to different pore sizes. The smaller the feedback current value, the smaller the final nanopore aperture thus the smaller the ionic current flow (or conductance) measured. Before the deposition the mean conductance was calculated to be 18.30 ± 0.07 nS; while it decreased to 12.40 ± 0.05 nS, 8.13 ± 0.04 nS, 1.62 ± 0.01 nS for feedback current halted at ∼ -2.5 nA, ∼ -1.5 nA and ∼ -1 nA respectively. The inset shows a zoom on the linear regime.

These considerations reinforced the idea of having such a feedback mechanism. In fact, by halting the deposition process at specific feedback current level it was possible to

precisely control the pore size as shown in **Figure 4.7 a,b**. Before the deposition nanopipettes exhibited a mean conductance of 18.30 $\pm$ 0.07 nS while the this value was calculated to be 12.40 $\pm$ 0.05 nS, 8.13 $\pm$ 0.04 nS, 1.62 $\pm$ 0.01 nS when the deposition was stopped at feedback current equalt to $\sim$ -2.5 nA, $\sim$ -1.5 nA and $\sim$ -1 nA respectively. This achievement represented a remarkable advantage because, as already demontrated, shrinking the pore, thus making it comparable to the analyte dimension, makes it more sensitive [25] (notably, the ionic current flow across a nanopore as well as any modulation caused by the passage of an analyte are a function of its diameter according to the equation 1.8).

To sum up, the feedback method allowed to transform a simple nanopore channel into a nanofluidic transistor by integrating a gold electrode around its aperture. At the same time, and with no-extra step in the fabrication, the process allowed to tune the nanochannel size to the desired volume with an evident gain in terms of single molecule sensitivity and SNR.

4.3.2 Single molecule detection

In this section the newly fabricated NanoFET was used in a single molecule detection study. In particular, the behaviour of DNA when translocating across the pore was studied before and after gold deposition. All of the reported translocation experiments were carried out using 10 kbp DNA and the ionic strength of the solution was kept constant throughout all experiments at 100 mM KCl.

The first set of experiments were performed with carbon deposited nanopipette (e.g. no gold was present on the surface). 400 pM 10 kbp was injected inside the open barrel. The ionic strength condition was kept symmetrical between the nanopipette and the bath. Importantly, the carbon electrode was left floating (e.g. not connected to any piece of equipment). As shown in the ionic current recordings in **Figure 4.8 a-b** single molecule events were detected in enhancement (e.g. Δ G > 0) when the bias applied between the electrode in the bath and the electrode in nanopipette was < 0 V.

Dwell times decreased while mean peak current values increased with the voltage applied. For instance, the dwell time was calculated to be 0.33 $\pm$ 0.13 ms and 0.18 $\pm$ 0.06 ms at -300 mV and -800 mV respectively; the faster translocation velocity was explained with the higher electric field and therefore a stronger electrophoretic force applied to DNA molecules. The peak current shifted from 24.40 $\pm$ 2.49 pA at -300 mV to 68.05 $\pm$ 14.42 pA at -800 mV whereas for the same voltages the equivalent charge deficit remained almost constant: 8.44 $\pm$ 2.19 fA s and 10.57 $\pm$ 3.15 fA s (**Figure 4.8 c**). This behaviour was perfectly consistent with translocations of DNA molecules of similar length, in similar ionic strength solutions and performed using uncoated quartz nanopipettes [26, 25, 27] (notably similar results were also achieved in chapter 2 using dual barrel nanopipettes without filaments).

These findings suggested that the open barrel nanopipette was not affected by the carbon deposition step which most certainly was confined to the other barrel only as confirmed by the SEM micrographs shown earlier (**Figure 4.3**).

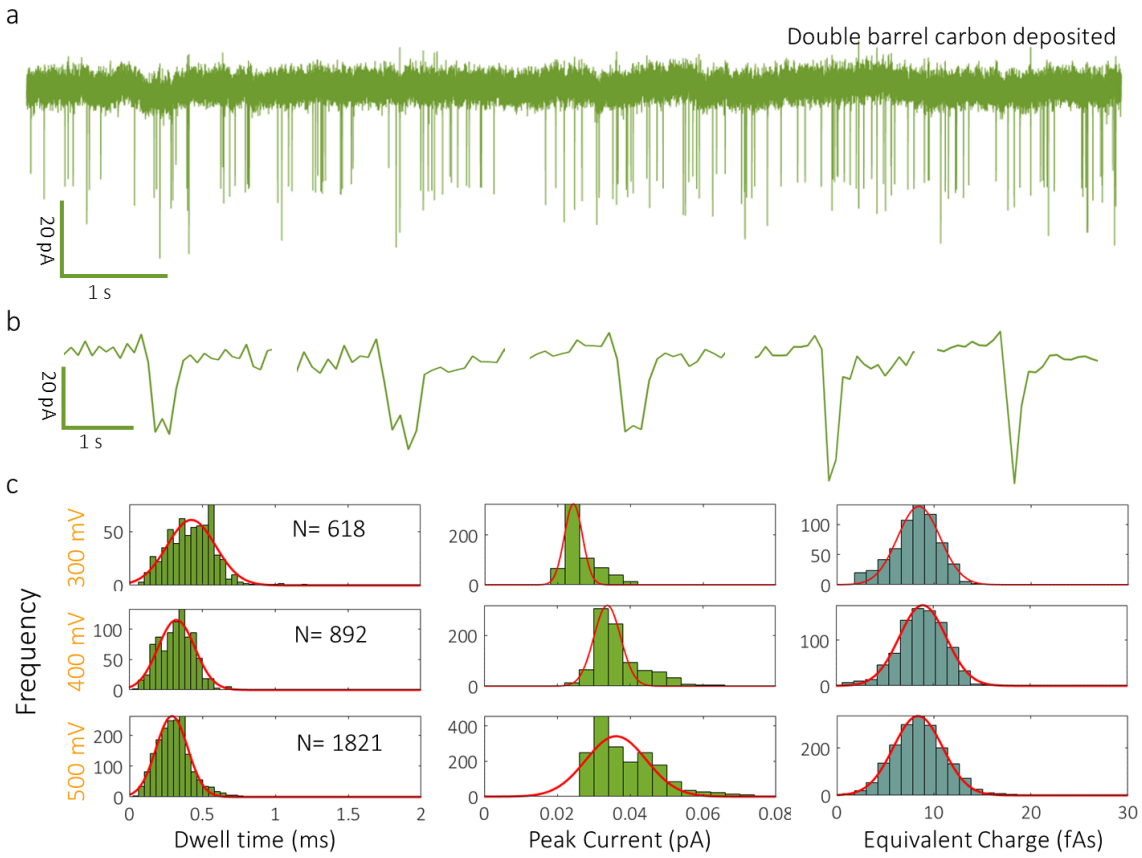

Fig. 4.8 10 kbp DNA translocation performed on dual barrel carbon coated nanopipette at 100 mM KCl TE pH 8.0. (a) Ionic current trace and (b) single translocation events recorded at -400 mV voltage applied. (c) showing histograms for dwell time, peak current and equivalent charge deficit for 3 different voltages: -300 mV, -400 mV, -500 mV. Mean dwell times were calculated to be 0.43 $\pm$ 0.17 ms, 0.33 $\pm$ 0.13 ms and 0.29 $\pm$ 0.11 ms; the mean peak currents were calculated to be 24.40 $\pm$ 2.49 pA, 33.80 $\pm$ 3.89 pA and 36.16 $\pm$ 8.3 pA; the mean equivalent charge was calculated to be 8.44 $\pm$ 2.19 fA s, 8.92 $\pm$ 2.41 fA s and 8.38 $\pm$ 2.53 fA s. As expected from literature, the peak current increased with the voltage applied whereas the dwell time decreased as a result of an increased electrophoretic force acting on DNA molecules (e.g. higher translocation velocity).

A different scenario was observed for the gold coated nanopipettes. To be consistent with the previous measurements, the gate electrode was left floating. When a negative bias was applied between the electrode in the pipette and the one in the bath, 10 kbp DNA was electrophoretically transported across the pore and events were clearly visible in the ionic current (**Figure 4.9 a,b**). The smaller conductance reflected the narrower pore size (G = 4.84 $\pm$ 0.10 nS for the gold deposited compared to G = 7.78 $\pm$ 0.03 nS for the carbon coated nanopipette), and the rectification increased due to the EDL being more prominent (**Figure 4.9 c**). In addition to the quartz surface, also the gold surface was negatively charged in KCl solutions due to Cl^{-} ions adsorption [28, 29]. The noise was only marginally higher.

As shown in **Figure 4.9 d**, at the same applied voltage the measured peak current for gold coated nanopipette was significantly higher: for instance at 700 mV, the mean peak was calculated to be 139.2 $\pm$ 11.5 pA which corresponded to an increase of $\sim$ 150 % compared to the carbon pipette where the mean peak current was calculated to be 54.1 $\pm$ 12.8 pA.

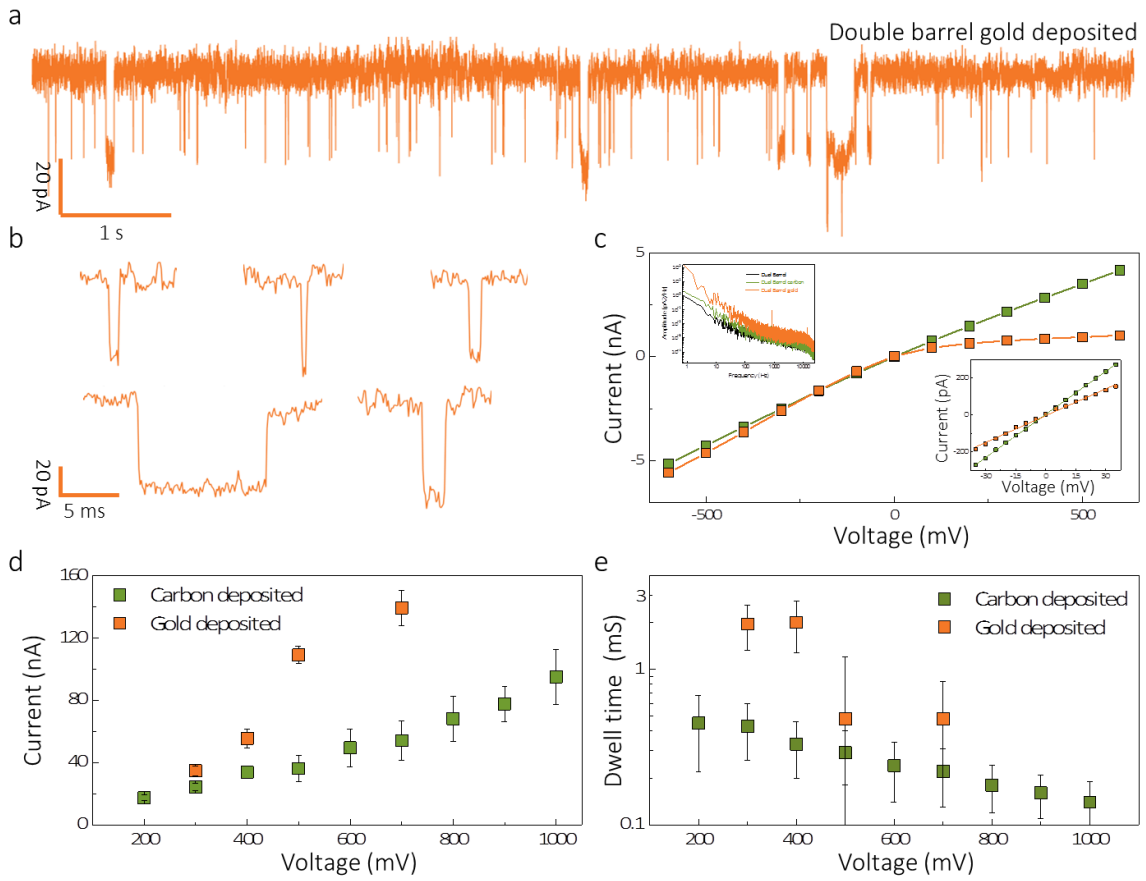

Fig. 4.9 10 kbp DNA translocations performed with dual barrel gold coated nanopipettes. (a) Showing ionic current recordings performed in 100 mM KCl, pH 8.0 with dual barrel gold coated nanopipettes at -400 mV voltage applied. The gold electrode was left floating for the entire recording. DNA (400 pM) was translocated from inside the nanopipette to the bath and (b) single molecule events were detected. (c) IV characteristics revealed a smaller conductance and a more pronounced rectification factor for the gold coated nanopipette compared to the carbon coated nanopipette (G = 4.84 $\pm$ 0.10 nS and G = 7.78 $\pm$ 0.03 nS for the gold deposited and carbon deposited respectively). These observations were the result of a smaller nanopore aperture, thus smaller measured ionic current. The higher rectification was due to Cl^- ions adsorption in the gold surface which resulted in an overall increased permselectivity behaviour of the nanochannel. The insets shows the power spectral densities (top-left) of ionic current signals of a gold deposited nanopipette versus a carbon deposited one and a zoom of the conductance in the linear regime (bottom-right). (d) Peak current and (e) dwell time comparison between a carbon coated nanopipette and a gold deposited nanopipette.

The duration of translocation events appeared to be only moderately longer: at 300 mV the mean dwell time was calculated to be 1.95 $\pm$ 0.63 ms and 0.43 $\pm$ 0.18 ms for gold coated and carbon deposited nanopipette respectively. In good agreement with literature, when the pore diameter decreases DNA translocations are partly governed by interactions with the nanopore walls [30] resulting in longer translocation times.

The opposite scenario, where DNA molecules were translocated from the bath to the nanopipette was also analyzed. DNA molecules were initially injected in the bath and electrophoretically translocated when a positive bias was applied across the pore. Results were comparable and a smaller pore was at the base of a significantly higher SNR for the events detected with gold coated nanopipettes compared to the carbon-coated ones. As illustrated in **Figure 4.10 a**, at the same voltage applied of 200 mV, events went completely undetected with the carbon coated nanopipette while with the gold deposited nanopipettes, single molecule events were clearly visible in the ionic current trace. with mean dwell time of 0.83 $\pm$ 0.6 ms and SNR equals to 20.4 $\pm$ 6.3 **Figure 4.10 b-c**. It was observed experimentally that DNA molecules got stacked more frequently when using a gold coated nanopipette, irrespectively of the translocation direction (e.g. from inside the nanopipette to the bath and vice-versa).

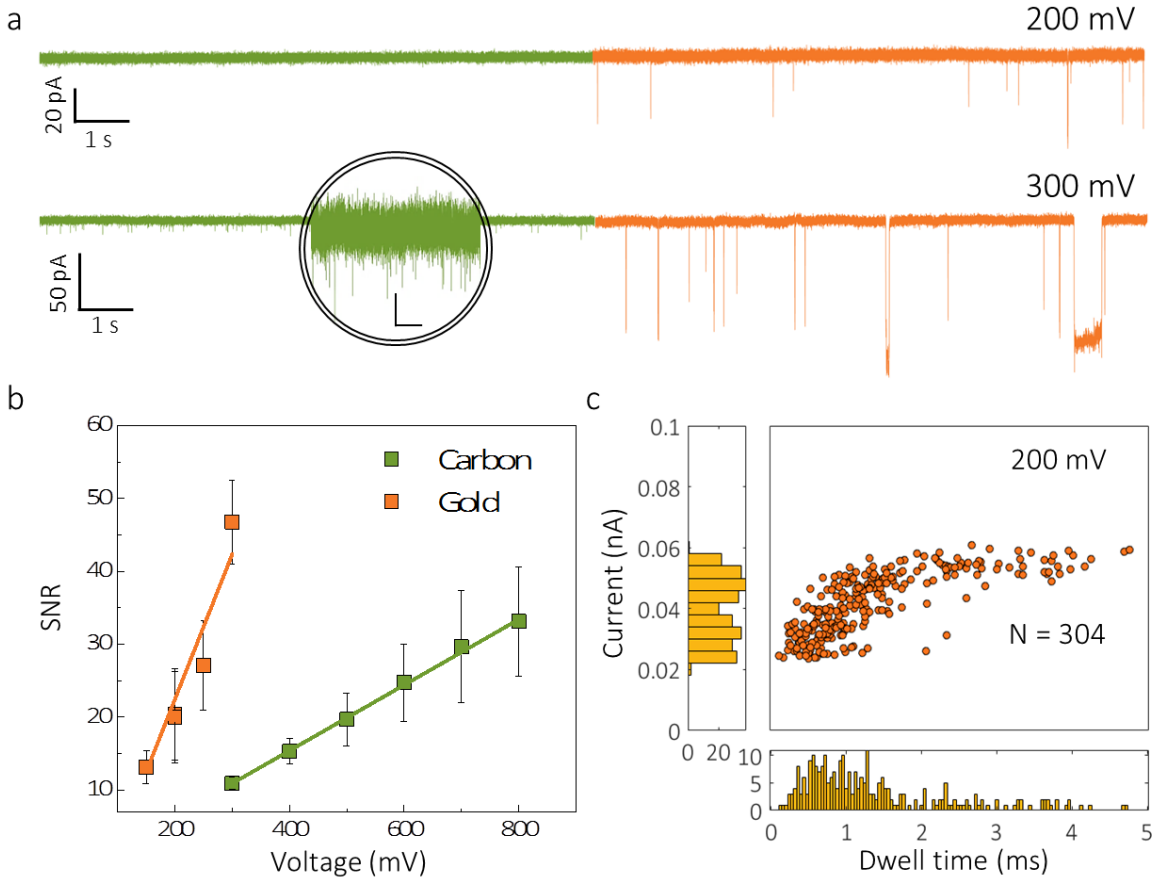

Fig. 4.10 Comparison between carbon coated (green) and gold coated (orange) dual barrel nanopipette. 10 kbp DNA molecules were translocated from the bath to the nanopipette and the ionic current traces (a) were recorded at 100 mM KCl at 200 mV and 300 mV voltage applied (top and bottom traces respectively). Due to the smaller pore size, the mean peak current generated by DNA molecules threading across the gold coated pore was higher than the carbon deposited nanopipette leading therefore to higher SNR values (b). The mean dwell time of the translocations performed with gold coated nanopipette were only marginally higher (c) with the vast majority of the events being detected around $\sim$ 1 ms. Scale bars: zoom in the bottom trace of panel (a): 0.5 s, 5 pA.

4.3.3 Gating ionic transport

In general, in ionic FET architectures the gate potential is used to tune the surface charge leading to electric-field mediated control of the electroosmotic flow in the nanochannel [31, 32].

For this reason, experiments were carried out to characterized the ionic transport properties of gold deposited nanopipettes when a bias was applied to the gate electrode. In this case, the experimental setup consisted of two independent recording channels: one was used to control the gate voltage while the second channel was employed to apply a voltage and record the ionic current flowing across the nanopore. A common electrode acting as ground was placed in the bath. Both the nanopipette and the bath consisted of 100 mM KCl solution buffered at pH 8.0.

In **Figure 4.11** are illustrated the field effect modulation of the open pore current for gate voltages V_g ranging from -500 mV to +400 mV. In particular, when $V_g < 0$ was applied the ionic current, thus the conductance, was considerably reduced whereas at $V_g > 0$ the conductance was marginally increased. For instance, in the case illustrated in **Figure 4.11 a** G = 3.82 $\pm$ 0.17 nS, G = 2.69 $\pm$ 0.09 nS and G = 4.1 $\pm$ 0.18 nS for V_g = 0 mV, V_g = -400 mV and V_g = +400 mV respectively. In other words, at V_g = -400 mV the conductance dropped by approximately 30% whereas at V_g = +400 mV it increased by only 7%. In some cases, as shown in **Figure 4.11 b** the ionic current flow was completely unresponsive to the gate voltage when a positive voltage was applied between the nanopipette and the bath. Notably this gating effect was attributed to the active role played by the gold channel electrode. Indeed, no ionic current modulation was recorded when a similar experiments were carried out with bare carbon deposited nanopipette.

The physical mechanism behind the ionic current modulation has been already described for similar cases [33–35]. The general idea consisted on tuning the potential, thus the charges and the counter-ions concentration around the nanochannel walls by applying a bias to the gate electrode. In particular, when a negative voltage was applied across the nanopore without any V_g bias, K^+ ions move from the nanopipette to the bath while Cl^- ions do the opposite. However for negative V_g, Cl^- ions were electrostatically repulsed whereas K^+ were attracted. In other words the gate electrode modulate the EDL thickness by locally changing the concentration of both ionic species. As Cl^- were repulsed from the pore proximity, electroneutrality forced the concentration of K^+ to decrease as well. A further increase in the gate voltage resulted in a wider ion-depleted region which decreased even further the number of K^+ ions available for transport hence the overall ionic current.

In case of $V_g > 0$, we were supposed to visualize the opposite scenario where the ion-depleted region decreased leading to a stronger ion current across the pore. This was not,

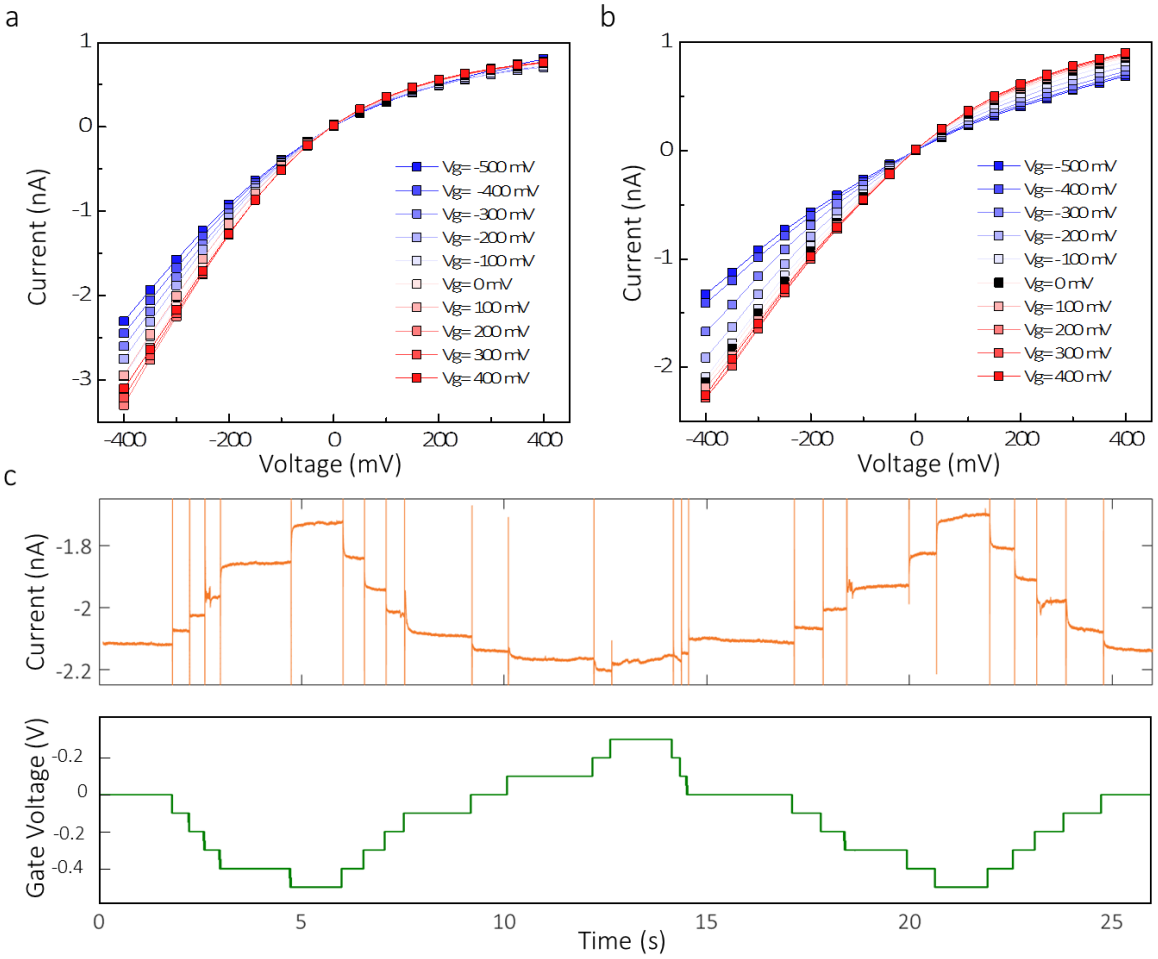

Fig. 4.11 Conductance modulation in dual barrel gold coated nanopipette. Gold coated nanopipette were immersed in a bath of 100 mM KCl solution at pH 8.0 identical to the solution being injected in the open barrel. (a), (b) IV characteristics acquired by holding the gate voltage at a fixed potential and swiping the bias across the nanopore between -500 mV and +400 mV. The ionic current flow was modulated when applying a bias to the gold electrode. In particular the nanopipette was more responsive (meaning that an higher current variation was recorded), when applying a negative voltage to the gate electrode; in contrast a positive gate voltage caused marginal, and sometimes irrelevant variation in the ionic current. (c) Showing an example of ionic current trace were the bias across the pore was held at -300 mV (top panel) while the gate voltage was varied between -500 mV and 300 mV(bottom panel).

however, what we observed experimentally. At $V_g > 0$, the current across the pore was only marginally higher or, as recorded in some cases not affected at all. Perhaps higher gate bias were necessary to overcome the negative charges present at the surface. However voltages above 500 mV were avoided due to rapid gold electrode degradation, most probably as a result of electrochemical reactions. In addition one should consider the fact that the EDL thickness at 100 mM KCl was calculated to be smaller than 1 nm; therefore a positive bias, which diminished the overall negative charge of the quartz surface and therefore the EDL thickness would not be appreciated at this salt concentration. Most likely operating at lower salt concentration will produce a more significant change also at positive voltages.

Manipulation of DNA translocation

To investigate the impact of the electric field applied to the gate electrode a series of translocation experiments were carried out using 10 kbp DNA in 100 mM KCl solution. The DNA was initially injected in the open barrel. Similarly to what has been shown above, the gate electrode and open barrel were controlled by two independent channels. **Figure 4.12** shows a snapshot of the results obtained. At V_g = 0 mV as well as positive gate voltage (V_g =

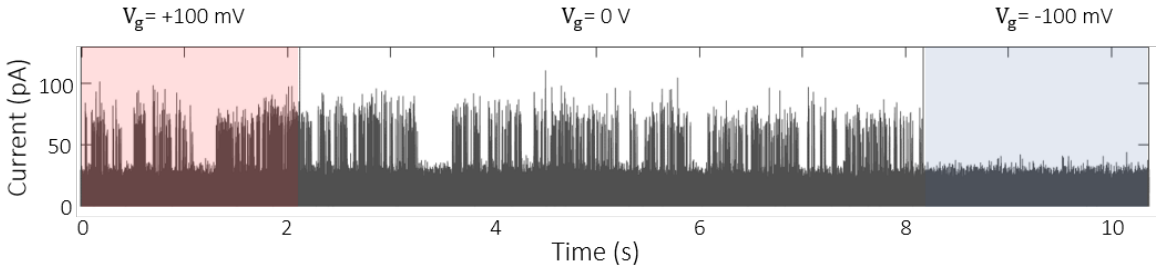

Fig. 4.12 Modulating the translocation of 10 kbp DNA across a three-electrodes nanopipette system. The dual barrel gold coated nanopipette is filled with 100 mM KCl TE pH 8.0 with 400 pM 10 kbp DNA. The nanopipette is immersed in a bath of similar ionic strength where a common reference Ag AgCl electrode is used for both the open barrel and the gate channel which control the nanopore electrode. When a negative bias was applied between the open barrel and the bath, translocations were detected when V_g = 0 V or $V_g > 0$ V whereas they were inhibited when $V_g < 0$ V.

+100 mV), single molecule events (recorded in current depletion) corresponding to 10 kbp translocations were clearly visible; whereas at negative gate voltage (V_g = -100 mV) no translocation event was recorded. In both cases a constant potential of -300 mV was applied between the open barrel and the bath. Further analysis revealed that at $V_g > 0$ V, dwell times and mean peak current of DNA translocations were completely comparable to the events recorded when V_g = 0 V as shown in **Figure 4.13 a-c** (peak current $\sim$ and dwell time $\sim$ in both cases). This appeared to be in contrast with what we expected. In particular when a positive voltage is applied to gate one would expect DNA molecules to be subjected to a strong Coulombic attraction leading to a reduced translocation velocity of the molecule

across the pore. However this was not the case. A partial explanation of this results were anticipated in **Figure 4.11**, where it was observed that a positive potential had a negligible impact on the open pore current. Perhaps much higher potential (>1 V) would be required to achieve longer translocation times. For instance, a nanopore-FET study [36] demonstrated that λ-DNA was decelerated by approximately one order of magnitude, when 9 V were applied to the gate electrode which covered a 20 μ m long , 50 nm wide channel.

Notably such a high potentials were not compatible with our architecture due electrochemical reactions and gas generation at the electrode surface. Experiments were carried out up to V_g = 300 mV, however no significant effect was observed. Another key aspect to take into account was the pore dimensions. To avoid DNA irreversibly blocking the pore while threading through, relatively large nanopores were employed (the gold deposition was stopped when the feedback current was higher than 1 nA). However, to achieve a stronger FET effect, smaller apertures would be preferable.

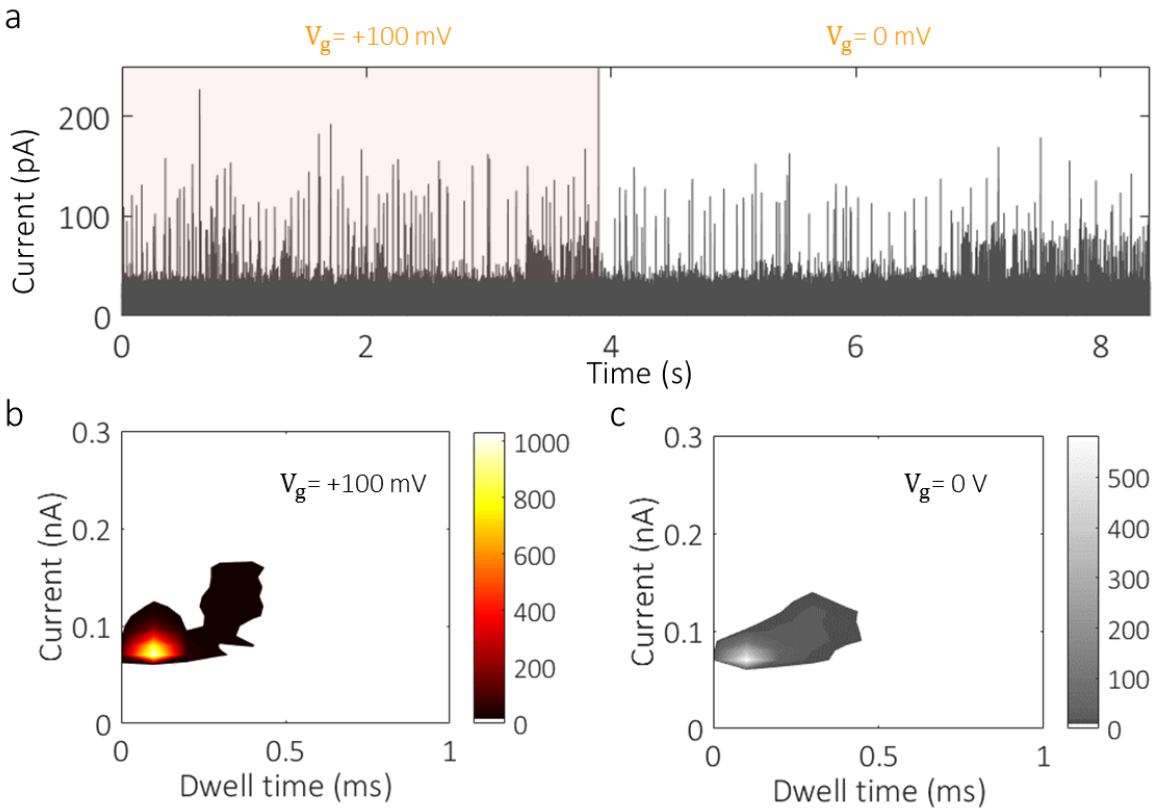

Fig. 4.13 10 kbp DNA translocations when V_g > 0 V. (a) Baseline-adjusted, ionic current trace of 10 kbp DNA (400 pM injected inside the nanopipette) translocations performed in 100 mM KCl at pH 8.0 when V_g = 100 mV and V_g = 0 mV. In both cases the bias across the pore was held at -400 mV. (b) and (c) showing the peak current versus dwell time distribution for V_g = 100 mV and V_g = 0 mV. No significant difference was observed between the distributions (peak current $\sim$ 70 pA and dwell time $\sim$ 0.1 ms in both cases) meaning that a positive gate voltage produced negligible effects on the transloction dynamics.

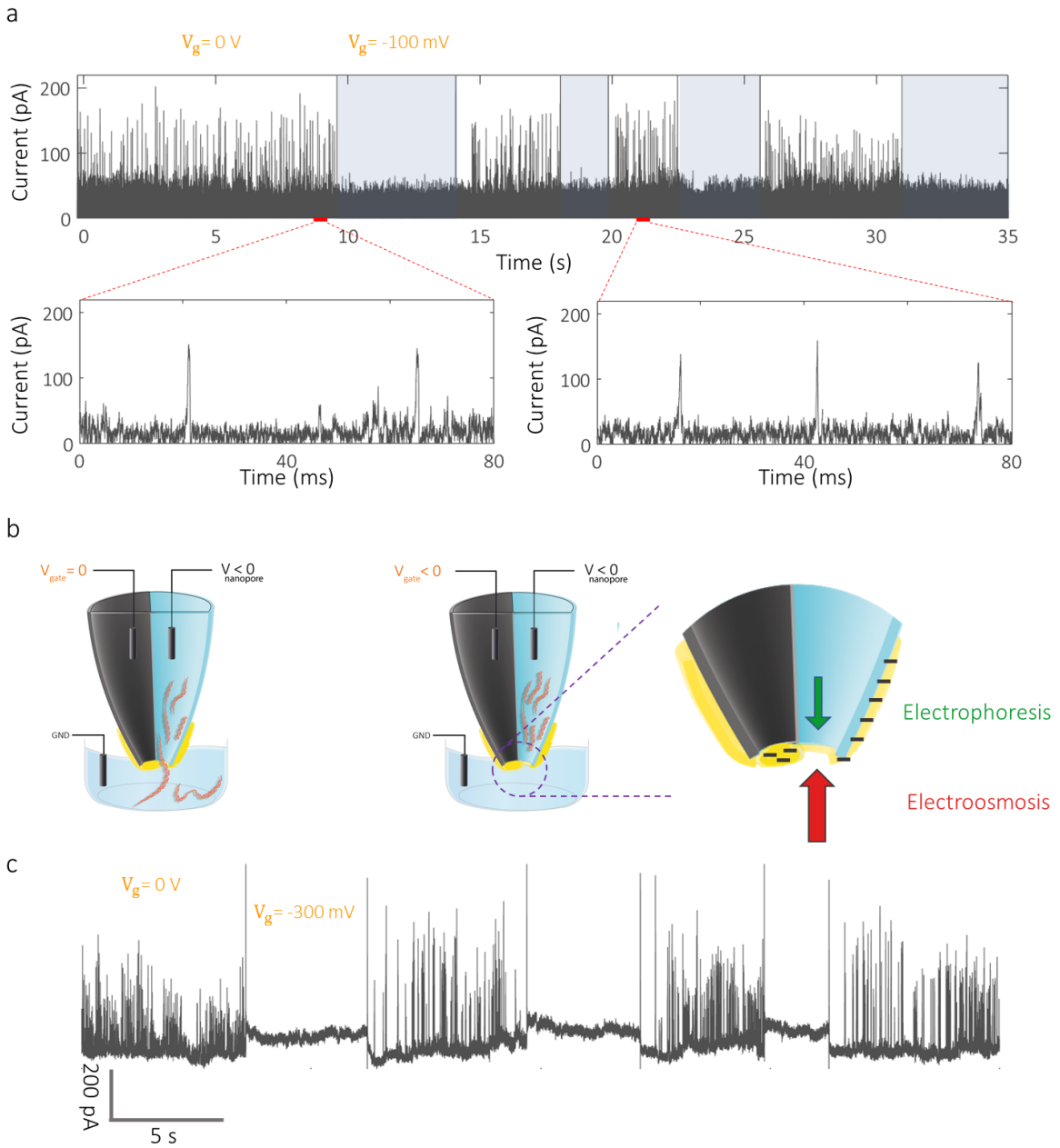

Fig. 4.14 10 kbp DNA translocations when V_g < 0 V. (a) Baseline-adjusted, ionic current trace of 10 kbp DNA translocations performed in 100 mM KCl at pH 8.0 varying the gate voltage while helding at a constant value (-400 mV) the potential across the channel. When V_g = 0 mV DNA molecules were normally translocated across the pore whereas at V_g = -100 mV translocation were inhibited. This mechanism (b) was explained with a combination of electro-osmotic flow (EOF) acting in the opposite direction of the electrophoretic flow and it was also due to the electrostatic repulsion between DNA and the negatively charged gate electrode. The combination of these two effects resulted in a rejection of DNA molecules from approaching, thus threading through, the pore. (c) Ionic current trace when -600 mV was applied between the open barrel and the bath. In this case the EOF flow and electrostatic repulsion generated by -100 mV applied to the gate electrode was not sufficient to stop DNA from translocating whereas, at V_g = -300 mV the gating effect was successfully restored with translocation being completely halted. The voltage applied to gate electrode did not affect the noise levels of the ionic current measurements across the open barrel.

When applying a negative voltage to the gold electrode, translocations ceased instantly. Effectively, the gate electrode acted as a switch. As illustrated in **Figure 4.14** we performed a series of ON/OFF experiments where the gate voltage was continuously varied between -100 mV and 0 mV whereas the open voltage in the open barrel was held at -400 mV. Notably as soon as V_g was reset to 0 mV translocations resumed without any noticeable difference in dwell time or peak current (**Figure 4.14a**).

The explanation was most likely related to a modulation of the electrosmotic flow inside the channel alongside the electrostatic repulsion between DNA and gate electrode. The gate attracted K^+ ions to the pore walls to compensate the increased negative charge resulting from the negative bias. As a consequence, the EDL thickness increases leading to a much stronger EOF. The former competes with electrophoretic flow because it is directed in the opposite direction. Therefore when the EOF is stronger than the electrophoretic flow, the pore rejects DNA molecules from entering it (**Figure 4.14b**).

This explanation was further confirmed when -600 mV was applied between the open barrel and the bath. In this case the EOF generated by -100 mV applied to the gate electrode was not sufficient to stop DNA from translocating whereas, at V_g = -300 mV DNA the gating effect was successfully restored as shown in **Figure 4.14 c**. This molecular switch type of behaviour was demonstrated to be reproducible, reversible and stable over multiple cycles (the time of both states was also varied without without any observable effect). Interestingly, it was observed that as a result of a prolonged off-state, where translocations were inhibited with $V_g < 0$, the DNA translocation rate of the following on-state increased. Perhaps, this might be related to a sort of DNA accumulation in close proximity of the pore entrance, albeit this hypothesis should be further investigated with more experimental results (for instance studying the impact of parameters such as magnitude of V_g, time of on-state and off-state, DNA concentration and DNA length on the event rate).

4.4 Conclusions

In conclusion we have presented a novel class of nanopore-based ionic-FET sensor based on dual barrel quartz nanopipettes that actively manipulate DNA molecules. The fabrication process, which was quick, robust and cost-effective, was based on pyrolysis of carbon from butane followed by a feedback-driven gold electrochemical deposition around the nanopore aperture. The newly developed feedback mechanism had a twofold impact. On one hand it convert a conventional nanopore into a FET-nanopore. On the other hand allowed to tune, in real time, the nanopore aperture to the desired dimensions which are normally associated with the analyte under investigation. Another consequence is that this strategy

overcomes all the limitations associated with the current fabrication methods for precisely positioning metal electrodes at the nanopore entrance. Gold is not the only material that could be electrodeposited onto the carbon nanoelectrodes. The generality of the method presented here could be extended to a vast library of materials with different physico-chemical properties (among others: platinum, copper, nickel, polypyrrole, polyaniline). Tuning the chemical properties adds an extra degree of freedom in the platform. Functionalizing the nanopore-FET surface could be used for improving not only the transport but also the selectivity. This could be achieved with a self assembled monolayer onto the gold surface or for instance, by embedding antigens or alternatively nucleic acids on a polymeric matrix or alternatively an electrodeposited hydrogel.

We demonstrated that, by applying a voltage to the gate electrodes, it was possible to modulate the charge density inside the nanopore channel and thus the overall ionic current conductance. After validating the field-effect capacity, we investigated the device effectiveness on detecting and actively controlling single molecule. Towards this goal, translocation experiments were carried using DNA molecules. Initially, in the absence of gate voltage applied, we showed that this newly developed nanopore-FET devices exhibited an improved SNR with respect conventional nanopore. This was associated with the diminished pore dimension resulting from the gold deposition.

Finally the nanofluidic transistor devices were used to manipulate DNA translocations using the gate electrode and thus applying a transverse electric field across the nanopore aperture. The findings showed that the gate electrode acted as a molecular switch and, depending on the bias applied, DNA molecules were enabled or prevented to translocate across the aperture.

Altought these results demonstrate that it is possible to actively modulate the ion flow as well as the molecules dynamics inside the nanopore channel, a follow up study should be conducted to explore the possibility of using this nanofluidic transistor to reduce the analyte translocation velocity across the pore and thus increasing the amount of information extracted from a single molecule.

References

[1] A. K. Vijh, "Some fundamental analogies between solid, molten and aqueous materials: application of the concepts of energy levels and the band theory of solids," *J. Mater. Sci.*, vol. 10, no. 1, pp. 123–135, 1975.

[2] B. Lovrecek, A. Despic, and J. O. M. Bockris, "Electrolytic Junctions with Rectifying Properties," *J. Phys. Chem.*, vol. 63, no. 5, pp. 750–751, 1959.

[3] S. A. Gajar, "An Ionic Liquid-Channel Field-Effect Transistor," *J. Electrochem. Soc.*, vol. 139, no. 10, p. 2833, 1992.

[4] H. Chun and T. D. Chung, "Iontronics," *Annu. Rev. Anal. Chem.*, vol. 8, no. 1, pp. 441–462, 2015.

[5] Y. Ai, J. Liu, B. Zhang, and S. Qian, "Field Effect Regulation of DNA Translocation through a Nanopore," *Anal. Chem.*, vol. 82, no. 19, pp. 8217–8225, 2010.

[6] D. Son, S. Y. Park, B. Kim, J. T. Koh, T. H. Kim, S. An, D. Jang, G. T. Kim, W. Jhe, and S. Hong, "Nanoneedle transistor-based sensors for the selective detection of intracellular calcium ions," *ACS Nano*, vol. 5, no. 5, pp. 3888–3895, 2011.

[7] S. Wu, F. Wildhaber, A. Bertsch, J. Brugger, and P. Renaud, "Field effect modulated nanofluidic diode membrane based on Al 2O3/W heterogeneous nanopore arrays," *Appl. Phys. Lett.*, vol. 102, no. 21, pp. 1–5, 2013.

[8] W. Guan, S. X. Li, and M. a. Reed, "Voltage gated ion and molecule transport in engineered nanochannels: theory, fabrication and applications.," *Nanotechnology*, vol. 25, no. 12, p. 122001, 2014.

[9] W. L. Hsu and H. Daiguji, "Manipulation of Protein Translocation through Nanopores by Flow Field Control and Application to Nanopore Sensors," *Anal. Chem.*, vol. 88, no. 18, pp. 9251–9258, 2016.

[10] A. P. Ivanov, E. Instuli, C. M. McGilvery, G. Baldwin, D. W. McComb, T. Albrecht, and J. B. Edel, "DNA tunneling detector embedded in a nanopore," *Nano Lett.*, vol. 11, no. 1, pp. 279–285, 2011.

[11] M. Tsutsui, Y. He, M. Furuhashi, S. Rahong, M. Taniguchi, and T. Kawai, "Transverse electric field dragging of DNA in a nanochannel," *Sci. Rep.*, vol. 2, no. 1, p. 394, 2012.

[12] H. W. Ch Postma, "Rapid sequencing of individual DNA molecules in graphene nanogaps," *Nano Lett.*, vol. 10, no. 2, pp. 420–425, 2010.

[13] F. Traversi, C. Raillon, S. M. Benameur, K. Liu, S. Khlybov, M. Tosun, D. Krasnozhon, A. Kis, and A. Radenovic, "Detecting the translocation of DNA through a nanopore using graphene nanoribbons.," *Nat. Nanotechnol.*, vol. 8, no. 12, pp. 939–45, 2013.

[14] P. Xie, Q. Xiong, Y. Fang, Q. Qing, and C. M. Lieber, "Local electrical potential detection of DNA by nanowire–nanopore sensors," *Nat. Nanotechnol.*, vol. 7, no. 2, pp. 119–125, 2011.

[15] Y. Takahashi, A. I. Shevchuk, P. Novak, Y. Zhang, N. Ebejer, J. V. MacPherson, P. R. Unwin, A. J. Pollard, D. Roy, C. A. Clifford, H. Shiku, T. Matsue, D. Klenerman, and Y. E. Korchev, "Multifunctional nanoprobes for nanoscale chemical imaging and localized chemical delivery at surfaces and interfaces," *Angew. Chemie - Int. Ed.*, vol. 50, no. 41, pp. 9638–9642, 2011.

[16] K. McKelvey, B. P. Nadappuram, P. Actis, Y. Takahashi, Y. E. Korchev, T. Matsue, C. Robinson, and P. R. Unwin, "Fabrication, Characterization, and Functionalization of Dual Carbon Electrodes as Probes for Scanning Electrochemical Microscopy (SECM)," *Anal. Chem.*, vol. 85, no. 15, pp. 7519–7526, 2013.

[17] A. Rutkowska, K. Freedman, J. Skalkowska, M. J. Kim, J. B. Edel, and T. Albrecht, "Electrodeposition and Bipolar Effects in Metallized Nanopores and Their Use in the Detection of Insulin," *Anal. Chem.*, vol. 87, no. 4, pp. 2337–2344, 2015.

[18] A. Rutkowska, J. B. Edel, and T. Albrecht, "Mapping the Ion Current Distribution in Nanopore/Electrode Devices," *ACS Nano*, vol. 7, no. 1, pp. 547–555, 2013.

[19] P. See, G. Wilpers, P. Gill, and A. G. Sinclair, "Fabrication of a Monolithic Array of Three Dimensional Si-based Ion Traps," *J. Microelectromechanical Syst.*, vol. 22, no. 5, pp. 1180–1189, 2013.

[20] C. Song and J. Zhang, *Electrocatalytic Oxygen Reduction Reaction*, pp. 89–134. London: Springer London, springer ed., 2008.

[21] P. Actis, S. Tokar, J. Clausmeyer, B. Babakinejad, S. Mikhaleva, R. Cornut, Y. Takahashi, A. López Córdoba, P. Novak, A. I. Shevchuck, J. A. Dougan, S. G. Kazarian, P. V. Gorelkin, A. S. Erofeev, I. V. Yaminsky, P. R. Unwin, W. Schuhmann, D. Klenerman, D. A. Rusakov, E. V. Sviderskaya, and Y. E. Korchev, "Electrochemical Nanoprobes for Single-Cell Analysis," *ACS Nano*, vol. 8, no. 1, pp. 875–884, 2014.

[22] Y. Zhang, J. Clausmeyer, B. Babakinejad, A. López Córdoba, T. Ali, A. Shevchuk, Y. Takahashi, P. Novak, C. Edwards, M. Lab, S. Gopal, C. Chiappini, U. Anand, L. Magnani, R. C. Coombes, J. Gorelik, T. Matsue, W. Schuhmann, D. Klenerman, E. V. Sviderskaya, and Y. Korchev, "Spearhead Nanometric Field-Effect Transistor Sensors for Single-Cell Analysis," *ACS Nano*, vol. 10, no. 3, pp. 3214–3221, 2016.

[23] D. Woermann, "Electrochemical transport properties of a cone-shaped nanopore: high and low electrical conductivity states depending on the sign of an applied electrical potential difference," *Phys. Chem. Chem. Phys.*, vol. 5, no. 9, pp. 1853–1858, 2003.

[24] W. J. Lan, M. A. Edwards, L. Luo, R. T. Perera, X. Wu, C. R. Martin, and H. S. White, "Voltage-Rectified Current and Fluid Flow in Conical Nanopores," *Acc. Chem. Res.*, vol. 49, no. 11, pp. 2605–2613, 2016.

[25] L. J. Steinbock, R. D. Bulushev, S. Krishnan, C. Raillon, and A. Radenovic, "DNA translocation through low-noise glass nanopores," *ACS Nano*, vol. 7, no. 12, pp. 11255–11262, 2013.

[26] K. Chen, N. A. W. Bell, J. Kong, Y. Tian, and U. F. Keyser, "Direction- and Salt-Dependent Ionic Current Signatures for DNA Sensing with Asymmetric Nanopores," *Biophys. J.*, vol. 112, no. 4, pp. 674–682, 2017.

[27] C. R. Crick, J. Y. Y. Sze, M. Rosillo-Lopez, C. G. Salzmann, and J. B. Edel, "Selectively Sized Graphene-Based Nanopores for in Situ Single Molecule Sensing," *ACS Appl. Mater. Interfaces*, vol. 7, no. 32, pp. 18188–18194, 2015.

[28] C. Yang, P. Hinkle, J. Menestrina, I. V. Vlassiouk, and Z. S. Siwy, "Polarization of Gold in Nanopores Leads to Ion Current Rectification," *J. Phys. Chem. Lett.*, vol. 7, no. 20, pp. 4152–4158, 2016.

[29] M. Nishizawa, V. P. Menon, and C. R. Martin, "Metal Nanotubule Membranes with Electrochemically Switchable Ion-Transport Selectivity," *Science*, vol. 268, no. 5211, pp. 700–702, 1995.

[30] M. Wanunu, J. Sutin, B. McNally, A. Chow, and A. Meller, "DNA Translocation Governed by Interactions with Solid-State Nanopores," *Biophys. J.*, vol. 95, no. 10, pp. 4716–4725, 2008.

[31] S.-W. Nam, M. J. Rooks, K.-B. Kim, and S. M. Rossnagel, "Ionic Field Effect Transistors with Sub-10 nm Multiple Nanopores," *Nano Lett.*, vol. 9, no. 5, pp. 2044–2048, 2009.

[32] R. B. M. Schasfoort, S. Schlautmann, L. Hendrikse, and a. van den Berg, "Field-effect flow control for microfabricated fluidic networks," *Science*, vol. 286, no. 5441, pp. 942–945, 1999.

[33] E. B. Kalman, O. Sudre, I. Vlassiouk, and Z. S. Siwy, "Control of ionic transport through gated single conical nanopores," *Anal. Bioanal. Chem.*, vol. 394, no. 2, pp. 413–419, 2009.

[34] Y. He, M. Tsutsui, C. Fan, M. Taniguchi, and T. Kawai, "Controlling DNA translocation through gate modulation of nanopore wall surface charges," *ACS Nano*, vol. 5, no. 7, pp. 5509–5518, 2011.

[35] K. H. Paik, Y. Liu, V. Tabard-Cossa, M. J. Waugh, D. E. Huber, J. Provine, R. T. Howe, R. W. Dutton, and R. W. Davis, "Control of DNA capture by nanofluidic transistors," *ACS Nano*, vol. 6, no. 8, pp. 6767–6775, 2012.

[36] Y. Liu and L. Yobas, "Slowing DNA Translocation in a Nanofluidic Field-Effect Transistor," *ACS Nano*, vol. 10, no. 4, pp. 3985–3994, 2016.

Chapter 5

Conclusions

5.1 Project aims

It has been two-and-a-half decades since methods for single molecule detection and manipulation were initially introduced in the biochemical field. During this time, the number of applications making use of these methods has boomed, leading the way to new discoveries and quickly establishing a new gold-standard for measurement in chemistry and biology. This revolution, which is far from being over, has been made possible by continuous technological advances which have improved performance, in terms of sensitivity, spatial, and temporal resolution, and have simplified fabrication processes and operating procedures. The subject of this thesis detailed the development of new strategies aimed at improving the spatial and temporal control over the dynamics of biomolecules during the two main phases of the detection process: the phase in which molecules are transported towards the detection volume, and the phase in which molecules are actually sensed in the detection volume. Both tasks, performed at single molecule level, were achieved by leveraging the flexibility of nanofluidic devices, called nanopipettes, which are cheap, robust and simple to be reconfigured for sensing or manipulation. In addition, they are easy to handle at a macroscopic level, while capable of operating with nanoscale objects.

Several reasons were identified as guiding motives for improving control over the analyte transport throughout the detection steps. These reasons, which constituted the backbone of this work, were as follows. Firstly, since single molecule detection goes hand-in-hand with single molecule manipulation, a better molecular control enables the study of individual molecules over a wider range of time and length scale. Effectively, the amount of extracted information (e.g. physico-chemical, mechanical, structural etc.) increases significantly. Secondly, active manipulation has profound implications when operating with small volumes (nL to pL), especially at low concentration of analyte. Overcoming the diffusion process that

limits and governs molecules at this scale is fundamental for improving the limit of detection and decreasing the measurement time, so that molecules can be isolated and probed despite their immersion in a complex environment (most single-molecule studies are performed in-vitro using only a few purified components). Finally, the motivation for tackling detection and manipulation of single molecules by using nanopipettes was a reduction in the overall system complexity. Nanopipettes are extremely versatile. Versatility, as opposed to complexity, should not only be intended in terms of portability or device footprint. By making a device highly flexible it could be integrated with existing techniques without, for instance, the necessity of custom-made read-out equipment.

5.2 List of achievements

This thesis has made important contributions towards the realization of the aims mentioned above. Firstly, in **Chapter 2** we provided a framework to perform nanopore sensing experiments with enhanced detection resolution. Based on a controlled confinement of the molecule within an aqueous zeptoliter nanobridge formed across two nanopores at the tip of a quartz nanopipette, we showed that it was possible to slow down the transport of analyte across the bridge by up to 3 orders of magnitudes. This method enabled the detection of smaller analytes than would otherwise be detected in standard nanopore configurations. Conventional nanopore sensing approaches, whereby the translocation velocity is normally reduced by increasing the solution viscosity, are typically limited by broad current/dwell time distributions and low SNR which prevent application to complex samples. In contrast, the nanobridge exhibited superior SNR performance due to tighter peak current distributions and lower noise levels, which lead to a robust discrimination of multiple dsDNA species present in the same sample.

The impact of the new approach was demonstrated for a wide range of analytes (e.g. dsDNA, ssDNA and protein) irrespective of their dimensions (from as large as 6.6 MDa for 10 kbp DNA, down to 14.5 kDa for α-synuclein). Finally, we demonstrated that improving the spatial and temporal resolution had no additional costs in terms of complexity: we showed that the nanobridge was still capable of operating with label-free, sub-nM analyte concentrations in quasi-physiological buffer conditions. Moreover, sampling rates as low as 1 kHz could be used, enabling the use of simpler, more compact, less expensive read-out electronics.

Another part of this thesis project (**Chapter 3**) was dedicated to the manipulation of molecules and particles at the nanoscale. We developed a new tool called DEP nanotweezers, which consists of two adjacent carbon nanoelectrodes located at the tip of a quartz dual

barrel nanopipette. As a result of the dielectrophoretic force generated by a variable bias applied between the two nanoelectrodes, it was possible to manoeuvre particles and biological molecules.

DEP has previously been used for manipulation of biomolecules, typically comprising a set of micro/nano fabricated electrodes embedded in a microfluidic circuit. The DEP-based nanotweezers detailed here offer several advantages. Firstly, due to the interelectrode distance, we have shown both with FEM simulations and experimentally, that it was possible to generate a highly localized, intense force, while still maintaining low power. As a consequence, it has been calculated that the heat dissipation, which can be a serious limitation for conventional DEP architectures, is diminished in magnitude and confined in space (e.g. an increase of less than 1°C in the first few nanometres when operating in a 1 mM KCl solution).

Secondly, we have demonstrated that by modulating the voltage and frequency of the applied signal, nanotweezers could operate with a broad range of different molecules (e.g. dsDNA, ssDNA, proteins, polystyrene beads), with different dimensions (from λ-DNA to 20-oligonucleotides long ssDNA), and in different quantities (e.g. single or multiple molecules at a time).

Thirdly, the nanotweezers were shown to be a flexible tool, simply integrated with conventional optical microscopes (including bright field and fluorescence) and efficient at manoeuvring molecules over relevant distances. Indeed, we described how nanotweezers can be used to select and extract dsDNA suspended in solution and to subsequently use them to successfully perform further analysis such as PCR amplification. This encompasses the nanotweezers paradigm. Their interoperability bridges the gap between single molecule approaches and common methods and equipment used in molecular biology, biochemistry and genetics, within the same setup. Finally, we designed a new technique which exploits these benefits: minimally invasive single cell nanobiopsy. We demonstrated that dielectrophoresis, coupled with nanotweezers, enables the isolation and extraction of biological material (e.g. nucleic acids) from a specific location in a targeted cell. It was then shown that the extracted molecules could be used to investigate the presence of a specific gene (β-Actin, in this case) by running a standard PCR routine. In contrast with previously reported work, we showed that there was no need for specific apparatus (aside from a function generator and nanotweezer), nor nanofabricated substrates onto which cells had to be seeded. Here, cells were cultured with standard media on standard chambered coverglass.

In the last part of the thesis, our efforts were focused on combining nanopore sensing and ionic field effect transistors: merging single molecule sensing with active, field-effect control over the molecular transport (**Chapter 4**). We established a simple and robust 2-step process to integrate a gold electrode at the tip of a quartz nanopipette which, in under 10 minutes and

without the use of expensive equipment, converted a conventional nanopore sensor into a nanopore-FET sensor.

The nanometric channel of one barrel was used for sensing while the second barrel acted as the gate terminal of an ionic FET. This was used to regulate the bias applied to the gold electrode wrapped around the nanopore, hence to regulate the charge density at the nanopore interface. Interestingly, we showed that the same fabrication procedure used to deposit the gate electrode was extremely effective at precisely tuning the nanopore dimensions. As a consequence, we demonstrated that the SNR of dsDNA molecules detected with the nanopore-FET was superior compared to standard nanopores. Finally, we characterized the nanopore-FET and showed that modulation of the gate potential could lead to modulation of the ionic current flow across the nanochannel. By using 10 kbp DNA as a test sample, we observed that a negative bias applied to the gate electrode prevented translocation from taking place. Since this process was completely reversible, the nanopore-FET behaved effectively as a molecular switch, turning the molecular transport across the pore "on" and "off".

5.3 Future directions

We identified key improvements that, based on the work presented in this thesis, should lead to a new class of devices with even higher performance in terms of single molecule detection and manipulation.

The first improvement aims at actively tuning the zeptolitre nanobridge, in particular to tune the charge distribution inside the droplet. As described in the characterization of the nanobridge's stability, one can imagine immersing the nanopipette in an immiscible phase (e.g. an organic solvent such as 1,2-Dichloroethane) which contains an electrolyte dissolved in it. As shown in **Figure 5.1 a**, a voltage applied across the interface would lead to a variation in the EDL layer and thus in the effective droplet volume. By enhancing the electrostatic interaction with the confined analyte, this new nanopore-FET platform would most likely improve the overall system sensitivity allowing very small molecules to be probed (e.g. proteins below 10 kDa and short oligonucleotides).

The second improvement aims at merging the advantages provided by nanobridge sensing with the ones provided by the nanotweezers. This marriage could be elegantly implemented with quad-barrel nanopipettes (**Figure 5.1 b**), whereby two carbon-coated barrels would be dedicated to DEP, while the other two would be for sensing (notably quad-barrel devices have been already reported in literature mainly for electrochemical and microfluidics applications).

The addition of two totally independent nanochannels paves the way for many exciting applications. For instance, operating in nanobridge configuration, the two carbon electrodes

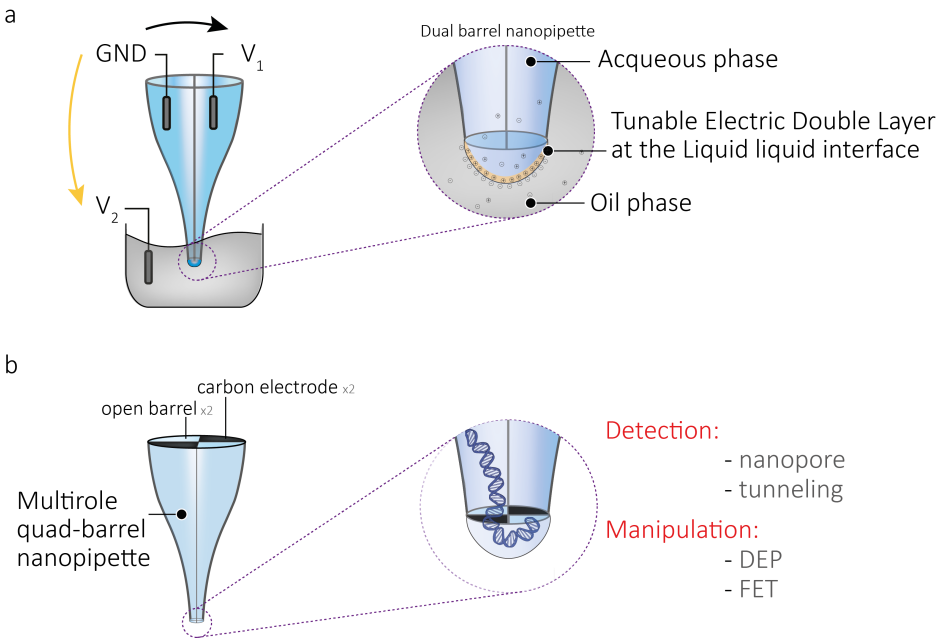

Fig. 5.1 Future directions of nanopipette-based devices. (a) Illustrates a nanopore-FET platform consisting on a dual barrel nanopipette operating in nanobridge configuration. The gate channel is represented by the aqueous droplet which is interfaced with an immiscible phase. As a result of voltage applied across this interface it would be possible to tune the charge distribution and thus enhance electrostatic interaction with the confined analyte. (b) Showing a schematic of a quad barrel nanopipette with 2 carbon electrodes and 2 open barrel operating in nanobridge configuration. Such a device might be employed to perform simultaneous detection (nanopore and/or tunnelling sensing) and manipulation (FET, DEP).

might be used for tunnelling sensing of the analyte while it passes through the confined space. Alternatively, the quad-barrel could be used as if it were a conventional nanopore sensor dipped in an electrolyte bath. In this case, the carbon electrodes would attract, via DEP, molecules towards the nanopipettes and the open channel would provide the sensing. As we briefly showed for the dual barrel nanopipette, even the quad-barrel device would not be limited to electrical detection/manipulation, and optical techniques such as fluorescence or Raman spectroscopy could be employed.

5.4 Outlook

It is clear that single molecule techniques will continue to shape the way we do research in the biomedical field, from routine analysis methods performed in a laboratory environment to end-user home-based diagnostic devices. As the field matures, applications may arise in areas which are quite different to those they were originally designed for. Earlier in 2017, Yaniv Erlich and co-workers brilliantly demonstrated a novel architecture strategy they called DNA fountain which could store data within DNA molecules at unprecedented density (215 petabytes per gram of DNA!). This is the response to the incredible amount of digital

data that an individual is responsible for from the time of their inception. The demand for more reliable, more secure and quickly accessible data is growing and DNA, with its high information density, durability and high quality reproduction which has been refined over the course of evolution, potentially offers a solution.

I recognize that there are current technical difficulties associated with achieving a proof-of-concept 3D device (where 3D stands for DNA Data Storage) capable of reading and writing information, and I somewhat agree that published works on next-generation DNA storage platforms (Erlich is only the most recent to demonstrate the potential of such a device) are expensive and inefficient, since they are largely based on conventional biochemical equipments and assays (e.g. DNA-sequencers, DNA-synthesizers, PCR). A device for widespread, real-world applications, must be able to read and write at single molecule level, thus detecting and manipulating DNA molecules in the same way that thousands of hard drives are read, written and moved in large cloud-storage facilities.

Due to the ongoing progress in the field, it would not be surprising if, instead of obeying Moore's law, within the next 10 years hard drives obeyed Watson and Crick's rules of base pairs.

List of Publications

V. A. Turek*, Y. Francescato*, P. Cadinu*, C. R. Crick, L. Elliott, Y. Chen, V. Urland, A. P. Ivanov, L. Velleman, M. Hong, R. Vilar, S. A. Maier, V. Giannini, and J. B. Edel, “Self-Assembled Spherical Supercluster Metamaterials from Nanoscale Building Blocks,” *ACS Photonics*, vol. 3, no. 1, pp. 35–42, 2016.

P. Cadinu, B. Paulose Nadappuram, D. J. Lee, J. Y. Y. Sze, G. Campolo, Y. Zhang, A. Shevchuk, S. Ladame, T. Albrecht, Y. Korchev, A. P. Ivanov, and J. B. Edel, “Single Molecule Trapping and Sensing Using Dual Nanopores Separated by a Zeptoliter Nanobridge”, *Nano Letters*, 2017.

V. Rakers, P. Cadinu, J. B. Edel and R. Vilar, "Development of microfluidic platforms for the synthesis of metal complexes and evaluation of their DNA affinity using online FRET melting assays", accepted, *Chemical Science*.

B. P. Nadappuram*, P. Cadinu*, A. Barik, M. Kang, A. J. Ainscough, J. Gonzalez-Garcia, B. Wojciak-Stothard, K. R. Willison, R. Vilar, P. Actis, S.H. Oh, A. P. Ivanov, and J. B. Edel, "Single-cell Biopsy Using Single Molecule Nanotweezers", *submitted*.

P Cadinu*, G. Campolo*, S. Pud*, J. B. Edel, C. Dekker, A. P.Ivanov, "Double barrel nanopores as a new tool for controlling single-molecule transport", *submitted*.

NANO LETTERS

Letter

pubs.acs.org/NanoLett

Single Molecule Trapping and Sensing Using Dual Nanopores Separated by a Zeptoliter Nanobridge

Paolo Cadinu,[†,‡] Binoy Paulose Nadappuram,[†] Dominic J. Lee,[†] Jasmine Y. Y. Sze,[†] Giulia Campolo,[†] Yanjun Zhang,[§] Andrew Shevchuk,[§] Sylvain Ladame,[‡] Tim Albrecht,[†] Yuri Korchev,[§] Aleksandar P. Ivanov,*[,†] and Joshua B. Edel*[,†]

[†]Department of Chemistry, [‡]Department of Bioengineering, [§]Department of Medicine, Imperial College London, SW7 2AZ, United Kingdom

S *Supporting Information*

ABSTRACT: There is a growing realization, especially within the diagnostic and therapeutic community, that the amount of information enclosed in a single molecule can not only enable a better understanding of biophysical pathways, but also offer exceptional value for early stage biomarker detection of disease onset. To this end, numerous single molecule strategies have been proposed, and in terms of label-free routes, nanopore sensing has emerged as one of the most promising methods. However, being able to finely control molecular transport in terms of transport rate, resolution, and signal-to-noise ratio (SNR) is essential to take full advantage of the technology benefits. Here we propose a novel solution to these challenges based on a method that allows biomolecules to be individually confined into a zeptoliter nanoscale droplet bridging two adjacent nanopores (nanobridge) with a 20 nm separation. Molecules that undergo confinement in the nanobridge are slowed down by up to 3 orders of magnitude compared to conventional nanopores. This leads to a dramatic improvement in the SNR, resolution, sensitivity, and limit of detection. The strategy implemented is universal and as highlighted in this manuscript can be used for the detection of dsDNA, RNA, ssDNA, and proteins.

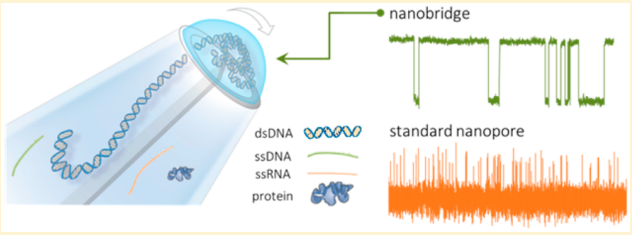

KEYWORDS: *Single molecule zeptoliter confinement, DNA recoiling dynamics, dual nanopore, nanoscale droplet, SNR enhancement, DNA profiling*

Rapid advances in label-free single molecule sensing strategies are transforming the way biological systems are studied, especially with a view on developing novel diagnostic and therapeutic strategies. The remarkable spatial and temporal resolution offered by these techniques, along with their increasing availability, have dramatically improved the ability of researchers to detect and manipulate single molecules such as nucleic acids and proteins, enabling the investigation of their physicochemical, mechanical, and biological characteristics in a wider range of time/length scales and complexity than previously thought possible.[1] Over the past decade, nanopore sensors have been gaining prominence for detection[1−3] and even delivery of analytes,[4] in part due to their inherently simple operating principle which is based on recording the changes in the ionic current through a nanoscale pore that is separated by two electrolyte-filled reservoirs. Nanopores have been successfully used for a wide range of sensing applications (e.g., for nucleic acid sequencing[5]), the current state-of-the-art of both biological and solid-state nanopore technology faces significant challenges due to the limited control over molecular transport[6] and inability to confine and study individual molecules over longer time scales.

For example, small nucleic acid fragments (e.g., cell-free DNA and microRNA) are often challenging to detect due to their fast translocation times with rates being as high as 50 000 nucleotides per ms,[7] resulting in a poor signal-to-noise ratio (SNR), and limited resolution. Proteins are even more challenging to detect, due to their heterogeneous charge and fast diffusion rates resulting in only a small fraction of the total population being detected. For example, it has been estimated that, for a sub-100 kDa protein, only the slowest 0.1% fraction of the proteins transported through the nanopore are usually observed.[8,9] Therefore, nanopore experiments are normally carried out at analyte concentration several orders of magnitude higher than the clinically relevant range.[10]

Much effort has been placed towards finding solutions to circumvent these limitations including using high bandwidth amplifiers,[11−13] or alternatively and perhaps more challenging, controlling and tuning transport of analytes across the pore. Apart from the straightforward method of lowering the voltage applied which slows molecules down but at the not negligible cost of lowered SNR and capture rate, traditional approaches have included but are not limited to (i) increasing solution viscosity[14,15] and making use of different electrolyte solutions,[16] (ii) modifying nanopore shape, geometry, and composi-

Received: July 27, 2017
Revised: September 1, 2017
Published: September 1, 2017

DOI: 10.1021/acs.nanolett.7b03196
Nano Lett. XXXX, XXX, XXX−XXX

tion,[17−21] (iii) applying pressure gradients to counterbalance electrophoretic forces,[22] and (iv) making use of mechanical forces.[23−26] A method capable of slowing and controlling the transport without affecting the SNR, capture rate, detection efficiency, and detection limit that can be used equally well for nucleic acids and proteins is as of yet unresolved.

Herein, we demonstrate a simple to fabricate and operate, yet powerful detection platform that addresses many of the above challenges and allows for the controllable confinement of individual molecules in a zeptoliter nanobridge formed across two nanopores separated by a 20 nm gap at the tip of a nanopipette, as in Figure 1. The droplet or bridge formation is very similar to what has been initially documented by Rodolfa et al.[27,28] albeit on a much smaller scale, allowing for the confinement of one molecule at a time. Upon application of a bias between the two nanopores, the analyte is transported from one nanopore to the other via the nanobridge. Due to molecular confinement, we show that it is possible to slow down transport by up to 3 orders of magnitude and detect small molecules without using any complex fabrication strategies or modifying the analyte or electrolyte composition. This considerable slowdown enables the detection of species which would otherwise go undetected in a conventional nanopore platform. It is possible to perform fragment sizing based on current amplitudes alone, which we show enhances the detection resolution and does not require further data processing. To demonstrate the generality of our approach, enhanced temporal resolution was achieved for a broad range of analyte such as dsDNA, ssDNA, RNA, and small proteins such as monomeric α-synuclein.

The fabrication of the dual nanopore platform was implemented via pipet pulling of dual-barrel quartz capillaries (see methods for fabrication parameters), resulting in the reproducible formation of two adjacent pores, each 20−30 nm in diameter, as measured by TEM and SEM, Figure 1a−c, Supporting Information (SI) S1. Each pipet barrel was filled with an electrolytic solution which resulted in the formation of a nanoscale bridge between the two nanopores held in place by surface tension. Ag/AgCl electrodes (patch and ground) were inserted into each barrel with the bridge between the nanopores being the only connection point.

To characterize the formed nanobridge, current−voltage measurements were performed on the same device in three distinct configurations at 100 mM KCl and pH 8.0: (i) *in a conventional nanopore configuration*, where the ground electrode is placed in the bath and the patch electrode is in one of the barrels, (ii) *in dual nanopore configuration without a nanobridge*, where the ground and the patch electrodes are placed in different barrels and the nanopipette tip is immersed in a bath with the same electrolyte, and (iii) *in a nanobridge configuration*, where the ground and the patch electrodes are placed in different barrels and the nanopipette tip is in air. A comparison of exemplar current−time traces is shown for 5 kbp DNA for the three configurations and highlights the slowing of DNA transport, as in Figure 1e. The conductance, Figure 1f, as calculated from the linear region (±100 mV) of the *IV* curves measured for each nanopore in configuration (i) was G_1 = 4.75 ± 0.52 nS (barrel 1) and G_2 = 4.45 ± 0.43 nS (barrel 2). This mode of operation showed negative rectification ($|I_{-600mv}/I_{+600mv}|$ = 1.56 ± 0.08) which is consistent with negatively charged glass nanopores previously reported,[29,30] as the negatively charged surface of the quartz nanopore leads to increased Cl^- ion selectivity.[31] In configuration (ii) the *IV* curves were predominantly linear up to ±600 mV and conductance approximately halved to 2.20 ± 0.22 nS. This is expected due to the increase in total resistance because of the introduction of second nanopore in the electrical circuit and closely matches the total conductance of the two nanopores in series ($1/G_{TOT} = 1/G_1 + 1/G_2$), G_{TOT} = 2.30 nS. In this configuration, the loss of rectification at negative voltages was attributed to enhanced Cl^- selectivity originating from both nanopores, effectively canceling out the rectification.

Interestingly, the nanobridge configuration exhibited a quasi-sigmoidal behavior with a conductance of 2.04 ± 0.13 nS. The sigmoidal behavior at higher voltages is likely due to the electric field inducing localized changes in surface tension. These results indicated that the nanobridge resistance accounted for up to 11% of the total conductance, while the remaining is almost equally split between the nanopores in each barrel. A simple model with the nanobridge connected as a third resistor in series to the two nanopores indicates that the resistance associated with the nanobrigde is ∼55 MΩ compared to the total nanobridge/nanopore resistance of ∼490 MΩ. This indicates that ∼11% of the total voltage bias drops in the nanobridge. At the same time, the conductance dependence on electrolyte concentration (5−400 mM KCl at pH 8.0) followed a linear trend similar to what is typically observed in a conventional configuration (i) suggesting that salt concentration has a negligible effect on droplet formation and shape (SI S2).

An estimation of the nanobridge dimensions is critical in understanding the molecular confinement. From TEM and SEM (Figure 1) the dimensions of the nanopores and their separation can be determined; however, to estimate the height of the nanobridge, alternative strategies are needed. A series of approach experiments were performed using scanning electrochemical cell microscopy (SECCM) with full feedback control, which allowed us to measure the height of the fluidic nanobridge.[32] The ionic current across the bridge was used as a feedback signal to detect contact between the formed droplet meniscus and a silanized glass substrate during the approach (Figure 2a). A stable ionic current (I_0) was observed until the droplet meniscus first made contact with the surface. As the nanopipette moved closer to the surface, the ionic current decreased rapidly until the tip of the nanopipette came into near physical contact with the substrate. The measured decrease in ionic current is generally attributed to the hindered flow of ionic species across the nanobridge, which in our case was directly dependent on distance and proximity to the surface.[33,34] As the ionic current cannot be completely blocked, to precisely define the surface contact point, the pipet approach was continued even after the lowest ion current (full surface contact) was observed, until it crashes into the glass substrate, breaking the tip and increasing its diameter and hence the ionic current at which point the approach was halted. Averaging over multiple approaches, the droplet height (Δz), defined as the difference between initial and full surface contact, was measured to be 30 ± 5 nm. Assuming a semiellipsoidal nanobridge, the radius of the major and minor axes can be approximated as x = 21 ± 2 nm and y = 48 ± 2 nm, as measured by SEM and TEM. This corresponds to an average nanobridge volume of 63 ± 19 zL, which is a highly confined space, orders of magnitude smaller than what is typically used for single molecule fluorescence microscopy. To confirm molecular confinement and transport from one barrel to the other through the nanobridge, translocations were imaged optically using 10 kbp

DOI: 10.1021/acs.nanolett.7b03196
Nano Lett. XXXX, XXX, XXX−XXX

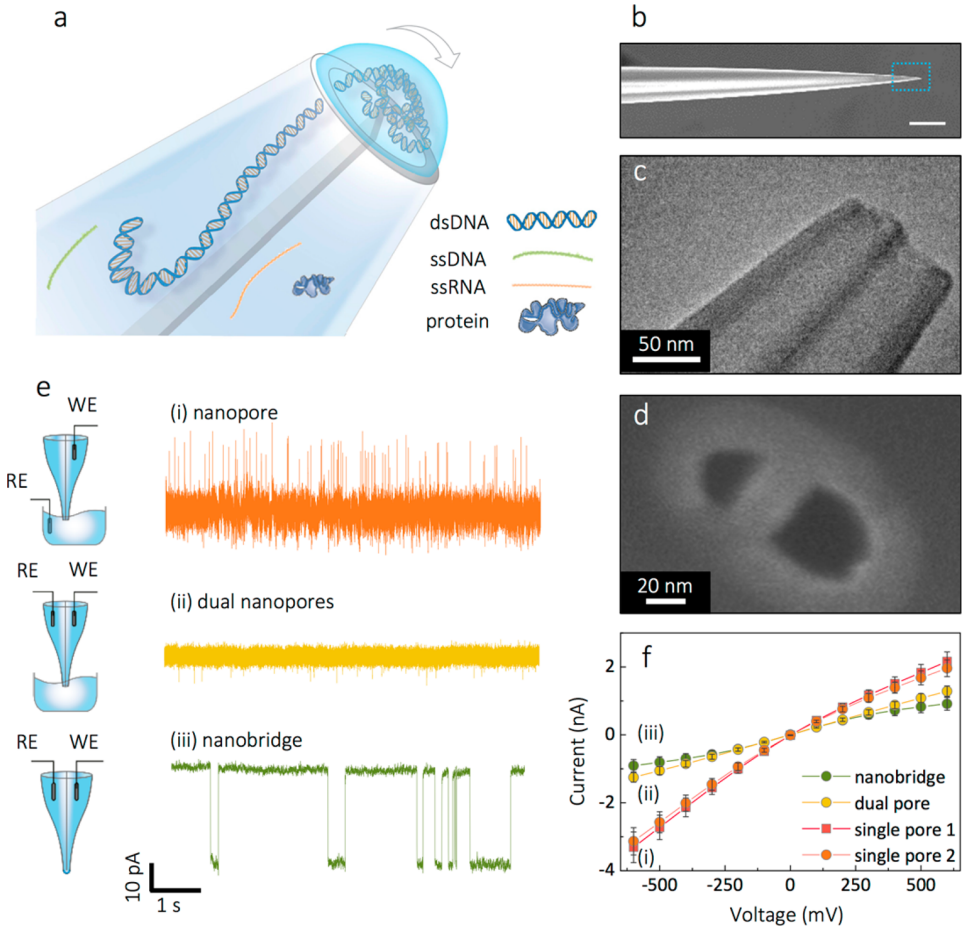

Figure 1. Experimental setup and characterization of nanobridge configuration. (a) Schematic representation of the nanobridge formed at the tip of a nanopipette. (b) SEM of the dual barrel nanopipette visualized laterally, scale bar 10 μm. (c) TEM and (d) SEM micrographs of the tip of the nanopipette displayed an ellipsoidal profile with representative dimensions of the major and minor axes being approximately $x = 21 \pm 2$ nm and $y = 48 \pm 2$ nm in radius. (e) Ionic current recordings of 5 kbp DNA translocations in 100 mM KCl buffered in TE at 350 mV voltage applied, performed in different double barrel nanopipette configuration as illustrated in the schematic: (i) conventional nanopore configuration, (ii) dual nanopore configuration without a nanobridge, (iii) nanobridge configuration. Traces have been refiltered and resampled for visualization purposes. (f) Current−voltage plots of dual barrel nanopipttes measured in the three different configurations at 100 mM KCl.

DNA fluorescently labeled with YOYO-1 (Figure 2b−e, SI S3). Under an applied bias, translocations could be visualized optically as a blinking highly confined ellipsoidal spot at the tip of a nanopipette using an emCCD camera. Importantly no accumulation of DNA at the tip was observed, confirming that DNA translocates from one barrel to the other via the nanobridge. It should be noted that the measurement was diffraction limited; therefore, the signal (e.g., along one axis corresponds to 2 pixels = 534 nm) arises from a significantly smaller droplet volume.

In spite of its size, the nanobridge exhibited very high stability with the baseline current remaining stable for over an hour (1.12 pA rms at 200 mV voltage applied at 100 mM KCl) indicating no observable change in droplet dimensions due to evaporation, SI S4. Importantly, the nanobridge devices demonstrated nearly identical *IV* characteristics in air and when immersed in fluorinated oil (FC-70), again indicating that evaporation played no role in the device functionality, SI S5. To evaluate the role molecular confinement played in the detection process, experiments were performed in nanobridge and conventional nanopore configurations using dsDNA of different lengths. Recently, Pud et al.[35] have presented a planar dual nanopore configuration where the ends of the same DNA molecule were threaded in two different pores resulting in a mechanical trapping; however, their architecture did not allow for an efficient molecular confinement, leading to a trapping efficiency of less than 1%. Although dual nanopore systems with internal cavities have been previously used as nanoreactors to measure chemical reactions,[36] the electrophoretic time-of-flight of DNA molecules,[37] and escape times from an entropic barrier,[38] the operation of these platforms overlaps with the dual nanopore configuration without a nanobridge (ii) shown in Figure 1. In contrast, the nanobridge operates in a different regime: where the radius of the confining volume, $R_{confine}$, is significantly smaller than R_g, the radius of gyration of the particle to be confined.

In our platform, DNA was threaded inside the nanobridge Figure 3a (i), resulting in volumetric expansion until the surface energy of the bridge matches the energy of DNA confinement. Much like the open nanopore current, DNA translocations were equally stable over similar time scales, SI S6. A closer look at the onset of individual translocation events revealed a monoexponential decay with time constant, τ, upon delivery of DNA from the initial nanopore into the nanobridge (Figure

DOI: 10.1021/acs.nanolett.7b03196
Nano Lett. XXXX, XXX, XXX−XXX

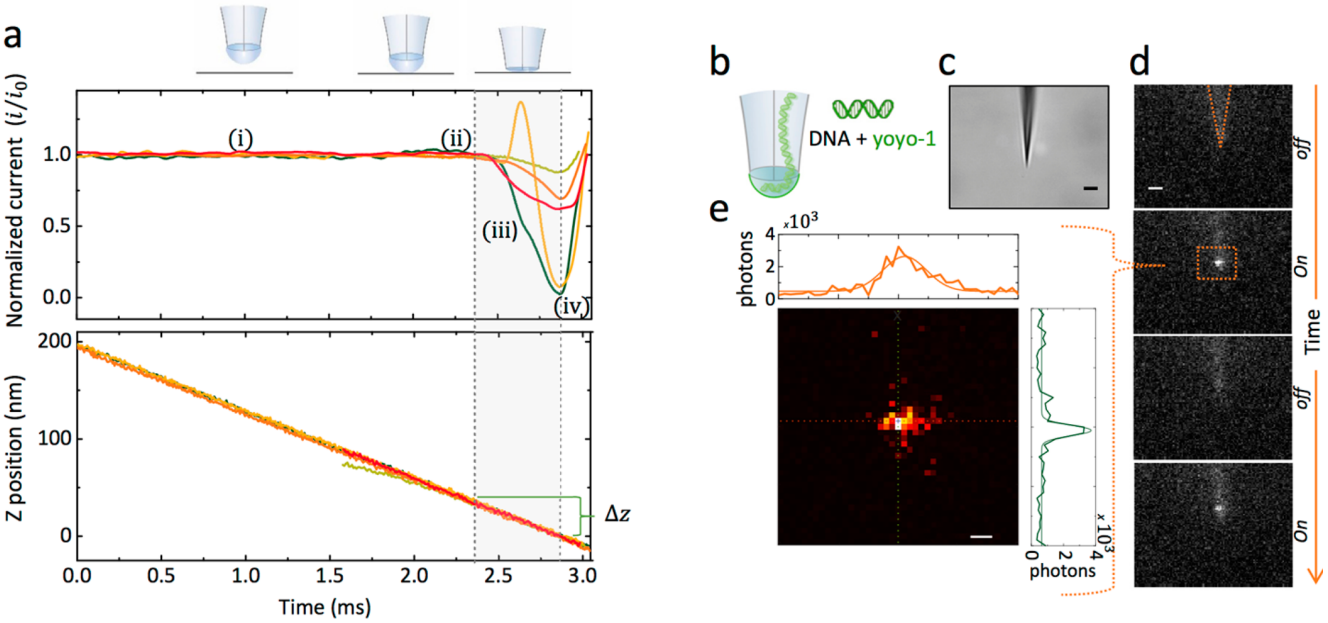

Figure 2. Electrolyte nanobridge characterization. (a) The height of the nanobridge at the tip of the nanopipette was measured by using a scanning electrochemical cell microscopy (SECCM) with ionic current feedback. Both nanopipette barrels were filled with 100 mM KCl buffered with 10 mM Tris, 1 mM EDTA, at pH 8.0. The nanopipette was mounted on a piezo stage perpendicular to a silanized glass surface. The ionic current (top panel) was recorded along with the *Z*-position (bottom panel) of the piezo stage. During approach the current remains unchanged (i) and decreases when contact is made between the nanobridge and glass substrate (ii). The tip is lowered further (iii) until it crashes into the glass substrate, breaking the tip and increasing its diameter and hence the ionic current (iv). The current in all cases cannot be completely shut off due to surface conductivity and surface contact. The nanobridge height (Δz), defined as the difference between the initial nanobridge to surface contact (i) and tip to surface contact (iv), was measured to be 30 ± 5 nm. (b) Schematic of optical fluorescence detection used to confirm molecular confinement and DNA transport via the electrolyte nanobridge. 10 kbp DNA stained with YOYO-1 was used in 100 mM KCl solution buffered with 10 mM Tris, 1 mM EDTA, at pH 8.0. (c) Bright field of the nanopipette (scale bar shows 5 μm). (d) Fluorescence images recorded with an emCCD camera (100 ms exposure time) showing that upon the application of a bias (300 mV), a fluorescent spot, owing to DNA translocation, was detected at the tip of the nanopipette (scale bar shows 5 μm). (e) A close-up of a representative DNA optical translocation showing the fluorescent profile along $x-y$ axis. Measurements were diffraction limited; therefore, despite the DNA being confined, the fluorescence appeared to be larger than the dimensions of the nanobridge (scale bar shows 1 μm).

3b), which is attributed to the increased entropic barrier. The decay was linearly dependent on DNA fragment size, e.g. 0.34 ± 0.10 ms for 1.5 kbp increasing to 1.69 ± 0.39 ms for 10 kbp DNA. τ was significantly larger than the amplifier rise/fall time (35 μs at 10 kHz cutoff frequency), not dependent on the event duration, and only minimally dependent on the applied voltage (Figure 3c). In comparison, threading in a conventional nanopore configuration results in sharp current transitions, which are commonly attributed to DNA molecule entering the nanopore, SI S7. The increasing τ corresponds well with DNA size and the increase in total volume of the nanobridge due to expansion generated by insertion of DNA. For example, the radius of gyration using a worm-like chain model with modified Kuhn length (96 nm) taking into account 100 mM KCl is 90 nm for 1.5 kbp and 233 nm for 10 kbp.[39] At the same time decay constants are only marginally slower than the Zimm relaxation times[37] and much slower than the total translocation times observed in nanobridge configuration implying that the DNA fully recoils into the nanobridge prior to translocating into the receiving nanopore, Figure 3a (ii). This is consistent with the optical data whereby a transient fluorescent spot is localized at the tip.

Under this model, the recoiled DNA acts to restrict ion flow between both barrels resulting in a current blockade. This is different to the conventional configuration in nanopores, where DNA molecules crossing the diffuse electrical double layer results in current enhancement as previously reported in the literature;[4] see Figure 1e. As will be seen later, the current blockade in the nanobridge configuration correlates with DNA size. Under the same translocation model, due to the separation between both nanopores, a molecule confined in the nanobridge would experience a weaker electric field. As only a small fraction of the total voltage bias drops in the nanobridge, the effect of the electric field on the DNA is negligible, and once inside the nanobridge, diffusion will be dominant. Considering the DNA requires sufficient time to sample all available configurations[40] within this restricted space to enter the second barrel, it is expected that this would also lead to a longer and broader dwell time due to the stochastic nature of the process and the random orientation of the molecule in the nanobridge, as in Figure 3a (iii). The diffusion time to find a configuration that will allow for the molecule to leave the pore (for instance, an end of the DNA entering the second nanopore) seems to be much slower than what is expected for normal nanopore diffusion. A possible explanation for this would be the difference in electric field strength between the nanopores and the bridge, as well as the fact that the molecule now has to diffuse laterally across the bridge, where the available space for diffusion is limited by the elastic energy required to expand out the bubble forming the nanoscale bridge. The DNA molecule may be forced into a tight coil by the electric field in the nanopore and resisting elastic forces in the nanobridge. There may also be tangling of the molecule through diffusion, due to recoils with the bubble and nanopore walls, before the DNA

DOI: 10.1021/acs.nanolett.7b03196
Nano Lett. XXXX, XXX, XXX−XXX

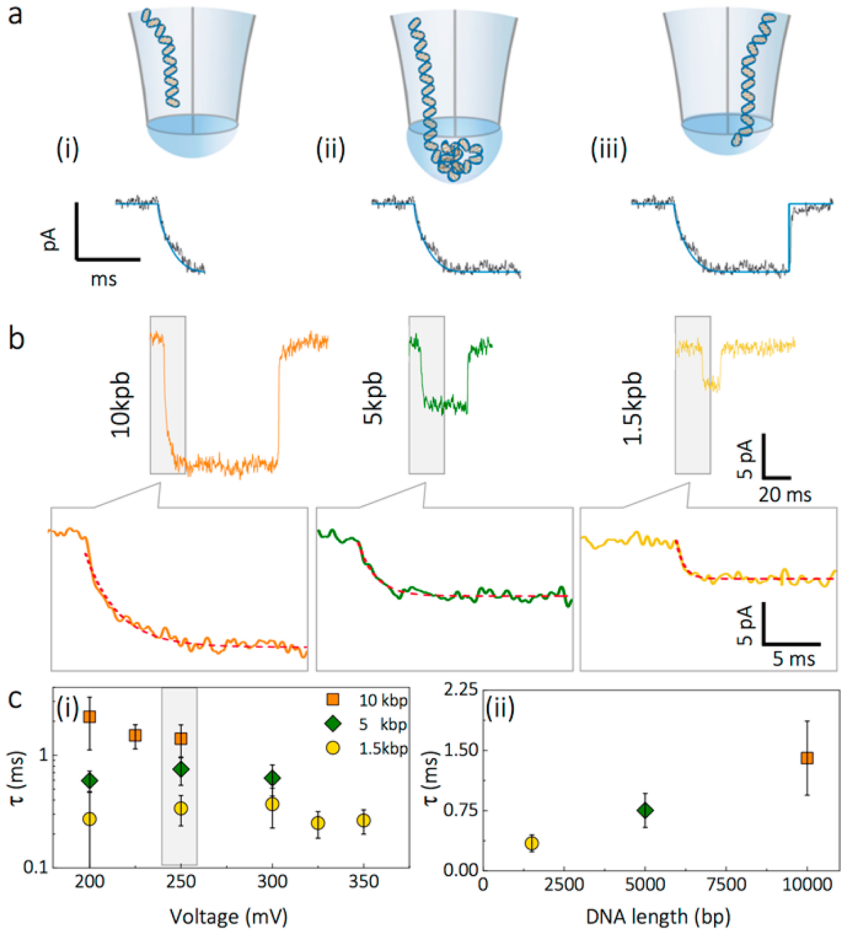

Figure 3. DNA threading model in nanobridge configuration. (a) Schematic of the threading process: (i) The dsDNA molecule is threaded inside the nanobridge leading to its expansion. The threading process results in the ionic current exhibiting a monoexponential decay with time constant τ. (ii) The DNA recoils inside the bridge until the surface energy of the bridge matches the energy of the DNA confinement. As the DNA in the droplet is predominately governed by Brownian motion, the duration of the blockade is governed by the time it takes the DNA to rearrange and become inserted and finally (iii) threads into the second barrel. (b) Examples of 10, 5, and 1.5 kbp DNA translocation events recorded in nanobridge configuration in 100 mM KCl. The onset of each translocation event was fit with a monoexponential decay function. (c) Dependence of threading time τ on voltage applied (left panel) for 10, 5, and 1.5 kbp DNA. Threading time dependence on DNA length for events recorded at 250 mV (right panel).

completely enters the bridge. Such molecular crowding, as well as tangling, through compactification may significantly slow down the diffusion process to find a suitable configuration with which to leave the nanopore. Indeed, diffusing molecular segments may be hindered by an increased density of other segments in the way, within such a compact state, enhancing the self-avoiding aspect of the diffusion.

A direct comparison of experimental nanopore data obtained in nanobridge and conventional configurations, for the same device revealed several key nanobridge advantages. First, an improved temporal resolution due to confinement, leading to slowdown up to 3 orders of magnitude, was observed; see Figure 4a. For instance, the detection of 5 kbp DNA using a conventional nanopore configuration and dual nanopore in bath gave mean dwell times of 0.13 ± 0.03 ms and 0.19 ± 0.08 ms, respectively (SI S8, S9), which is comparable with what has been reported in literature.[4] Using the same nanopipette in a nanobridge configuration resulted in an increase in event duration, up to 100 ms as shown in Figure 4a (i). This remarkable slowdown of molecular transport applied also to the detection of shorter fragments such as 200 bp DNA, where dwell times as long as 20 ms could be detected. In comparison, in a conventional nanopore configuration under the same electrolyte conditions (100 mM KCl) and instrumental bandwidth, 200 bp fragments went undetected due to their fast translocation times and poor SNR; see Figure 4a (ii).

The voltage dependence on current blockade for 1.5 kbp DNA is shown in Figure 4b. Similar trends are observed whereby to the standard configuration where the peak current increases proportionally with voltage. However, an interesting property was revealed: when the applied voltage was increased, DNA fragments, irrespective of size, were subjected to an even more pronounced slowing down, resulting in an increased SNR and effectively acting as a single molecule trap (Figure 4b). More typically it would be expected that the dwell time decreases due to the larger electrophoretic force experienced by the translocating analyte.[41] This distinctively different behavior in the nanobridge configuration fits well with our explanation for the slow translocation times. An increased bias voltage will likely cause the molecule to compress more on entering the droplet, which could increase the degree of molecular crowding and tangling slowing down the internal diffusion of the DNA.

DOI: 10.1021/acs.nanolett.7b03196
Nano Lett. XXXX, XXX, XXX−XXX

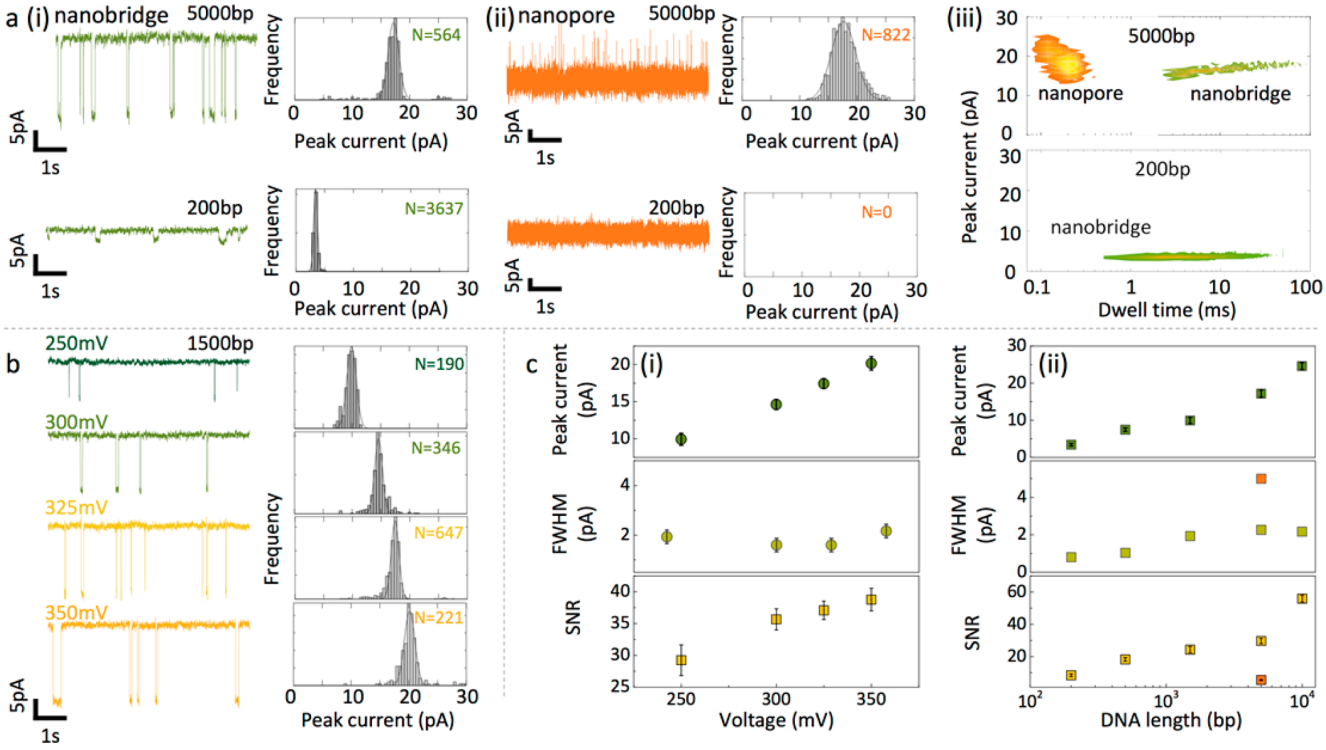

Figure 4. dsDNA detection comparison between conventional and nanobridge configurations. (a) (i) Nanobridge configuration. Ionic current recordings for 5 kb DNA (top) and 200 bp DNA (bottom) recorded in 100 mM KCl at 250 mV voltage applied. Measurements and analysis were performed using a 10 kHz low-pass filter. For visualization purposes only, the trace was filtered at 200 Hz. The measured peak current was 17.17 ± 0.96 pA and 3.42 ± 0.34 pA respectively. (ii) Corresponding measurements in a conventional nanopore configuration. For 5 kbp the peak current was 17.65 ± 2.11 pA. No events were detected for 200 bp. (iii) Scatter plots showing the dwell time and peak current distribution for 5 kbp DNA (top) and 200 bp DNA (bottom) detected in the nanobridge and conventional configurations. (b) Voltage dependence on current blockade for 1.5 kbp DNA. The peak current as determined by Gaussian fitting was 9.94 ± 0.82 pA at 250 mV, 14.62 ± 0.68 pA at 300 mV, 17.43 ± 0.68 pA at 325 mV, and 20.16 ± 0.92 pA at 350 mV, respectively. (c) (i) Peak current, fwhm, and SNR dependence on voltage applied using the nanobridge configuration. The fwhm remained largely unchanged at 1.83 ± 0.28, while SNR increases from 29.2 ± 2.4 at 250 mV to 38.8 ± 1.8 at 350 mV due to decrease in DNA translocation time at higher voltages. (ii) Peak current, fwhm, and SNR dependence on DNA length at a fixed voltage (250 mV). In the nanobridge configuration the mean peak current scales with the radius of gyration squared of the DNA molecule: from 3.42 ± 0.34 pA for 200 bp to 24.59 ± 0.92 pA for 10 kbp. A similar trend was observed for the SNR, whereas the fwhm values remained similar. As point of reference SNR and fwhm for 5 kbp detected using a conventional configuration are plotted in the graph (orange square).

The ease of detection of a short fragment in a nanobridge configuration with a conventional amplifier in relatively low salt concentrations (100 mM KCl) is particularly useful as it simplifies the need of using a custom high-speed amplifier in conjunction with high salt concentrations or the use of electrolytes such as LiCl that binds strongly to DNA and has limited applicability for protein samples. Second, noise performance was significantly improved in the nanobridge configuration both in the low- and high-frequency regime, when compared to a conventional configuration, SI S10. Third, we also observed a significant enhancement of the SNR in nanobridge configuration. For example, in the case of 5 kbp, the measured SNR in the nanobridge configuration was ca. 540% higher than that of a conventional nanopore using the same device (Figure 4c). Finally, and uniquely, was the ability to accurately discriminate fragment sizes by peak currents alone with the full width half-maximum (fwhm) being below 2.5 pA for dsDNA fragments ranging from 200 bp to 10 kpb, as in Figure 4c. As an example, the mean peak current for 5 kbp DNA was 17.17 ± 0.96 pA in the nanobridge configuration compared to 17.96 ± 2.12 pA measured in a standard configuration at an applied bias of 250 mV. As is described below, the mean peak current for each fragment size closely follows the radius of gyration squared using a worm-like chain model with and without self-avoidance[39,42] correction indicating that the peak current is proportional to the cross-sectional area of the DNA blocking the nanobridge. Furthermore, the lower spread in the current blockade distribution are indicative of the ability to discriminate DNA strands of different lengths based solely on peak current distributions as opposed to more conventionally the event charge deficit (ECD).[43]

Utilizing the added advantage of using the nanobridge, we showed that it is possible to perform fragment sizing using peak amplitudes alone. For this, a solution consisting of a mixture of 500 bp, 1500 bp, and 5 kbp (Figure 5a–d) at a concentration of 100 pM was used as was a 1 kbp DNA ladder (fragment sizes: 500 bp, 1 kbp, 1.5 kbp, 2 kbp, 3 kbp, 4 kpb, 5 kbp, 6 kbp, 8 kbp, 10 kbp, Figure 5e–h). As shown in the current–time trace, Figure 5a, it was possible to identify the different species in solution with mean peak currents being 2.4 ± 0.5 pA, 5.1 ± 0.5 pA, and 10.7 ± 0.6 pA for 500 bp, 1.5 kbp, and 5 kbp, respectively (Figure 5c). The total number of detected events accurately reflected the equal concentration for the three species within the solution.

Because of the narrow peak current distribution in the nanobridge configuration, DNA can be identified based not

DOI: 10.1021/acs.nanolett.7b03196
Nano Lett. XXXX, XXX, XXX–XXX

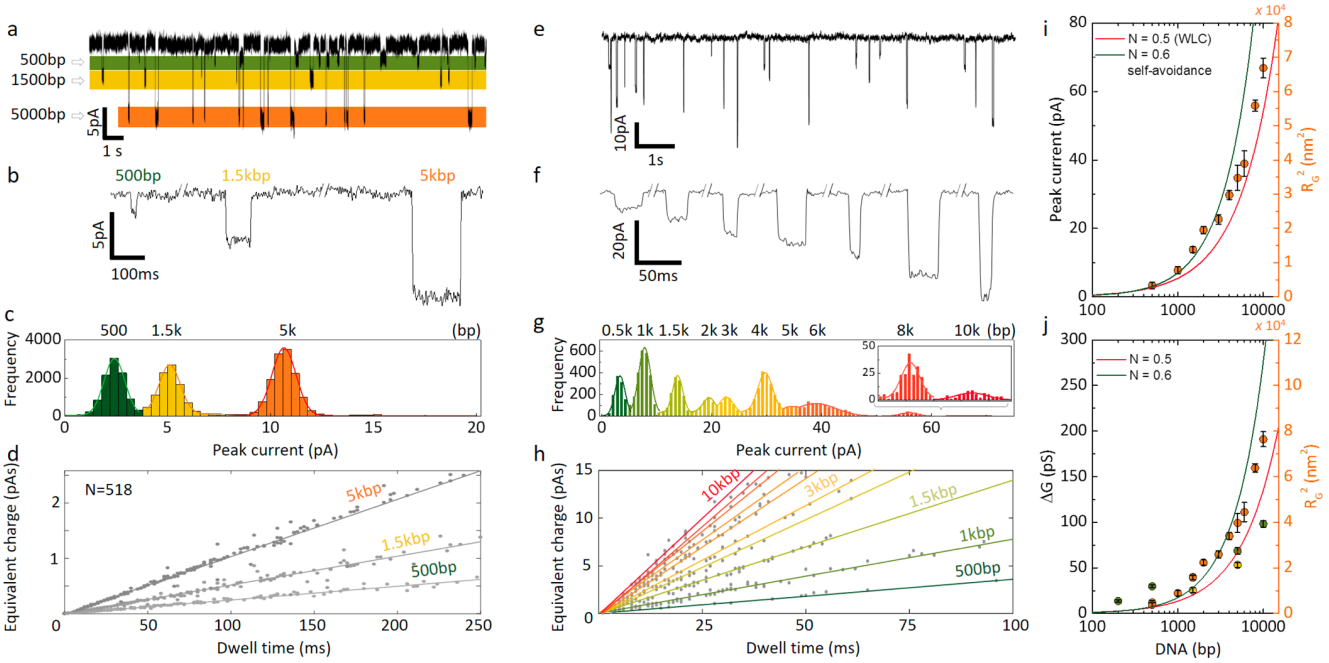

Figure 5. Detection of mixed dsDNA sample in the nanobridge configuration. (a) Translocation signals of a sample containing 500 bp, 1.5 kbp, and 5 kbp at a concentration of 100 pM each in 100 mM KCl buffered in TE (pH 8.0) at 200 mV. (b) Representative current blockade traces of 500 bp, 1.5 kbp, and 5 kbp DNA. (c) Peak current histogram for a mixture containing 500 bp, 1.5 kbp, and 5 kbp. The mean peak current was obtained via Gaussian fitting (2.4 ± 0.5 pA for 500 bp, 5.1 ± 0.5 pA for 1.5 kbp, and 10.7 ± 0.6 pA for 5 kbp). (d) Equivalent charge plot was used to identify the different DNA population and was shown to be linear dependent on dwell time. The calculated slopes were 2.5 pA for 500 bp, 5.2 pA for 1.5 kbp, and 10.3 pA for 5 kbp. (e) Translocation signal of a 1 kbp DNA ladder, containing 10 DNA fragments (500 bp, 1.5 kbp, 2 kbp, 3 kbp, 5 kbp, 6 kbp, 8 kbp, and 10 kbp) at a total concentration of 100 pM in 100 mM KCl buffered in TE (pH 8.0) at 350 mV. (f) Representative current blockades and (g) peak current histogram. (h) Equivalent charge plot for the same sample as shown in g. (i) Peak current and (j) conductance for the 10 DNA fragments in the 1 kbp ladder (orange), sample from panel a (yellow), and data from Figure 4c (green). The scaling is in excellent agreement with the DNA radius of gyration squared (right axes) using a worm-like chain (WLC) model with and without self-avoidance.

only on the current blockade but also by looking at the integrated area of the region bounded by each recorded event (equivalent charge). This should not be confused with the event charge deficit whose values, in conventional nanopore experiments, are related to the amount of charges carried by a specific analyte. In a nanobridge configuration, broadly dispersed dwell time distributions do not allow for a similar interpretation. Notably, in a nanobridge configuration, the integrated event profile was distributed along a straight line allowing accurate identification of DNA strands by linear fitting of the equivalent charge. The linear relationship between equivalent charge and dwell time is consistent with the proposed model; that is, the current blockade is constant for the duration of time the DNA spends in the nanobridge. For instance, for mixed fragment samples, three distinct slopes were calculated: 2.48 pA for 500 bp, 5.19 pA for 1.5 kbp, and 10.31 pA for 5 kbp (Figure 5d). These fits result in slightly lower values than in Figure 5c due to the boundaries used in the integration of individual events. This again marked a difference with a conventional nanopore approach where the event charge deficit is generally clustered rather than dispersed (SI S8). This method can be used for more complex samples, as shown by using a 1 kbp DNA ladder whereby 10 peaks can be clearly seen based on the peak current distributions alone (Figure 5g). Importantly, much like previously discussed, the peak current distributions and conductance are proportional to the DNA radius of gyration squared and hence surface area, see Figure 5i–j.

To confirm the generality of our approach, experiments were also performed with other analytes including a 1 kb RNA ladder (Figure 6a), ssDNA (M13mp18, 7.2 kb long, Figure 6b), and small protein monomers such as α-synuclein (14.5 kDa, hydrodynamic diameter 1.7–2.2 nm, 700 pM, Figure 6c). Much like the DNA ladder, it was possible to discriminate between different RNA fragment sizes albeit with lower precision due to the smaller radius of gyration and less well-defined structure. ssDNA often translocates very quickly <0.2 ms for M13; however, the detection in the nanobridge showed a ×200 slowdown, SI S11, S12. This effect is substantial considering alternative slow down strategies (sub-micro-seconds) often rely on buffer exchange such as use of high ionic strength LiCl[22] which is not commonly compatible with biological analytes. α-synuclein has a central role in neuro-degenerative disorders and particularly Parkinson's disease; however, it is exceptionally challenging to detect with conventional nanopore technology. The detection of proteins within this size regime at low concentration is not typical due to their fast translocation times and event rates significantly lower than those predicted from Smoluchowski rate equation, often requiring protein concentrations well in excess of 10–100nM.[9] As shown in Figure 6c, α-synuclein was significantly slowed down with the vast majority of the events ranging between 0.1–0.75 ms at 600 mV, while the current blockade was well-defined with a mean of 30 ± 3 pA and high SNR = 11.5 440 ± 1.1.

In summary, we have presented a new detection method for solid state nanopores based on dual barrel nanopipettes for the

DOI: 10.1021/acs.nanolett.7b03196
Nano Lett. XXXX, XXX, XXX–XXX

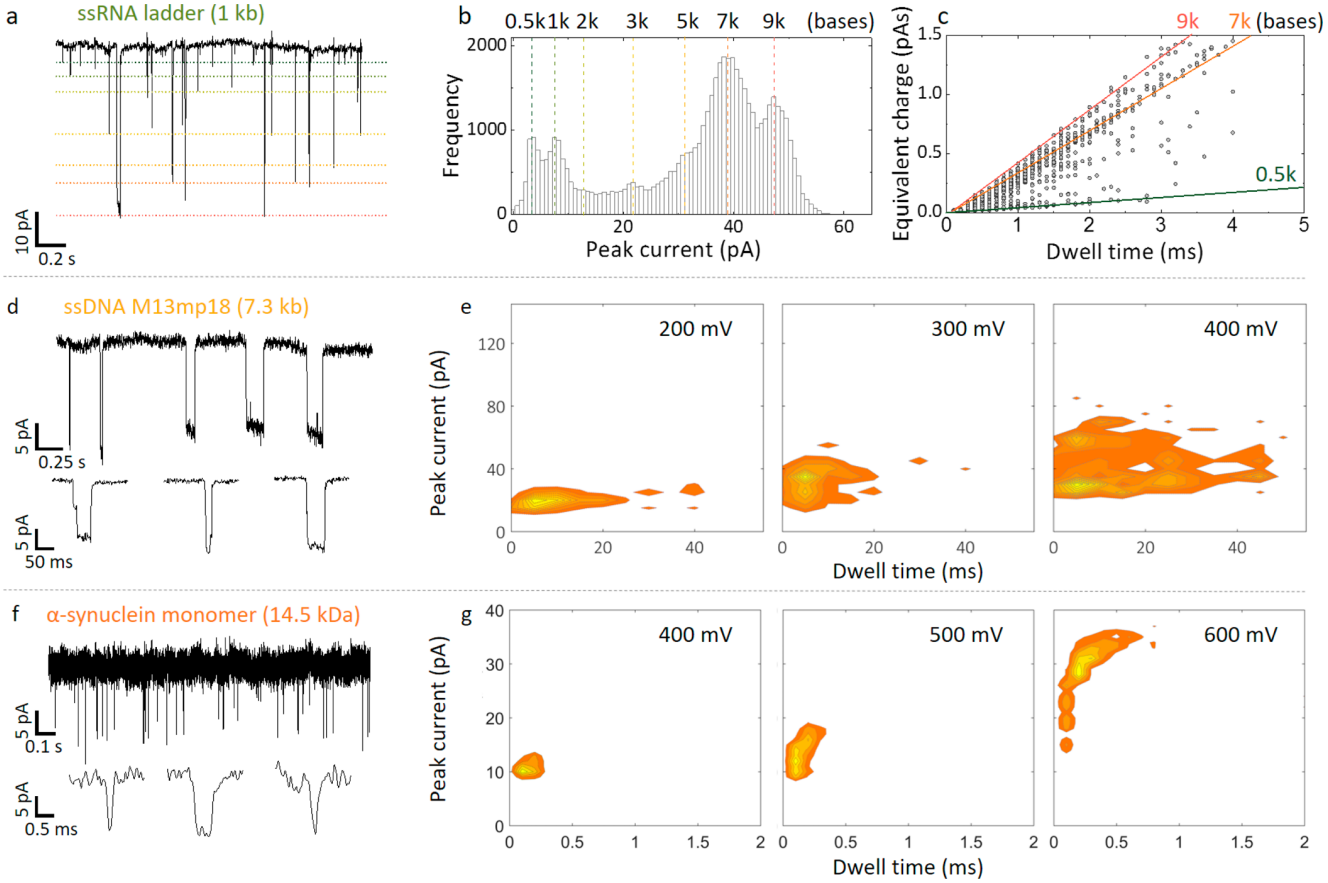

Figure 6. Detection of ssRNA, ssDNA, and α-synuclein in the nanobridge configuration. (a) Current−time trace for a 1 kb ssRNA ladder (2 μg/mL) in 100 mM KCl at an applied bias of 400 mV. For visualization purposes, approximate levels are designated for each fragment size (0.5, 1, 2, 3, 5, 7, 9 kb). (b) Peak current histogram and (c) corresponding equivalent charge plot. (d) Current time trace for a 100 pM sample of M13mp18 ssDNA in 100 mM KCl at an applied bias of 200 mV. (e) Current−dwell time contour plots are shown for voltages of 200 mV, 300 mV, and 400 mV, respectively. Similar to dsDNA, the dwell times increase with voltage due to compacting of the DNA in the nanobridge. Events as slow as 40 ms could be detected which is substantially slower than in a conventional nanopore configuration. (f) Current−time trace for monomeric α-synuclein for a concentration of 700 pM in 100 mM KCl and recorded at an applied bias of 400 mV. (g) Current−dwell time contour plots are shown for voltages of 400 mV, 500 mV, and 600 mV, respectively.

confinement and high-resolution detection of single molecules within a zeptoliter volume. The presented method does not require clean room facilities, is low-cost, and is time-efficient to fabricate and operate. We demonstrate that nanobridges can slow down molecules by several orders of magnitude compared to conventional nanopores with the same dimension. This is a substantial improvement over existing nanopore methods that reduce translocation speeds by modulating viscosity, electrophoretic force, and pressure, which often result in broadening of current/dwell time distributions and lower SNR, and in turn hinders the discrimination of multiple analytes in complex samples. Sampling rates can be as low as 1 kHz, which results in significantly lower noise facilitating the rejection of local interference and at the same time enabling the use of simpler/cheaper amplifiers. We demonstrated that, compared to conventional nanopores, nanobridge translocation peak currents exhibit tighter distributions with lower fwhm values and superior SNR performance. As direct consequence, an accurate molecular size readout can be performed solely on the current amplitude or alternatively, as in the case of multiple DNA populations, from the equivalent charge/dwell time distributions.

We showed that it is possible to extend our platform to single molecule protein detection. Generally, in nanopore sensing, an optimal SNR is achieved with low nanopore channel depth and pore dimensions closely matching those of the analyte. Different protein analytes have dimensions spanning several orders of magnitude which require a broad range of nanopore sizes for optimal detection. In contrast, nanobridge detection is particularly versatile as it allows to confine single analyte in the nanobridge independent of the analyte dimensions. Importantly, the method capabilities can be extended to confine and detect a wide range of analytes including RNA, ssDNA, and small proteins which are particularly challenging to detect with conventional nanopore as the diffusion volume is restricted. We believe that this platform can be adapted for detection of targeted analytes in biological fluids, by incorporation of a sieving matrix such as a hydrogel within the nanopipettes.

Built upon nanopore foundations, the reported method offers substantial technological advantages including single molecule confinement and slowdown of molecular transport, enabling longer detection times at higher signal-to-noise ratios. As such, the presented method opens the door for future possibilities to measure a wide range of biological analytes and extract, label-free, single molecular and conformational

DOI: 10.1021/acs.nanolett.7b03196
Nano Lett. XXXX, XXX, XXX−XXX

information usually inaccessible with conventional nanopore technology.

■ ASSOCIATED CONTENT

Supporting Information

The Supporting Information is available free of charge on the ACS Publications website at DOI: 10.1021/acs.nanolett.7b03196.

SEM images of the nanopores, salt dependence, characterization of stability, translocation statistics, and power spectral density (PDF)

■ AUTHOR INFORMATION

Corresponding Authors

*E-mail: joshua.edel@imperial.ac.uk; phone number: 020 7594 0754.

*E-mail: alex.ivanov@imperial.ac.uk.

ORCID

Tim Albrecht: 0000-0001-6085-3206

Joshua B. Edel: 0000-0001-5870-8659

Funding

J.B.E. has been funded in part by an ERC starting (NanoP), proof of concept (NanoPP), and consolidator (NanoPD) grants. A.I., Y.Z., Y.K., and J.B.E. acknowledge support from EPSRC grant EP/P011985/1. A.I. acknowledges the support of the IC Research Fellowship.

Notes

The authors declare no competing financial interest.

■ ACKNOWLEDGMENTS

We are grateful to Prof. Y. Rabin and Prof. A.Y. Grosberg for useful and stimulating discussions.

■ REFERENCES

(1) Howorka, S.; Siwy, Z. *Chem. Soc. Rev.* **2009**, *38*, 2360−2384.

(2) Miles, B. N.; Ivanov, A. P.; Wilson, K. A.; Doğan, F.; Japrung, D.; Edel, J. B. *Chem. Soc. Rev.* **2013**, *42*, 15−28.

(3) Wanunu, M. *Phys. Life Rev.* **2012**, *9*, 125−158.

(4) Ivanov, A. P.; Actis, P.; Jönsson, P. P.; Klenerman, D.; Korchev, Y.; Edel, J. B. *ACS Nano* **2015**, *9*, 3587−3594.

(5) Clarke, J.; Wu, H. C.; Jayasinghe, L.; Patel, A.; Reid, S.; Bayley, H. *Nat. Nanotechnol.* **2009**, *4*, 265−270.

(6) Carson, S.; Wanunu, M. *Nanotechnology* **2015**, *26*, 1−14.

(7) Venkatesan, B. M.; Bashir, R. *Nat. Nanotechnol.* **2011**, *6*, 615−624.

(8) Pedone, D.; Firnkes, M.; Rant, U. *Anal. Chem.* **2009**, *81*, 9689−9694.

(9) Storm, A. J.; Storm, C.; Chen, J.; Zandbergen, H.; Joanny, J. F.; Dekker, C. *Nano Lett.* **2013**, *13*, 658−663.

(10) Rissin, D. M.; Kan, C. W.; Campbell, T. D.; Howes, S. C.; Fournier, D. R.; Song, L.; Piech, T.; Patel, P. P.; Chang, L.; Rivnak, A. J.; Ferrell, E. P.; Randall, J. D.; Provuncher, J. K.; Walt, D. R.; Duffy, D. C. *Nat. Biotechnol.* **2010**, *28*, 595−599.

(11) Fraccari, R. L.; Ciccarella, P.; Bahrami, A.; Carminati, M.; Ferrari, G.; Albrecht, T. *Nanoscale* **2016**, *8*, 7604−7611.

(12) Rosenstein, J. K.; Wanunu, M.; Merchant, C. A.; Drndić, M.; Shepard, K. L. *Nat. Methods* **2012**, *9*, 487−492.

(13) Shekar, S.; Niedzwiecki, D. J.; Chien, C. C.; Ong, P.; Fleischer, D. A.; Lin, J.; Rosenstein, J. K.; Drndić, M.; Shepard, K. L. *Nano Lett.* **2016**, *16*, 4483−4489.

(14) Feng, J.; Liu, K.; Bulushev, R. D.; Khlybov, S.; Dumcenco, D.; Kis, A.; Radenovic, A. *Nat. Nanotechnol.* **2015**, *10*, 1070−1076.

(15) Fologea, D.; Gershow, M.; Ledden, B.; McNabb, D. S.; Golovchenko, J. A.; Li, J. *Nano Lett.* **2005**, *5*, 1905−1909.

(16) Kowalczyk, S. W.; Wells, D. B.; Aksimentiev, A.; Dekker, C. *Nano Lett.* **2012**, *12*, 1038−1044.

(17) Garaj, S.; Hubbard, W.; Reina, A.; Kong, J.; Branton, D.; Golovchenko, J. A. *Nature* **2010**, *467*, 190−193.

(18) Larkin, J.; Henley, R.; Bell, D. C. *ACS Nano* **2013**, *7*, 10121−10128.

(19) Liu, S.; Lu, B.; Zhao, Q.; Li, J.; Gao, T.; Chen, Y.; Zhang, Y.; Liu, Z.; Fan, Z.; Yang, F.; You, L.; Yu, D. *Adv. Mater.* **2013**, *25*, 4549−4554.

(20) Squires, A. H.; Hersey, J. S.; Grinstaff, M. W.; Meller, A. *J. Am. Chem. Soc.* **2013**, *135*, 16304−16307.

(21) Freedman, K. J.; Crick, C. R.; Albella, P.; Barik, A.; Ivanov, A. P.; Maier, S. A.; Oh, S. H.; Edel, J. B. *ACS Photonics* **2016**, *3*, 1036−1044.

(22) Lu, B.; Hoogerheide, D. P.; Zhao, Q.; Zhang, H.; Tang, Z.; Yu, D.; Golovchenko, J. A. *Nano Lett.* **2013**, *13*, 3048−3052.

(23) Peng, H.; Ling, X. S. *Nanotechnology* **2009**, *20*, 185101−185101.

(24) Verschueren, D. V.; Jonsson, M. P.; Dekker, C. *Nanotechnology* **2015**, *26*, 234004−234004.

(25) Crick, C. R.; Albella, P.; Ng, B.; Ivanov, A. P.; Roschuk, T.; Cecchini, M. P.; Bresme, F.; Maier, S. A.; Edel, J. B. *Nano Lett.* **2015**, *15*, 553−559.

(26) Anderson, B. N.; Muthukumar, M.; Meller, A. *ACS Nano* **2013**, *7*, 1408−1414.

(27) Rodolfa, K. T.; Bruckbauer, A.; Zhou, D.; Korchev, Y. E.; Klenerman, D. *Angew. Chem., Int. Ed.* **2005**, *44*, 6854−6859.

(28) Rodolfa, K. T.; Bruckbauer, A.; Zhou, D.; Schevchuk, A. I.; Korchev, Y. E.; Klenerman, D. *Nano Lett.* **2006**, *6*, 252−257.

(29) Crick, C. R.; Sze, J. Y. Y.; Rosillo-Lopez, M.; Salzmann, C. G.; Edel, J. B. *ACS Appl. Mater. Interfaces* **2015**, *7*, 18188−18194.

(30) Freedman, K. J.; Otto, L. M.; Ivanov, A. P.; Barik, A.; Oh, S. H.; Edel, J. B. *Nat. Commun.* **2016**, *7*, 10217−10217.

(31) Wei, C.; Bard, A. J.; Feldberg, S. W. *Anal. Chem.* **1997**, *69*, 4627−4633.

(32) Ebejer, N.; Schnippering, M.; Colburn, A. W.; Edwards, M. A.; Unwin, P. R. *Anal. Chem.* **2010**, *82*, 9141−9145.

(33) Hansma, P. K.; Drake, B.; Marti, O.; Gould, S. A. C.; Prater, C. B. *Science* **1989**, *243*, 641−643.

(34) Korchev, Y. E.; Bashford, C. L.; Milovanovic, M.; Vodyanoy, I.; Lab, M. J. *Biophys. J.* **1997**, *73*, 653−658.

(35) Pud, S.; Chao, S.-H.; Belkin, M.; Verschueren, D.; Huijben, T.; van Engelenburg, C.; Dekker, C.; Aksimentiev, A. *Nano Lett.* **2016**, *16*, 8021−8028.

(36) Liu, X.; Skanata, M. M.; Stein, D. *Nat. Commun.* **2015**, *6*, 6222−6222.

(37) Langecker, M.; Pedone, D.; Simmel, F. C.; Rant, U. *Nano Lett.* **2011**, *11*, 5002−5007.

(38) Pedone, D.; Langecker, M.; Abstreiter, G.; Rant, U. *Nano Lett.* **2011**, *11*, 1561−1567.

(39) Wenner, J. R.; Williams, M. C.; Rouzina, I.; Bloomfield, V. A. *Biophys. J.* **2002**, *82*, 3160−3169.

(40) Mihovilovic, M.; Hagerty, N.; Stein, D. *Phys. Rev. Lett.* **2013**, *110*, 1−5.

(41) Steinbock, L. J.; Lucas, A.; Otto, O.; Keyser, U. F. *Electrophoresis* **2012**, *33*, 3480−3487.

(42) Flory, P. J. *Principles of Polymer Chemistry*; Cornell University Press, 1953.

(43) Bell, N. A. W.; Muthukumar, M.; Keyser, U. F. *Phys. Rev. E: Stat. Phys., Plasmas, Fluids, Relat. Interdiscip. Top.* **2016**, *93*, 022401.

DOI: 10.1021/acs.nanolett.7b03196
Nano Lett. XXXX, XXX, XXX−XXX